Doctorate Dissertation

博士論文

Development of a frequency dependent squeezed vacuum source for broadband quantum noise reduction in advanced gravitational-wave detectors

第二世代重力波検出器における広帯域量子ノイズ低減のための周波数依存スクイーズ真空源の開発

A Dissertation Submitted for Degree of Doctor of Philosophy

September 2020

令和２年９月博士（理学）申請

Department of Astronomical Science, School of Physical Sciences,
The Graduate University for Advanced Studies, SOKENDAI
総合研究大学院大学物理科学研究科天文科学専攻

Yuhang Zhao

ユハン　ザオ

Supervisors: Matteo Leonardi, Raffaele Flaminio,
Ryutaro Takahashi, Yoichi Aso

論文の内容の要旨

Development of a frequency dependent squeezed vacuum source for broadband quantum noise reduction in advanced gravitational-wave detectors

(第二世代重力波検出器における広帯域量子ノイズ低減のための周波数依存スクイーズ真空源の開発)

Yuhang Zhao
ユハン　ザオ

Abstract

In the last five years, Advanced LIGO and Advanced Virgo detectors have already made several groundbreaking scientific discoveries. These detectors recently terminated the third observation run and are now undergoing an upgrade phase to further improve their sensitivity. Up to now, more than seventy gravitational wave candidates were detected, allowing to study various unknown systems, such heavy mass black hole binary systems, neutron star - black hole systems and add further information to know stellar systems such as binary neutron star systems. KAGRA, the Japanese gravitational wave detector, has terminated the construction phase last year and has recently joined the network.

In the third observation run, LIGO and Virgo started using frequency independent squeezing. This technology, already in use at GEO600 since 2010, allowed for a substantial improvement of the detectors' sensitivity, reducing the impact of the quantum noise. In particular, the way frequency independent squeezing was used in LIGO and Virgo, allowed for a reduction of mainly the shot noise component of the quantum noise, at the expense of an increase of the radiation pressure noise component. The increase of the radiation pressure noise was not an issue so far, since it was not one of the dominating noises, up to the last observation run. It was in fact reported by LIGO that the low frequency radiation pressure noise started to limit the detection range of interferometer during the third observation run. This makes the frequency independent squeezing not optimal anymore. Luckily, the use of a frequency dependent squeezing allows to circumvent this limitation, allowing for a broadband reduction of the detector's quantum noise.

My work aims to develop such frequency dependent squeezing source, which can be used to achieve a broadband quantum noise reduction for advanced gravitational wave detector. The project started in 2015 and takes places in the former TAMA300 facility, at the National Astronomical Observatory of Japan. The project's goal is to measure a 9dB frequency independent squeezing in the gravitational detector frequency bandwidth (10Hz-10kHz) and measure between 4dB to 6dB of frequency dependent squeezing. When I joined this project in 2017, the construction of the filter cavity (a 300m long Fabry-Perot optical cavity) was already finished and its characterization was ongoing. I contributed to it and measured its optical losses, a key parameter which define the limitation for the achievable frequency dependent squeezing level. I mainly worked on the development of a frequency independent squeezed vacuum source which is capable of producing 6dB of squeezing down to 10Hz. Around the world, very few laboratories can achieve squeezing at so low frequency and our project is the first group to demonstrate this technique within the KAGRA collaboration. By combining the filter cavity to the frequency independent squeezed vacuum source, we were able to perform the first measurement of frequency dependent squeezing with sub-shot noise in the whole gravitational wave detectors' frequency band.

This result is of paramount importance, not only because it is the first demonstration, but also because it shed light on the future implementation of frequency dependent squeezing in advanced gravitational wave detectors and pave the way for its use even in future generation gravitational wave detectors.

Contents

Introduction

Gravitational-wave (GW) astronomy started in 2015 with the detection of a binary black hole coalescence by the two Advanced LIGO detectors. Advanced Virgo came online in 2017 and recently also the Japanese detector KAGRA joined the gravitational wave detectors network. The detection of gravitational waves provides an innovate and unique insight to understand the Universe, bringing important results for fundamental physics, astrophysics, nuclear physics, astronomy and cosmology.
Nowadays, Earth-based gravitational-wave detectors can reach events at a redshift smaller than 1. The increase of their detection ability will bring more scientific benefit to all the relevant research fields. Therefore, the improvement of their sensitivity is of great importance.
Current and future gravitational-wave detectors are limited by quantum noise in a large part of their spectrum. Quantum noise in interferometers is caused by quantum fluctuations of the vacuum field entering their output port. Recently, gravitational-wave detectors have introduced the so-called squeezing, as a mitigation strategy. This technique consisted in replacing the standard vacuum field with manipulated vacuum states whose amplitude and phase uncertainties (which are equal in ordinary vacuum) were respectively increased and reduced. For such states, referred to as squeezed states, the Heisenberg uncertainty principle makes amplitude and phase uncertainties not possible to be reduced simultaneously. Squeezed states are usually represented as an ellipse in the quadrature plane. If the reduced-noise quadrature is aligned with the GW signal, the result is a reduction of the quantum noise. However, since the opto-mechanical coupling of the laser light with the interferometer test masses induces a rotation of the squeezing ellipse, by injecting a simple squeezing, known as frequency independent squeezing (where the ellipse orientation does not depend on the frequency) only one part of the quantum noise can be reduced.
A quantum noise reduction in the whole spectrum can be obtained by injecting a squeezed vacuum with a frequency dependence able to counteract the rotation caused by the interferometer so to keep GW signal always aligned with the

reduced-noise quadrature. Such frequency dependence can be achieved by reflecting a frequency-independent squeezed state off a detuned optical cavity with the appropriate bandwidth. This cavity is known as filter cavity. Obtaining a rotation at low frequency is particularly demanding, as it needs a filter cavity with high storage time. A rotation at a frequency smaller than 100 Hz, as required for advanced detectors, corresponds to a cavity storage time of more than 2 ms.
My PhD research focused on an experiment which managed to realize a source of frequency dependent squeezed vacuum, suitable for broadband quantum noise reduction of advanced GW detectors. To this purpose, a 300 m long filter cavity, has been installed in an arm of the former TAMA300 at NAOJ and a source of frequency independent squeezing has been developed. When I joined this project, the filter cavity integration and control were already achieved. I work on the cavity characterization, on the realization of the frequency independent squeezing source and on the coupling of the squeezing into the cavity which allowed to obtain the final results: a frequency dependent squeezed state with ellipse rotation at frequencies lower than 100 Hz.
Filter cavity characterization and losses measurement: optical losses in the filter cavity are one of the main limitations to the achievable squeezing level. In particular, what is important are the losses per unit length and therefore, in order to reduce such losses two approaches can be used: reduce the overall losses themselves, or increase the length of the filter cavity. Our 300m long filter cavity significantly relax the losses requirement with respect to shorter cavities, but nevertheless requires high-quality mirrors. Since this parameter is so crucial, we spent a considerable effort to fully characterize it. The measurement is performed obtaining a set of on and off resonance measurements of the reflected power. By comparing the amount of light promptly reflected by the cavity and the one reflected after circulating in it we could obtained the amount of power lost inside it and computed the cavity optical losses. The measurement result is in agreement with the expectation and has been published on PRD [1] and I am one of the author of this paper.
Development of a squeezer for gravitational wave detectors: a frequency independent squeezed vacuum source is a complex optical system based on a parametric down conversion process inside a non-linear crystal. I gave a major contribution in the construction of this system which includes four optical cavities (two of which contains non-linear crystals which require thermal stabilization), a Mach-Zehnder interferometer, two optical phase lock loops, two optical phase shifter, and eleven control loops. Our squeezer can generate 6 dB of squeezing in the whole

gravitational-wave detector frequency band (from 10Hz to 100kHz). NAOJ is now one of the few laboratories in the world that can produce low-frequency squeezing suitable for GW application and it is the first within the KAGRA collaboration.

Frequency dependent squeezing measurement: in order to produce frequency dependent squeezing, we coupled the frequency independent squeezed vacuum into the filter cavity. The matching is obtained by a telescope composed of two curved mirrors, hosted in-vacuum. The filter cavity is also in vacuum and the mirrors are suspended to reduce the effect of seismic noise. The reflection from the filter cavity is characterized by a balanced homodyne detector. A squeezing level of more that 3 dB above the rotation frequency was measured, along with a squeezing level of at least 1 dB at the rotation frequency and below. Our result is crucial for the gravitational wave community as we could demonstrate a key technology that allows to improve quantum noise in the whole detection bandwidth. Moreover, since we are using a full-scale filter cavity prototype, we developed a useful experience for future implementation in GW detectors. The paper presenting this result, of which I'm first author, has been published on PRL [2].

Chapter 1

Gravitational waves: theory and scientific payoff from their detection

Gravitational waves (GW) are generated by any object with time-varying quadrupole momentum of masses. The amplitude of such effect is so small that at present only astrophysical sources (fast moving, very compact and with large mass) can generate detectable gravitational waves. Several information about the astrophysical sources can be extracted from the GW waveform. Gravitational-wave detectors has recently "allowed us to listen" to these new messengers bringing important new results in fundamental physics, astrophysics and cosmology.

In this chapter I will review how GWs are generated and detected and I will briefly describe the scientific payoff of their detection. A much more complete review on GWs' theory, experiment and data analysis can be found in the book written by Creighton and Anderson [3].

1.1 Gravitational waves theory

Gravitational waves are predicted by the theory of general relativity [4][5]. They propagate at the speed of light deforming the space-time. The first direct detection of a gravitational-wave was done in 2015 by two earth-based large scale laser interferometers (LIGO Hanford and LIGO Livingston) [6]. Since then, there have been tens of GW events detected [7], which opened the exciting new field of *gravitational-wave astronomy.*

A key feature of gravitational waves is that the induced spacetime change can transfer energy from the waves to the objects they pass by. However, this energy transfer is so small that the induced motion of objects is very difficult to be detected. This is also beneficial since gravitational waves are almost not influenced by their interaction with matter.

1.1.1 Gravitational Waves From General Relativity

The theory of general relativity (GR) is a generalization of the theory of special relativity, which postulates the principle of relativity and invariance of the speed of light. Special relativity is built on lots of inertial coordinates which exist with various velocities and orientations. The transformation among them is done with Lorentz transformation and physics keeps invariant. As a result, this transformation builds a close relation between space and time, which breaks our usual view of them.

To extend the principle of relativity to the principle of general covariance, there is the demand to have no preferred coordinate system. Besides, we can always find locally inertial frame in the vicinity of any space-time point because of the principle of equivalence. Similarly, manifold locally resembles Euclidean space near each point. So general relativity is formulated on manifolds.

The following is an excerpt from Carroll's book [8]. For a more complete review of general relativity, refer to the book. Let's start with the definition of distance

$$ds^2 = g_{\mu\nu} dx^\mu dx^\nu \tag{1.1}$$

where ds is a sufficiently small distance between two points, $g_{\mu\nu}$is the metric tensor which contains the geometry information of space-time, dx represents an infinitesimal change in one of the spatial indices' dimension. The indices μ and ν stand for the dimension of spacetime and, according to the Einstein summation convention, we need to run over all of them, for example, in our flat spacetime we have $\{t, x, y, z\}$ dimensions and metric takes the form

$$\eta_{\mu\nu} = \begin{pmatrix} -1 & 0 & 0 & 0 \\ 0 & 1 & 0 & 0 \\ 0 & 0 & 1 & 0 \\ 0 & 0 & 0 & 1 \end{pmatrix} \tag{1.2}$$

after we run over $\eta_{00}dx^0dx^0, \eta_{01}dx^0dx^1, \eta_{02}dx^0dx^2, \eta_{03}dx^0dx^3, \eta_{10}dx^1dx^0...$ until $\eta_{33}dx^3dx^3$, we have the distance between two points in flat spacetime as

$$ds^2 = \eta_{\mu\nu}dx^\mu dx^\nu = -c^2dt^2 + dx^2 + dy^2 + dz^2 \tag{1.3}$$

The transformation between two coordinates is to induce a change of metric as

$$g_{\alpha\beta} = g_{\mu\nu}\frac{\partial x^\mu}{\partial x^\alpha}\frac{\partial x^\nu}{\partial x^\beta} \tag{1.4}$$

The change of coordinate actually translate to a modification of the metric. Thanks to this equation, we can freely define any coordinate systems. This is called gauge freedom.

As we said at the beginning, manifold locally resembles flat space. So the curvature comes from how do we put these sufficiently small and flat space together. How we can connect them translates on how we can parallel transport a vector from one point to another. In differential geometry, any vector is a directional derivative. Directional derivative is not a derivative along 'x' direction or a partial derivative, but a derivative along a direction described by the combination of all dimensions. Parallel transport means that such vector doesn't change direction

$$0 = \lim_{\Delta t\to 0}\frac{v^\alpha(t+\Delta t) - v^\alpha(t)}{\Delta t} = \frac{dv^\alpha}{dt} =: u^\mu\nabla_\mu v^\alpha \tag{1.5}$$

this equation represents a vector v^α parallel transport along the curve $\mathbf{u}$. The connection ∇_μ doesn't always take the form of $\frac{\partial}{\partial x^\mu}$, however, we can always find a transformation to a new coordinates to make it be an ordinary derivative. In this case, we can find connection coefficient

$$\Gamma^\gamma_{\alpha\beta} := \frac{\partial x^\gamma}{\partial x'^\mu}\frac{\partial^2 x'^\mu}{\partial x^\alpha \partial x^\beta} \tag{1.6}$$

also called Christoffel symbol. From the fact that the inner product of two vectors will remain the same if they are parallel transported, we can have

$$\Gamma^\gamma_{\alpha\beta} = \frac{1}{2}g^{\gamma\delta}(\frac{\partial}{\partial x^\alpha}g_{\beta\delta} + \frac{\partial}{\partial x^\beta}g_{\delta\alpha} - \frac{\partial}{\partial x^\delta}g_{\alpha\beta}) \tag{1.7}$$

In this way we connect the metric to the Christoffel symbol. The parallel transportation for motion is a straight line in Newtonian mechanics. However, in a curved space time, the "straight" lines are represented by geodesics. Following the same principle

with equation 1.5, we can construct an equation for motion with tangent vector **u**

$$u^\mu \nabla_\mu u^\alpha = \frac{dx^\mu}{dt}\frac{\partial}{\partial x^\mu}(\frac{dx^\alpha}{dt}) + \Gamma^\alpha_{\mu\nu}\frac{dx^\mu}{dt}\frac{dx^\nu}{dt} = 0 \tag{1.8}$$

For the middle part of above equation, it's important to notice that the first term actually is the acceleration of a particle. Besides, the connection coefficient will vanish if the spacetime is flat. So we see how the connection coefficient contains the information of the gravitational field.

The curvature of our spacetime is determined by the parallel transportation of vectors. If a vector is transported in a closed circle and return to its original point with different orientation, we say spacetime is curved in the vicinity of that point. By following this method, we could define Riemann tensor as

$$R^\delta_{\alpha\beta\gamma} = -\frac{\partial}{\partial x^\alpha}\Gamma^\delta_{\beta\gamma} + \frac{\partial}{\partial x^\beta}\Gamma^\delta_{\alpha\gamma} - \Gamma^\delta_{\alpha\mu}\Gamma^\mu_{\beta\gamma} - \Gamma^\delta_{\beta\mu}\Gamma^\mu_{\alpha\gamma} \tag{1.9}$$

By using the fact that metric $g_{\mu\nu}$ can be used to raise or lower indices and the same upper and lower index will compose Kronecker delta, we can get another two useful tensors from Riemann tensor

$$R_{\alpha\beta} := R^\mu_{\alpha\mu\beta} \quad and \quad R := g^{\mu\nu}R_{\mu\nu} \tag{1.10}$$

which are usually called Ricci tensor and Ricci scalar or scalar curvature. After considering the contracted Bianchi identity, we can get Einstein tensor

$$G_{\alpha\beta} := R_{\alpha\beta} - \frac{1}{2}g_{\alpha\beta}R \tag{1.11}$$

Based on the fact that geometry of spacetime is decided by matter (stress-energy tensor $T_{\alpha\beta}$), the Einstein field equation have the form

$$G_{\alpha\beta} = \frac{8\pi G}{c^4}T_{\alpha\beta} \tag{1.12}$$

For cases far from gravitational force sources or where the gravity potential is low, like our solar system, we can take following approximation for the metric close to us

$$g_{\alpha\beta} = \eta_{\alpha\beta} + h_{\alpha\beta} \tag{1.13}$$

where $h_{\alpha\beta} \ll 1$. By combining this linearized metric and trace-reversed metric per-

turbation expression and Lorenz gauge, we can have a simplified version of Einstein equation

$$-\Box\bar{h}_{\alpha\beta} = \frac{16\pi G}{c^4}T_{\alpha\beta} \tag{1.14}$$

This is a wave equation where $\Box = -(1/c^2)\partial_t^2 + \nabla^2$ implies that gravity perturbations, also said GWs, travel at the speed of light and the matter stress-energy tensor acts as a source to generate gravitational waves. We will set the right hand side of the above equation to be zero when we consider the propagation of GWs. This is because the universe is close to vacuum on average. [9]

1.1.2 Propagation of gravitational waves and its effect

As said at the end of last part, the propagation of GWs satisfy

$$\Box\bar{h}_{\alpha\beta} = 0 \tag{1.15}$$

and from the Lorenz gauge condition, $\frac{\partial\bar{h}_{\alpha\beta}}{\partial x_\alpha} = 0$, we can easily find $h^{\alpha\beta}k_\beta = 0$ and this means that the wave oscillation must be orthogonal to its propagation direction. This indicates the wave is transverse. Considering the property of wave operator, we also have $h^\alpha_\alpha = 0$ and $h_{\alpha\beta}u^\beta = 0$. The first equation indicates the wave is traceless and the second equation tells $h_{\alpha 0} = 0$. So the only non-vanishing components are

$$h_{11} = -h_{22} \tag{1.16}$$

$$h_{12} = h_{21} \tag{1.17}$$

Recall that Riemann tensor can be represented by the two derivatives of the metric from equation 1.7 and 1.9. So we can relate the non-vanishing terms to the ones in Riemann tensor.

$$R_{0101} = -R_{0202} = -\frac{1}{2}\frac{\partial^2}{\partial t^2}h_{11} := -\frac{1}{2}\ddot{h}_+ \tag{1.18}$$

$$R_{0102} = R_{0102} = -\frac{1}{2}\frac{\partial^2}{\partial t^2}h_{12} := -\frac{1}{2}\ddot{h}_\times \tag{1.19}$$

So the non-vanishing components in Riemann tensor prove that GWs are not an artificial effect from the choice of gauge.

Now that the theory of GWs has been intruduced, let's have a look into the ef-

fect of GWs on the space-time. When GWs pass by, they will change the curvature of spacetime. Let's imagine there are two nearby freely falling particles separated by $\xi(sin\theta cos\phi\hat{x} + sin\theta sin\phi\hat{y} + cos\theta\hat{z})$, the passing by GWs will cause them to follow different geodesics. This tidal effect causes a relative acceleration of these two particles, which can be derived from the definition of acceleration and from the Riemann tensor. The result of this tidal acceleration for weak field slow motion is $a_j = -R_{0i0j}\xi^j$. The induced motion of particles in different directions can be written as

$$a_x = -R_{0x0x}\xi^x - R_{0y0y}\xi^y = \frac{1}{2}\ddot{h}_+\xi sin\theta cos\phi\hat{x} + \frac{1}{2}\ddot{h}_\times\xi sin\theta sin\phi\hat{y} \tag{1.20}$$

$$a_y = -R_{0y0y}\xi^y - R_{0y0x}\xi^x = -\frac{1}{2}\ddot{h}_+\xi sin\theta sin\phi\hat{x} + \frac{1}{2}\ddot{h}_\times\xi sin\theta cos\phi\hat{y} \tag{1.21}$$

$$a_z = 0 \tag{1.22}$$

where we have fixed the GW traveling direction to be the z direction. The equation above tells us the position dependent motion on the plane of $\theta = \pi/2$. Figure 1.1 shows why we put subscript '+' and '×' for the two degree of freedoms of linearized metric which correspond to the two polarization of GWs. Two different motion styles are related to the non-vanishing linearized metric sign, location of particles on x-y plane (sign of $cos\phi$ or $sin\phi$) and base vector (final direction is the combination of $\hat{a_x}$ and $\hat{a_y}$). For example, for the first quadrant of plus polarization, the sign for $\hat{a_x}$ is positive (positive metric and $cos\phi$ is positive in the first quadrant) and sign for $\hat{a_y}$ is negative (negative metric and $sin\phi$ is positive in the first quadrant). Following the same principle, we can compute the moving trend in each quadrant for two polarization motions. For plus polarization, the combination of particles motion in different quadrants is squeezing y direction and stretching x direction. Due to the oscillation of h, the squeezing and stretching will change with the frequency of gravitational wave signal. In the end, this plus polarization forms a motion style like a 'plus' shape. On the other hand, for cross polarization, the squeezing and stretching exchanges along '$y = x$' and '$y = -x$' direction. As a result, it forms a motion style like a 'cross' shape. This is a differential motion and is crucial for the detection principle of gravitational waves.

Then at any point on the $\theta = \pi/2$ plane, a combination of a_x and a_y forms the geodesic deviation acceleration vector. After the integration over time, the separation of two nearby points can be written as

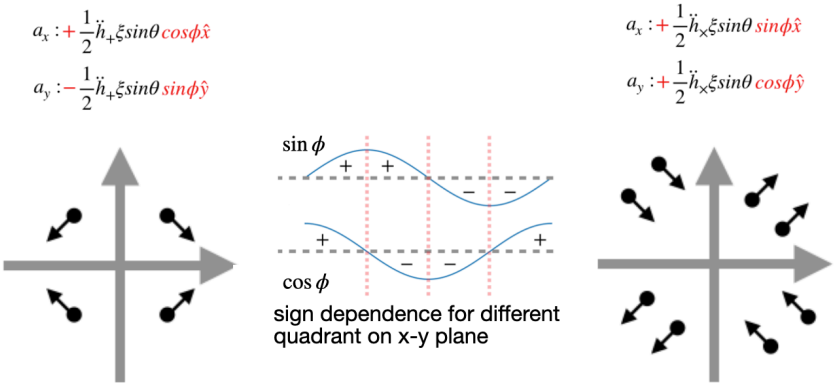

Figure 1.1: Particles motion caused by plus/cross-polarized GWs.

$$\xi(t) = \xi(0)\left(1 + \frac{1}{2}h_+ sin^2\theta cos2\phi + \frac{1}{2}h_\times sin^2\theta sin2\phi\right) \tag{1.23}$$

For $\theta = 0$ or $\theta = \pi$, $\xi(t)$ will vanish which means the GW will not change the relative distance between particles. This is due to the GWs is transverse and also causes the loss of detector's sensitivity along those directions. For $\theta = \pi/2$, the separation effect is maximized. This is one of the reasons why we need a global GW detector network prepare for GWs coming for all sky directions.

1.1.3 Generation of gravitational waves

From the propagation of GWs, we understand the spatial dependence of its signal. However, the time dependence of this signal, which is h_+ and $h_\times$ in equation 1.23, originates from the GW's source behavior. From the last section, we could see that the wave equation for gravitational field has a quite similar form compared to the electromagnetic wave. However, the gravitational wave is different in the aspect of generation. For example, as we know, once a charged particle has acceleration, it will radiate energy which is usually called dipole radiation [10]. While, in the case of gravitational wave, the second derivative mass dipole moment is

$$\ddot{D} = \sum_i m_i \ddot{x}_i = \dot{p} \tag{1.24}$$

It is obvious that gravitational wave can not be generated from this mass dipole moment because of the conservation of momentum. Instead, GWs are generated

from quadrupole moment. The solution of equation 1.14 is

$$\bar{h}^{ij}(t,x) \simeq \frac{2G}{c^4 r}\ddot{I}^{ij}(t-r/c) \tag{1.25}$$

where $I^{ij}$is the quadrupole moment witch takes the form

$$I^{ij} = \int (x^i x^j - \frac{1}{3}r^2\delta^{ij})\rho d^3x \tag{1.26}$$

By using the above equations 1.25 and 1.26, we can do some simple estimation based on the amplitude of GWs. Let's consider a rotating bar with mass M, length l and spinning with angular frequency ω, then we have $I \sim MR^2$ and $\ddot{I} \sim Mv^2 = M\omega^2 l^2$. Assuming all the parameters of the bar to be order of 1 ($M = 1kg$, $l = 1m$, etc.) and considering the distance should be much farther than the wavelength of GW ($r \gg c/\omega$), we will have $h \ll 10^{-53}$ which leads to a non-measurable deformation of space-time. However, if we have a binary neutron star system with equal mass of $3M_\odot$ and is located in the $20Mpc$ distance Virgo cluster, it will generate GW with magnitude of 10^{-21} at the time of the merge. By comparing above two estimation with the current generation GW detectors, we can understand why the focus of GWs detector are GWs from astronomical sources.

The generated signal amplitude is estimated as above, and the time evolution clearly depends on the change of quadrupole moments according to equation 1.25. For the well-investigated compact binary coalescence (CBC) process, the frequency of gravitational wave signal is twice the frequency of orbital frequency. The orbital frequency increases with the evolving of the system, and it is related with chirp mass $M = \frac{(m_1 m_2)^{3/5}}{(m_1+m_2)^{1/5}}$ (m_1 and m_2 are the two masses of the binary system) and time of coalescence t as [11]

$$f_{GW}^{-8/3}(t) = \frac{(8\pi)^{8/3}}{5}\left(\frac{GM}{c^3}\right)^{5/3}(t_c - t) \tag{1.27}$$

This equation shows the frequency is inversely proportional to mass and time to coalescence. For example, the first detection GW150914 is a CBC of two $\sim 35M_\odot$ black holes which gives final instantaneous frequency of $\sim 200Hz$. This frequency is located in the most sensitive part of aLIGO.

1.1.4 Astronomical sources for GWs

As discussed in the last section, the generation of gravitational wave signal depends on the evolution of the quadrupole momentum of its source. The characteristics of the source and its dynamic behavior determine the amplitude and the frequency of the emitted gravitational wave. This is the reason why the astrophysical sources are usually classified by their characteristic frequency. Gravitational-wave detection focus on four frequency bands: the extremely low frequency band (10^{-15} to 10^{-18} Hz), the very low frequency band (10^{-7} to 10^{-9} Hz), the low frequency band (10^{-4} to 1 Hz) and the high frequency band (1 to 10^4 Hz) [12]

This classification of frequencies corresponds to different gravitational wave sources and detection methods as the following introduction:

High frequency sources (1 to 10^4 Hz):

1. **Binary neutron stars (BNS) and binary black holes (BBH) ($1M_\odot - 10^3M_\odot$)**: A number of astrophysical scenarios can produce such binary systems. Gravitational waves are generated during the entire inspiral phases of the system.

2. **Core-Collapse supernovae**: With the evolution of stellar (initial mass of $8M_\odot - 70M_\odot$), gravitational collapse happens when core mass exceeds the maximum supportab

   le by electron degeneracy pressure. Gravitational waves are generated from this process and subsequent explosion.

3. **Neutron Stars**: Gravitational waves can be generated from coalescing neutron stars, which evolves for different stages of binary neutron stars coalesence. Continuous gravitational waves are expected from spinning neutron stars with small 'mountains'. Burst gravitational wave is also expected from magnetar giant flares and pulsar glitches.

4. **Stochastic gravitational wave backgrounds**: It may come mainly from astrophysical sources, which is the superposition of a large number of unresolved sources of gravitational waves from BBH and BNS [13].

Low frequency sources (10^{-4} to 1 Hz): supermassive black hole binaries ($10^3M_\odot - 10^9M_\odot$), extreme mass ratio inspirals, dwarf/white dwarf binaries, astrophysical stochastic gravitational wave backgrounds.

Very low frequency sources (10^{-7} to 10^{-9} Hz): supermassive black hole binaries ($10^9 M_\odot$) and the stochastic gravitational wave backgrounds from it.

Ultra low frequency sources (10^{-15} to 10^{-18} Hz): cosmological stochastic gravitational wave backgrounds

1.2 Detection of gravitational waves

As shown in figure 1.1, GWs cause the relative motion of nearby particles. Since the GWs modulate the distance between objects, a direct way to measure them is to continuously monitor such distance. Since the velocity of the light is always constant, we can use it as a ruler to perform this measurement.

The Michelson interferometer as schematically shown in Fig. 1.2 was firstly developed by Michelson for the famous Michelson-Morley experiment [14]. Such instrument is capable of measuring the differential change in the length of its two arms. A laser light (originally Michelson used yellow light from a sodium flame for alignment and white light for the actual observations) is injected into interferometer and it is separated in two part by a 50:50 beamsplitter. Each part is sent along one of the interferometer arms. The two beams are reflected back to the beamsplitter and they recombine. A differential change in the arm length results in a change of the relative phase of the two beams, thus producing a change in the power reaching the output photodetector. As shown in Figure 1.2, the fields reflected from each end mirror in an interferometer with arm length L can be expressed as $\frac{1}{2}E_0 e^{2ik(L+x_1)}$ and $\frac{1}{2}E_0 e^{2ik(L+x_2)}$ respectively. Where E_0 is the modulus of electric field and k is the wavenumber. These two electric fields carry the information of mirror movement x_1 and x_2. At the beamsplitter, they interfere with each other and propagate to output port as

$$E_{output} = \frac{1}{2}E_0 e^{2ikL}(e^{2ikx_1} - e^{2ikx_2}) \tag{1.28}$$

$$P_{output} = \bar{P} sin^2(k(x_1 - x_2)) \tag{1.29}$$

GWs cause differential arm length change and this information is magnified by interferometer and gives output as equation 1.28. As shown in figure 1.3, the interferometer output power is different for different working points. To limit the impact of many noises, detectors are usually operated close to dark fringe.

The arm length difference $x_1 - x_2$ induced by GWs is not a constant. If we assume a GW coming from z direction with one polarization and have a wavelength

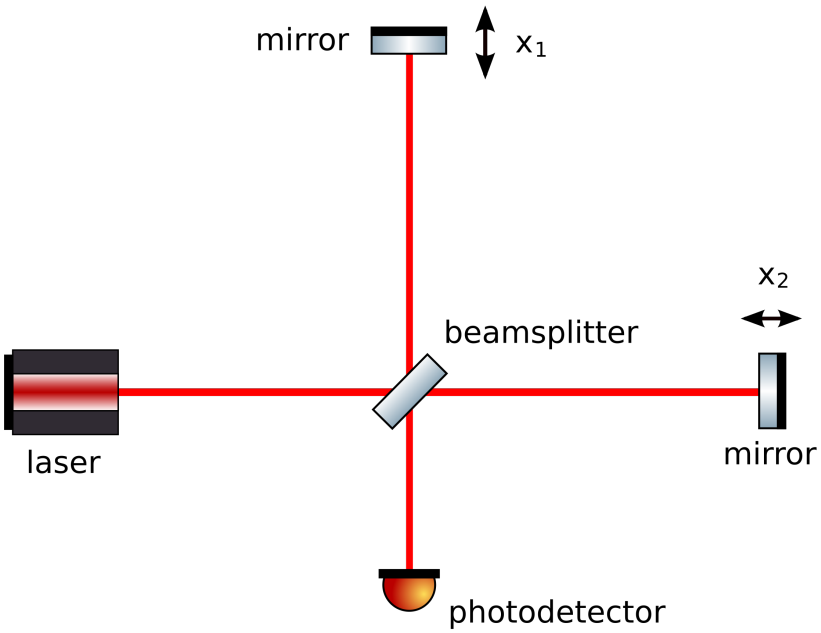

Figure 1.2: Scheme of a Michelson interferometer. A laser light (originally Michelson used yellow light from a sodium flame for alignment and white light for the actual observations) is injected into interferometer it arrives to a 50:50 beamsplitter, where it is separated in two parts. Each part is sent along one of the interferometer arms. After the reflection from end mirrors, the light beam will carry information of each end mirror's motion x_1 and x_2. Interference happens when the two beams come back to the beamsplitter and recombine. A differential change in the arm length results in a change of the relative phase of the two beam, thus producing a change in the power reaching the output photodetector.

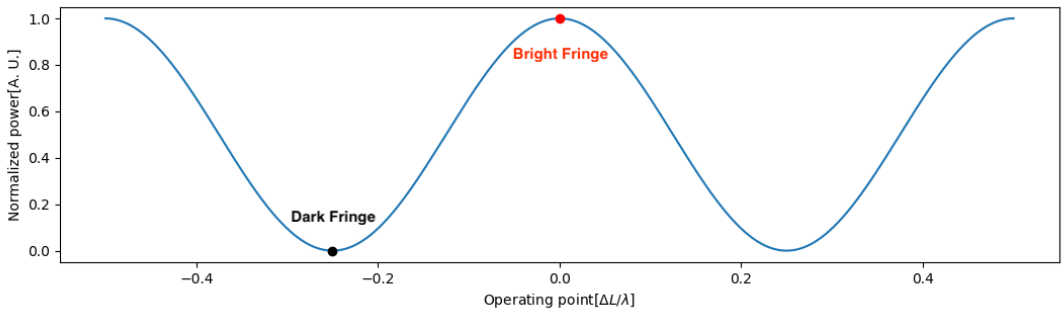

Figure 1.3: Operating point of Michelsone interferometer. Interferometer works close to dark finge to make output signal insensitive to common mode noises, like input power fluctuations.

larger than the arm of interferometer, we can get the relative phase change between two arms $\int_{-\infty}^{\infty} H(\omega)h_+(\omega)e^{i\omega t}d\omega$, where $H(\omega)$ is the frequency dependent response of interferometer [15]

$$H(\omega) = \frac{\Omega_{laser}}{\omega} \sin\gamma e^{-i\gamma} \tag{1.30}$$

As seen in the last section, the frequency of the gravitational wave signals will be basically less than several tens of kHz for many astronomical sources. The phase term in the above equation tells us the maximum response, which indicates hundreds of kilometers arm is appreciable for simple Michelson interferometer but we know that such instruments are impossible to realize on Earth.

Nowadays, kilometric GW detectors based on this principle are used to detect gravitational wave signals in the region between few tens of Hz to few kHz. Such detectors (as Advanced LIGO [16] and Advanced Virgo [17]) are enhanced by several leading-edge techniques which will be introduced in the next chapter. They have already detected many GW signals [7], including the first direct detection of gravitational wave done by two LIGO detectors [6] in 2015.

In addition to ground-based laser interferometers, there are other projects aiming to detect gravitational waves in a different frequency regions. A summary of their expected sensitivities and frequency range can be appreciated in Fig. 1.4.

The low-frequency terrestrial detectors such as torsion bar antenna [18] and atom interferometers [19] take advantage of either novel arrangement of torsion bars or the nature of atomic clouds to beat low frequency noise such as seismic noise, suspension noise and so on. However, recent results on the newtonian noise makes it necessary to reexamine the noise influence of this type of detectors.

At the same low frequency region, there is also proposed space detector DECIGO [20] and BBO [21]. The test mass of these detectors are separated by $1000km$ so that the their frequency response is optimal for 0.1 to 10Hz. They will fly along an earth-like heliocentric orbit. So that the gravity field change from earth is negligible. Due to the high sensitivity design, the primordial gravitational wave background is highly possible to be detected.

The Laser interferometer space antenna (LISA) [22] is a space detector which aims for frequency range from $20\mu Hz$ to $1Hz$. It uses 2.5 million kilometers away spacecrafts to measure the gravitational wave induced laser phase change between them. Three spacecrafts are used and forms triangular shape. One important difference relative to ground based detector is that LISA uses heterodyne laser interferometer. These low frequency gravitational waves will give information about the

formation of binary systems in the Milky Way, about the verification binaries, about the early stage of coalenscence which could be detected by ground based detectors and about the early Universe at TeV energy scales.

GW at very low frequencies ($10^{-7} \sim 10^{-9}$Hz) are currently under-investigation by pulsar timing arrays (PTA) [23]. PTA uses a network of millisecond pulsars. The passage of GWs are imprinted on the measured pulse arrival times. Up to now, no detection is announced from PTA, but stochastic background of supermassive black hole merger is the most promising source.

A GWs background originated less than $\sim 10^{-20}$s after the Big Bang was predicted, which could be detectable with CMB method at ultra low frequency region ($10^{-15} \sim 10^{-18}$Hz). During the inflation, quantum fluctuations of the spacetime metric gave rise to both the observed primordial density perturbations and a potentially observable background of GWs. The GWs may show up as a B mode in the cosmic microwave background polarization. The detection of inflationary(cosmological) GWs is of great interest for cosmology. Unfortunately, the Planck experiment shown that the B-mode polarization detected by BICEP2 is due to the polarized emission from dust in our own galaxy. However, there is still plan to upgrade to BICEP3, which may give a detection. [24]

1.3 Science benefit of gravitational wave detection

From detections obtained during the first and second observation run (for a total of about 12 months of observation time), it was possible to extract several major scientific results. According to the expected improvement of detector's sensitivity, a deeper and wider universe will be explored in the future.

1.3.1 Highlights of science from the detected gravitational wave signals

In the first gravitational wave transient catalog (GWTC-1), ten BBH and one BNS mergers were announced [7]. At 90% confidence level, merger rate are inferred as $110 - 3840 Gpc^{-3}y^{-1}$ for binary neutron stars, $9.7 - 101 Gpc^{-3}y^{-1}$ for binary black holes. An upper limit at 90% confidence level for neutron star - black hole merger rate is determined as $610 Gpc^{-3}y^{-1}$. The merger rate is larger for BNS but the number of detections is lower because the generated signal is weaker than the BBH one. During the third observation run detection rate of one signal per week was

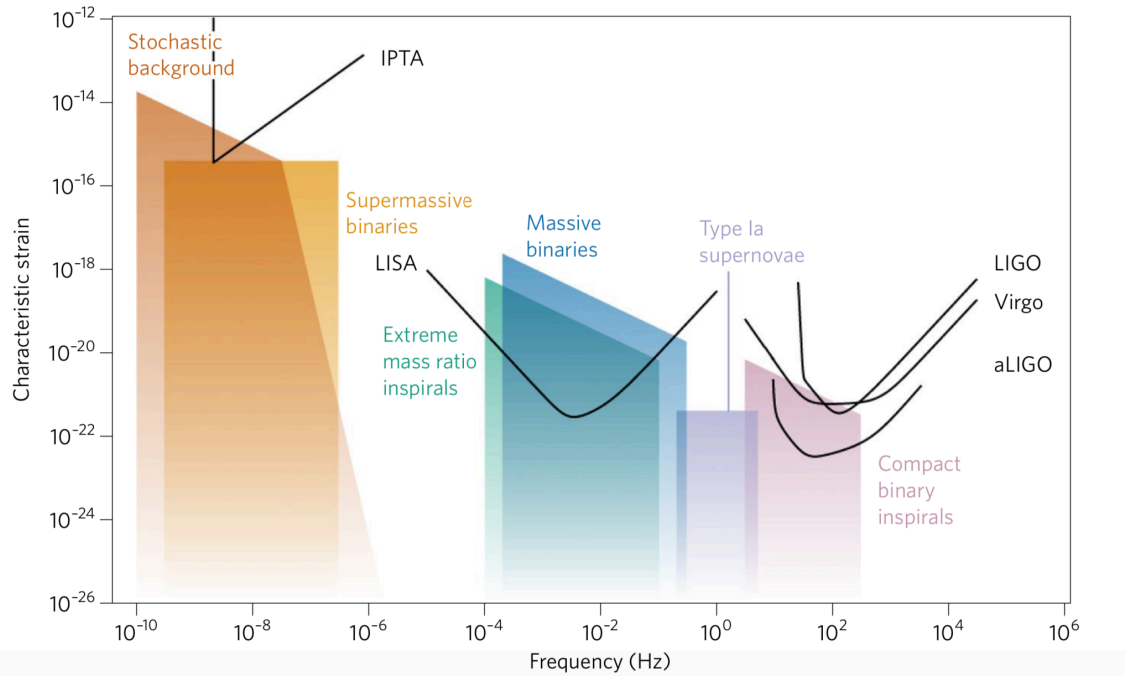

Figure 1.4: Sensitivity curves of different detection methods (marked in black) and different estimated magnitude of GWs [25].

achieved, thanks to the improvement in the detector sensitivity.

Black holes

A completely new class of BHs is discovered, which is much heavier than those detected through the observation of X-ray binaries. This provides the most robust evidence for the existence of heavy stellar-mass BHs, which leads to a re-evaluation of the models of stellar evolution in binary systems [26].

The generation of gravitational wave from the nearly last moment of compact binary coalescence inherently involves the physics beyond Newtonian gravity. The detection of GW150914 provides moderate SNR (signal to noise ratio) of 24 to test non-linear conservative and dissipative effects which are not accessible from binary pulsars. The estimation of waveform coefficients provides information for corresponding general relativity values. By analysing GW150914, no violations of general relativity was found [27].

Neutron stars

The neutron star equation of state (EoS) is measured according to the constraints of GW170817 on the tidal effects of the coalescing bodies [28]. However, the constrain

is too weak to discriminate between realistic models. Especially the post merger part is missing due to insufficient sensitivity at several kHz region.

GW170817 was observed together with gamma-ray burst (GRB) GRB170817A [29]. The probability of near-simultaneous observation of them by chance is 5.0×10^{-8}. BNS is confirmed to be one of the progenitors of short GRBs. It proves that BNS mergers contribute for the formation of heaviest elements through r-process. The time delay between these two observations confirmed that the speed of GW is the same as the speed of light to about a part in 10^{15}.

The multi-messenger observation of GW170817 allows it to be used as a standard siren. Without using the traditional 'distance ladder', GW170817 provides an independent measurement of Hubble constant to be $70.0^{+12.0}_{-8.0}$km s^{-1} Mpc^{-1} (maximum a posteriori and 68% credible interval) [30].

1.3.2 Expected science from next-generation gravitational wave detectors

In the future, the sensitivity of the next generation of GWs detectors will be increased by an order of magnitude with respect to the current ones. Besides, a broaden detection frequency band is also expected. The science of next-generation detectors can be found in many documents such as [31, 32].

For all the events similar with the detected ones, higher SNR will be obtained. This is of great importance for the test of GR and the test of neutron star EoS. Although these scientific pay-offs have already been realized by O1 and O2, we are just at the beginning of many relevant research topics. Higher sensitivity will also increase the possibility of detecting core-collapse supernovae, which were not detected up to now. The test of gravity models will also benefit from higher SNR.

Higher sensitivity will enable the detection of signals with large redshift, allowing to test several cosmology theory. In this way, an independent way for estimating Hubble parameter, modified gravity and dark energy EoS will be provided.

Larger detection rates will be achieved, which is important for statistical research about BH formation/evolution, NS formation/evolution, heavy elements formation, Hubble parameter estimation and much more.

Chapter 2

Quantum noise limited earth-based gravitational wave detectors

The current operating earth-based GW detectors are all based on Michelson interferometer principle. After almost 50 years of investigation and development, several additional techniques were added to the basic Michelson interferometer. Some of such improvements are for example arm Fabry-Perot cavities, power recycling cavities and signal extraction cavities. Such new configurations have been proven to increase the response magnitude or bandwidth of GW interferometers. The interferometer configuration which achieved the first detection is usually called Dual-Recycled-Fabry-Perot Michelson interferometer (DRFPMI) [33].

Several types of noises limit the sensitivity of GW detectors. They mainly act by inducing spurious moments of the test masses or decreasing the precision of the interferometric readout. Among them, the ones which are the most impactful are the Newtonian or gravity gradient noise, the coating and suspension thermal or Brownian noises and the quantum noise. After reaching the design sensitivity, advanced LIGO, advanced Virgo and KAGRA are expected to be limited by quantum noise at almost the entire detection bandwidth.

In this chapter, I will introduce the main noise sources for advanced gravitational wave detectors as well as explain the DRFPMI configuration focusing on the KAGRA case.

2.1 KAGRA

The first generation of kilometer-scale GW detectors (LIGO and Virgo) was developed in the early 2000s and was unsuccessful in detecting GWs. The interferometer advanced LIGO (aLIGO) and advanced Virgo (adVirgo) are usually addressed as second generation gravitational wave detectors. aLIGO achieved the first detection in 2015 and was joined by adVirgo in 2017.

KAGRA is the first 2.5 generation gravitational wave detector. In Figure 2.1 (left) the schematical optical layout of KAGRA, which is similar to that of aLIGO. What differentiates KAGRA from the 2G detectors are two innovative features: it operates underground and the test masses, made of sapphire, are cooled down to a cryogenic temperature of about 20K. Such features are of key importance to reduce the impact of several noises and are expected to be used in 3G detectors, therefore KAGRA has a key role, not only as additional GW detector in the 2G network but also as a technological benchmark to help bridging the gap between second and third generation detectors.

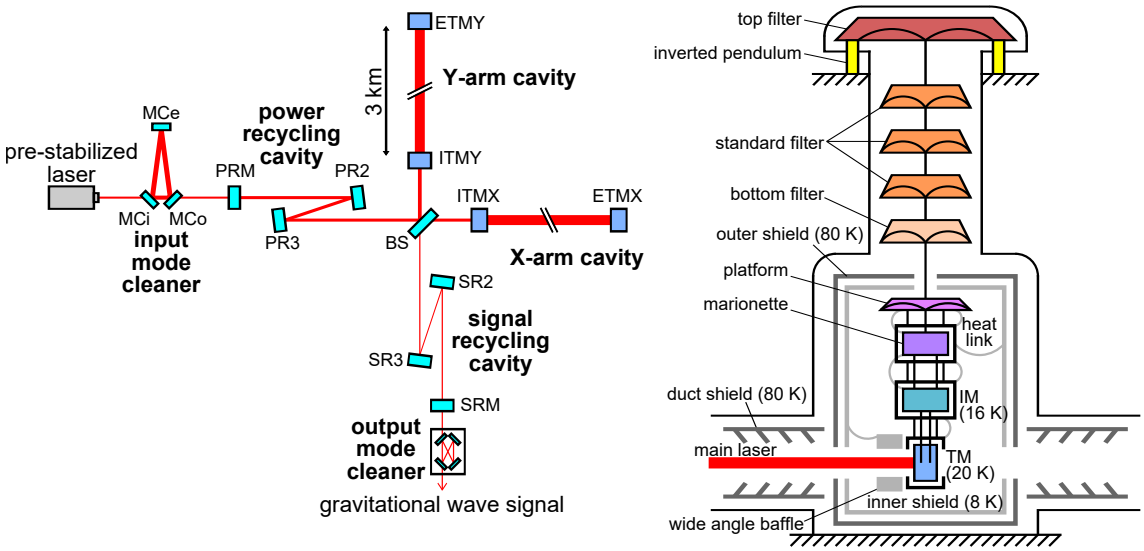

Figure 2.1: Left side shows the optical layout of KAGRA which is similar with the DRFPMI configuration of aLIGO. Right side shows the suspension for test masses which isolate them from ground motion (note that the height is not in-scale and the 5 stages outside cryogenic shield are much longer). The accumulated heat in the test mass is transferred through sapphire fibers and heat links (high purity aluminum cable) to maintain 20K cryogenic temperature. The marionette, the intermediate mass (IM) and the test mass (TM) are surrounded by their respective recoil mass for position and alignment control [34] .

In Japan, the research aiming for gravitational wave detection started in the 1980s. One important milestone was the construction of TAMA300, a Michelson interferometer with 300m long arm cavities, which started in 1995 and reached its best sensitivity of $5 \times 10^{-21}/\sqrt{Hz}$ in 1998. The operation of TAMA [35] played an important role in the science and technology development of gravitational wave detection. The operation of TAMA300 was stopped after the Tōhoku earthquake of 2011. Almost at the same time, KAGRA was funded and tunnel excavation started in 2012. KAGRA collaboration announced the completion of KAGRA construction in 2019. The construction of KAGRA was amazingly fast despite the fact that it required to face several new challenges and implement novel techniques.

Figure 2.2: KAGRA is about 1000m underground, here it shows one of the 3km arms inside KAGRA tunnel

In 2020, KAGRA has finished its first observation run. The best binary neutron range achieved was around 1Mpc during this observation run. A simultaneous observation was done together with GEO, which has a similar sensitivity with KAGRA.

As said before, one of the main features of KAGRA is underground operation. In the underground site of KAGRA, the seismic noise from 1Hz to 100Hz is almost two order of magnitude lower than other GW detectors' sites (see 2.6.1). Moreover, the Newtonian noise caused by seismic surface wave is reduced in the condition of underground operation (see 2.6.2). However, underground operation will not relax the requirement of micro-seismic motion control. Although this motion is not located in the frequency band of gravitational wave observation but around 0.1 to 0.2 Hz,

its control is necessary for the stable operation of the whole interferometer.

The other main innovative feature of KAGRA is cryogenic temperature of test masses. Low temperature helps to reduce all type of thermal noise. Moreover, the high thermal conductivity of sapphire (the material of which the test masses are made) makes thermal lensing effect quite small. Therefore, wave front aberration will also be negligible in KAGRA. However, the absorbed heat needs to propagate away from the test masses through the suspension sapphire fibers. Since the thermal noise of the suspension increases proportionally to the fiber diameter and we would like to reduce such noise, while the thermal conductivity also increases proportionally to the fiber diameter and we would like to maximize it, a trade-off between this two processes must be found. Sapphire has also very good mechanical parameters at cryogenic temperatures compared to other materials like fused silica. This is beneficial for the reduction of thermal noise. Unfortunately, the formation of an ice ad-layer was reported during the cryogenic operation of KAGRA [36]. The growth of this layer changes the reflectivity of mirror and affects the perfomances of the interferometer.

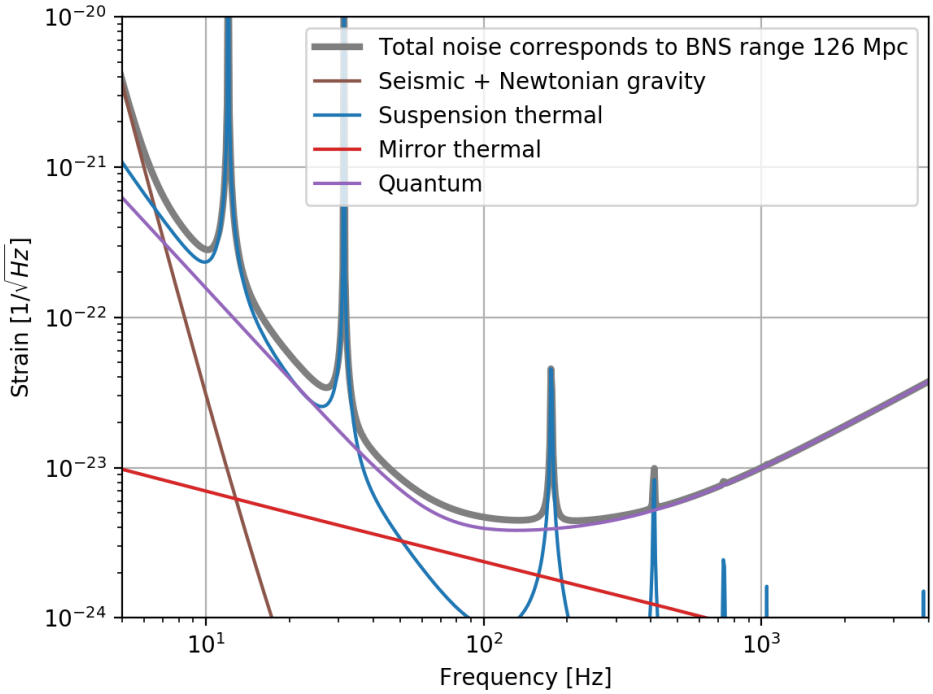

Figure 2.3: Expected KAGRA sensitivity. Data for each curve is available on KAGRA document website (JGWdoc) [37]. The calculation of binary neutron star range is based on a python code inspiral range master [38].

Apart from features of underground and cryogenic, KAGRA has folded recycling cavities (see PR2-PR3 and SR2-SR3 mirrors in Fig. 2.1 left panel), which is bene-

ficial for a stable optical design of the interferometer. This is provide a convenient solution for injecting auxiliary control laser beams through PR2 and SR2. These auxiliary lasers are used to achieve the initial arm length stabilization before using the main laser to lock them [39]. The arms of KAGRA contains Fabry-Perot cavities with higher finesse (approx. 1500) compared with LIGO/Virgo (approx. 450). This choice was done to reduce the circulating power inside power recycling cavity, therefore reducing the power inside input mirror substrate. This helps to relax the requirement of mirror absorption, which is crucial for a cryogenic detector. The arm cavity circulating power will be 400kW. Since different mirrors have different angular/displacement noise requirement, KAGRA is also featured to have four different suspension systems.

As shown in figure 2.3, KAGRA sensitivity is expected to be limited by mainly the suspension thermal noise at low frequency, by the mirror thermal noise in the middle frequency and by quantum noise at higher frequency.

Underground and cryogenic operations help to reduce seismic and thermal noise. The most promising technique to reduce the quantum noise of GW detector is the injection of squeezed vacuum states into the dark port of the interferometer. The implementation of frequency independent squeezing is equivalent to increase arm cavity power. It will either increase shot noise or radiation pressure noise. Only frequency dependent squeezing can have broadband squeezing. The realization of a full-scale source of frequency dependent squeezing suitable for the broadband reduction of quantum noise in GW detectors is the goal of my thesis.

2.2 Laser and Gaussian beam

In this section I will briefly introduce the laser system used in current GW detectors and some theory related to lasers. A more comprehensive discussion can be found in [40, 41, 42]

2.2.1 GW detectors' lasers and injection system

The laser system used for all the current gravitational wave detectors consists of a 1064nm source able to provide several tens of Watt of power in a single spatial mode and with very narrow linewidth (few Hz). Since there are no commercial solution that can achieve all the mentioned features, the laser sources of the current GW detectors are all custom made [43, 44, 45]. For most of them, the initial source

is a monolithic non-planar ring-oscillator (NPRO) Nd:YAG crystal to provide few Watt output 1064nm laser beam with a linewidth of few Hz. Then, the laser coming out from laser source usually goes through medium power amplifier, mode cleaner cavities, several telescopes and its frequency is locked to a reference cavity and to the suspended mode cleaners. After passing through an injection telescope, the laser is finally injected into the interferometer.

2.2.2 Gaussian beam

The laser beam coming out from laser source is called Gaussian beam and the corresponding electromagnetic field satisfies wave equation. The solution of this wave equation is a plane-wave evolving with time and spatial axis, which gives a usual phase term $kz - \omega t$. At the same time, it has also a transverse spatial mode described by $U(r)$. So it has the form

$$U(r,t) = U(r)e^{i(kz-\omega t)} \tag{2.1}$$

The transverse mode is described by the cylindrical equation

$$U(r) = A_0 \frac{\omega_0}{\omega(z)} \exp\left(\frac{-r^2}{\omega(z)^2}\right) \exp\left(-ik\frac{r^2}{2R(z)} + i\phi(z)\right) \tag{2.2}$$

where A_0 is the amplitude of this field. ω_0 is the beam size at the waist (where the beam has its minimum size) and $\omega(z)$ is the size of the beam at a distance z from the waist position. $e^{\frac{-r^2}{\omega(z)^2}}$ shows that the power is maximized in the beam center and decreases with beam radius with a Gaussian profile. This term describes the energy distribution of cross section of the beam at a position z. Using it we can calculate how much energy goes through an aperture of radius of r as follow:

$$R = 1 - \exp\left(\frac{-2r^2}{\omega(z)^2}\right) \tag{2.3}$$

When the above percentage take value of 86.5%, the corresponding r is defined as the radius of beam. This parameter is crucial to define the amount of energy which is transmitted through different apertures. In typical optical setups such apertures can be electro-optic modulators (EOM),acousto-optic modulators (AOM), Faraday isolators, photodiodes, etc. When we consider the use of these devices, we need to pay attention to two aspects. The first is the beam size with respect to the aperture dimension. Through the calculation of percentage R, we will have 99.97% of energy

transmission when the aperture is twice the size of beam. A larger aperture will be usually since the beam may not centered in the real case. Second thing to consider is the power density ρ_{power}, and the damage threshold of the component. A good approximation of this power density can be written as [46]

$$\rho_{power} = \frac{250}{d^2} \times P \tag{2.4}$$

Note that the unit for power density is W/cm^2 while the unit for beam diameter d is mm. Here P is the total power and its unit is W. Another important term of equation 2.2 is $e^{-ik\frac{r^2}{2R(z)}}$ which shows that the Gaussian beam is actually not a plane wave and its wavefront depends on position and beam radius. The last term $\phi(z)$ is the Gouy phase, which equals to $arctan(z/z_0)$. It introduces an additional phase shift of π at an infinity distance from the waist. The mentioned beam size can be written as function of z as

$$\omega(z) = \omega_0 \sqrt{1 + (\frac{z}{z_R})^2} \tag{2.5}$$

where z_R is called Rayleigh range, defined as

$$z_R = \frac{\pi \omega_0^2}{\lambda} \tag{2.6}$$

and it is the position where the beam cross section is doubled. From the above equation, we can see that a beam will diverge fast if the beam waist is small. On the contrary, a larger beam will be more collimated. The radius of curvature for a Gaussian beam reaches its minimum at the position of Rayleigh range and it is infinity at waist. The formula describes this is

$$R(z) = z + \frac{z_R^2}{z} \tag{2.7}$$

2.2.3 Propagation of Gaussian beam

The solution of wave function can also be written as a function of q [40] where

$$\frac{1}{q} = \frac{1}{R} - j\frac{\lambda}{\pi \omega^2} \tag{2.8}$$

The introduction of this parameter is very useful since it is easy to demonstrate that the q parameter has its real part to vanish at the waist position and can be written

as

$$q_0 = j\frac{\pi\omega_0^2}{\lambda} \tag{2.9}$$

We can use the ABCD transfer matrices for paraxial optics to compute how the q parameter evolves after beam propagation or after interacting with different optics. Such ABCD matrices can be found in many textbook, for example[41]. Using this technique we can write the total transfer matrix as the product of a sequence of matrices, following the usual matrix product rules. The q' parameter of the final beam can be calculated as

$$q' = \frac{Aq_0 + B}{Cq_0 + D} \tag{2.10}$$

where A, B, C, D are the components of the ABCD transfer matrix and q_0 is the q parameter of the initial beam.

2.3 Fabry-Perot cavity

A Fabry-Perot cavity, like the one shown in Figure 2.4, is an optical resonator composed by two reflecting surfaces. It was invented in 1899 by Charles Fabry and Alfred Perot [42]. We define the amplitude reflection/transmission coefficient as r_1, it_1 for the input mirror (where laser is injected) and r_2, it_2 for the end or output mirror. The imaginary unit for transmission coefficient is used to indicate the phase change of field. This phase change is necessary to have the determinant of the matrix associate to each mirror to be one. There are other possibilities to achieve the same condition, but this was the choice for this thesis. The square of the amplitude reflection/transmission coefficient is usually called reflectivity/transmissivity. To describe a cavity, other important parameters are the cavity length L and input/end mirror radius of curvature R_1, R_2.

2.3.1 Mathematical description of Fabry-Perot cavity

To derive the relationship between the field in different position (as in Figure 2.4), we need to consider the effect of the input and output mirrors on the input electric

Figure 2.4: Fabry-Perot cavity. Different arrow marked with alphabet 'a' to 'g' indicates different fields amplitude. These fields are electric fields, the square of them corresponds to power. We could also see that the red line which represents the laser light is thicker inside the cavity which means the light is stored inside the cavity and the power is enhanced.

field. The relationship between the input and output beams is as follows

$$\begin{aligned} b &= a \cdot \imath t_1 + e \cdot r_1 \\ c &= b \cdot e^{\imath kL} \\ d &= c \cdot r_2 \\ e &= d \cdot e^{\imath kL} \\ f &= a \cdot r_1 + e \cdot \imath t_1 \\ g &= c \cdot \imath t_2 \end{aligned} \tag{2.11}$$

This is a set of equation which can be solved to obtain respectively the amplitude transmissivity, reflectivity and gain of the cavity. The amplitude reflectivity is

$$\frac{f}{a} = r_1 - \frac{r_2 t_1^2 e^{2\imath kL}}{1 - r_1 r_2 e^{2\imath kL}} \tag{2.12}$$

The cavity amplitude gain[1] is

$$\frac{b}{a} = \frac{\imath t_1}{1 - r_1 r_2 e^{2\imath kL}} \tag{2.13}$$

and the amplitude transmittivity is

$$\frac{g}{a} = \frac{-t_1 t_2 e^{\imath kL}}{1 - r_1 r_2 e^{2\imath kL}} \tag{2.14}$$

[1]The cavity power gain for a resonant cavity can be written as $g_P = \frac{t_1^2}{(1-r_1 r_2)^2}$. If r_2 can be approximated to be 1, the cavity power gain can be written as $g = \frac{t_1^2}{(1-r_1)^2}$. If t_1 is small, We can also have following approximation $r_1 = \sqrt{1-t_1^2} \approx 1 - \frac{t_1^2}{2}$. In the end, the power gain can be written as $g_P = \frac{4}{T_1}$ in this special case.

These three values allow us to predict how much power we will have in transmission and in reflection and how much power we can expect inside the cavity, for a given input power.

As introduced in section 2.3.1, the phase term $\imath kL$ is usually the only term we can dynamically change for a certain optical set up (the reflectivities and radii of curvatures are generally fixed and cannot be easily change in most of the cases). This phase term can be changed if the laser frequency f or the cavity length L are changed. By monitoring cavity transmission and/or reflection field as function of laser frequency or cavity length, lots of information about the cavity can be extracted. The action of changing the laser frequency or cavity length is called cavity scan.

Resonance condition of a Fabry-Perot cavity

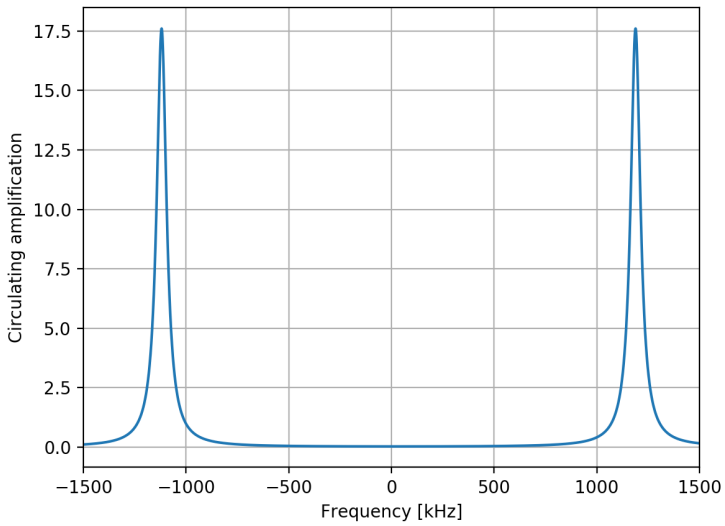

Figure 2.5: Cavity circulating field while cavity scan. This plot is the specific case of the KAGRA power recycling cavity, for which the transmission coefficient for two mirrors are 0.05 and 0.1 and the cavity length is 65m. The scan parameter for this plot is the frequency of the laser.

Let's take the practical example of the circulating field during a cavity scan 2.13. The condition for which the circulating power is maximized is called 'on-resonance'. When the circulating field about zero, the cavity is said to be 'off-resonance'.

The physical meaning of the empirical definition of 'on-resonance' condition can be understood from equation 2.13. The 'on-resonance' condition is achieved when

the phase term of the equation is equal to an integer number of 2π. By visually representing the electric field of a laser light, the resonant condition can be described as figure 2.6.

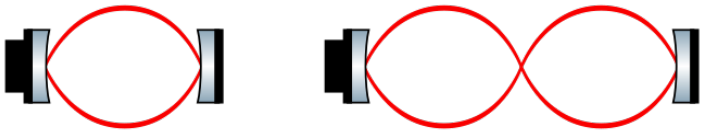

Figure 2.6: Resonance can be achieved in several different conditions. The different resonant condition corresponds to a length difference of half wavelength, which corresponds to a round trip difference of one wavelength. Note that this picture works just for the fundamental mode of a cavity.

2.3.2 Fabry-Perot cavity parameters

Several useful parameters are commonly used to describe the main properties of FP cavities. Some of them are reported below:

The **free spectral range** describes the frequency/length change necessary to move from one resonance to the next resonance condition. As shown in figure 2.6 (a linear cavity), this means that the cavity length must be related with wavelength in the following way

$$2L = N \times \lambda \tag{2.15}$$

This equation is equivalent with

$$f = N \times \frac{c}{2L} \tag{2.16}$$

The frequency change from one resonance to the next is defined as free spectral range (FSR) as follows

$$FSR = c/2L \tag{2.17}$$

Correspondence between frequency and length is important since sometimes we need to convert them between each other. As mentioned, frequency and length change are equivalent for what concerns the cavity scan. From figure 2.6 and the definition of free spectral range, we have

$$\frac{\delta f}{\delta L} = \frac{FSR}{\lambda/2} \tag{2.18}$$

The **full width half maximum (FWHM)**, also called cavity linewidth is used to characterize the width of the resonant peak. To derive its value, we can use the square of equation 2.14,

$$A_{tra} = \frac{T_1 T_2}{(1 - r_1 r_2 e^{2\imath kL})^2} \tag{2.19}$$

Then by using some basic trigonometric formulas and Euler equation, equation 2.19 becomes

$$A_{tra} = \frac{T_1}{(1 - r_1 r_2)^2 + 4 r_1 r_2 \sin^2(kL)} \tag{2.20}$$

The half maximum will be reached when the following condition is satisfied

$$(1 - r_1 r_2)^2 = 4 r_1 r_2 \sin^2(\imath \Delta\phi) \tag{2.21}$$

Then we have

$$\Delta\phi = \arcsin\left(\frac{1 - r_1 r_2}{2\sqrt{r_1 r_2}}\right) \tag{2.22}$$

To convert phase into frequency, we can use the relationship $\Delta f / 2\Delta\phi = FSR/\pi$. The frequency difference becomes

$$FWHM = FSR \frac{2}{\pi} \arcsin\left(\frac{1 - r_1 r_2}{2\sqrt{r_1 r_2}}\right) \tag{2.23}$$

Half of FWHM is called half width half maximum (HWHM) or cavity pole. This means we can use FP cavities as a filters for light field.

The **Finesse** is defined as the ratio between FSR and FWHM

$$\mathcal{F} = \frac{FSR}{FWHM} = \frac{\pi}{2 \arcsin\left(\frac{1 - r_1 r_2}{2\sqrt{r_1 r_2}}\right)} \tag{2.24}$$

For a high finesse cavity, which means r_1 and r_2 are close to 1, the equation can be approximated as

$$\mathcal{F} = \frac{\pi \sqrt{r_1 r_2}}{1 - r_1 r_2} \tag{2.25}$$

The finesse is independent of cavity length and is proportional to the number of 'bounces' the photons perform inside the cavity.

The **storage time** of FP cavity is defined as

$$\tau = \frac{2L}{\pi c} \mathcal{F} \tag{2.26}$$

and it is inversely proportional to the FWHM. When the injection power to cavity is

suddenly removed, cavity transmission light power P_T leaking from cavity decreases exponentially with time constant $\tau_{ring-down}$ according to $P_T = P_0 e^{-t/\tau_{ring-down}}$. Cavity storage time is two times $\tau_{ring-down}$.

The **Airy function** [47] is the mathematical formulation of the cavity transmission/reflection/circulating power when cavity is being scanned. After introducing finesse and FSR, equation 2.20 can be written as

$$A_{tra} = \frac{a}{1 + 4(\frac{\mathcal{F}}{\pi})^2 \sin^2(\frac{\pi(t-t_0)}{FSR})} \tag{2.27}$$

where the parameter a depends on the gain of photodetector and t_0 depends on the starting point of scan. Therefore, equation 2.27 can be used directly to fit the measurement of cavity transmission and finesse and FSR information can be extracted.

Under/over coupled cavity and impedance matched cavity

Depending on the relation of transmissivity for input and end mirror (under the assumption that they are much larger than the optical losses), optical cavities can be classified into three different kinds:

- **Under-coupled cavity** ($T_1 < T_2$): For the same finesse, under-coupled cavities have lower circulating power because the laser power coupled into cavity is smaller. Compared with other types, the phase change in reflection is small.

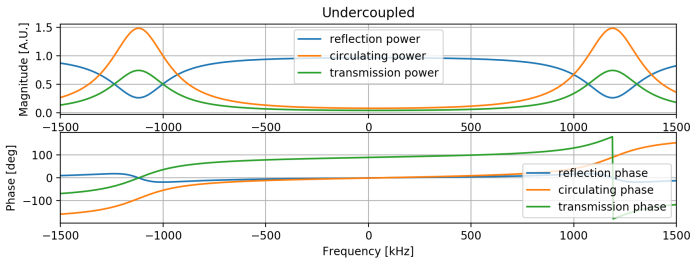

Figure 2.7: Reflection/transmission/circulating power and relative phase for an under-coupled cavity with finesse of around 7 ($T_1 = 0.2$, $T_2 = 0.5$).

- **Over-coupled cavity** ($T_1 > T_2$): Over-coupled cavities have larger circulating power compared to under-coupled cavities. But the reflection and transmission are the same for both over-coupled and under-coupled cavities. We will see later in section 2.3.3 that the situation for a high-finesse cavities where

the losses play a much larger role will be different. An example of over-coupled cavities are the GW interferometers arm cavities as seen by the carrier light.

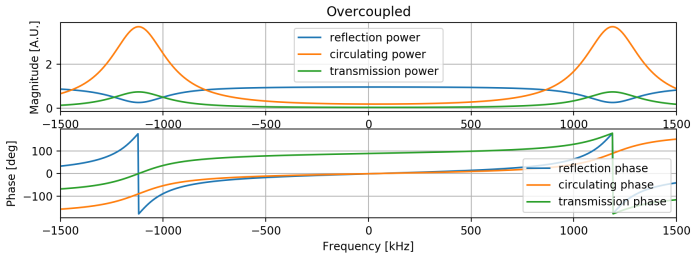

Figure 2.8: Reflection/transmission/circulating power and relative phase for an over-coupled cavity with finesse of around 7 ($T_1 = 0.5$, $T_2 = 0.2$).

- **Impedance matched cavity** ($T_1 = T_2$): Impedance matched cavities have cavity transmission equals to 100%. The cavities introduced at the beginning of this chapter for laser injection are all designed to transmit as much power as possible and therefore aim to be impedence matched cavities.

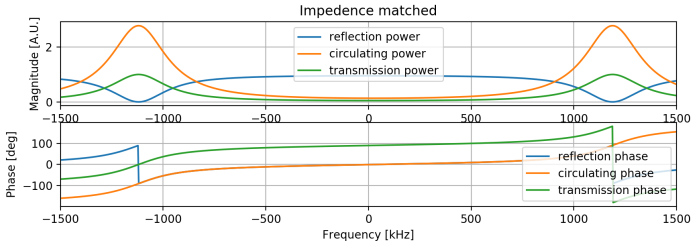

Figure 2.9: Reflection/transmission/circulating power and relative phase for an impedance matched cavity with finesse of around 7 ($T_1 = 0.36$, $T_2 = 0.36$).

2.3.3 Optical losses

In the previous sections, the optical losses of mirrors or optical components were considered negligible. In this section, we will address how to treat optical losses when they cannot be neglected. We will use L to describe optical losses. This is not to be confused with the cavity length L. Since both those terms rarely appear in the same equation, no confusion is expected. Due to energy conservation, we can write the following relationship

$$R + T + L = 1 \tag{2.28}$$

where R is the reflectivity of the mirror/component and T is the transmissivity of the mirror/component.

There are severla different sources of losses. For example, the diffraction losses caused by the finite size of mirror, the absorption of the mirror, the scattering from the mirror coating and substrate defects. For mirrors used in optical metrology, minimizing the optical losses is a huge deal. Optical losses for large mirrors are hard to reduce and as it is difficult to have a homogeneous distribution over very large surfaces.

Here I list some of the effects of optical losses related to my experiment:

- In the case of an impedance matched cavity previously defined, due to optical losses in the propagation, the interference happening at input mirror is not totally destructive. Therefore, some power is reflected and some power is lost. This effect is especially visible for a high finesse cavities.
- Optical losses degrades squeezing. This will be discussed in chapter 4.
- Over-coupled and under-coupled cavity introduced in the last section have the same reflection and transmission when losses are negligible. However, in the presence of optical losses inside the cavity, a portion of the circulating light will be lost and this will result in a smaller amount of reflected light in the case of an over-coupled cavity. This can be seen in figure 2.10. In the case of gravitational wave detector, this optical losses put fundamental limitation for sensitivity [48]. We will see later that filter cavity introduced in this thesis is an over-coupled cavity and suffers from optical losses, which causes the drop of reflected power.

2.4 Gaussian beams in cavities

We introduced Gaussian beams and optical cavities in the previous sections. In this section we will discuss how the geometrical properties of optical component can affect the beam shape. For example, the use of lens can change laser beam parameters, including beam waist and waist position. To couple a laser beam into an optical cavity means to make the beam waist size to be the same as the cavity waist size and make the beam waist position overlap with the cavity waist position. An excellent review of this was done by Kogelnik and Li [40]. However, since this knowledge is crucial for understanding my work about squeezing and filter cavity, I will summarize few important formulas here.

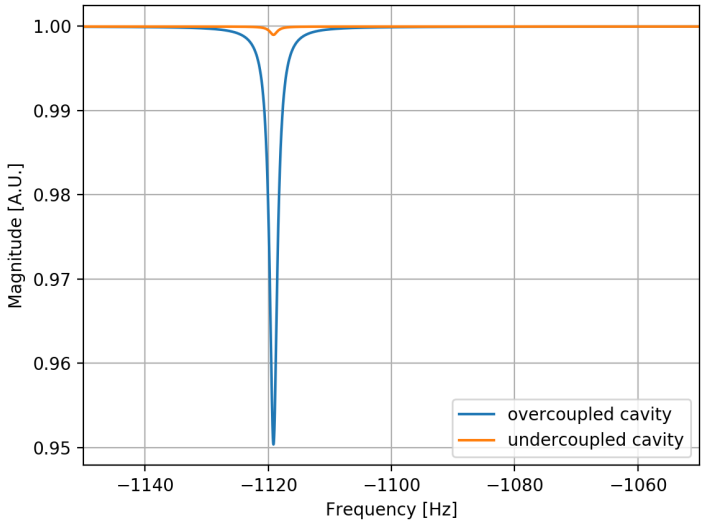

Figure 2.10: Comparison of reflection for an over-coupled and an under-coupled cavity for high finesse (around 1500). The optical losses of 50ppm causes the reflection power to drop for the over-coupled cavity while it has no effect on the under-coupled one.

2.4.1 Fundamental mode of cavity

In order to match a Gaussian beam into a cavity, the first thing to know is the target beam parameters which corresponds to the fundamental mode of cavity. The calculation of cavity fundamental mode relies on ABCD matrices introduced in equation 2.10. In order to have a stable cavity, we need to ensure that the beam properties are unchanged after one round-trip. This mathematically means to require the input beam to be equal to the beam after one propagation through the ABCD matrix of the cavity. With this method we can compute, for example, the beam size at input mirror, end mirror and waist as follows

$$\omega_{input}^4 = (\lambda R_1/\pi)^2 \frac{R_2 - d}{R_1 - d} \frac{d}{R_1 + R_2 - d} \tag{2.29}$$

$$\omega_{end}^4 = (\lambda R_2/\pi)^2 \frac{R_1 - d}{R_2 - d} \frac{d}{R_1 + R_2 - d} \tag{2.30}$$

$$\omega_0^4 = (\lambda/\pi)^2 \frac{d(R_1 - d)(R_2 - d)(R_1 + R_2 - d)}{(R_1 + R_2 - 2d)^2} \tag{2.31}$$

A similar approach can be done to compute the beam waist position inside an optical cavity, as shown in [40].

2.4.2 Preparation of a proper beam

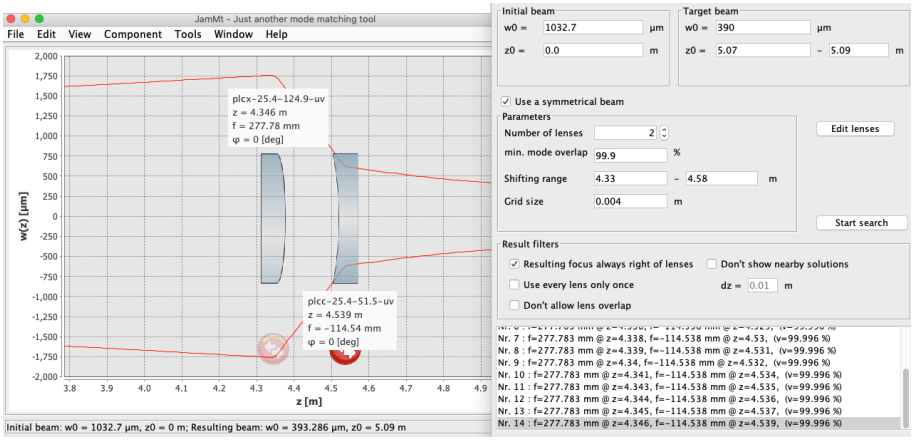

Figure 2.11: An example of the use of JamMt for designing a telescope.

Based on ABCD matrix, we can choose the place to put lenses and other optical components to have correct beam parameters to match into a cavity. At the same time, we need to pay attention to some practical issues. For example, we should try to use lens with a longer focal length, because astigmatism has a smaller effect in this case. During the practical implementation, we should always try to make beam as flat as possible and go through optics at their center. Besides, telescopes sometimes are realized by using a set of curved mirrors, which is beneficial to reduce loss. In this case, it's better to reduce the incident angle on this mirror to avoid astigmatism. To design a proper telescope, we often use the software JamMt (Just another mode matching tool) [49].

In our experiment, the initial beam parameters are obtained from measurements done with BeamMaster USB Knife-Edge Based Beam Profiler, which is based on the measurement of the integral of Gaussian function - erf function [50]. Sometimes, we perform the basic Knife-Edge scanning when the beam is too dim. The reconstruction of Gaussian beam with the measurement of beam size at different position gives us the waist size and waist position of initial beam.

The choice of available lens is, of course, limited in real life. In order to have a realistic simulation, we need to provide several parameters to the program. Main parameters are material's Sellmeier coefficients [51], lens thickness and lens surface radius of curvature.

By taking in input the initial beam parameters, the target beam parameters and the available lenses, the mode matching assistant of JamMt will automatically calculate possible telescope solutions. In figure 2.11, we could see an example of the

use of JamMt to find a proper telescope. We used this tool for most of the telescope we implemented. Of course, as the name of the software suggests, this is just another mode matching tool, and the same result can be obtained with a variety of different simulation programs or analytical computation.

2.4.3 Misalignment and mode mismatch

In the case where the real beam and the target one have different beam parameters, we have misalignment or mode mismatch. The paper from Dana Z. Anderson [52] is a very comprehensive summary of both misalignment and mode mismatch. Both issues make laser power couple to not only fundamental mode but also to other modes called higher order modes. When the input axis is not aligned to the cavity axis, we have misalignment, and the corresponding coupled modes are described by Hermite-Gauss modes. If the waist size or waist position is not matched to the cavity ones, this causes mode mismatch, and the corresponding coupled modes are described by Laguerre-Gaussian modes.

Hermite-Gaussian mode

Any misalignment can be defined as a linear combination of an axis shift and a tilt (for each direction). This causes power to couple to Hermite-Gaussian modes. The HG modes are labeled using m and n to indicate the order of the mode, for example TEM_{mn}. Here TEM means transverse electromagnetic mode. And m always stands for yaw (horizontal) higher order mode, while n stands for pitch (vertical) higher order mode. The mathematical equation for its complex amplitude is

$$U(r) = (2^{n+m-1} n! m! \pi)^{-1/2} \frac{1}{\omega(z)} H_m\left(\frac{\sqrt{2}x}{\omega(z)}\right) H_n\left(\frac{\sqrt{2}y}{\omega(z)}\right) \exp\left(\frac{-r^2}{\omega(z)^2} - \imath k \frac{r^2}{2R(z)} + \imath(m+n+1)\phi(z)\right) \tag{2.32}$$

Here $\omega(z)$ is usually taken to be ω_0 to simplify calculation, since the wavefront radius of curvature will be infinity in this case. Then we can neglect the phase term related to $R(z)$ in calculation. This means computing the complex amplitude at the waist position.

Since the equation is symmetric for m and n exchange, we can limit the discussion to only one of them, in particular let's have a look to yaw. The lower order mode is for $m = 1$ and $n = 0$. Hermite polynomials have different values for different order.

For example, $H_0(x) = 1$ and $H_1(x) = x$. By using this last two into the previous equation, we can express the relationship between the fundamental mode and the first high order mode as

$$U_1 = \frac{2x}{\omega_0} U_0 \tag{2.33}$$

Then let's see how a beam shift in yaw changes the power coupling into different modes.

When there is a translation of beam position x_0, the corresponding changed term is the phase term responsible for power Gaussian distribution. This corresponds to a change in coordinate system from x to $x - x_0$. Therefore we have

$$\exp\left(-\frac{(x-x_0)^2}{\omega_0^2}\right) = \exp\left(\frac{(-x^2 - x_0^2 + 2x \cdot x_0)}{\omega_0^2}\right) \tag{2.34}$$

If we assume x_0 to satisfy $x_0/\omega_0 \ll 1$, the terms containing second order of x_0 can be neglected. Then the phase term in equation 2.34 becomes

$$\exp\left(\frac{-x^2 + 2xx_0}{\omega_0^2}\right) \tag{2.35}$$

Using Maclaurin series, exponential function e^x can be approximated as $1 + x$ and then we have phase term as

$$\exp\left(\frac{2xx_0}{\omega_0^2}\right) \exp\left(-\frac{x^2}{\omega_0^2}\right) = \left(1 + \frac{2xx_0}{\omega_0^2}\right) \exp\left(-\frac{x^2}{\omega_0^2}\right) \tag{2.36}$$

Using the expression of fundamental mode and first higher order Hermite-Gaussian mode, we can express the transverse field function as

$$U_{translation} = U_0 + \frac{x_0}{\omega_0} U_1 \tag{2.37}$$

The last equation shows how a shift of the beam can be represented as a linear combination of zero- and first-order TEM where the coupling factor is x_0/ω_0.

The effect of beam tilt requires some schematic to start with. We have already realized that in the case of beam shift misalignment introduces phase change. For a laser beam, the phase is represented by wavefront and shown like the left side of 2.12. So for a small angle change, the phase of this beam is changed by an amount of p as shown on the right side of 2.12.

This translates in a phase change introduced by a beam tilt α. This phase change

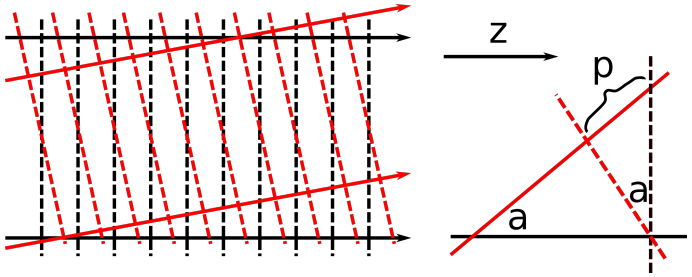

Figure 2.12: Beam propogates in z direction. For the beam part which is close to beam waist, we can consider it as plane wave. The left side shows the overall beam tilt around the waist position. The dashed lines represent the wavefront. The right side shows a zoom of two dashed lines taken from left side, and the induced phase change is indicated as p = a×x.

can be written as

$$\phi(x) = \frac{2\pi\alpha x}{\lambda} \tag{2.38}$$

So the beam tilt will make the transverse field be

$$U_{tilt} = U_0 \exp\left(\imath\frac{2\pi\alpha x}{\lambda}\right) = U_0 + \frac{\pi\imath\alpha\omega_0}{\lambda}U_1 \tag{2.39}$$

where we used again the Maclaurin series to expand the exponential and express the field as function of zero- and first-order modes. In this case the coupling factor is $\pi\imath\alpha\omega_0/\lambda$. It is interesting to notice that this time the coupling factor is imaginary, while for tilt it was a real number. This translates into a $\pi/2$ phase difference between the high order modes a shift and a tilt couple to, making them distinguishable by a properly designed alignment system.

To avoid these higher order Hermite-Gaussian modes, several auto-alignment methods were developed in the past. Among them there are dither alignment [53] (currently used to maintain our filter cavity alignment), differential wavefront sensing in reflection [54, 55] (planned to be used for our filter cavity), differential wavefront sensing in transmission [52],etc.

Laguerre-Gaussian mode

Laguerre-Gaussian modes are used to describe mode mismatch of the beam incident on a cavity. Laguerre-Gaussian modes is another full set for the description of eigenmodes of a cavity, as much as the Hermite-Gaussian modes set was. This set is defined in cylindrical coordinates and can be written as

$$U_{p,l}(r,\phi,z) = \frac{1}{\omega(z)}\sqrt{\frac{2p!}{\pi(|l|+p)!}}\exp((2p+|l|+1)\Phi(z)) \times \left(\frac{\sqrt{2}r}{\omega(z)}\right)^{|l|} L_p^{|l|}\left(\frac{2r^2}{\omega(z)^2}\right)\exp\left(-k\frac{r^2}{2q(z)}+l\phi\right) \tag{2.40}$$

where p and l are radial and angular mode numbers. Since there is a factor of 2 in front of p, the first higher order Laguerre-Gaussian mode is actually second order. By taking into $p = 1$ and $l = 0$, we will have

$$U_{10} = \left(1 - \frac{2r^2}{\omega_0^2}\right) U_{00} \tag{2.41}$$

If the mismatched beam size ω_0' can be written as function of the correct beam size ω_0 as $\omega_0' = \omega_0(1+\epsilon)$ where $\epsilon \ll 1$, then the phase term in equation 2.40 will be

$$\exp\left(\frac{-r^2}{\omega_0^2}\right) \longrightarrow \exp\left(\frac{-r^2}{\omega_0^2}(1+\epsilon)^2\right) \tag{2.42}$$

By using the Maclaurin expansion for the exponential and also considering the change of beam size parameter in the equation of Laguerre-Gaussian mode, we have

$$U_{size} = U_{00} + \epsilon U_{10} \tag{2.43}$$

In the case of waist position mismatch, the transverse field will be

$$U_{position} = U_{00} + \imath\frac{\lambda b}{2\pi\omega_0^2}U_{10} \tag{2.44}$$

where b is the waist position mismatch.

The problem of mode mismatch is usually tackled by fine tuning the position of lens/curved mirrors. However, in the case of laser interferometer, with hundreds of Watt of circulating power inside cavities, the mode matching will change as function of injection power. Nowadays, there are thermal compensation systems to sense the matching condition and correct the radii of curvature of mirrors using high power CO_2 lasers [56]. There is also another technique under investigation in the University of Padova, which uses an electro-optic lens to generate Laguerre-Gaussian mode sidebands and use them to sense the mode matching condition [57].

2.4.4 Cavity lock and PDH technique

Pound-Drever-Hall (PDH) technique [58] is an ubiquitous technique used to stabilize the length of an optical cavity to the input laser wavelength or vice versa. Practically speaking, locking a cavity means to stop the scan at a certain point, usually when the transmission reaches the top of the resonance peak, and hold it.

In order to stabilize the length of a cavity, we need an error signal. The difference of cavity field for all the possible frequencies/length with respect to the condition of resonance can be used as error signal. However, not every error signal is suitable for cavity lock. Let's look back to figure 2.8. We could think to use the cavity transmission or reflection as error signals and keeping the cavity locked by maintaining them at a fixed level. This error signal could work well on the shoulder of the Airy function, but is not a good error signal for the resonance condition since at that point it has the first derivative equal to zero. The phase seems a much better error signal around the resonance condition, however it does not have a linear response, which is very much advisable property when deciding which error signal to use. The PDH technique used as an error signal is the beat between the carrier and the sidebands. We will show in the following as this particular error signal is very suitable to stabilize a cavity around the resonance condition. For a more comprehensive description of the PDH technique we refer to [58].

The beat between the carrier and sidebands contains the information on the phase, and, for the case of cavity reflection after the demodulation, we can write it as

$$S_{error} = 2\sqrt{P_c P_s}\,\mathrm{Im}[f(\omega)f^*(\omega+\Omega) - f^*(\omega)f(\omega-\Omega)] \tag{2.45}$$

where P_c is the power of carrier, P_s is the power of sideband, ω is the frequency of carrier field and Ω is the frequency difference between the sidebands and the carrier. Function f is taken from equation 2.12, and it is the frequency dependent reflectivity of a cavity. By using real cavity parameters, we can plot the error signal as shown in figure 2.13.

Let's analyze some general properties of the PDH error signal and have a look on how this signal is a good error signal for cavity length control:

- **PDH signal shape**: the three peaks represent the frequency spacing of sidebands or carrier in frequency space. When the scanning of frequency crosses the frequencies of sidebands or carrier, the error signal will have a very steep linear response crossing zero. These two features, linear response and zero crossing, are very good properties of this error signal.

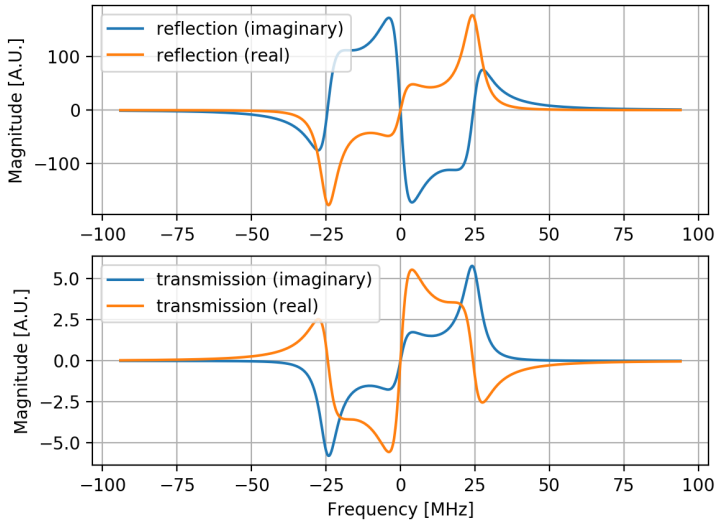

Figure 2.13: PDH signal for cavity reflection/transmission with different demodulation phase. The sidebands frequency is at 25MHz.

- **Use PDH signal to lock cavity**: the crossing line's slope has opposite sign for sidebands and carrier. This allows us to discriminate when locking on the carrier or on the sideband by looking on the sign of the control loop.

- **Demodulation phase of the PDH signal**: in the real case, PDH signal doesn't take exactly the form of equation 2.45. The PDH signal depends on the phase of local oscillator used for the demodulation. Thus it will be a combination of real and imaginary part of the beat term in equation 2.45. We use this additional degree of freedom to carefully chose the best shape/highest linear gain for our error signal.

- **PDH signal for cavity reflection and transmission**: The transmitted error signal will be always smaller than reflection. This is due to the fact that the sidebands are usually located outside the linewidth of cavity and mostly reflected. As a result, the use of error signal in reflection of cavity is generally preferred. However, for some specific case where the reflection is not available, we can also use the error signal from the cavity transmission.

2.4.5 Mode spacing

Higher order modes have different Gouy phase depending on the mode order. Therefore they will have different resonant condition inside a cavity. For the case of a not

symmetric linear cavity, the Gouy phase ϕ_G for higher order mode is [40]

$$\phi_G = (m + n + 1) \arccos \sqrt{(1 - d/R_1)(1 - d/R_2)} \tag{2.46}$$

where m and n represent the numbersused to characterize the order of higher order modes. (For example, the sum of m and n is 1 for TEM01, and it is 2 for LG10.) Using this relationship, we can compute where the higher order modes will appear in the cavity scan.

2.5 Cavity enhanced Michelson interferometer

As discussed in chapter 1, the GW interferometers which performed the first detection where an upgraded version compared to the Michelson interferometer. The main enhancement are three different type of cavities applied to the basic Michelson interferometer. They are Fabry-Perot cavity enhanced arms, power recycling cavity and signal extraction cavity. In the following I will describe how the sensitivity of a GW interferometer is enhanced by this three additional type of cavity.

2.5.1 Fabry-Perot enhanced arm cavity

The phase difference induced by GWs between two arms is proportional to the arm length. This means that having the arm length of hundreds of kilometers could drastically improve the sensitivity of GW detectors. Unfortunately this is not possible yet on earth. An alternative way to increase the effective arm length is to make photons bounce inside each arm for many times before recombining at the beamsplitter. This can be realized by replacing a normal arm with a Fabry-Perot cavity. As shown in [15], an arm cavity modifies the response by a factor

$$\frac{a_{cav}}{1 - r_1 r_2 e^{-2ikL}}$$

with $a_{cav} = \frac{t_1^2 r_2}{1 - r_1 r_2}$ and r_1, r_2 the reflectivities of the input and output mirror of the arm cavity. In figure 2.14, it is shown how the response of a simple Michelson interferometer with arm length of 300 km can be obtained using a Michelson interferometer with 3 km Fabry-Perot arm cavities with a finesse of approximately 160.

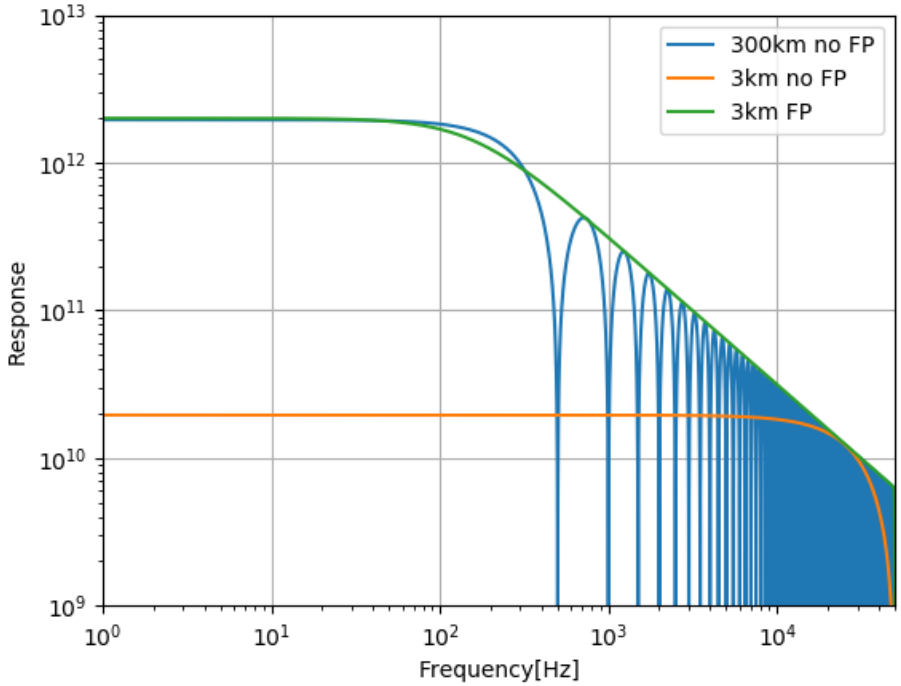

Figure 2.14: The response to GW for a simple Michelson interferometer with 3 km arm length (organge), for a 300 km arm length (blue) and for a Michelson interferometer with 3 km long FP arm cavities with finesse of 160 (green). The latter two curves shows very similar response to GWs.

2.5.2 Power recycling cavity

The quantum noise, which includes shot noise and radiation pressure noise, will be introduced in section 2.6.5. There we will show how the shot noise is proportional to the square root of the input power. Since the signal response to GW is linearly proportional to the input power, the signal to noise ratio of the shot noise improves when increasing the input power. This may indicate that a larger input power could be beneficial, therefore new laser technology needs to be pursue to increase the laser power. Unfortunately, building a more powerful laser source is not trivial, since we don't want to introduce additional intensity or frequency noise. A solution is to use power recycling technique.

When the interferometer is operated in the dark fringe condition, almost all the power injected goes back to the laser system. This is provided that the arm cavities are strongly over-coupled with almost perfect reflecting mirrors as end test masses, which for GW detectors is always the case. In this condition, adding an additional mirror in between the beam splitter and the injection system (see figure 2.1) will allow us to recycle a portion of the injected light and enhance the circulating power. Such mirror is called power recycling mirror (PRM). When the interferometer is locked, we can imagine the two arm cavities as a single FP cavity and the PRM as the mirror of an additional coupled cavity. This coupled cavity is made as close as a trans-impedance cavity which means that most of the power goes to arm cavity and few goes back to main laser side. When the optical losses inside power recycling cavity equals the transmission of power recycling mirror, the power recycling gain is

$$G_{PR} \simeq \frac{\mathcal{F}_{PRC}}{\pi} \tag{2.47}$$

where $\mathcal{F}_{PRC}$ is the finesse of the power recycling cavity. This gain is around 10 in the case of KAGRA. Which means that the circulating power is enhanced by approximately one order of magnitude with respect to the Fabry-Perot Michelson interferometer.

2.5.3 Signal extraction cavity

When the interferometer is locked in the dark fringe condition, only signals that create a differential variation of the arm length can reach the output detector. By adding a partially reflective mirror between the beam splitter and the output de-

tector (see figure 2.1), we can create a cavity which affects only such signals. This mirror is called signal recycling mirror (SRM) and the cavity is called signal recycling or extraction cavity (SRC or SEC). As well as for the PRC, this cavity will create a coupled cavity together with the arm cavity of the interferometer.

The effect of this cavity on the GW response of the interferometer depends on the detuning condition of the cavity. If the detuning is zero, which means that the SEC is on resonance with respect to the carrier, the reflectivity of the equivalent mirror composed by the SRM and the input mirror of the FP arm cavity will be reduced. Therefore the finesse of this compound cavity will be smaller compared to the initial FP cavity, which will lead to a broadened frequency response, at the cost of a smaller gain at low frequency. The opposite situation will happen for detuning equal to $\pi/2$, which means that the SEC is in the anti-resonance condition for the carrier. In this case the equivalent reflectivity will be maximized, increasing the finesse of the equivalent cavity, therefore reducing the bandwidth but increasing the low frequency response. For intermediate detuning conditions, the bandwidth and the low frequency gain will have intermediate value with respect to the 0 or $\pi/2$ condition, and a peak in the response will appear at frequencies related to the detuning condition.

The detuning parameter of the SEC can be arbitrarily changed, allowing for a fine tuning of the sensitivity if specific frequencies need to be investigated. In the case of aLIGO, (AdV did not installed the SRM so far), a broadband configuration was preferred and the SEC is operated with a detuning equal to zero.

2.6 Noise sources for advanced detectors

The noises that affect the GWs detection can act directly by moving the test mass or reducing the precision of the interferometric measurement. The differential arm length change in equation 1.28 can be expressed as

$$\Delta L = (x_{cl1} - x_{cl2}) + (x_{q1} - x_{q2}) + Lh \tag{2.48}$$

where we highlighted a differential arm length fluctuation coming from classical noise, quantum noise and the last term represents the real gravitational wave signal. The basic idea is to reduce these noise sources until the GW signal is the dominant one. To achieve this goal, we need to reduce these noise sources and the first thing is to know where are they from and how we can reduce them. This section is aimed

to answer these questions and particularly for the case of KAGRA.

Classical noise (from mirror motion)

- Seismic noise: it is caused by ground vibration which couples into the test mass.
- Newtonian noise: it is caused from the gravitational field change around test mass.
- Suspension thermal noise [59]: it comes from the mechanical loss of the suspension material, which stems from the imaginary part of its Young's modulus.
- Coating Brownian noise [60]: it is caused by the mechanical loss of dielectric coatings.
- Coating thermo-optic noise [61]: it is caused by thermal dissipation via the thermoelastic and thermorefractive mechanisms.
- Substrate Brownian noise: it comes from the mechanical loss inside test mass substrate.
- Substrate thermo-elastic noise [62]: it comes from statistical temperature fluctuation.
- Excess gas noise: it is caused from the test mass motion scattered by some residual gas.

Classical noise (from optical carrier)

- Power and frequency fluctuation of the carier: as we see from equation 1.28, the signal reaching the interferometer output port is proportional to P_0, the carrier power, and the differential arm length change is multiplied by the carrier wave number k. These two terms contain noise from the optical carrier, namely the main laser intensity noise and frequency noise.

Quantum noise This is the term $x_{q1} - x_{q2}$ in equation 2.48. A more detailed picture will be given in section 2.6.5, while here the semiclassical interpretation of this noise is provided.

- Radiation pressure noise: in the semiclassical picture, this noise comes from the momentum exchange between the photon and the test masses. This noise is proportional to the amount of photons hitting the test masses.

- Shot noise: the photon reaching the detector have a random arrival time, described by Poissonian distribution. This random arrival time translates into power fluctuation which can be mistaken for GWs.

There are also other noise which is related to the operation of interferometer and scattering light. They are also important noise sources and are usually addressed as technical noises (e.g. control noise, scattering noise, etc.).

2.6.1 Seismic noise and its attenuation

To detect gravitational wave, the test mass should behave as a free mass in the detection frequency (from 10 to 10kHz). However, the seismic motion can cause optics' vibration, which will be in general uncorrelated if optics are far away from each other. The seismic noise is always separated into three different frequency regions

- At frequencies smaller than 1 mHz, the seismic noise comes from tidal deformation of ground.
- At frequencies between 0.1 and 0.5 Hz, the seismic noise, usually called microseismic noise, comes from ocean waves and large water mass movements.
- At frequencies above 1 Hz, seismic noise comes from weather condition or human activity and is proportional to f^{-2}.

In the case of KAGRA, the underground feature makes the seismic noise much lower compared to other GWs detectors' sites in the region above 1Hz. Figure 2.15 shows the seismic noise in TAMA, VIRGO and KAGRA during day and night. We could also see that the day/night difference is even smaller in the case of KAGRA.

The requirement of seismic noise for gravitational wave detection at 10Hz is on the order of $10^{-20}m/\sqrt{Hz}$. This means that the ground motion needs to be reduced by approximately 10 order of magnitudes. To achieve this suppression, the pendulum principle is used. For a mass m object suspended by a l long wire, a force $m\ddot{x}_{obj} = -mg(x_{obj} - x_{seis})/l$ will be applied. The Fourier transform [2] of this force equation gives us the transfer function from the suspension point to object $x_{obj}/x_{seis} = 1/(1 - \frac{\omega^2}{\omega_0^2})$. It is easy to see that one stage of pendulum offers a f^{-2} attenuation above resonant frequency $\omega_0 = \sqrt{g/l}$. Note that in the case of KAGRA, the Type-A suspension has height of 13.5m which is aimed to have a

[2] The Fourier transform relation of $\mathscr{F}\{\frac{d^n f(t)}{dt^n}\} = (i\omega)^n f(\omega)$ is used.

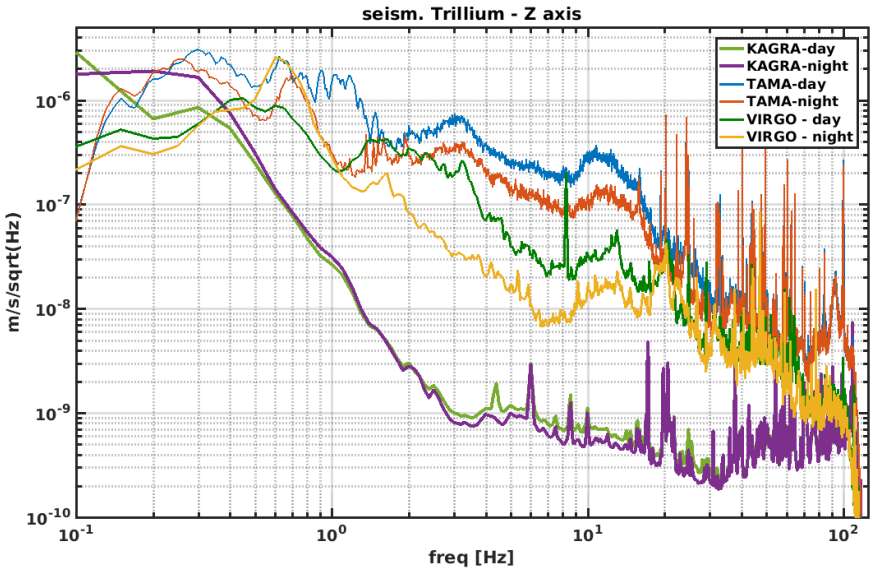

Figure 2.15: Seismic noise comparison for KAGRA (light green-day, purple-night), VIRGO (dark green-day, yellow-night) and TAMA (blue-day, orange-night)

smaller value for resonant frequency $\sqrt{g/l}$. Accumulated stages of pendulum offers accumulated attenuation. But at the same time, mechanical resonance should be damped carefully. The mechanical resonances are damped by actuators controlled by an active feedback loop working at the mechanical resonance frequencies. Therefore high frequency noise will not be introduced by these actuators. The details of KAGRA actuators are summarized in [63].

2.6.2 Newtonian noise and its cancellation

Newtonian noise comes from gravity field fluctuations around the test mass and limits the sensitivity below around 30Hz. The sources can be divided into following items

- Seismic body waves which propagate through media in all directions, including shear waves and compression waves. As shown in [64], these waves become much more dominant when gravitational wave detector go further underground.
- Seismic surface waves which propagate on surfaces of homogeneous media. This noise is the main limitation for interferometer built on the ground [65].
- Atmospheric gravity perturbations including pressure (sound or wind), tem-

perature and humidity. The infrasound is investigated in [66] to be a limiting noise for Advanced Virgo and needs to be paid attention for future generation gravitational wave detectors.

- Moving objects including motion with constant speed, oscillating and rotating objects. For example, traffic nearby the site of GWs detector, or in the case of KAGRA, water bodies moving inside the mountain or on top of it (snow).

The Newtonian noise can be calculated from seismic spectra as explained in [67]. Rayleigh waves seemed to be the main limitation for LIGO, therefore the measurement of vertical displacement by seismometer provides information for the calculation of Newtonian noise. This noise is proportional to f^{-4} and will become smaller for longer arm length.

The Newtonian noise is difficult to reduce because we can not shield gravity field. But there are still ways to avoid or mitigate it. The easiest way to passively reduce these noise is to go to underground and select a good location for the infrastructure. In addition, an experiment taking advantage of seismic metamaterials was shown to be able to shield the noise from surface waves. This passive way was test at frequency of 50Hz and achieved a factor of 2 reduction [68]. The active way to mitigate this noise is to do realtime/offline data processing. The spectrum measurement provided by sensor (seismometers, accellerometers or microphones) is used to estimate the coherence from this noise to signal, then to be subtracted. For the third generation gravitational wave detectors, the low frequency requirement is very challenging and the mitigation of this noise will be essential.

2.6.3 Thermal noise

All the thermal noises are related to mechanical or thermal dissipation. In the work of Callen and Welton [69], this process is explained as an energy transfer from a periodic motion to a random fluctuation caused by system internal losses. The random fluctuating force in one degree of freedom is given as $< F_x^2 >= (2/\pi)kT\eta \int d\omega$ where η is the real part of the impedance, which is equivalent to

$$< F_x^2 >= 4kT\eta \tag{2.49}$$

where k is the Boltzman constant and T is temperature. The above theorem is usually called Fluctuation dissipation theorem (FDT). For a mechanical system, the mechanical impedance is a measure of how much a structure resists motion when

subjected to a force. The definition is $F = Zv$ where F is the force, Z is the impedance and v is velocity. By considering the Fourier transform from velocity to displacement, we can get the power spectrum of random fluctuation displacement as

$$S_x(f) = \frac{kT}{\pi^2 f^2} \mathrm{Re}\{Y(f)\} \tag{2.50}$$

This random fluctuation power spectrum is proportional to the temperature of the system. In the case of KAGRA, its cryogenic operation aims for the reduction of thermal noise and especially the coating thermo-optic noise which is the main limitation in the mid-frequency region for aLIGO and AdV.

Suspension thermal noise

The suspension system is subjected to perturbation coming from the excitation of seismic motion, then the mechanical loss inside the suspension material makes the system absorb energy and induces suspension thermal noise.
Compared with a simple one-stage pendulum introduced in the section of seismic noise, the equation of motion will include an additional dissipative term $\gamma\dot{x}$ which represents the viscous force due to mechanical loss. Once we have the equation of motion, we can have the admittance and spectrum of thermal noise. In the case of KAGRA, this particular noise is expected to be one of the main limitation in the GW sensitivity. This is not the case for aLIGO and AdV. The sapphire fibers suspending the test masses are, compared to the fused silica fibers of the other GW detectors, much shorter and thicker. This is to maximize the heat transfer from the mirror to the suspension, but at the cost of increasing the suspension thermal noise.

Coating and substrate Brownian noise

Different from the case of suspension thermal noise, for all the thermal Brownian noise related to mirror coating/substrate, the excitation of mirror motion is from radiation pressure noise. This radiation pressure, together with the test-mass internal elastic forces and internal dissipation, will lead to a time evolution $x(t)$ of the observable x. The connection of them is provided by Levin as [70]

$$|\,\mathrm{Re}[Y(f)]| = \frac{2W_{diss}}{F_0^2} \tag{2.51}$$

where $W_{diss} = 2\pi f U_{max}\phi(f)$ with $U_{max} = \frac{1}{2}|F||x(f)|$. Here we need to notice that the response $x(f)$ to the excitation needs to consider thematerial loss angle, which

is expressed as [60] $x(f) = |x(f)| \exp(-i\phi) \approx |x(f)|(1 - \imath\phi)$. The loss angle is composed with loss from substrate and coating and weighted by the different elastic energy U stored.

$$\phi = \frac{1}{U}(U_{subs}\phi_{subs} + U_{coat}\phi_{coat}) \tag{2.52}$$

For the elastic energy U, a detailed explanation can be found in the appendix of [70]. For coating, the elastic energy is discussed in [71]. Without considering anisotropic layer structure of the coating, thermal noise can be expressed as

$$S_x(f) = \frac{2kT}{\pi^{3/2} f} \frac{1-\sigma^2}{\omega Y} \phi_{subs} + \frac{2}{\sqrt{\pi}} \frac{1-2\sigma}{1-\sigma} \frac{d}{\omega} \phi_{coat} \tag{2.53}$$

where ω is the beam radius, Y is Young's modulus, σ is Poisson's ratio and d is the thickness of coating. From this equation, we can see how to reduce this noise: we can reduce temperature, increase stiffness of the material, reduce the thickness of coating or increase the beam size. In the case of KAGRA, cryogenic operation reduces the temperature and the use of sapphire mirror increase the stiffness relative to fused silica. The coating Brownian noise is one of the main limitations for aLIGO and AdV, while, thanks to the mentioned choice, it is expected not to be a main limitation for KAGRA sensitivity.

Coating and substrate thermo-elastic noise

For coating, there is also thermal dissipation apart from mechanical dissipation. The temperature dependent quantity will experience fluctuation due to thermal dissipation, for example the refractive index and coating thickness. The thermal fluctuation was calculated by Levin [72] based on the injection of periodic entropy, tracking all thermal relaxation processes in the system and FDT theorem.

$$S_T = \frac{2\sqrt{2}}{\pi} \frac{kT^2}{\omega^2 \sqrt{2\pi f \kappa C}} \tag{2.54}$$

where k is Boltzmann's constant, T is temperature, ω is beam radius, κ is thermal conductivity, C is heat capacity per volume, f is frequency. Considering the thermal expansion and temperature dependent refractive index, the thermal optic noise is [61]

$$S_x = S_T(\bar{\alpha}_C d - \bar{\beta}\lambda - \bar{\alpha}_s d \frac{C_c}{C_s}) \tag{2.55}$$

where $\bar{\alpha}_C$ is the effective coefficient of thermal expansion of the coating, d is the coating thickness, $\bar{\beta}$ is the effective thermorefractive coefficient, λ is the beam wave-

length, $\bar{\alpha}_s$ is the effective coefficient of thermal expansion of the substrate. The first two terms represents the coating thermal-optic noise while the last term represents substrate thermo-elastic noise.

2.6.4 Excessive gas noise

The vacuum level for gravitational wave detectors needs to reach level around $10^{-9}Pa$ to have negligible influence of residual gas. The power spectrum density is expressed as [73]

$$S_{gas} = \frac{(4\pi\alpha)^2\rho}{v_0 L^2}\int_0^L \frac{exp[-2\pi f\omega(z)/v_0]}{\omega(z)}dz \tag{2.56}$$

where α is the polarizability, ω is the beam radius, L is the interferometer arm length, ρ is the number density, v_0 is the most probable speed for the particle.

2.6.5 Quantum noise in semi-classical picture

Quantum noise comes from the quantum nature of light. In this chapter I will introduce it in a semi-classical way. I will describe the quantum picture in chapter 3. As stated before the quantum noise is usually divided into shot noise, which comes from the random arrival time of the photons on the photodetector, and into radiation pressure noise, coming from the momentum exchange of the photons with the mirrors. There are two semi-classical methods to understand them, one is the so-called sidebands picture while another is from Schottky shot-noise formula. There have been already lots of thesis and papers describing this noise, for example [74]. I will discuss this noise based on Schottky formula in this section.

Shot noise

The semi-classical shot noise of light comes from the shot noise formula of electrical devices developed by Walter Schottky [75]. This shot noises are all caused by the random arrival of particles which can be described by Poisson distribution. In the case of a photodetector, the formula which gives the shot noise power spectral density is

$$S_I(f) = 2e\bar{I} \tag{2.57}$$

with e the electron charge and $\bar{I}$ the mean photo current. To calculate the interferometer shot noise, we need to rewrite the last equation in terms of light power.

Assuming a perfect response from the photo diode, we can have the relation between $\bar{I}$ and $\bar{P}$ as

$$\bar{I} = e \times \bar{N} = e \times \frac{\bar{P}}{\hbar\omega} \tag{2.58}$$

where $\hbar$ is the reduced Planck constant and $\omega = 2\pi f$ with f the frequency of the light. The unit of one-sided power spectral density for current is $A^2 Hz^{-1}$. To calibrate it to optical power unit $W^2 Hz^{-1}$, the transformation $S_P = S_I(\hbar\omega/e)^2$ derived from equation 2.58 is required. Then we can have

$$S_P(f) = 2e\bar{I} \times \frac{(\hbar\omega)^2}{e^2} = 2e \times e\frac{\bar{P}}{\hbar\omega} \times \frac{(\hbar\omega)^2}{e^2} = 2\hbar\omega\bar{P} \tag{2.59}$$

$\bar{P}$ is the power from the signal port of interferometer, which has already been described as in equation 1.28. If the differential motion of the two interferometer arms is small and the interferometer is operated at the dark fringe, we can approximate the output power as $P = P_0 \times k^2\Delta x^2$. Then we can have the response of interferometer as

$$\frac{dP}{dx} = 2P_0 k^2 \Delta x \tag{2.60}$$

Taking the above response into equation 2.59, we can calibrate it into length.

$$S_x(f) = 2\hbar\omega\bar{P} \times \frac{1}{4P_0^2 k^4 \Delta x^2} = \frac{\hbar\omega}{2P_0 k^2} = \frac{\hbar c^2}{2P_0\omega} \tag{2.61}$$

The square root of the above equation is the shot noise in unit of $m\sqrt{Hz}^{-1}$, which is

$$\Delta L_{SN} = c\sqrt{\frac{\hbar}{2\omega P_0}} \tag{2.62}$$

The last equation shows a white spectrum which scales with the inverse of the square root of the input power.

Radiation pressure noise

Radiation pressure noise comes from the same principle of shot noise which is the random arrival of photons. To translate the photon counting fluctuation into differential length fluctuation, we need to consider two additional steps which are from optical power to radiation pressure and from force to displacement. The spectrum of radiation pressure caused by a beam with power $P(\Omega)$ has already been investigated [76] and we can write it as

$$F(\Omega) = \frac{2P(\Omega)}{c} \tag{2.63}$$

where Ω is the sideband frequency with respect to the carrier. As shown at the beginning of this chapter, we can consider the test masses as a free mass for frequencies above the mechanical resonance frequency of the suspension system. The equation of motion for a free mass M is $F = M\ddot{x}$, and considering its Laplace transformation we can write it in the frequency domain as

$$x(\Omega) = -\frac{F(\Omega)}{M\Omega^2} \tag{2.64}$$

Combining equation 2.59, 2.63 and 2.64, we get the power spectral density of differential arm length due to radiation pressure noise, which can be written as

$$S_{RPN}(\Omega) = \frac{8\hbar\omega P_0}{M^2\Omega^4 c^2} \tag{2.65}$$

The square root of this PSD is the amplitude spectrum density

$$\Delta L_{RPN} = \frac{2\sqrt{2\hbar\omega P_0}}{M\Omega^2 c} \tag{2.66}$$

This spectrum decreases as $1/\Omega^2$ due to its dynamical feature. Moreover, it is proportional to the square root of the optical power.

Total quantum noise spectrum

By adding shot noise and radiation pressure noise together, we can get the total quantum noise spectrum as shown in figure 2.16 for the case of a simple Michelson interferometer.

To change the shape of quantum noise spectrum, three parameters can be adjusted in the shot noise and radiation pressure noise equations. Apart from that, squeezing technique can also reduce it. They are summarized as following:

- Interferometer arm length: increasing the arm length will amplify the GW signal response, therefore, since neither shot noise or radiation pressure noise depends on the arm length, the total sensitivity will be improved.

- The mass of mirror (test mass): increasing mirror mass the radiation pressure noise will be reduced.

- Arm power: changing the arm power, the quantum noise will be modified as figure 2.17. As seen in the previous two paragraph, the shot noise spectrum

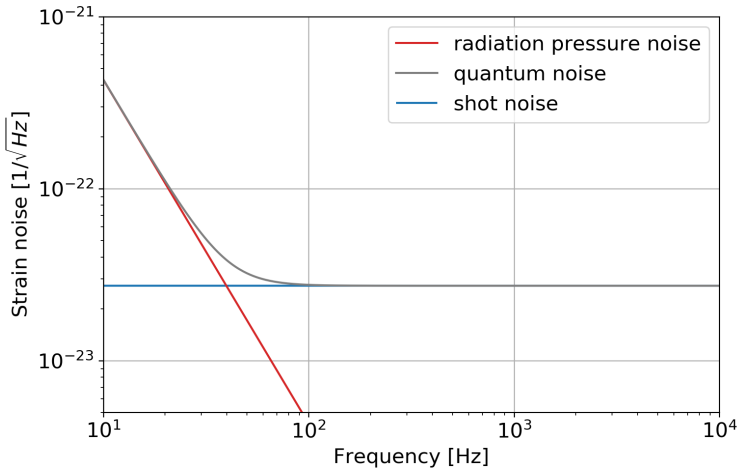

Figure 2.16: Quantum noise without considering the effect of arm cavity filtering and signal extraction cavity. The arm cavity power is assumed to be 400kW, arm length to be 3km and mirror mass to be 20kg.

is proportional to $P_0^{-1/2}$ while the radiation pressure noise spectrum is proportional to $P_0^{1/2}$, therefore by increasing the power, for example, the effect of the radiation pressure noise will be larger, while the one of the shot noise will be reduced.

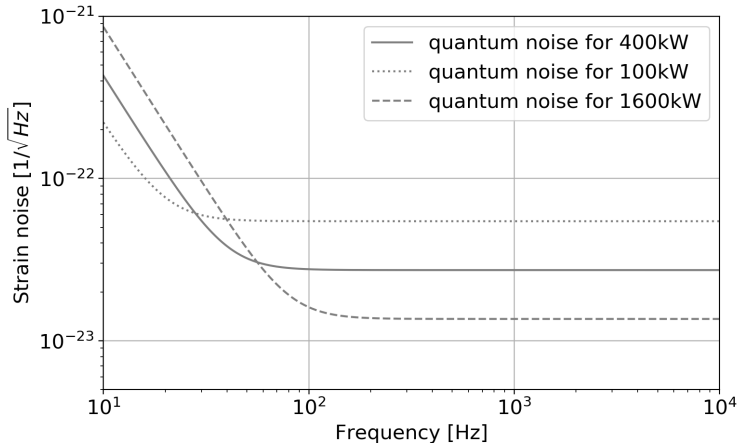

Figure 2.17: Quantum noise for different arm power. All the other parameters are the same with figure 2.16.

- Squeezed state of light: quantum noise can be reduced using squeezing technique. The production and characterization of squeezed states of light is the main topic of this thesis and the related theory will be explained in detail in the next chapter.

By considering all the mentioned effects, we can conclude that the ideal configuration could be: longer arm interferometer with higher arm power and heavier test mass with respect to the current ones. Unfortunately, such enhancements are not easily achievable, therefore, the use of squeezed light technique is of paramount importance to reduce the impact of the quantum noise in GW detectors.

Chapter 3

Quantum states and their manipulation to reduce quantum noise for gravitational wave detector

Although the semi-classical picture of quantum noise is easier to understand, a quantum picture is necessary if we want to fully understand quantum noise of an interferometer and its reduction using squeezing. About forty years ago, Caves developed such quantum noise picture to prove that the this noise is the vacuum fluctuation entering from the output port of interferometer [77]. Just one year later, he proposed the idea of replacing such vacuum state with a squeezed vacuum state [78]. This work paved the way to the application of squeezed state in gravitational wave detector.

In 1985, the first squeezing observation was achieved through a four-wave mixing process [79]. One year later, a squeezing observation was achieved through a parametric down conversion process [80]. In 1987, the first reduction of shot noise by using squeezed vacuum was achieved [81, 82]. After that, strong efforts were made to achieve higher squeezing level and push down the squeezing bandwidth toward the low frequency. Up to now, the highest achieved squeezing level is 15dB in the MHz region [83]. For audio band (down to $\sim$ 10 Hz), a squeezing level of 12dB has been realized [84]. The implementation of frequency independent squeezed vacuum source into gravitational-wave detectors was first realized in 2010 in GEO600 [85]. In the last joint observation run of LIGO and Virgo, frequency independent squeez-

ing was also introduced and its use improved the sensitivity at high frequency of more than 3dB [86, 87].

However, at the time Caves proposed the use of squeezed state, the interferometer didn't have any cavity. The low power inside interferometer arm makes radiation pressure noise almost negligible. After introducing Fabry-Perrot cavities in the arm, the radiation pressure increased consistently. For this reason, frequency dependent squeezing, which can be used to reduce both radiation pressure noise and shot noise, has been proposed by Kimble twenty years ago [88]. In the same paper, Kimble re-derived the quantum noise by following the method proposed by Caves in the case of a Fabry-Perot Michelson interferometer. Almost at the same time, a work done by Buonanno and Chen completed the calculation of quantum noise for the full configuration of current generation gravitational-wave detectors [89].

The implementation of frequency independent squeezing is equivalent to increase the input laser power. For example, 10dB squeezing can reduce shot noise by a factor of 10 ($\sqrt{10}$ in the case of amplitude spectrum density), which can also be realized increasing 10 times the arm cavity power. Both LIGO and Virgo use less than half of their design input power due to the problems related with high power. Therefore, frequency independent squeezing is a suitable alternative to meet the current requirement. Usually the limiting factors which prevent a laser power increase [90] are uniform absorption, radiation pressure changing alignment plants, parametric instability, laser reliability, beam jitter, inhomogeneous absorption and radiation pressure driven instability. Both LIGO and Virgo are putting efforts to solve these problems in order to increase the laser power. Since the radiation pressure noise starts to be relevant for the sensitivity of LIGO, the use of frequency dependent squeezing starts to become crucial.

In this chapter, the concept of quantum states, generation of squeezed states, characterization of squeezed states, quantum noise in the quantum picture and its reduction by using squeezing are revisited. This is an essential background for understanding the necessity of developing a frequency dependent squeezed vacuum source.

3.1 Quantum states and their quantum uncertainty

Vacuum states and their fluctuations are introduced in this section. Two well-known properties from quantum mechanics that we need to remember throughout this chapter are:

1. A light vacuum state has a non-zero energy of $\hbar\omega/2$ (which we will demonstrate later on), and

2. Non commuting operators of position and momentum satisfy Heisenberg uncertainty principle $\Delta x \Delta p \geq \hbar/2$

Since the light vacuum state has energy, its fluctuation is present and causing quantum noise. We will see in this section that the vacuum can be squeezed by applying a squeeze operator. As a result, vacuum fluctuation can be reduced. However, due to Heisenberg uncertainty principle, the reduction of vacuum fluctuation in one quadrature (corresponding to one operator) leads to the increase of vacuum fluctuation in the other quadrature. More information about the subjects presented in this section can be found for example in [91, 92, 93, 94].

3.1.1 Quantum harmonic oscillator

The theory of quantum optics develops from the theory of quantum harmonic oscillator. For an harmonic oscillator, annihilation operator $\hat{a}$ and its Hermitian conjugate $\hat{a}^\dagger$ (creation operator) are defined as

$$\hat{a} = \frac{1}{(2m\hbar\omega)^{1/2}}(m\omega\hat{x} + i\hat{p}) \tag{3.1}$$

$$\hat{a}^\dagger = \frac{1}{(2m\hbar\omega)^{1/2}}(m\omega\hat{x} - i\hat{p}) \tag{3.2}$$

from the commutator $[\hat{x}, \hat{p}_x] = i\hbar$, $[\hat{a}, \hat{a}^\dagger] = 1$ can be derived. Here, $\hat{a}$ is called annihilation operator because

$$\hat{H}\hat{a}\psi_n = (E_n - \hbar\omega)\hat{a}\psi_n \tag{3.3}$$

where $\hat{H} = \hbar\omega(\hat{a}^\dagger\hat{a} + \frac{1}{2})$ is the Hamiltonian of our system and $\hat{H}\psi(x) = E\psi(x)$ its Schrödinger equation. The application of the annihilation operator $\hat{a}$ causes the eigenenergy E_n of state ψ_n to decrease by $\hbar\omega$.
To prevent the energy from going negative, we need to have $\hat{a}\psi_0 = 0$. So $\hat{H}\psi_0 = \hbar\omega(\hat{a}^\dagger\hat{a} + \frac{1}{2})\psi_0 = \frac{1}{2}\hbar\omega\psi_0$, which tells us that the zero-point energy is

$$E_0 = \frac{1}{2}\hbar\omega \tag{3.4}$$

The state ψ_0 is called vacuum state and usually written as $|0\rangle$. The energy for state ψ_n is

$$E_n = E_0 + n\hbar\omega = \left(n + \frac{1}{2}\right)\hbar\omega \tag{3.5}$$

These results can be extended to physical systems whose Hamiltonian is equivalent to an harmonic oscillator.

From the fourth Maxwell equation, the change of magnetic field in space equals to the change of electric field in time. This property makes these two field have phase difference of 90 degrees, which is the same phase difference between displacement x and momentum p of an harmonic oscillator. Therefore, the Hamiltonian of electromagnetic wave can be written in the form of harmonic oscillator and above results can be applied to electromagnetic waves. The quantized electric field can be expressed as [95]

$$\hat{E}(z,t) = \varepsilon_0 \sin(kz)(\hat{a}e^{-\imath\omega t} + \hat{a}^\dagger e^{\imath\omega t}) \tag{3.6}$$

where ε_0 is the amplitude of the field. This formula will be used many times in this chapter.

Coherent state

Coherent state is defined by "displacing" a vacuum state,

$$|\alpha\rangle = D(\alpha)\,|0\rangle \tag{3.7}$$

Here $D(\alpha) = \exp\left(\alpha\hat{a} - \alpha^*\hat{a}^\dagger\right)$ is called displacement operator. The average photon number of coherent state is

$$\bar{n} = \langle\alpha|\,\hat{n}\,|\alpha\rangle = |\alpha|^2 \tag{3.8}$$

A coherent state can be expressed as a combination of photon number states $|\alpha\rangle = \Sigma_n c_n\,|n\rangle$ with $c_n = \exp(-|\alpha|^2/2) * \alpha^n/\sqrt{n!}$. The probability of measuring n photons is the square of c_n and this shows that the photon statistic of a coherent state follows the Poission distribution.

Squeezed state

A squeezed state is generated by applying a squeeze operator on a vacuum state:

$$|\xi\rangle = S(\xi)\,|0\rangle \tag{3.9}$$

The squeeze operator is defined as $S(\xi) = \exp\left(\frac{1}{2}(\xi^*\hat{a}^2 - \xi(\hat{a}^\dagger)^2)\right)$. The squeeze parameter ξ is defined as $r\exp(\imath\theta)$ where r is squeeze magnitude and θ is squeeze angle.

3.1.2 Quadrature operators and phasor diagrams

The introduction of quadrature operators helps to understand the physical meaning of quantum state and related quantum uncertainty. Quadrature operators are defined as

$$\begin{aligned} \hat{X} &= \frac{1}{2}(\hat{a}^\dagger + \hat{a}) \\ \hat{Y} &= \frac{\imath}{2}(\hat{a}^\dagger - \hat{a}) \end{aligned} \tag{3.10}$$

From $[\hat{a}, \hat{a}^\dagger] = 1$, $[\hat{X}, \hat{Y}] = \frac{\imath}{2}$ can be derived. Considering equation 3.10, equation 3.6 can be rewritten using quadrature operators as

$$\hat{E}(z,t) = 2\varepsilon_0 \sin(kz)(\hat{X}\cos(\omega t) + \hat{Y}\sin(\omega t)) \tag{3.11}$$

These two quadrature operators represent the real and imaginary part of electric field. A plane-polarized electromagnetic monochromatic wave within a cavity may be written as

$$E(z) = \varepsilon_0(z)e^{\imath\phi} = \varepsilon_0(z)\cos\phi + \imath\varepsilon_0(z)\sin\phi \tag{3.12}$$

where $\varepsilon_0(z) = \varepsilon_0 \sin(kz)$. A phasor diagram is a 2-D plot where the x-axis is the real-axis and y-axis is the imaginary-axis (as shown in figure 3.1). The electric field can be shown in the phasor diagram as an arrow. The length of the arrow is the amplitude of electric field, while the phase is the angle between the arrow and the x-axis. Although the reference frame for amplitude and phase changes with the evolution of the electric field, amplitude and phase axis are always orthogonal with each other. Therefore, the quadrature plane is also called amplitude-phase quadrature plane.

3.1.3 Quantum uncertainty of vacuum states

The variance of a measured value X is defined as

$$(\Delta X)^2 = \langle X^2 \rangle - \langle X \rangle^2 \tag{3.13}$$

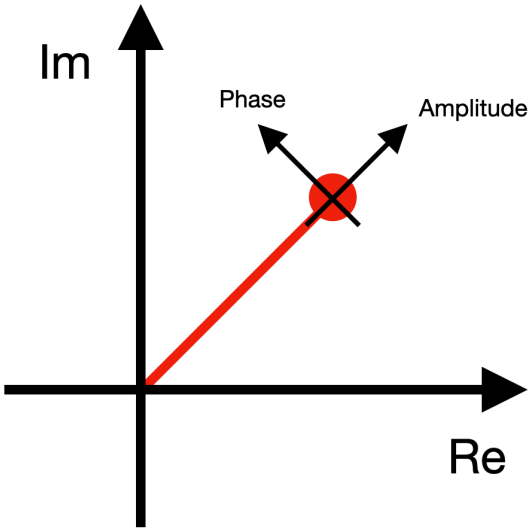

Figure 3.1: Phasor diagram for an electric field. The red point represents the value (amplitude and phase) of the field and its uncertainty.

Here $\langle\,\rangle$ represents the average of the repeated result of a measurement (corresponding to the operator X) on a state. We remark that if the operators X and Y have a commutator $[X, Y]$ which is not zero, they cannot be measured simultaneously with arbitrary precision. Their variances follow the Heisenberg uncertainty principle

$$(\Delta X)^2(\Delta Y)^2 \geq |[\hat{X}, \hat{Y}]|^2/4 \tag{3.14}$$

Recalling the expression of the commutator for quadrature operators, we can obtain

$$(\Delta X)^2(\Delta Y)^2 \geq \frac{1}{16} \tag{3.15}$$

For vacuum or coherent state, the two quadrature (phase and amplitude) have a phase difference of 90 degrees and they have equal minimum quantum uncertainty of

$$\Delta X = \Delta Y = 1/2 \tag{3.16}$$

This vacuum fluctuation of $1/2$ is usually referred to as **coherent vacuum fluctuation** and it is the minimum fluctuation achievable without using squeezing technique. This minimum uncertainty is the same for vacuum and coherent states.

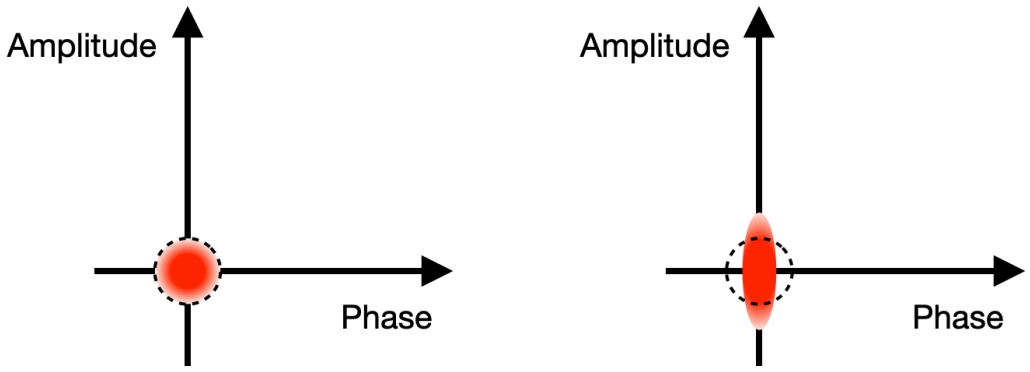

Figure 3.2: Representation of a vacuum state (left) and a squeezed vacuum states (right) in a phasor diagram.

3.1.4 Quantum uncertainty of squeezed vacuum states

According to the squeeze (characterized by r) and rotation (characterized by ϕ) operation for a vector in quadrature space, squeeze operator S can be written in matrix form as [96]

$$\begin{aligned}\mathbf{S}(r,\phi) &= \mathbf{R}(\phi)\mathbf{S}(r,0)\mathbf{R}(-\phi) = \mathbf{R}_\phi \mathbf{S}_r \mathbf{R}_\phi^\dagger \\ &= \begin{pmatrix}\cos\phi & -\sin\phi \\ \sin\phi & \cos\phi\end{pmatrix}\begin{pmatrix}\mathrm{e}^r & 0 \\ 0 & \mathrm{e}^{-r}\end{pmatrix}\begin{pmatrix}\cos\phi & \sin\phi \\ -\sin\phi & \cos\phi\end{pmatrix}\end{aligned} \tag{3.17}$$

which, after computing the matrix product, becomes

$$\mathbf{S}(r,\phi) = \begin{pmatrix}\cos^2\phi\mathrm{e}^r + \sin^2\phi\mathrm{e}^{-r} & \cos\phi\sin\phi(\mathrm{e}^r - \mathrm{e}^{-r}) \\ \cos\phi\sin\phi(\mathrm{e}^r - \mathrm{e}^{-r}) & \sin^2\phi\mathrm{e}^r + \cos^2\phi\mathrm{e}^{-r}\end{pmatrix} \tag{3.18}$$

So when we apply the squeeze operator to a vacuum state, its quadrature fluctuations become:

$$\begin{pmatrix}\Delta X' \\ \Delta Y'\end{pmatrix} = \begin{pmatrix}\cosh(r) + \sinh(r)\cos 2\phi & \sinh(r)\sin 2\phi \\ \sinh(r)\sin 2\phi & \cosh(r) - \sinh(r)\cos 2\phi\end{pmatrix}\begin{pmatrix}\Delta X \\ \Delta Y\end{pmatrix} \tag{3.19}$$

and they can be explicitly written as:

$$(\Delta X')^2 = \frac{1}{4}(\cosh^2 r + \sinh^2 r + 2\sinh r \cosh r \cos\phi) \tag{3.20}$$

$$(\Delta Y')^2 = \frac{1}{4}(\cosh^2 r + \sinh^2 r - 2\sinh r \cosh r \cos\phi) \tag{3.21}$$

When $\phi = 0$, we have $(\Delta X')^2 = \frac{1}{4}e^{2r}$ and $(\Delta Y')^2 = \frac{1}{4}e^{-2r}$. The quantum uncertainty for squeezed vacuum in two different quadratures is then

$$\Delta X_s = \frac{1}{2}e^{r} \tag{3.22}$$

$$\Delta Y_s = \frac{1}{2}e^{-r} \tag{3.23}$$

We see that the Heisenberg uncertainty principle is still verified and that squeezed vacuum can be represented as an ellipse in the phasor diagram.

Besides, the change of phase ϕ causes the rotation of squeezing ellipse.

3.1.5 Photon statics

Different quantum states have been introduced and we mentioned that coherent state photon statistics satisfies Possonian distribution. We will see that photon statistic distribution is an important feature for different quantum states.

For a totally random arrival time of photons, the photon statistic is given by the binomial distribution. When the photon number is large, it becomes a Poisson distribution. This corresponds to the case of coherent states.

For a thermal coherent state of light, the spectrum follows Planck's law and is described by a Bose-Einstein distribution. When it has the same average photon number of a coherent state, it has a much larger variance. This corresponds to a super-Poissonian distribution.

If, as in the case of a squeezed state, the arrival time of photons is more regular than for a coherent state, the distribution will becomes sub-Poissonian distribution. The observation of this kind of distribution is a signature of the quantum properties of light.

In figure 3.3, the photon static case of coherent, thermal coherent and squeezed states with the same average Fock number are plotted.

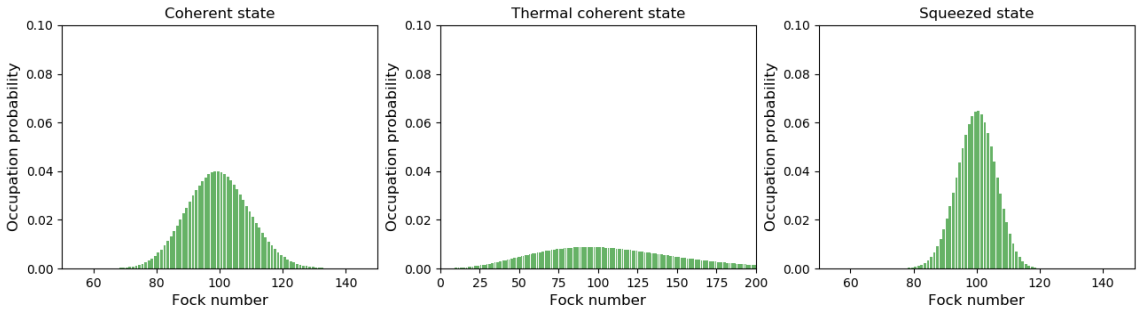

Figure 3.3: The photon static for coherent state, thermal coherent state and squeezed state when they have the same average photon number. They show Poissonian, super-Poissonian and sub-Possonian distribution, respectively. The plot is done using Python quantum toolbox QuTiP [97]

3.2 Generation of squeezed vacuum state and its detection

Before talking about the application of the squeezing in interferometers, let's have a look at how squeezed vacuum states are generated and detected.

3.2.1 Generation of squeezed vacuum state

The generation of squeezed vacuum is based on the interaction between a fundamental and a second harmonic field. In our case the fundamental field is vacuum and the second harmonic field is a high power pump light. If the fundamental field is a bright field, the so-called parametric amplification/de-amplification process will be observed.

If there is only linear interaction, waves at different frequencies cannot interfere. So squeezing generation relies on the use of a non-linear crystal. Optical non-linear processes that lead to squeezing generation are for example parametric down-conversion, four-wave mixing and Kerr effect.

For a parametric down-conversion process, we consider a vacuum field with annihilation operator $\hat{a}$ at frequency ω and a pump field with annihilation operator $\hat{b}$ at frequency $\omega_p = 2\omega$. The interaction between these two fields takes place thanks to a second order polarization $\chi^{(2)}E^2$, which corresponds to an Hamiltonian [95]

$$\hat{H} = \hbar\omega\hat{a}^\dagger\hat{a} + \hbar\omega_p\hat{b}^\dagger\hat{b} + \imath\hbar\chi(\hat{a}^2\hat{b}^\dagger - \hat{a}^{\dagger 2}\hat{b}) \tag{3.24}$$

In most of the cases (including ours), the pump can be treated classically and its

depletion can be neglected. Then Hamiltonian in interaction picture becomes

$$\hat{H}_I = \imath\hbar\chi(\beta e^{\imath\omega_p t}(\hat{a}e^{-\imath\omega t})^2 - \beta e^{-\imath\omega_p t}(\hat{a}e^{-\imath\omega t})^{\dagger 2}) \tag{3.25}$$

Since $\omega_p = 2\omega$, the time evolution part cancels out, correspondingly, the time-evolution operator is

$$\hat{U}_I(t) = e^{-\imath\hat{H}_I t/\hbar} = e^{\chi\beta^* t\hat{a}^2 - \chi\beta t\hat{a}^{\dagger 2}} \tag{3.26}$$

This time-evolution operator has the same form of the squeeze operator introduced in section 3.1.1, which indicates that parametric down conversion can generate squeezed state. Besides, term $2\chi\beta t$ reveals that the squeezing magnitude is proportional to pump field strength β and to the interaction time t.

3.2.2 Detection of squeezed vacuum state

There are several ways to detect squeezed light vacuum states. Since the squeezed vacuum state has too few photons, a bright field is usually required to amplify it. One way is shown in figure 3.4, squeezed vacuum state is injected into an interferometer and will be amplified by the carrier field of interferometer. In the end, the squeezed vacuum state is measured with a single photo detector. The other way is shown in figure 3.5, the squeezed vacuum state is amplified by the local oscillator of homodyne detector. In the end, the squeezed vacuum state is measured by two photo detectors. These two cases, extensively discussed in [98] are briefly summarized in the following.

Measurement by a photodiode

We already mentioned that a large part of GW detector spectrum is limited by quantum noise. Nowadays, interferometers operate close to dark fringe with squeezing injection, so the output light is actually a bright squeezing state with annihilation operator as $\hat{a} = \langle\hat{a}\rangle + \delta\hat{a}$. The corresponding photon-number operator will be

$$\begin{aligned}\hat{n} &= (\langle a\rangle^* + \delta\hat{a}^\dagger)(\langle\hat{a}\rangle + \delta\hat{a}) \\ &= |\alpha|^2 + 2|\alpha|\delta\hat{X}_\phi + \delta\hat{a}^\dagger\delta\hat{a}\end{aligned} \tag{3.27}$$

where α is the expected value of bright squeezed field while ϕ is its phase. $\delta\hat{X}_\phi$ is the fluctuation term of the quadrature operator $\hat{X}_\phi$ along the direction of α. The last term $\delta\hat{a}^\dagger\delta\hat{a}$ can be neglected since it is the second order of small number.

When this field hits a photodiode, the variance (the square of the second term in

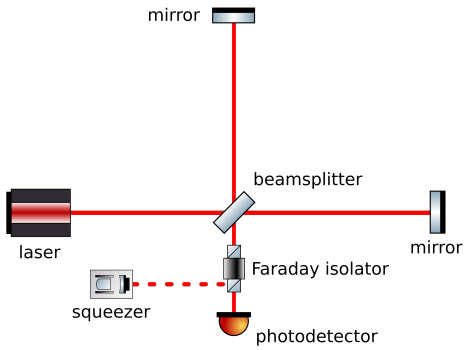

Figure 3.4: Squeezing injection and detection through interferometer. Squeezed state is generated from squeezer and injected through a Faraday isolator. The squeezed field is represented as a dashed line. In the end, the measurement of squeezing is done on a single photo detector.

equation 3.27) can be minimized by adjusting the relative phase between squeezing and interferometer carrier light θ, having

$$\mathrm{Var}(\hat{n}) = |\alpha|^2 e^{-2r} \tag{3.28}$$

For a comparison, in the case of no squeezing injection the output field of the interferometer is just a coherent state and its variance will be

$$\mathrm{Var}(\hat{n}_{coh}) = |\alpha|^2 \tag{3.29}$$

We remark that in the two cases the noise level is proportional to carrier power $|\alpha|^2$ but not to the carrier quantum noise properties.

Measurement by balanced homodyne detector

In order to suppress noises other than quantum noise, balanced homodyne detector (BHD) is often used in table-top quantum optics experiments. A schematic version of a BHD is shown in figure 3.5, where the left side is the optical configuration and the right are two possible electronic configuration. In contrast with hetoerodyne detection, this technique is called homodyne as the squeezing (SQZ) and the local oscillator (LO) have the same frequency.[99]. For signal to be measured, LO serves as a frequency reference which causes the signal to change frequency after a mixing

process.

Balanced homodyne detector is crucial for the measurement of quantum limited states. Squeezed states easily covered by classical noises, for example, the amplitude noise can sometimes dominate the noise spectrum until the MHz region. Especially at lower frequency, which is important for gravitational-wave detection, there are many noises such as beam pointing, non-stationary events and parasitic interference [100] which can mask the effect of squeezing. Proper operation of BHD and a careful design of the optical/electrical system help to push down these classical noises in order to reveal the quantum nature of light.

As discussed in [100], the electronic design shown by the middle scheme in figure 3.5, which is usually called variable gain design, is inevitably affected by flicker noise and gain unbalances. This will lead to a non perfect suppression of the common mode noises. The right side scheme in figure 3.5, which is usually called "current subtracting design", is more commonly used. Balanced homodyne aims for a current subtraction to have a zero DC output. In this case, all the common mode classical noises are cancelled and the measurement becomes quantum noise limited.

If we assume signal field to be $\hat{a}$ and local oscillator to be $\hat{b}$, after their combination at the beamsplitter, the output $\hat{c}$ and $\hat{d}$ will be

$$\begin{pmatrix} \hat{c} \\ \hat{d} \end{pmatrix} = \frac{1}{\sqrt{2}} \begin{pmatrix} 1 & -1 \\ 1 & 1 \end{pmatrix} \begin{pmatrix} \hat{a} \\ \hat{b} \end{pmatrix} = \begin{pmatrix} \frac{1}{\sqrt{2}}(\hat{a} - \hat{b}) \\ \frac{1}{\sqrt{2}}(\hat{a} + \hat{b}) \end{pmatrix} \tag{3.30}$$

The fields $\hat{c}$ and $\hat{d}$ will, at the photodiode level, induce the photo-currents $< \hat{i}_c >$ and $< \hat{i}_d >$ which will than be subtracted to suppress the common mode noises.

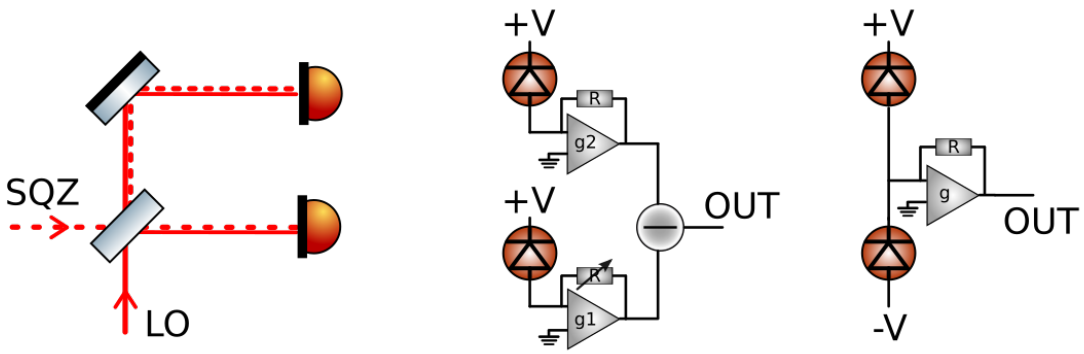

Figure 3.5: Left: BHD optical layout in our experiment. Middle: variable gain BHD. Right: current subtracting BHD.

The result of the subtraction will be

$$< \hat{i}_c > - < \hat{i}_d > \propto < \hat{n}_c > - < \hat{n}_d > = < \hat{c}^\dagger \hat{c} - \hat{d}^\dagger \hat{d} > = < \hat{a}^\dagger \hat{b} + \hat{b}^\dagger \hat{a} > \tag{3.31}$$

When measuring the quantum properties of a squeezed state or a vacuum state in general, the local oscillator is assumed to be much more powerfull, therefore can be treated as a classical field and be written as $\beta e^{i\phi}$, where ϕ is its phase difference with respect to the signal. So the photo-current difference becomes

$$< \hat{i}_c > - < \hat{i}_d > \propto |\beta| < \hat{a}^\dagger e^{i\phi} + \hat{a} e^{-i\phi} > \tag{3.32}$$

From the last formula it is clear that by changing the relative phase, different quadratures can be measured. Moreover the output of a BHD is proportional to the amplitude of the local oscillator field but not affected by its quantum properties.

3.2.3 Quantum noise in quantum picture for a GW interferometer

Although the full configuration GW detector has different quantum noise compared with simple Michelson configuration, we can use this simple case to explain the calculation mechanism. We start with the configuration shown in figure 3.6. Note that we don't consider mirror motion caused by classical noise in this section.

As shown in figure 3.6, the carrier field combines with vacuum fluctuation entering from the output port. Due to the motion of mirrors, the phase of these fields get modulated. Considering the effect of beamsplitter from equation 3.30 and mirror motion, the fields in the two arms (before recombining at the BS) are:

$$E_1(t) = \frac{1}{\sqrt{2}} \left[\varepsilon_0 \cos \omega (t - \frac{2x_1(t)}{c}) + E_v \right] \tag{3.33}$$

$$E_2(t) = \frac{1}{\sqrt{2}} \left[\varepsilon_0 \cos \omega (t - \frac{2x_2(t)}{c}) - E_v \right] \tag{3.34}$$

Where E_v represents the vacuum field $\varepsilon_v(\hat{X} \cos \omega t + \hat{Y} \sin \omega t)$, its phase dependence induced from the mirror motion is neglected since it is small. Using trigonometry

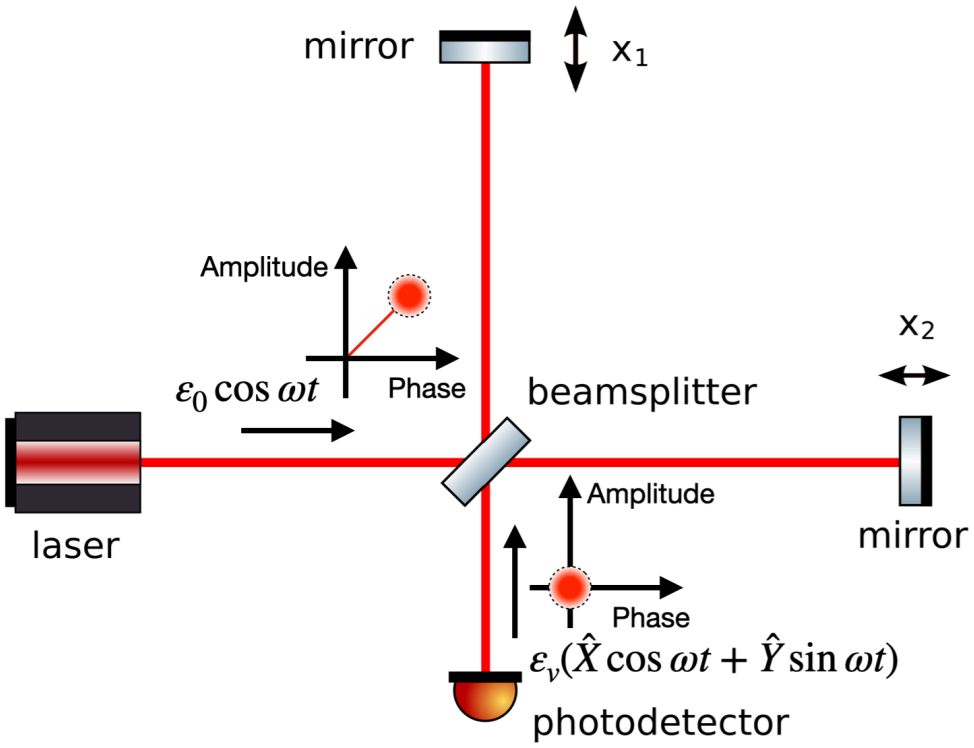

Figure 3.6: Scheme for interferometer's quantum noise. The carrier is a coherent state and enters interferometer's input port with the convention of cosine wave. The vacuum state enters interferometer's output port with the form of equation 3.11.

relations, we can expand the cosine term and get

$$E_1(t) = \frac{1}{\sqrt{2}}\left[\varepsilon_0 \cos(\omega t) - \varepsilon_0 \sin\omega t \frac{2\omega x_1(t)}{c} + E_v\right] \tag{3.35}$$

$$E_2(t) = \frac{1}{\sqrt{2}}\left[\varepsilon_0 \cos(\omega t) - \varepsilon_0 \sin\omega t \frac{2\omega x_2(t)}{c} - E_v\right] \tag{3.36}$$

The field at the interferometer's output port will be the difference between E_1 and E_2 as the interferometer is operated in the so-called "dark fringe" state. Term by term what will happen is:

- the subtraction of the first terms cancel out the carrier at the output port,
- the subtraction of the second term contains the information of mirror differential motion which is caused by the gravitational-wave signal and the radiation pressure noise. Note that this term is proportional to $\sin\omega t$, which means that gravitational wave signal and radiation pressure noise are in the phase quadrature,
- the subtraction of the third term shows that the vacuum field entering the output port is totally reflected. So fluctuations in both amplitude and phase quadrature are present in the output signal.

We can write the output fluctuations as a function of the input fluctuation of the amplitude quadrature ΔX_{in} and phase quadrature ΔY_{in}:

$$\begin{aligned} \Delta X_{out} &= \Delta X_{in} \\ \Delta Y_{out} &= \Delta Y_{in} - \mathcal{K}\hat{X}_{in} - \sqrt{\frac{P\omega}{\hbar c^2}} L h(\Omega) \end{aligned} \tag{3.37}$$

where P is the input power, ω is the laser angular frequency, L is the arm length, $h(\Omega)$ is the GW signal and Ω the GW frequency. The second term of the phase fluctuation comes from radiation pressure noise, which originates from vacuum fluctuation in amplitude quadrature. This fluctuation beats with the carrier field creating the radiation pressure noise. The factor $\mathcal{K}$ takes the form of

$$\mathcal{K} = \frac{4P\omega}{c^2 M \Omega^2} \tag{3.38}$$

where M is the mirror mass. The frequency dependence appearing in $\mathcal{K}$ is caused by the frequency response of a free falling test mass. The third term of the phase fluctuation comes from gravitational wave signal.

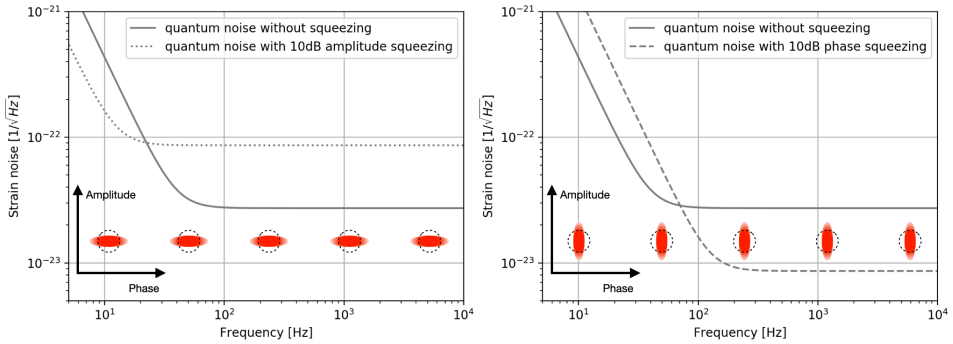

Figure 3.7: Quantum noise modified by 10dB frequency independent squeezing.

3.3 Reduction of quantum noise

We have seen that gravitational wave signal, shot noise and radiation pressure noise are in the phase quadrature and that these two noise components originates from the two quadrature of vacuum fluctuation.

It is straightforward that we can reduce quantum noise by reducing vacuum fluctuation. However, the vacuum fluctuations cannot be reduced simultaneously in both quadrature due to Heisenberg principle. This means that in order to achieve a broadband quantum noise reduction, squeezing must have a frequency dependence [88].

3.3.1 Quantum noise reduction using squeezing technique

If the vacuum state is replaced by an ordinary frequency independent squeezed vacuum, we can have the quantum noise reduction/enhancement as shown in figure 3.7. As we can see, it has the same effect as changing the arm power.

Based on the fact that phase quadrature fluctuation dominates quantum noise at high frequency and amplitude quadrature fluctuation dominates low frequency, we need to have a squeezed vacuum state which rotates with frequency in the same way as the quantum noise change. This means the squeezing rotation given by interferometer needs to be compensated by a rotation provided by an external device. Therefore, this rotation angle needs to be

$$\theta_{fds} = \arctan(\mathcal{K}) \tag{3.39}$$

According to the design of advanced gravitational wave detectors, this rotation needs

to happen below 100 Hz. With the injection of this frequency dependent squeezed state, the quantum noise will be reduced as in figure 3.8. In this case, broadband quantum noise reduction can be achieved.

3.3.2 Frequency dependent phase change of squeezed states

The squeezing generated from parametric down conversion process is frequency independent. This squeezed vacum state can be modified to have frequency dependence in many ways. Some of them are: the use of filter cavity [101, 94, 2, 102], electromagnetically induced transparency in atomic vapors [103, 104], the use of opto-mechanical induced transparency (OMIT) [105] and EPR entanglement [106]. The result of these experiments shows that optical losses could be much smaller through the use of filter cavity and OMIT suffers from practical issue of mechanical quality factor. Therefore, the most promising technique for the production of frequency dependent squeezed states for quantum noise suppression in GW detectors is the use of a filter cavity.

A detuned filter cavity modifies the phase of upper and lower sidebands relatives to interferometer's carrier in a non symmetric way. By exploiting this effect, the squeezing ellipse is rotated and a frequency dependence is imprinted. Here, 'detuned' means that the filter cavity is not resonant for carrier field but has a frequency offset. Figure 3.9 shows the magnitude and phase of a filter cavity reflection with detuning of 50Hz. The rotation angle θ_R of squeezing ellipse is defined as

$$\theta_R = \frac{\phi_{ref}(\Omega) + \phi_{ref}(-\Omega)}{2} \tag{3.40}$$

where $\phi_{ref}(\Omega)$ and $\phi_{ref}(-\Omega)$ are the filter cavity reflection phase at upper and lower

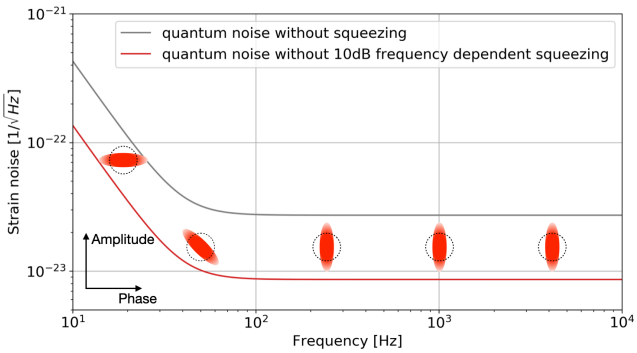

Figure 3.8: Quantum noise modified by 10dB frequency dependent squeezing.

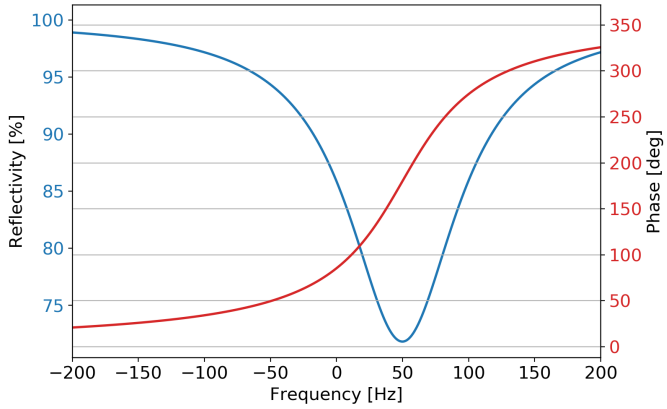

Figure 3.9: The reflectivity and phase response of a suitable filter cavity for GWs detector. X axis represents sidebands frequencies.

sidebands and Ω is the distance in frequency between the sideband and carrier frequency.

Considering a lossless filter cavity, to achieve the rotation defined in equation 3.39, the HWHM (i.e. the cavity pole) of filter cavity γ_{fc} needs to be [96]

$$\gamma_{fc} = \frac{\Omega_{SQL}}{\sqrt{2}} \tag{3.41}$$

for current generation GWs detectors, a suitable HWHM should be around $50Hz$. The optimal detuning $\Delta_{\omega_{fc}}$ for this lossless filter cavity needs to be the same with its HWHM, which means $\Delta_{\omega_{fc}} = \gamma_{fc}$. The real case, where the filter cavity losses play an important role in defining the bandwidth of the filter cavity as well as other parameter, is more complex. A comprehensive derivation the theory behind it can be found in [96].

Chapter 4

Development of frequency independent squeezing source for gravitational wave detectors

The use of squeezing started with the theoretical work of Yuen [107]. There are many physical processes that can be used to generate squeezed state of light. The system to generate squeezing is called squeezed vacuum source (or simply squeezer). After many years of development of the squeezing production technique, it is nowadays widely used in many different research fields either to help go beyond quantum limit or to be used to carry information. They include the enhancement of the resolution for bioimaging techniques [108], quantum computing and memory [109, 110], continuous-variable quantum key distribution [111] and quantum teleportation [112]. The development of squeezing for its implementation in a large scale laser interferometer took more than 20 years before its use in GEO600 interferometer. The squeezing techniques [113, 114] used or developed by GEO's team is of great importance for the whole GW community. During this project, we followed their scheme and developed our own squeezed vacuum source.

In the first section of this chapter, the overall working principle of the squeezer used in my experiment is reviewed. After that, the opto-mechanical design and characterization for each component of the squeezer is given. In the second section, the degradation sources and their influence on our squeezer are summarized. In the third section, the performances of the squeezer are given, including the measurement of squeezing with its degradation sources' characterization. In the last section, the application of frequency independent squeezing in the second generation GW detectors is reviewed.

4.1 Experimental setup

The goal of frequency independent squeezed vacuum source is to realize the measurement of 9dB squeezing. In this section, the set-up to realize this goal is introduced.

The squeezed vacuum source is constructed on a standard, in-air optical bench (size: $1.8m \times 1.2m$). The optical scheme is shown in figure 4.1. In order to suppress the acoustic noise coupling, the whole optical bench is covered with thick phono-absorbing boards and, to limit the impact of scattering due to air pollution, the optical bench is hosted inside a class 1000 clean room.

The in-air squeezed vacuum source has been assembled specifically for this experiment from scratch, following the design of the GEO600 squeezer. The core part is the optical parametric oscillator (OPO): a linear hemilithic cavity hosting a PPKTP (Periodically Poled Potassium Titanyl Phosphate) crystal in which the squeezed vacuum is produced through a parametric down-conversion process. This requires a pump beam at twice the squeezing frequency, which is produced by injecting a 1064 nm laser into a second harmonic generator cavity (SHG). The main laser, a 2-W 1064-nm Nd:YAG laser, is used to pump the SHG and produce green light (with a wavelength of 532 nm) and as a local oscillator for the balanced homodyne detector, used to characterize the squeezing. A mode cleaner cavity and a Mach-Zehnder interferometer (MZ) are installed respectively to spatially clean and to stabilize in power the green pump beam before it enters the OPO. Two auxiliary lasers, frequency offset locked with the main laser, are also used. The first one (AUX1), injected into the OPO with a different polarization (p-pol) with respect to the produced squeezed beam (s-pol), is used to control the OPO length,and it is usually referred to as "p-pol laser". The second one (AUX2) is also injected into the OPO and co-propagates with the squeezed vacuum beam up to the homodyne detector, to track the squeezing phase and lock it with respect to the local oscillator, this phase control loop, detailed in the following, is known as "coherent control loop" and for this reason the AUX2 laser is also called "CC laser". A part of the green beam produced by the SHG is used for the control of the filter cavity described in the next chapter. When I joined the experiment in October 2017 only the SHG was installed. I was responsible for the integration, characterization and operation of all the other components and thanks to this we could produce frequency independent squeezing. In the following a detailed description and the work relative to each component is reported. The performances of the frequency independent squeezing source are finally presented.

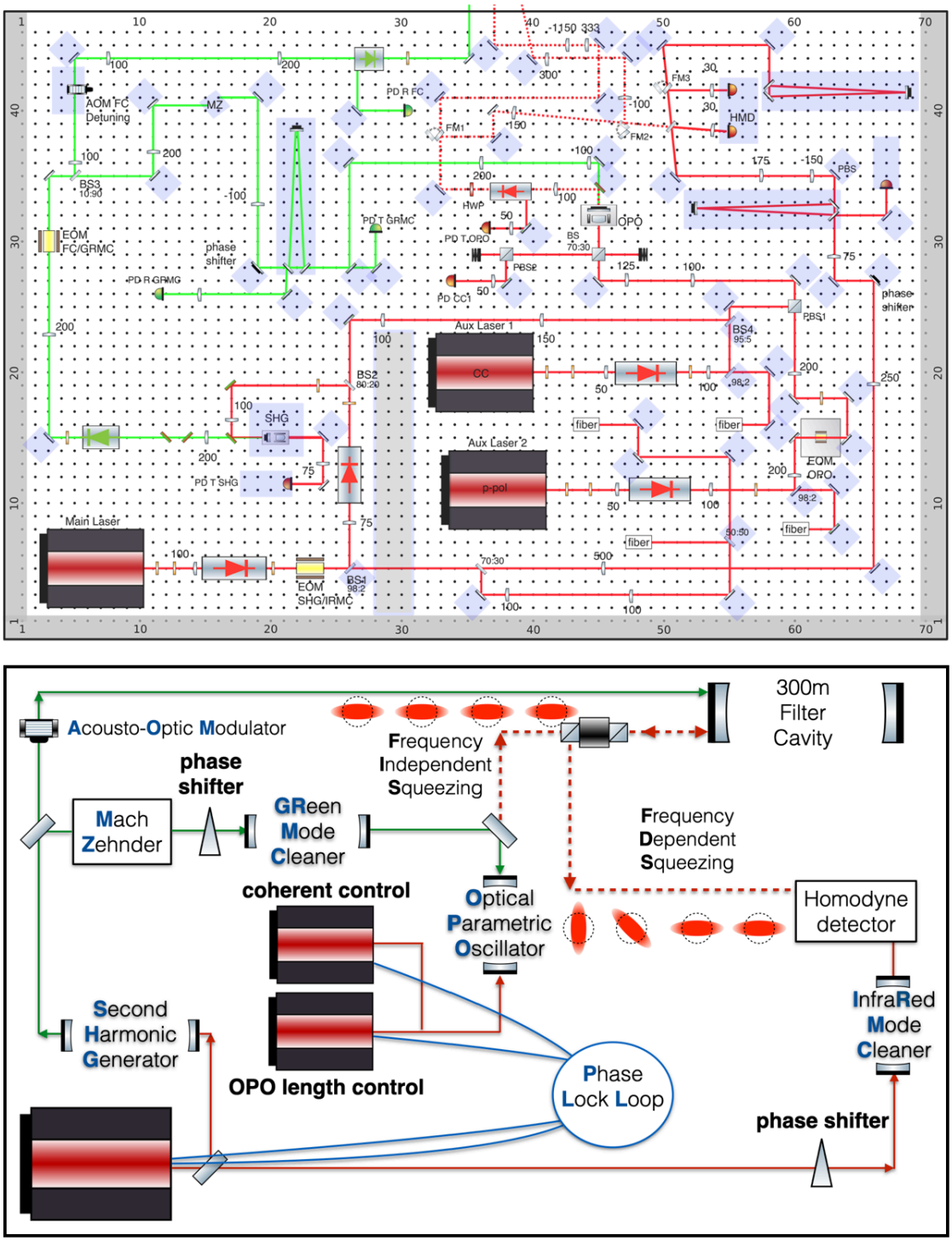

Figure 4.1: Upper: Detailed optical scheme for squeezed vacuum source. Lower: Simplified optical scheme for the whole experiment. SHG: generate pump beam. GRMC: spatially clean pump beam. MZ: stabilize pump power. OPO: generate frequency independent squeezing. AOM: detune filter cavity. Filter cavity: make frequency independent squeezing have frequency dependent rotation. IRMC: spatially clean local oscillator. PLL: phase lock auxiliary lasers to main laser. Phase shifter: stabilize squeezing phase and homodyne measurement phase.

4.1.1 Laser sources

The laser sources used in our experiment are 1064nm Nd:YAG Mephisto lasers from Coherent Inc. The main laser provides up to 2W of power, while the two auxiliary laser can provide up to 500mW of power. The characteristic NPRO design provides excellent intensity and frequency stability as well as polarization cleanness. Moreover, an internal noise eater is also present to provide an active amplitude noise suppression of the piezoelectric ceramic (PZT) resonances. The main oscillation frequency was characterized to be 310kHz for the 'CC' laser in our system. This high frequency noise usually does not create major problems since we focus on lower frequency ranges, however it is important to know its existence when looking into the high frequency parts of the spectra. Due to the thermal lensing effect of NPRO, the best performance is guaranteed by the constructor only for high power operation. In this section, some measurement and setting of our laser sources are introduced.

Laser power and its characterization

The laser power can be set by a pump diode current knob on the front panel of laser control box. For every laser, if the pump diode current doesn't go above a threshold, there is no laser output. In the case of the main laser in our lab, this threshold is around $0.7A$. When the pump diode current is above this threshold, the laser power increases linearly with the increase of pump diode current. The characterization of power stability is shown in figure 4.2, which is measured under situations of laser switching on, laser power change and no change after a long period of time. The characterization shows that at least half an hour is required for laser source to be well stabilized.

Apart from the low frequency laser power change caused by thermal effects, there are also lots of higher frequency intensity noise caused by PZT resonance. The noise eater can get rid of them. However, notice that this noise eater can be only engaged when the laser power is close to full power.

In order to control the laser output frequency, the NPRO crystal temperature can be finely tuned by means of a knob or an external voltage control and there is also the possibility to modulate the frequency output by acting on the laser PZT.

Laser frequency and mode hops

In our experiment, the main laser frequency needs to be locked to the filter cavity resonant condition. The frequency of auxiliary lasers needs also to be locked with

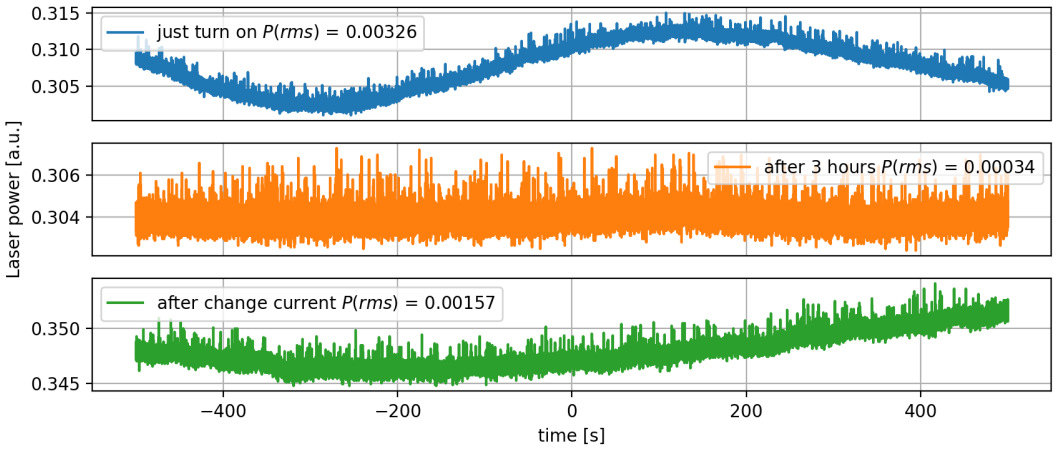

Figure 4.2: Output power change for three different situations: (1) laser just turned on - fluctuation = 1.1% (2) after three hours of operation - fluctuation = 0.11% and (3) after a change in the pump diode current - fluctuation = 0.45%. It is clear from the relative fluctuation value of these measurement as the lasers need some warm up time as well as some stabilization time after sudden power changes.

respect to main laser frequency by means of the phase locked loops.

To achieve frequency lock by acting on laser, Mephisto provide two control options: a temperature control and a laser PZT control. For the main laser, a PDH signal from our 300m filter cavity actuates on its PZT to achieve the frequency stabilization. While for auxiliary lasers, an optical phase lock loop controls the auxiliary lasers frequencies actuating both on laser's PZT and temperature.

All the laser sources used in the experiment shows the presence of mode hops. This makes two fundamental modes with different frequencies appear at the output of the laser which creates many problems with the cavity length controls and PLLs. We must avoid this problem.

The whole frequency range of Mephisto is about 30GHz. As shown in the specification of Mephisto, several mode-hops appear within this range. Both the tuning of pump diode current and temperature influences mode hops. According to the requirement of experiment, the pump diode current is fixed as table 4.1.

Main laser	Auxiliary laser(p-pol)	Auxiliary laser(CC)
1.832 A	1.338 A	1.185 A

Table 4.1: Set up of pump diode current

After fixing laser diode current, the crystal temperature is the only parameter

which needs to be adjusted to avoid mode hops. Usually mode hops are not difficult to be avoided. However, considerations about the limitation of PLL locking frequency and circuit bandwidth make the choice of three lasers' crystal temperature to be coordinated. The details of these limitations will be introduced in section 4.1.5 and section 4.1.7 separately. In the end, the temperature of each laser sources are fixed as summarized in table 4.2.

Main laser	Auxiliary laser(p-pol)	Auxiliary laser(CC)
23.10 $°C$	32.49 $°C$	38.15 $°C$

Table 4.2: Set up of crystal temperature

Laser PZT characterization

To design optical PLL, it's necessary to characterize the transfer function of laser PZT. PLL aims for a bandwidth of several tens of kHz, which means the bandwidth of PLL will be limited by PZT oscillation. Besides, the gain of PZT is also an important parameter to be used in the design of servo. From the specification, the gain of this PZT is $1MHz/V$. But there is no information of resonant peaks, which is important information and needs to be investigated.

By looking at the beat note of two laser sources and exciting the PZT of one of them, we could get a broaden beat note. By taking the width of beat note for different frequencies, we could construct a transfer function for each PZT. The broaden beat note and the result of this characterization is shown in figure 4.3. The gain of PZT below $70kHz$ is $1.8MHz/V$. The resonance starts to appear after around $70kHz$, and strong resonance appears above $100kHz$. Note that this characterization process assumes that the linewidth of the laser is negligible with respect to the broadening of the peak. All the three lasers PZT response have been characterized and they all shows the same response with the a flat gain of about $2MHz/V$ and resonances features above $100kHz$.

4.1.2 Second harmonic generator

Although the second harmonic generator (SHG) has already been constructed before I joined the project, I worked on the improvement and maintenance of this cavity. Due to the environmental temperature change and reported low conversion

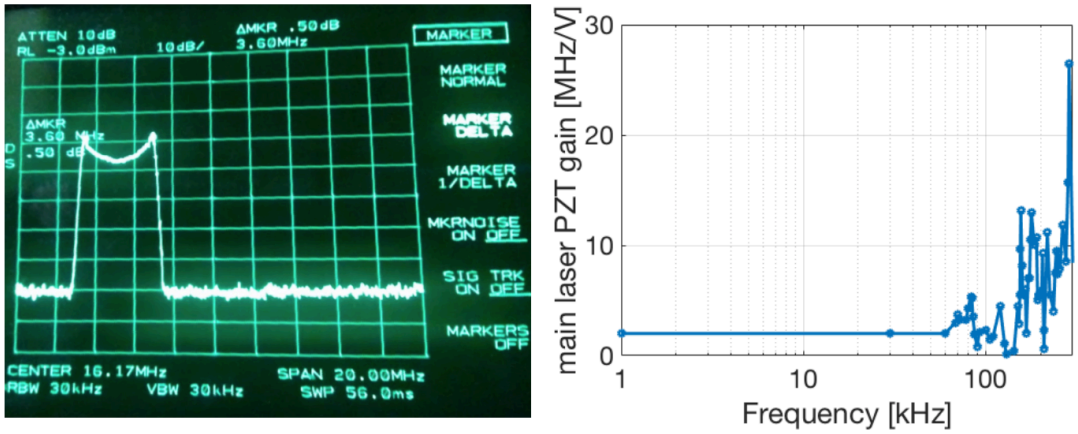

Figure 4.3: Left: The broaden beat note due to excitation sent to one of laser's PZTs. Right: main laser PZT transfer function.

efficient, I worked on the adjustment of temperature control, PDH locking improvement and matching improvement. Related background information and practical measurement are reported in this section.

Second harmonic generation process uses the second order electric polarization of a material and mixes two photons of a certain wavelength into one of half the wavelength. The classical theory of SHG is based on Maxwell's equation and non-linear polarization, which can be found, for example, in [115, 116]. This theory is the basic for both SHG and optical parametric oscillator (OPO), the two non-linear components used in our squeezed vacuum source. Therefore, I will summarize it briefly here. After that the the opto-mechanical design of SHG and its characterization is reported.

Second order non-linear optics

This section answers the question about how second harmonic field are generated from non-linear optical process. This section also tells us how non-linear crystal plays a role in this process.

Maxwell's equation tells us the relationship among electric field $\boldsymbol{E}$, magnetic field $\boldsymbol{B}$ and electric displacement $\boldsymbol{D}$:

$$\nabla \times \boldsymbol{E} = -\frac{\partial}{\partial t}\boldsymbol{B} \tag{4.1}$$

$$\nabla \times \boldsymbol{B} = \mu\frac{\partial}{\partial t}\boldsymbol{D} \tag{4.2}$$

where μ is the magnetic permeability. Taking the curl of equation 4.1, we have $\nabla \times \nabla \times \boldsymbol{E} = -\frac{\partial}{\partial t}\nabla \times \boldsymbol{B}$. Taking equation 4.2 into account, we arrive at $\nabla \times \nabla \times \boldsymbol{E} = -\mu\frac{\partial^2}{\partial^2 t}\boldsymbol{D}$. Then considering $\nabla \times \nabla \times \boldsymbol{E} = \nabla(\nabla \cdot \boldsymbol{E} - \nabla^2\boldsymbol{E})$, the definition of electric displacement $\boldsymbol{D} = \epsilon_0\boldsymbol{E} + \boldsymbol{P}$ and the definition of electric polarization $\boldsymbol{P} = \epsilon_0\chi^{(1)}\boldsymbol{E} + \epsilon_0\chi^{(2)}\boldsymbol{E}^2 + \epsilon_0\chi^{(3)}\boldsymbol{E}^3 + \ldots$ (where χ is the non-linear susceptibility), we can get

$$\nabla^2\boldsymbol{E} - \nabla(\nabla \cdot \boldsymbol{E}) - \mu\epsilon\frac{\partial^2}{\partial t^2}\boldsymbol{E} = \mu\frac{\partial^2}{\partial t^2}\boldsymbol{P}^{(2)} \tag{4.3}$$

where ϵ is electric permittivity and $\boldsymbol{P}^{(2)}$ is the second order electric polarization. Note that the electric polarization is considered only up to the second order and the first order $\epsilon_0\chi^{(1)}\boldsymbol{E}$ was absorbed into $\epsilon_0\boldsymbol{E}$. The second term $\nabla(\nabla \cdot \boldsymbol{E})$ becomes zero since there are no free charges inside the non-linear crystal. For a field propagating in the z direction written as $\boldsymbol{E}(z,t) = \frac{1}{2}[\boldsymbol{E}(z,\omega)e^{i(\omega t - kz)} + c.c.]$, the left side of equation 4.3 becomes $A * \boldsymbol{E}(z,\omega)e^{i(\omega t - kz)} + c.c.$ with

$$A = \frac{1}{2}\frac{\partial^2}{\partial z^2} - ik\frac{\partial}{\partial z} - \frac{1}{2}k^2 + \frac{1}{2}\mu\epsilon\omega^2 \tag{4.4}$$

After using the slowly varying envelope approximation $|\frac{\partial^2\boldsymbol{E}}{\partial z^2}| \ll |k\frac{\partial\boldsymbol{E}}{\partial z}|$ and considering $\mu\epsilon\omega^2 = k^2$, a simple result is achieved as $A = -ik\frac{\partial}{\partial z}$.
For the right side of equation 4.3, the property of the non-linear crystal needs to be considered. In this case, the second order electric polarization formula needs to be generalized as

$$P_i^{(2)} = \epsilon_0\Sigma_{j,k}\chi_{ijk}^{(2)}\varepsilon_j\varepsilon_k \tag{4.5}$$

Here, $\chi_{ijk}^{(2)}$ is generalized second order non-linear susceptibility and $\varepsilon_{j(ork)}$ represents an electric field. To achieve the SHG process, the frequency of electric field needs to be identical. Each index runs over x, y, z dimensions, but when index j or k exchange, the summation is the same. So the non-linear susceptibility has $3(i = x, y, z) \times 6(jk = xx, yy, zz, xy/yx, xz/zx, yz/zy) = 18$ components (the components can be reduced to 10 for a lossless medium which will not be considered here). So

the second order electric polarization is usually expressed as

$$\begin{pmatrix} P_x^{(2)} \\ P_y^{(2)} \\ P_z^{(2)} \end{pmatrix} = \begin{pmatrix} d_{11} & d_{12} & d_{13} & d_{14} & d_{15} & d_{16} \\ d_{21} & d_{22} & d_{23} & d_{24} & d_{25} & d_{26} \\ d_{31} & d_{32} & d_{33} & d_{34} & d_{35} & d_{36} \end{pmatrix} \begin{pmatrix} \varepsilon_x\varepsilon_x \\ \varepsilon_y\varepsilon_y \\ \varepsilon_z\varepsilon_z \\ 2\varepsilon_x\varepsilon_y \\ 2\varepsilon_x\varepsilon_z \\ 2\varepsilon_y\varepsilon_z \end{pmatrix} \tag{4.6}$$

In different crystal systems, some nonlinear susceptibilities vanish and additional permutation symmetries are allowed according to the crystal symmetries. In our SHG, we use lithium niobate, the corresponding nonlinear susceptibility tensor is given by

$$\begin{pmatrix} 0 & 0 & 0 & 0 & d_{31} & -d_{22} \\ -d_{22} & d_{22} & 0 & d_{31} & 0 & 0 \\ d_{31} & d_{31} & d_{33} & 0 & 0 & 0 \end{pmatrix} \tag{4.7}$$

In the case of z-polarized SHG output, in type-1 (ooe) phase matching, the effective nonlinearity is given by

$$d_{eff} = d_{31}\sin(\theta) - d_{22}\cos(\theta)\sin(3\phi) \tag{4.8}$$

where θ is the polar angle between z-axis and the wave vector and ϕ is the azimuthal angle. In our case, $\theta = 90°$, the effective nonlinearity is d_{31}. This value is measured to be $4.4pm/V$ by Shoji [117]. However, d_{33} of this material has a much higher value of $25.3pm/V$, which could be used in a quasi-phase matching condition.

Phase matching

The phase matching condition defines the optimal conditions, in our case the optimal temperature, to maximize the efficiency of the non-linear process.

Let's take equation 4.6, 4.8 and the approximation of equation 4.4 into equation 4.3, so we get

$$\frac{d\boldsymbol{\varepsilon}_{2\omega}}{dz} = \frac{\mu_0\omega^2}{2ik} d_{eff} * \boldsymbol{\varepsilon}_\omega^2 e^{-i(k_{2\omega}-2k\omega)z} \tag{4.9}$$

The phase matching condition is achieved when the exponential part on the right side of above equation vanishes, which means that $\Delta k = k_{2\omega} - 2k\omega = 0$ needs to be satisfied. Only in this case, the integral of right part can have non-zero result. The

solution of this equation is

$$\boldsymbol{\varepsilon}_{2\omega} = -i\frac{\omega d_{eff}}{c_0 n}\boldsymbol{\varepsilon}_{\omega}^2(0)\cdot z\cdot e^{i\Delta kz/2}\cdot sinc(\Delta kz/2) \tag{4.10}$$

In the case of a double-pass scheme, the second-harmonic electric field has an additional term caused by the phase shift between the first and second harmonics [118, 119]. Then equation 4.10 will be multiplied by a term $\cos^2(\frac{\phi+\Delta kL}{2})$. The same equation can be used to describe the behaviour of a standing wave SHG cavity, as it is in our case. The characterization of the phase matching condition as function of the non-linear crystal temperature is reported in figure 4.4. As expected, the behaviour is not described by a simple sinc function, as in the case of a single pass.

Periodic poling technique is widely used to achieve higher conversion efficiency by exploiting the quasi-phase matching (QPM) condition. Due to this technique, the use of high nonlinearity d_{33} becomes viable. In the case of QPM, the type 1 (eee) phase matching condition can be written as

$$k_{2\omega} - 2k_{\omega} - K_{QPM} = 0 \tag{4.11}$$

k depends on refractive index as $k = n\omega/c$, while the refractive index depends on temperature according to Sellmeier equation [120]

$$n_e^2 = a_1 + b_1 f + \frac{a_2 + b_2 f}{\lambda^2 - (a_3 + b_3 f)^2} + \frac{a_4 + b_4 f}{\lambda^2 - a_5^2} - a_6\lambda^2 \tag{4.12}$$

The formula is the same for o-ray but the coefficients are different. The temperature parameter f of the previous equation is defined as

$$f = (T - 24.5)(T + 570.82) \tag{4.13}$$

note that the unit for wavelength is μm and for temperature is $^{\circ}C$. The parameter of K_{QPM} is adjusted up by manufacturer by tuning the period of the periodically poling of the non-linear crystal.

The temperature control loop consists of temperature sensor (Thermistor 103 JT-025), Peltier heater and a temperature controller (Thorlabs TED200C), which will be introduced in the section of OPO. The stability of temperature should be less than 5mK [121].

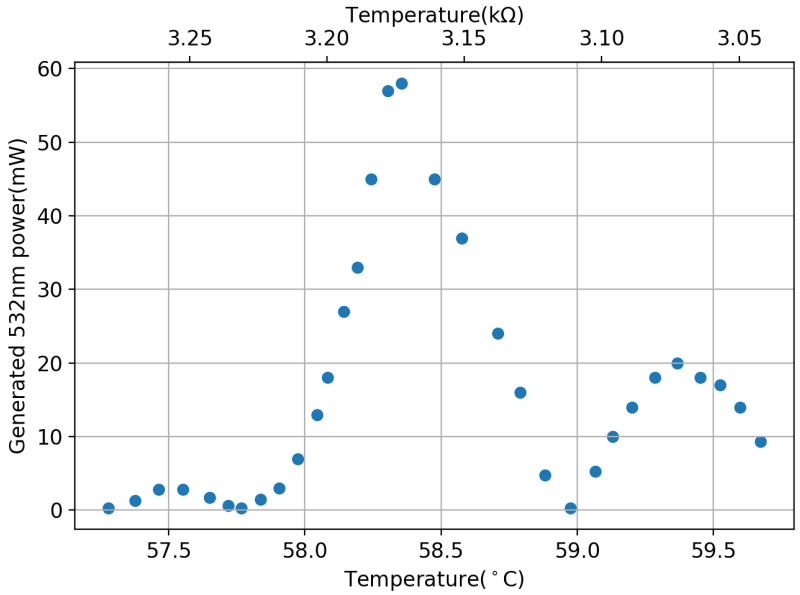

Figure 4.4: Measurement of SHG generated power as function of the crystal temperature. The upper axies shows the resistance of thermistor. Note that the phase matching temperature also depends on the real-time environmental temperature. For example, the optimal temperature is quite different between summer and winter season.

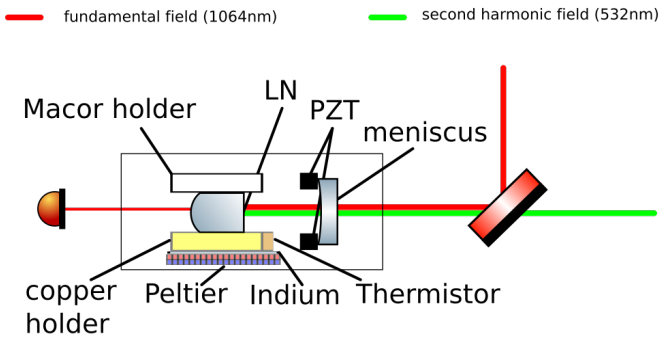

Figure 4.5: Schematic cross section of SHG cavity. The Lithium Niobate crystal is hosted in between a macor and a copper holder. The temperature is stabilized with a Peltier cell and monitored with a thermistor. The cavity length is optimized thanks to a PZT element which acts on the position of the input meniscous mirror. The locking error signal is obtained from a photodiode in transmission.

Opto-mechanical property of SHG

The conversion efficiency from infrared light into green light is not only influenced by phase matching condition but also by how much infrared light we can couple into the SHG cavity. This is called the mode matching condition. Mode matching includes both injection beam alignment and injection beam size mismatch. For very high matching condition and good beam alignment, the main laser power was found to be unstable. This was due to the back reflection from the SHG to main laser. Therefore, a new Faraday isolator was installed to prevent this power instability. To maximize the matching condition, the injection telescope was optimized several time. In this part, the SHG opto-mechanical parameters are reviewed.

name	value
crystal material	$MgO : LiNbO_3$ (LN)
dimension (mm)	2×2.5×6.5
flat surface curvature	∞
flat surface reflectivity	$< 0.1\%$ both IR and GR
curved surface curvature	$12mm$
curved surface reflectivity	$0.9995(IR)$ $0.998(GR)$
meniscus curvature	20mm (outside), 25mm (inside)
meniscus reflectivity	$0.92(IR)$ $0.02(GR)$
FSR	4GHz
finesse	75
FWHM	53MHz

Table 4.3: Opto-mechanical parameters for SHG cavity [122]. The FSR, finesse and FWHM are given for IR.

The optical length of SHG is 37.5mm, so the g factor $g = 1 - L/R$ could be derived from the information of optical length and mirror surface radius of curevature.

Note that, to compute the g factor inside the LN crystal, the effective radius of curvature needs to take into account the LN refractive index which is 2.2336 at 532nm.

The waist size is calculated from the g-factors as

$$\omega_0^2 = \frac{\lambda L}{\pi} \frac{\sqrt{g_1 g_2 (1 - g_1 g_2)}}{|g_1 + g_2 - 2 g_1 g_2|} \tag{4.14}$$

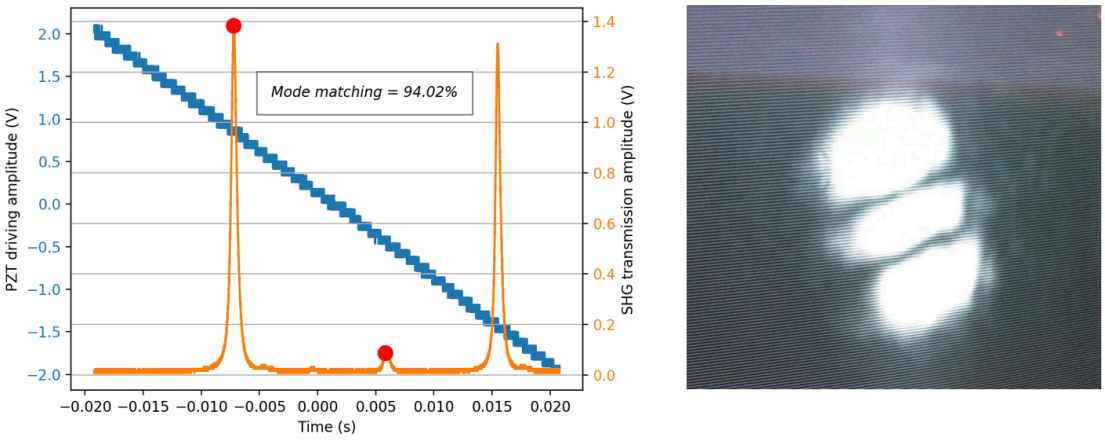

Figure 4.6: Left: the mode matching measurement for the SHG. The mode matching level is estimated by taking the ratio of two red point (offset is removed) since there are no other visible high order modes. Right: the higher order mode corresponding to the lower red dot in the measurement on the left is captured by putting a camera in the transmission of SHG. The existence of this shape can be due to either astigmatism of incident beam or non-spherical symmetric configuration of crystal/meniscus.

so the waist size (for 532nm) of SHG is calculated as 44 μm. The waist position is

$$z = L\frac{(1-g_1)g_2}{|g_1+g_2-2g_1g_2|} \tag{4.15}$$

which gives result of 20mm from the meniscus and inside the cavity. These information are necessary to infer the incident beam parameters. Since the meniscus works as a lens, a simulation of software JamMt was done to get the final result of incident beam parameters. The incident beam needs to have $48\mu m$ beam waist while the waist position is 21mm from the meniscus. This result was used to design telescope and improve the mode matching of SHG. After the improvement of mode matching, the efficiency of SHG was improved. The SHG conversion efficiency was improved from 13% to 35%. The mode matching measurement is shown in figure 4.6.

After improving the matching condition, the stability of main laser power was monitored. The power fluctuation became negligible after the addition of the second Faraday isolator.

SHG length lock

All the cavities in our experiment are locked by using the PDH technique (introduced in section 2.4.4). Since this is the first time a practical PDH loop is described, some crucial components of the loop, which are common to all the PDH loops in our experiment will be introduced.

- **Opto-mechanical set-up (SHG case):** as shown in figure 4.5, infrared laser is injected through a dichroic mirror, which reflects infrared laser and transmit green laser. The RF signal is taken from the transmission of SHG (this is reasonable since the sidebands frequency is located well within the FWHM of the SHG).

- **Photo detectors:** two kinds of photo detectors (PDs) are used in our set-up: transimpedance type and resonant type. In the case of SHG, a resonant PD was used with resonant frequency band between $14.9MHz$ and $15.5MHz$ and Q factor of 23.

- **Resonant electro-optic phase modulator (EOM):** the sidebands necessary for PDH control are created by means of an EOM. The modulation depth m defined in $e^{i(\omega t + m\sin(\Omega t))}$ is used to quantify the sidebands magnitude. The modulation depth is proportional to the amplitude of the applied RF signal multiplied by the EOM modulation depth parameter which is $0.15rad/V$ for infrared and $0.28rad/V$ for green in our set-up. A general output from our RF signal source is $12.6dBm$. Therefore, if we use full RF signal, the modulation depth we can achieve are $0.143rad$ for infrared and $0.267rad$ for green.

- **Demodulation electronics:** in order to obtain the PDH error signal, the reflection/transmission signal needs to be demodulated at the sideband frequency. Moreover, to optimize the error signal shape and gain, the phase of the local oscillator (LO) can be optimized digitally. The optimization process usually requires to finely tune the LO phase to make the PDH signal flat and then flip the phase by 90 degree. In order to suppress higher harmonics after demodulation, a low pass filter is implemented after every demodulation stage.

- **Opto-mechanical transfer function:** to design proper filters for control loop, the measurement of opto-mechanical transfer function is crucial. The frequency position of mechanical resonance peaks and the low frequency gain are important information. With such information, stable control loops can be

designed. Even if all such information could be obtained by FEM analysis of the cavity mechanics, for most of the cases in our setup was easier to measure the transfer functions instead of simulate them. The opto-mechanical transfer function of the SHG is shown in figure 4.7 left panel.

4.1.3 Green and infrared mode cleaners (GRMC/IRMC)

Both green mode cleaner (GRMC) and infrared mode cleaner (IRMC) are triangular travelling wave cavities. With respect to a linear cavity, triangular cavities offer an additional advantage which is polarization filtering. However, astigmatism, coming from the non-zero incident angle on the curved top mirror, could be an issue. A careful design needs to be done in order to avoid it [123].

The mechanical design of mode cleaners was done in collaboration with the University of Trento and the Advanced Technological Center of NAOJ. It is shown in the left side of figure 4.8. In order to minimize the astigmatism the length of the mode cleaner is chosen to be much bigger than its lateral dimension. However, it must also be not too long to keep the first longitudinal mode at frequencies higher than the control bandwidth. A simple estimation of the first longitudinal mode frequency can be done using the model of an elastic bar of length l with both ends free, then the resonant frequency f_0 will be

$$f_0 = \frac{1}{2l}\sqrt{\frac{E}{\rho}} \tag{4.16}$$

where E is the Young's Modulus of the material, ρ is its density and l is the length of the bar. For Invar36 which is the material of which the mechanics of our mode cleaners is made, Young's Modulus and density are $137Gpa$ and $8050kg/m^3$ respectively. Therefore, the resonant frequency is $7330Hz$. In order to get a more precise result, a FEM simulation would be needed. In figure 4.9 the opto-mechanical transfer function of GRMC shows some mechanical resonance around 10kHz. This could be compatible with the rough estimation of the first longitudinal resonance mode. The monolithic design make the mode cleaner very stable with respect to alignment drifts and thanks to the material chosen, due to its low thermal expansion coefficient, it is very stable with respect to room temperature fluctuations.

The optical parameters of GRMC and IRMC are listed in table 4.4.

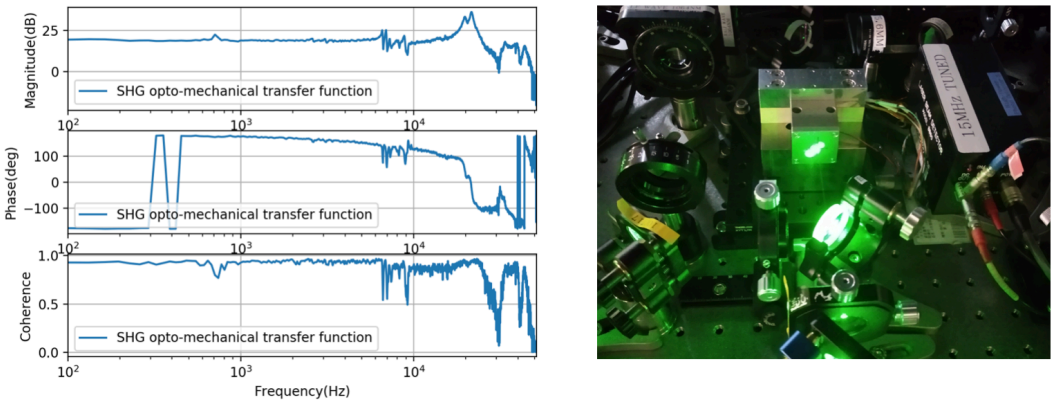

Figure 4.7: Left: Opto-mechanical transfer function for SHG. Several structure are visible above $7kHz$. Those are likely related to mechanical resonances of the cavity mechanics and are a limitation for the actuation bandwidth. At low frequency the response is flat. Right: a photo of the SHG cavity.

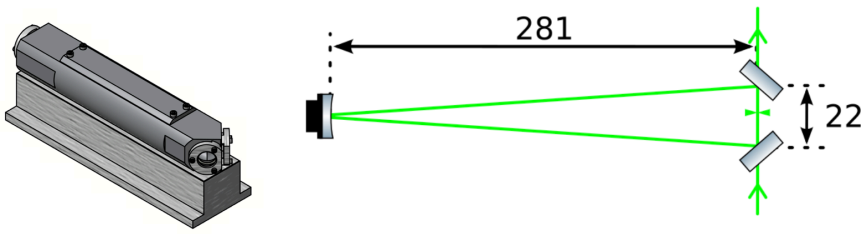

Figure 4.8: Left: mechanical design of green and infrared mode cleaners. Right: optical configuration of green and infrared mode cleaners. Number are expressed in millimeter. The mechanical design is the same for green and infrared mode cleaners, but the coating of mirrors are different. Note that the location of waist is indicated to be in the middle of two bottom mirrors.

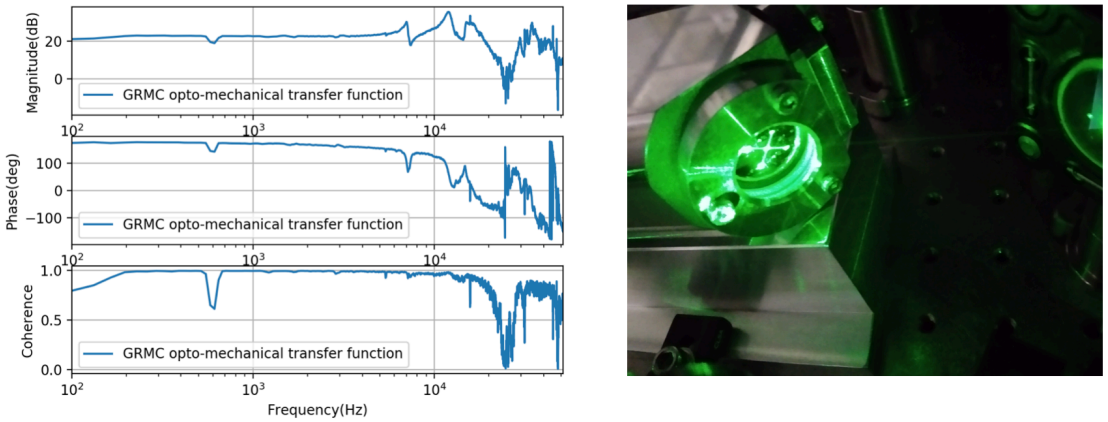

Figure 4.9: Left: the opto-mechanical transfer function of GRMC. Right: a picture shows the input port of green mode cleaner.

	GRMC	IRMC
top mirror ROC	1m	1m
bottom mirrors ROC	∞	∞
top mirror code	CVI(Y2-1025-0-1.00CC)	CVI(Y1-1025-0-1.00CC)
top mirror reflectivity	99.9%($0°AOI$)	99.9%($0°AOI$)
bottom mirrors reflectivity	99.2% (s-pol)	99.2% (s-pol)
nominal transmissivity	93%	93%
FSR	533MHz	533MHz
FWHM	1.36MHz	1.36MHz

Table 4.4: Mechanical and optical parameter of green and infrared mode cleaners.

Optical property of GRMC/IRMC

According to the mirror optical parameters, the nominal transmission of mode cleaner without considering optical losses is 93%.

The measured transmission of GRMC is only about 60% which is considered to be due to the existence of optical losses, green beam non-perfect shape and sidebands power. In the experiment, we have observed that the green light coming from the SHG has interference fringes, which was figured out to be due to a beam clipping effect.

The measured transmission of IRMC is about 80%. This is closer to the nominal value compared to the GRMC and it is suspected to be due to a better beam shape.

Opto-mechanical property of GRMC/IRMC

Based on the opto-mechanical design, we could calculate the beam waist for GRMC/IRMC. The calculation of beam waist is different from SHG because of different cavity geometry. Let's first remind the ROC of Gaussian beam R and its Rayleigh range z_R is

$$R = z(1 + (z_R/z)^2),\ z_R = \pi\omega_0^2/\lambda \tag{4.17}$$

To calculate the waist size inside mode cleaner, we need to consider the right side of figure 4.8. As is indicated in the figure, the waist is located in the middle of two bottom mirrors. This can be easily understood due to the symmetry properties of the mode cleaners. To have a stable cavity, the ROC of top mirror should match the ROC of beam. By considering this relation, we derive the waist size ω_0 as

$$\omega_0 = \sqrt{\frac{\lambda\sqrt{R \cdot z - z^2}}{\pi}} \tag{4.18}$$

where R is the ROC of top mirror, z is the propagation distance of beam from waist to top mirror and λ is the wavelength. As we see on the right side of figure 4.8, the beam hits the top mirror at an angle $\theta = 11/(11 + \sqrt{11^2 + 281^2})$. Based on the formula derived by Massey and Siegman [124], the effective horizontal and vertical ROC are

$$R_h = R/\cos\theta,\ R_v = R\cos\theta \tag{4.19}$$

The computed beam waist inside the mode cleaners are $\omega_0 = 380\mu m$ for the IRMC and $\omega_0 = 270\mu m$ for GRMC.

Another way to calculate the optical properties of a triangular cavity is provided by Raab [123]. Both in the work of Massey and Raab, the horizontal direction is called transverse direction and the vertical direction is called sagittal direction. The phenomenon caused by different beam ROC in different direction is usually called astigmatism. Two problems can be caused by this astigmatism: mode splitting and non-circular mode shape. Based on the introduction in chapter 2, the discussion about these problems in GRMC/IRMC is given.

Mode splitting

The mode spacing of an optical cavity was introduced with equation 2.46. For a triangular cavity, the FSR is a bit different from the one defined in equation2.17. This is because a mode needs to return to its original state by travelling twice cavity

length in a linear cavity, but only one cavity length in a travelling wave triangular cavity. In a travelling wave cavity, the FSR corresponds to a phase change of 2π. Based on this, the mode spacing in a triangular cavity from the fundamental mode can be expressed as

$$f_{ms(travelling)} = \arccos\left(1 - d/R\right) \times \frac{FSR}{2\pi} \tag{4.20}$$

So the mode splitting can be expressed as

$$f_{ms1} - f_{ms2} = \frac{FSR}{2\pi} \times \left(\arccos\left(1 - d/R_h\right) - \arccos\left(1 - d/R_v\right)\right) \tag{4.21}$$

By taking into account the parameters of our mode cleaners, the mode splitting frequency is 0.05MHz. Comparing this splitting frequency to the FWHM reported in table 4.4, it is clear that we can completely ignore this effect.

Mismatch due to non-circular mode shape

Another issue caused by triangular cavity is mode mismatch between ideal circular mode and non-circular mode shape. The overlap ratio O between a circular mode and an astigmatic mode can be expressed as [44]

$$O = \left(\frac{z_R\sqrt{z_{Rh}z_{Rv}}}{|q(z)|^2|q(z)_h q(z)_v|}\right)^2 \left|\frac{1}{\left(\frac{1}{2q_h(z)} - \frac{1}{2q}\right)\left(\frac{1}{2q_v(z)} - \frac{1}{2q}\right)}\right|^2 \tag{4.22}$$

Here q is defined in section 2.2.3. By taking into account all the parameters, the overlap ratio is more than 99.9999%. THerefore, the astigmatism effect is totally negligible thanks to the design of GRMC/IRMC.

Beam pointing noise mitigation

As shown in figure 4.1, IRMC is very close to the BHD. Apart from reducing phase noise and cleaning mode shape, IRMC plays an important role to reduce the beam pointing noise [125]. In our case, a large phase difference exists between the squeezing and local oscillator. This is due to the fact that the squeezing coming from OPO will travel a long distance to the FC and hit at least three suspended mirrors. Since these mirrors are far away from each other and each has an individual suspension system, their motion can be considered uncorrelated. To correct this large phase difference between squeezing and local oscillator, the phase shifter needs to be driven with a large dynamic range. This phase shifter acts on the local oscillator

beam path length and this will certainly cause a problem of beam pointing noise.

However, since we put this phase shifter as close as possible with IRMC, the beam pointing noise is suppressed by the IRMC. Due to the property of cavity, when IRMC is locked, mostly TEM00 is transmitted, and the high order mode coming from input beam misalignment are rejected. In this case, IRMC works as a filter for beam pointing noise. This is assuming that the induced beam pointing is small enough to neglect its coupling to the transmitted power. This is true for fast correction, however is not verified for long term actuation, where the full travelling range is exploited. In such cases the shot noise reference may vary and could be necessary to be measured again. Up to know, this problem was never encounter since the time scale of the measurement is much smaller than the one which induces this problem.

4.1.4 Mach-Zehnder interferometer

The Mach-Zehnder (MZ) interferometer is used to reduce the green laser intensity noise and adjust the green power level sent to OPO.

Optical design of MZ

As we can see on the right side of figure 4.10, MZ is designed to be a very compact device. In the middle, a large 50/50 beam splitter is used to both split and recombine the beams. After splitting, the two laser beams go separately to two mirrors. One mirror is fixed while the other is attached to a PZT. After the reflection from these two mirrors, they recombine on the large 50/50 beam splitter. In this configuration, the PZT moves one mirror changing the MZ arm length, therefore changing the interference condition, from bright to dark fringe. In this way, we can control the laser power. Due to the compact design, this system has a stable alignment. Unless some strong oscillation is excited, the alignment can be kept for several weeks.

As we can see in figure 4.1, the GRMC is located just after the MZ. This layout not only helps to reduce the beam jittering from the MZ but also help the alignment of the MZ. The alignment of the MZ can be done by taking advantage of GRMC and using it as a reference cavity. The strategy is to block one path in MZ and align the other path to GRMC as the first step. Then exchange the blocked paths, align again to GRMC. After these two steps, the combination of two paths will overlap very well.

A portion of the green beam transmitted from the GRMC is collected from a

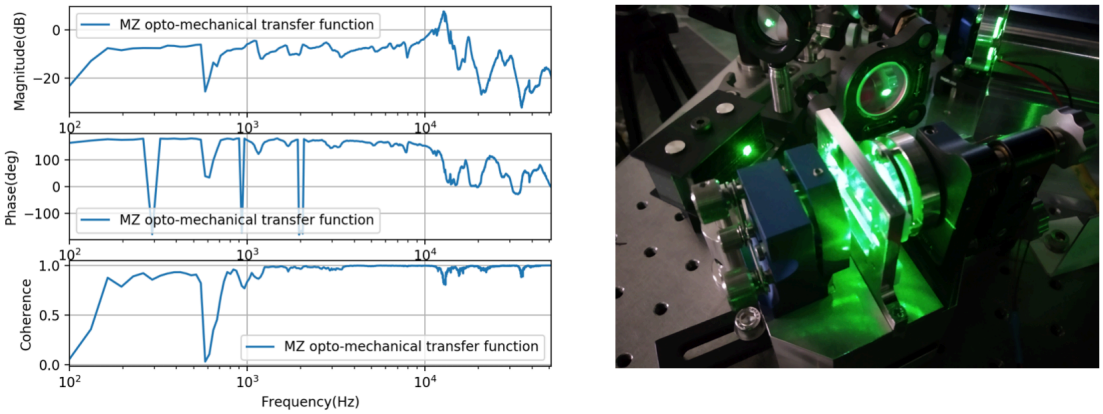

Figure 4.10: Left: the opto-mechanical transfer function of the MZ. Right: a picture of the MZ used in our experiment

photodetector. This signal is used as an error signal for the MZ PZT control to stabilize the green power reaching the OPO.

Offset lock for MZ

To control the MZ an offset lock is performed. The signal taken from GRMC transmission is sent to servo and compare to a fixed offset. The servo actuates on the MZ PZT to keep the difference between the GRMC transmission and the offset to zero. By changing the offset value, we can change the operating point of the MZ, changing therefore the amount of green reaching the OPO. Due to the very large visibility of the MZ which is almost 100%, the green power can be controlled in a very large linear region, as shown on the right side of figure 4.11.

4.1.5 Optical parametric oscillator

The optical parametric oscillator (OPO) is the device where squeezed vacuum is generated. Compared with the combination of two photons in SHG, OPO is operated to make one photon separate into two photons. In the OPO, a photon with frequency of 2ω converts into two photons with frequency of ω. Due to this spontaneous down conversion process, this device sometimes is also called 'SPDC'. It follows the same phase matching condition with SHG since all the frequency components are the same. The only difference in our experiment is the use of a different non-linear crystal, different cavity geometry and different operating pump power condition (below/above threshold). The parameters of OPO is summarized in table 4.5.

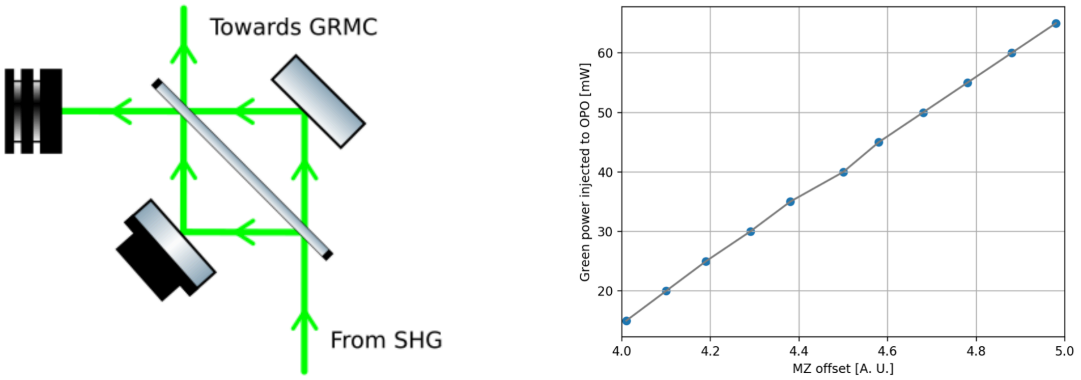

Figure 4.11: Left: the optical scheme of MZ. Right: the change of green power injected to OPO according to the offset of MZ. Here, the offset is provided by a potentiometer inside the servo control.

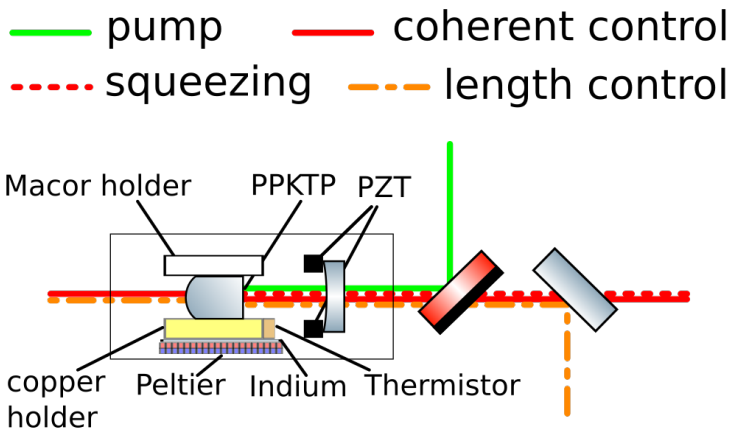

Figure 4.12: OPO optical scheme. Pump, coherent control and length control fields are injected into OPO. Squeezing and a new coherent control field are generated inside the cavity.

The main difference between SHG and OPO is the non-linear crystal. As reported in [126], a PPKTP crystal has comparable non-linear coefficient with PPLN. More importantly, PPKTP has poling losses much lower than PPLN. Moreover, the damage threshold, resistance to photo-refractive damage, resistance to thermal lensing are all higher. All these features makes the use of PPKTP crystals favorable for squeezing generation.

As shown in figure 4.12, two additional fields are injected into OPO which are not directly related with squeezing. To make optical situation more clear, a general introduction of light field related to the OPO is given as follows and shown in figure 4.13:

- **Vacuum** is permeated everywhere in spacetime. Therefore it must exist in the fundamental mode of OPO.
- **Pump** light is sent to OPO to drive the non-linear process.
- **Squeezing** (squeezed vacuum) is a squeezed vacuum field generated from optical parametric oscillation process.
- **Length control** (p-pol) is an infrared beam in p polarization provided by an auxiliary laser. It is used to lock the cavity length. Its frequency is carefully chosen to make s polarization also resonant at the same time.
- **Coherent control** (CC) is an infrared beam in s polarization provided by another auxiliary laser. It is used to sense the phase change of squeezing.
- **Bright alignment beam** (BAB) is an infrared beam which is not shown in figure 4.12 and is not injected into the OPO in normal operation. However, when alignment and matching operation are required downstream the OPO, this beam is injected and used to track the OPO cavity mode.

This section will concentrate on the detailed introduction of these fields and related characterization.

Opto-mechanical property of OPO

Mirrors curvature and distance are listed in table 4.5. By using the same formula used for SHG, the beam waist ω_{OPO} of OPO is calculated as

$$\omega_{OPO} = 25.5\mu m \tag{4.23}$$

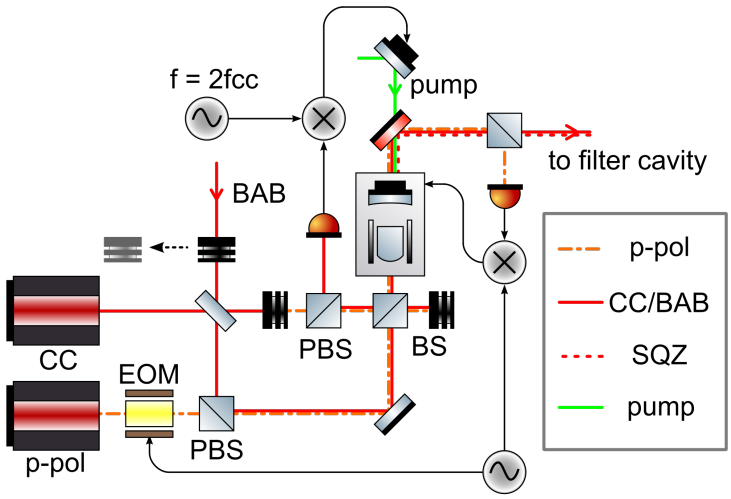

Figure 4.13: Optical and control scheme around OPO

The beam position z_{OPO} relative to meniscus is

$$z_{OPO} = 13.1mm \tag{4.24}$$

The desired waist size becomes $20.66\mu m$ and $11.1mm$ due to the presence of the meniscus. This result was used to match OPO. As we can see from table 4.5, OPO is resonant for infrared beam but not for green. For green beam, the in-coupling mirror reflectivity of 20% helps to amplify green power insider OPO by a factor of $1/(1-\sqrt{0.2}) \simeq 2$.

For an infrared beam, the nominal transmission of the OPO is 1%. However, we measured only about 0.2%. This difference could be easily explained by a higher reflectivity of crystal HR coating. For example, a reflectivity of 99.995% of crystal HR side will give a result compatible with the measurement.

A simulation of PDH signal was also done to compare the situation of taking the error signal from OPO transmission or reflection. The simulation is done with simulation tool finesse. According to the simulation, the OPO PDH error signal is obtained in transmission.

Optical phase lock loop

Two additional beams from two auxiliary lasers are injected into OPO. These two laser fields need to be phase locked to main laser. The control loop which allow us to phase lock the field is called phase locked loop (PLL) [127]. I was responsible for the implementation and maintenance of this system. The principle of PLL and its

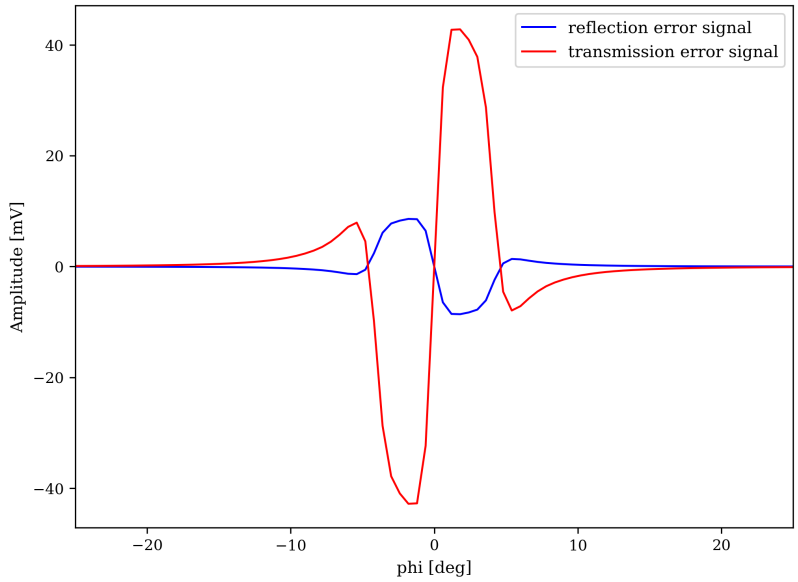

Figure 4.14: Simulation of OPO PDH signal in reflection and transmission of the cavity.

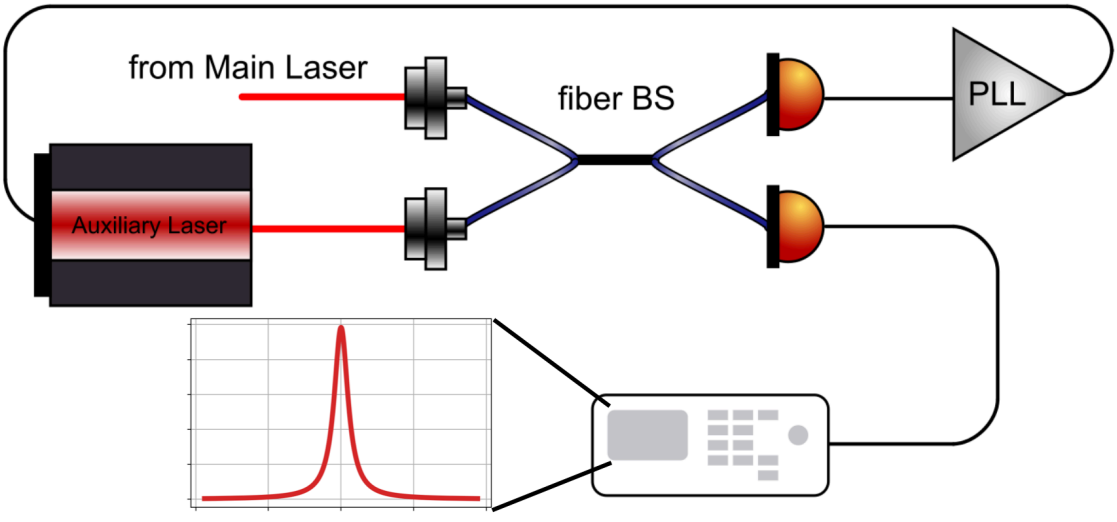

Figure 4.15: Optical phase lock loop optical scheme. The beat between two laser beams provides error signal for phase lock loop. The beat note shown on spectrum analyzer is used as a monitor and provides information on the locking status.

name	value
crystal material	$PPKTP$
dimension (mm)	1×1.5×9.3
flat surface curvature	∞
flat surface reflectivity	$< 0.3\%$ for both IR and GR
curved surface ROC	$8mm$
curved surface reflectivity	$> 99.975\%$ (IR) $> 99.975\%$ (GR)
meniscus curvature	20mm (outside), 25mm (inside)
meniscus reflectivity	92% (IR) 20% (GR)
FSR	4GHz
finesse	75

Table 4.5: Opto-mechanical parameters of OPO cavity. The FSR and finesse are given for IR.

characterization is reported in this part.

As shown in figure 4.15, the beat of main laser and auxiliary laser is realized in the fiber BS system. This beat contains information of phase difference between the two fields. This beat note is an RF signal sensed by a high speed, fiber coupled photo detector. A phase-frequency detector (ADF4002) is used to compare this beat note to a fixed local oscillator (LO). Then the phase difference between beat note and LO is fed back to the auxiliary lasers. In the end, the auxiliary laser phase follows the phase of main laser with a fixed frequency difference.

Characterization of PLL phase noise

PLL locks the beat note of two laser to a fixed frequency reference. To characterize how well the lock is performed, the monitor channel is used. This channel is connected to another phase detector and compared with the same LO signal. The characterization of phase noise is based on the principle of phase detector.

Let's assume the beat note V_{beat} and the local oscillator V_{LO} takes the form

$$V_{beat} = A_1 \sin \omega_0 t + \phi_1, \;\; V_{LO} = A_2 \sin \omega_0 t + \phi_2 \tag{4.25}$$

After sending them to a mixer, the beat of these two signals V_b will be

$$V_b = \frac{K_{mix} A_1 A_2}{2} (\cos(\phi_1 - \phi_2) + \cos(2\omega_0 t + (\phi_1 + \phi_2))) \tag{4.26}$$

The phase ϕ can be expressed as $\bar{\phi} + \Delta\phi$. The mixer's output is attached to a low pass filter. In our case, we use mini-circuits 'BLP-1.9+', which has a passband of 'DC-1.9MHz'. In this case, only the DC signal and the low frequency sideband can pass. So the signal will become

$$V_b = \frac{K_{mix} A_1 A_2}{2} \cos\left(\bar{\phi}_1 - \bar{\phi}_2\right) + \left(\Delta\phi_1 - \Delta\phi_2\right) \tag{4.27}$$

The phase difference of these two signals can be set to be 90°. We can check this phase difference by looking at the mixed signal on an oscilloscope. When the signal is around zero, the phase difference is 90°. In this case, the mixed signal will become

$$V_b = \frac{K_{mix} A_1 A_2}{2} \cos\left(\pi/2 + \left(\Delta\phi_1 - \Delta\phi_2\right)\right) \tag{4.28}$$

$$= \frac{K_{mix} A_1 A_2}{2} \sin\left(\Delta\phi_1 - \Delta\phi_2\right) \simeq \frac{K_{mix} A_1 A_2}{2} (\Delta\phi_1 - \Delta\phi_2) \tag{4.29}$$

The output signal is directly proportional to phase difference between beat note of PLL and LO. If LO is a stable signal, this phase difference is the phase noise of PLL. The spectrum of this mixed signal is the square of the above equation, and can be expressed as

$$S_b = (\frac{K_{mix} A_1 A_2}{2})^2 \times S_\phi \tag{4.30}$$

To calibrate the measured power spectrum into phase noise spectrum, a measurement of coefficient $\frac{K_{mix} A_1 A_2}{2}$ can be done when we change LO frequency by for example 100Hz and measure the pk-pk value A_{pk-pk} of the induced oscillation. So in the end the phase noise power spectrum is

$$S_\phi = \frac{S_b}{A^2_{pk-pk}} \tag{4.31}$$

If the measurement is amplitude spectrum, the calibration factor becomes A_{pk-pk}. The measurement result of PLL phase noise is shown in figure 4.16. At high frequency, the phase noise comes mainly from the frequency noise of the servo. However, the low frequency phase noise is dominated by the length fluctuation of filter cavity. This is due to the fact that the main laser is frequency locked to the filter cavity. At frequencies higher than 10Hz, the FC is a much more stable frequency reference compared to the laser itself, however, at lower frequencies, where the mechanical resonances of the suspension are present, it actually introduces noise in the main laser frequency, which is reflected into the PLL noise. In order to limit this effect, the low frequency portion of the FC length error signal is fed back to

the cavity mirror actuators, while the high frequency part is fed back to the main laser. This is clear when looking at the PLL performances when this type of hybrid actuation is chosen with respect to fully actuating on the main laser: in the first case the residual PLL noise is almost a factor of two smaller than in the latter case. More on the locking strategy for the FC will be explained in the next chapter.

OPO cavity assembly and cavity scan

OPO cavity has a similar mechanical configuration with SHG. The assembly of OPO starts from putting PPKTP crystal inside the housing. As shown in figure 4.12, for the crystal side of OPO housing, different parts are listed from lowest one to highest one as following:

- Peltier. Peltier can transfer heat from one side to the other side with the consumption of electrical energy. So it has a cold and hot side. Since we need to heat up PPKTP, the hot side is upside.
- Indium. A 0.1mm indium sheet is placed on top of Peltier to ensure a good thermal contact. This is also applied to one side of PPKTP holders which are in contact with PPKTP.
- Copper 'L' shape holder. This is used as a buffer for the heat coming from Peltier and a holder for PPKTP crystal.
- Thermistor. Thermistor (103 JT-025) is attached to the shorter vertical side of copper holder with a retainer. This is the sensor for thermal control.
- PPKTP. PPKTP needs to be put in the corner of holder and longitudinally in the middle. A marker indicates the HR side of crystal.
- Macor 'L' shape holder. It is used to fix crystal position and for thermal isolation. Two screws, acting on X or Y direction, provide pressure to fix the crystal.

After the assembly and alignment of the OPO, the optical characterization was performed by doing a cavity scan. By fitting the Airy function, the information of FSR or finesse can be derived. Especially, by increasing modulation depth on purpose, the sidebands of 87.6MHz can appear in the spectrum of cavity scan. By using this information, the estimation of FSR becomes more accurate. The fit result is shown in figure 4.17.

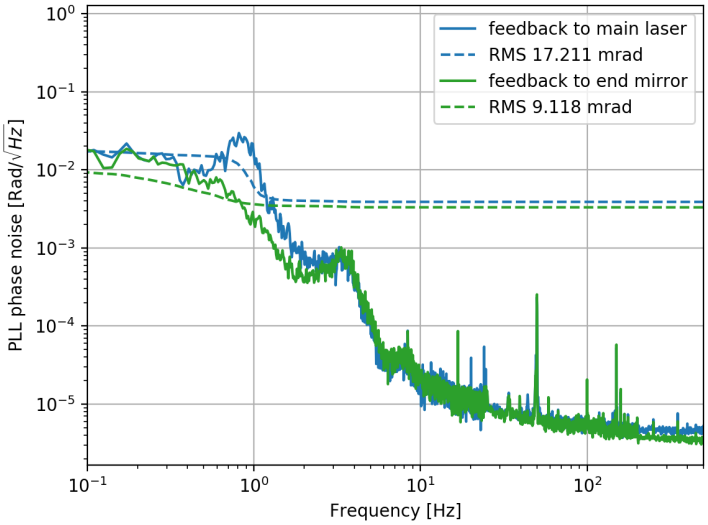

Figure 4.16: PLL phase noise for difference FC control actuation. When the low frequency part of the FC control is offloaded to the cavity mirror, the reduction of the PLL noise is clear. .

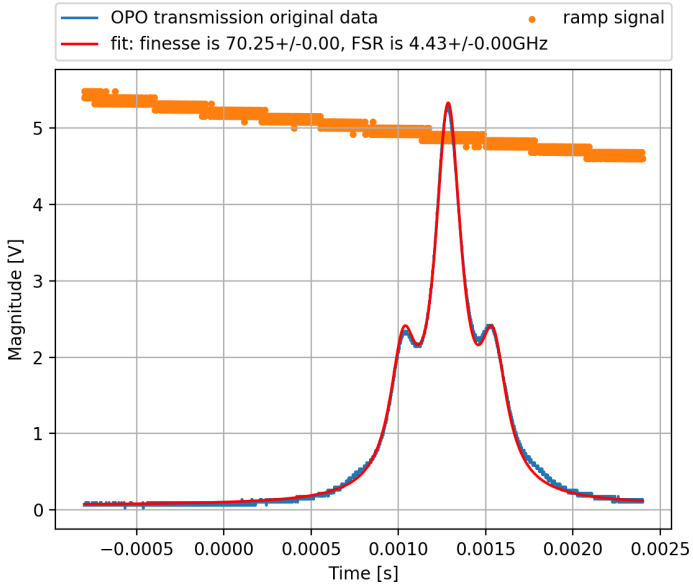

Figure 4.17: The measurement of OPO transmission when OPO is scanned. The ramp signal sent to PZT is also shown to prove that a good scan region was chosen

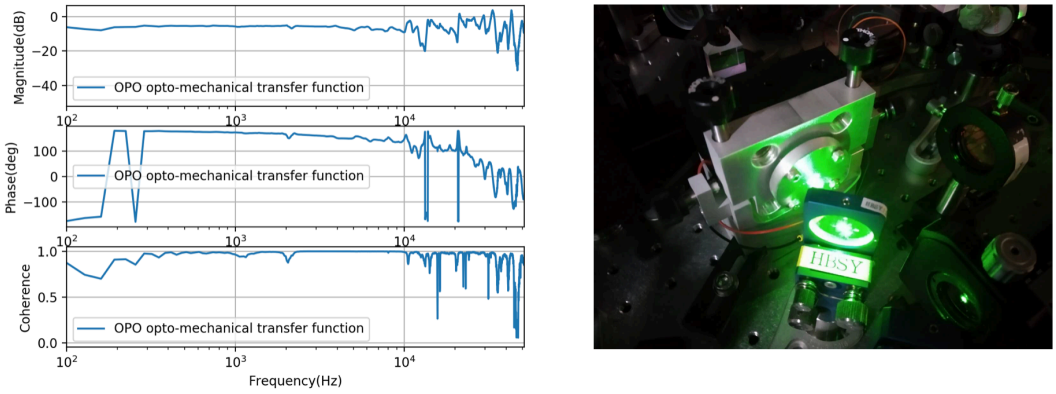

Figure 4.18: Left: OPO opto-mechanical transfer function. We could see that it is flat until 10kHz. Right: the OPO cavity on bench when green pump is injected into it.

OPO length control

The PDH lock sensing beam is chosen as p polarization because it will otherwise interact with the squeezed field. The opto-mechanical transfer function for OPO cavity is shown in figure 4.18, the servo filters are designed according to this measurement.

As introduced, this beam is provided by an auxiliary laser phase locked to main laser. PLL needs to set a frequency difference between two lasers. Due to the birefringence effect of PPKTP, two polarization have different resonant frequencies. Therefore, the LO frequency of PLL needs to be tuned carefully to make the two polarization co-resonant.

The frequency difference depends on temperature, because temperature can change crystal length and crystal refractive index. Note that this temperature dependence doesn't depend only on the crystal temperature controlled by the temperature control. Both the different green power and the resonance of infrared light can influence the internal temperature of crystal. These temperature influences were observed in the lab and are not negligible.

At beginning of this chapter, we introduced the set-up of laser diode's current and crystal temperature. Apart from the mode hops introduced at that moment, this co-resonance is the other requirement which needs to be met.

Although there are many factors which influence the p and s polarization co-resonance condition, it was observed that the frequency offset is dominated by the pump power level.

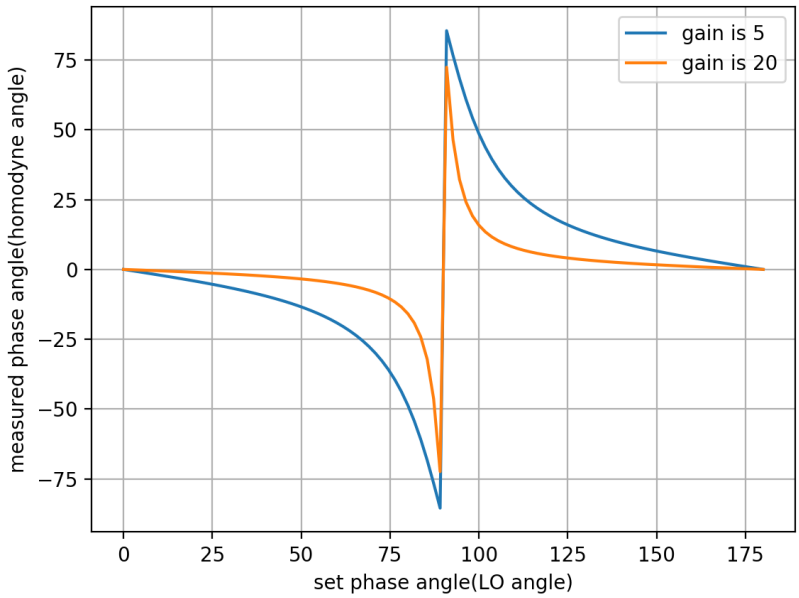

Figure 4.19: The relationship between LO angle and homodyne angle. The larger the parametric gain, the more non-linearity it has.

Coherent control

The coherent control (CC) technique [113] provides the phase information of squeezing and a stable phase is crucial for the stable operation of squeezer. The coherent control field comes from an auxiliary laser source which is phase locked to main laser with a frequency offset of 7MHz. The injection of this frequency offset field doesn't influence squeezing measurement, but we need to take care of the relative power between the CC sidebands and the homodyne LO. In particular, the power in the sidebands needs to be small compared to the one in the LO so the contribution to the shot noise of the first one is small compared to the latter.

As shown in figure, it is a scheme for coherent control in quadrature plane. Coherent control can also be conceived as a control for the squeezing ellipse. Since the frequency difference between CC sidebands and squeezing is small compared to the two field overall frequency, we can assume that CC field will experience the same phase noise with respect to the squeezing. Moreover, all the optics will have the same property for these two fields due to small frequency difference. Therefore, the influence of pump beam phase change is sensed by coherent control field. By sensing this field, the error signal can be used to control pump phase and LO phase.

In section 3.1.4, the squeeze operator was introduced with its effect on a vac-

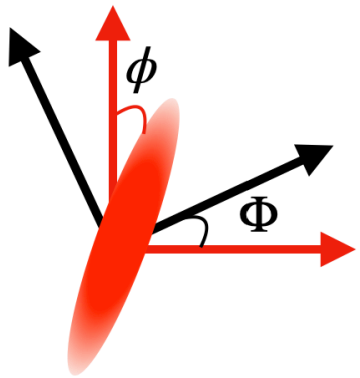

Figure 4.20: Coherent control scheme. Coherent control field represents the phase of squeezed vacuum field. By stabilize the phase difference of upper and lower sidebands of the coherent control field, the phase of squeezed vacuum field is also stabilized. This can be conceived as the stabilization of phase ϕ, this control loop is usually called 'CC1' in this experiment. After the lock of 'CC1', a quadrature plane of red color is constructed. The measurement of squeezed vacuum field relies on the phase difference between 'CC1' and the phase of 'LO'. The loop to stabilize their phase difference is called 'CC2' in this experiment.

uum state. For CC field, it has a frequency offset of Ω relative to carrier. So the annihilation operators for upper and lower sidebands are

$$< \hat{a}_+ > \equiv < \hat{a}(\omega_0 + \Omega) >= \alpha_\Omega \tag{4.32}$$

$$< \hat{a}_- > \equiv < \hat{a}(\omega_0 - \Omega) >= 0 \tag{4.33}$$

When it is expressed as quadrature operator, it takes form

$$\hat{a}_1 = \frac{1}{\sqrt{2}}(\hat{a}_+ + \hat{a}_-^\dagger) \tag{4.34}$$

$$\hat{a}_2 = \frac{1}{i\sqrt{2}}(\hat{a}_+ - \hat{a}_-^\dagger) \tag{4.35}$$

By taking the squeeze operator from section 3.1.4 and acting on the above quadrature operator, we will have a 'squeezed' CC field. By adding a term $e^{i\Omega t}$ for the corresponding term, the signal can be expressed in time space domain as [91]

$$\begin{aligned} E \propto & \frac{1+g}{\sqrt{2g}}\alpha_\Omega \cos(\omega_0 t + \Omega t) \\ & - \frac{1-g}{\sqrt{2g}}\alpha_\Omega \cos(\omega_0 t - \Omega t - 2\phi) \end{aligned} \tag{4.36}$$

Notice that the second sideband at $-\Omega$ is created inside the OPO due to the nonlinear interaction of the crystal. The first CC loop is used to stabilize the phase term of 2ϕ in the above equation by acting on the green pump phase. By feeding this signal back to a phase shifter acting on pump phase, this phase is controlled to be zero. Then when this field arrives at the homodyne detector, it will beat with local oscillator field $\cos\omega_0 t + \Phi$. To measure squeezing, the phase difference between them needs to be stabilize as well. As derived in [128], the low frequency component of beat $B(t)$ between LO and above equation will be

$$B(t) \propto (1+g)\cos(\Omega t + \Phi) - (1-g)\cos(-\Omega t + \Phi - 2\phi) \tag{4.37}$$

Using $\cos(a+b) = \cos a \cos b - \sin a \sin b$, the above equation can be separated into cosine and sine part of an oscillation field. The inverse trigonometric phase angle of this signal is the ratio of sine part coefficient and cosine part coefficient. It can be expressed as

$$\Phi_{measure} = \arctan \frac{-(1+g)\sin(\Phi) - (1-g)\sin(\Phi - 2\phi)}{(1+g)\cos(\Phi) - (1-g)\cos(\Phi - 2\phi)} \tag{4.38}$$

This measured phase is the error signal we use for the second CC loop. It is also referred as homodyne angle, which is defined as 0° for squeezing while 90° for anti-squeezing. The relationship between Φ and $\Phi_{measure}$ is shown in figure 4.19. This the non-linearity of the relation results in a small range of LO phase which corresponds to squeezing.

To actively control phase of squeezing or the measurement phase, both pump phase ϕ and LO phase Φ need to be controlled. The actuator is a mirror driven by a PZT. To have the desired opto-mechanical response, the post for mirror was modified from a commercial one to a monolithic one. The opto-mechanical transfer function for different set-up is measured and shown in figure 4.21, 4.22 and 4.23. We could see the continuous improvement we got by upgrading the mechanics of this devices.

Bright alignment beam

Since squeezing field has too few photons, lots of OPO characterization cannot be done with it. The injection of a bright field will help to characterize OPO and its matching to other cavities. We call this field bright alignment beam (BAB). When a cavity is on resonance, all the transmission of cavity comes from the resonant mode. So when OPO is locked with BAB on TEM00, the geometry of OPO transmission is the same as the geometry of the vacuum/squeezing field from it[1]. As a result, BAB is used to align and match OPO cavity with other cavities or light beams. We need to note that this beam should come directly from main laser. For example, CC field is also bright, but it has a frequency offset so it cannot be used. The usage of BAB is summarized as following in our experiment:

1. aligning filter cavity,
2. measuring filter cavity locking accuracy for squeezing,
3. aligning homodyne and checking its visibility,
4. measuring parametric gain and
5. aligning green pump into OPO.

[1]It is necessary to make sure the BAB is matched as well as possible into OPO. Although higher order modes are usually not considered to be transmitted, there is very little percentage actually transmitted. So to make sure BAB represents a good geometry, a good matching between BAB and OPO is necessary.

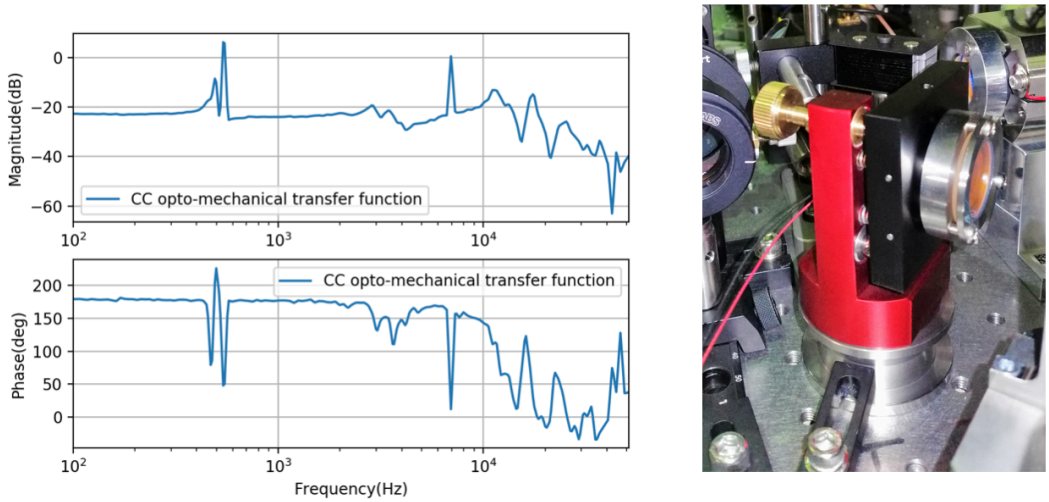

Figure 4.21: The first version phase shifter by using a commercial mirror mount. Left: the opto-mechanical transfer function. Right: the set-up of phase shifter

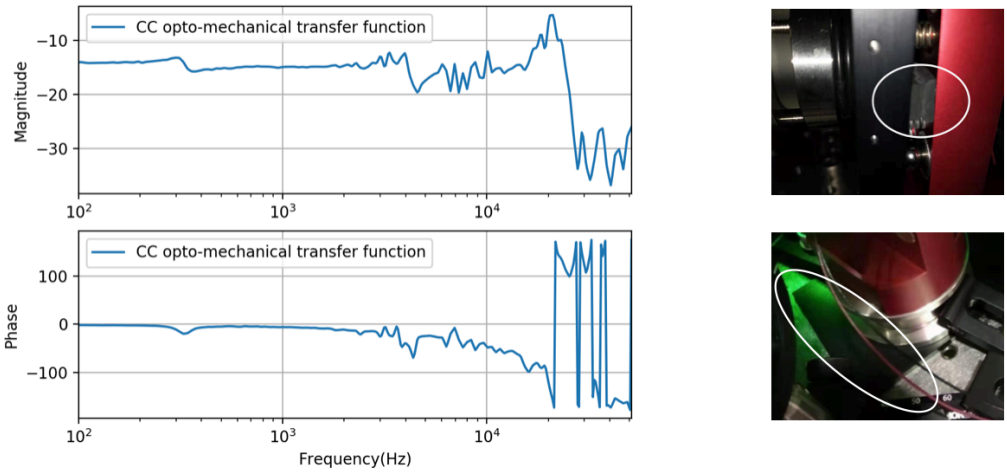

Figure 4.22: The second version phase shifter by using a modified commercial mirror mount. Left: opto-mechanical transfer function. Right: modifications done by putting rubber under mirror mount and around the spring part

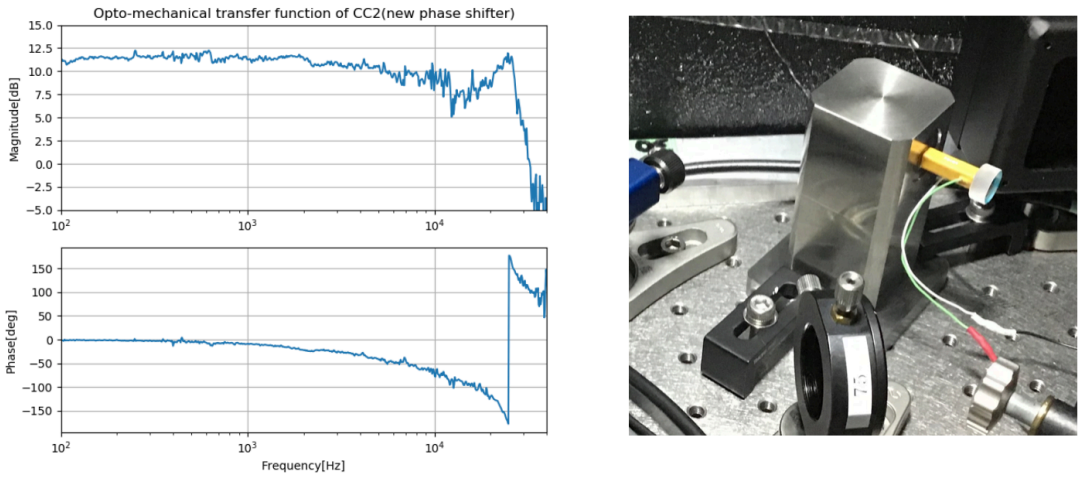

Figure 4.23: The third version phase shifter by using a customized mirror mount. Left: opto-mechanical transfer function. Right: a monolithic post with PZT glued on it, while a half inch diameter mirror glued on PZT.

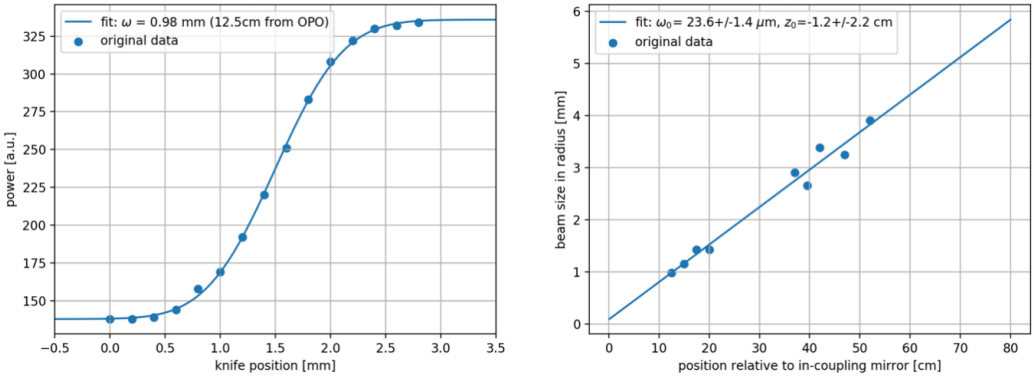

Figure 4.24: Left: the first measurement point of green beam generated from OPO with the method of knife cutting. Right: the fit of beam size in different to find green beam waist size and waist position.

As we see the listed usages of BAB are mainly related with alignment. The first four usages will be introduced later, here I will introduce the alignment of green pump beam into OPO. As we said at the beginning of the subsection, OPO has very similar configuration with respect to the SHG. If we send a bright infrared beam into OPO, green beam will be generated. However, since the infrared power is not large, we have very weak generated green ($0.3\mu W$) from OPO. So the measurement of beam parameter was done in a knife edge cutting method. A beam propagating along z-direction has Gaussian intensity profile $I(x, y)$ as

$$I(x, y) = I_0 e^{-2x^2/\omega_x^2} e^{-2y^2/\omega_y^2} \tag{4.39}$$

where ω_x is the beam radius in x direction. Then the total power P_t can be expressed as

$$P_t = I_0 \int_{-\infty}^{\infty} e^{-2x^2/\omega_x^2} dx \int_{-\infty}^{\infty} e^{-2y^2/\omega_y^2} dy = \frac{\pi}{2} I_0 \omega_x \omega_y \tag{4.40}$$

In the real case, we cut beam only along one direction at a time, then the power $P(x)$ at different cut position will follow

$$P(x) = P_t/2 - \sqrt{\frac{\pi}{2}} I_0 \omega_y \int_0^X e^{-2x^2/\omega_x^2} dx \tag{4.41}$$

So in the actual case we need to use an erf function to fit data. The variable in erf function, we set it as $\sqrt{2}(x - x_0)/\omega$. Then the fit result of ω gives directly the beam radius. One example of this fit is shown on the left side of figure 4.24. After taking all the points, we fit with a Gaussian beam propagation function and found beam waist is $23.6 +/- 1.4\mu m$ and waist position is $-1.2 +/- 2.2cm$.

We then align and match this generated green beam into GRMC. Although this beam is very weak, both camera and photo detector are sensitive enough to see it. This represent just a preliminary alignment for this process. The dark noise of photo detector is a bit high. In order to refine the alignment of the green field into the OPO, we used the OPO parametric gain measurement. In fact, the maximum parametric gain for a fixed green pump power is the final criteria for a good alignment.

Thermal control

A stable temperature is essential for maintaining a good phase matching for squeezing production. The control loop is composed of a Thorlab temperature controller (TEC200C), a Peltier cell (CP0.8-31-06L) and two thermistors (103JT-050).

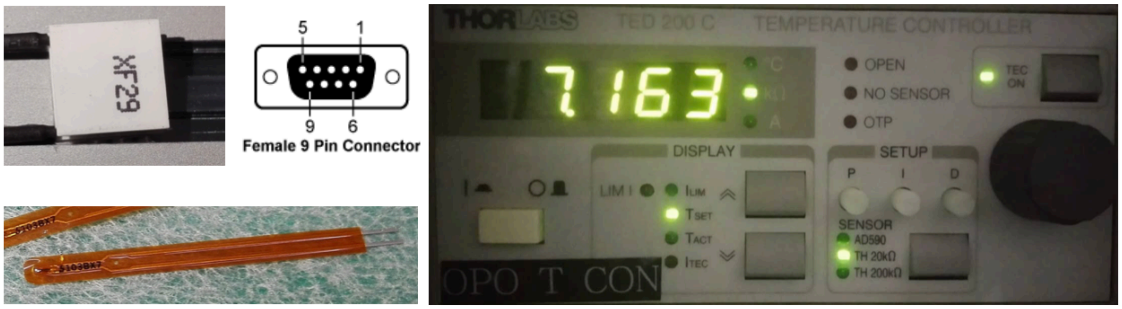

Figure 4.25: Left upper corner: Peltier. Left lower corner: thermistor. Upper middle: 9-pin layout for TEC200C. (connection assignment: 2-thermistor +, 3-thermistor -, 4-Peltier +, 5-Peltier -) Right: TEC200C front panel

A Peltier cell (or just Peltier) is a voltage controlled thermal transformer. The relationship between voltage and thermal difference is almost linear. This ensure its good performance in the application to the thermal control loop. The direction of thermal transfer depends on the direction of current, so we can easily change it from a cooler to a heater by changing the current direction. A Peltier is usually composed of many P-type and N-type semiconductors. Each P and N are placed in parallel while they are electrically connected in series. The Peltier has maximum current and voltage value which can tolerate. For our CP0-8-31-06L, the maximum current is 2.1A while the maximum voltage is 3.75V.

Our thermistor is a temperature dependent resistor where the change of resistor is inversely proportional to the change of temperature. By knowing the temperature and resistor relation in advance, the real temperature can be derived. The relation is

$$T = \frac{B * T_0}{B + T_0 * \log \frac{R}{R_0}} \tag{4.42}$$

where T_0 is the nominal temperature of $298.15K$, B is the energy constant provided by manufacture of thermistor, R_0 is the resistor at nominal temperature provided by manufacture. Two thermistors are used in the set-up (103JT-025). One is used to provide real-time temperature for control loop. Another thermistor is used as a monitor.

The servo used for temperature control is Thorlab TED200C. Some important functions on the panel are listed as following:

- Sensor (TH 20kΩ): This means that TED200C measures resistance from 0 to 20kΩ. There is another option which is 200kΩ. Difference between them

determines the resolution of resistance measurement.

- Display (T_{SET} and T_{ACT}): Since we are using thermistor, these two tell us the resistor of the thermistor. There is a knob on the panel, which is used to change the value of T_{SET}.

- Set up (PID): Knobs for adjusting PID parameters.

- TEC ON: this is the switch to open or close the loop.

From picture 4.25, we have the pin layout of the servo connector. Since thermistor is only a resistor, it doesn't matter which side is connected to positive or negative. However, polarity is very important for Peltier. The polarity can be checked by testing if the temperature can be stabilized after closing loop.

This thermal control loop provides control precision of $4mK$ and control stability of less than $2mK$ within 24 hours.

OPO phase matching condition

As we did for the SHG, also in the case of the OPO we measured the phase matching condition. In order to perform this measurement we injected the BAB, changed the crystal temperature of the OPO and measured the green production as function of the temperature. The result can be seen in figure 4.26. The optimal temperature is around 34°C, but it has a quite large peak of about 1°C.

Parametric gain measurement

The non-linear effect of OPO can be described by the formalism developed by Gardiner and Collet [129]. A summary of this theory was done in [127]. As long as there is any non-linear interaction happening inside the OPO, the energy will go from pump to signal and interfere with the original signal field [130]. But depending on different phase of pump, the interference amplifies or de-amplifies the signal field. This is the parametric amplification/deamplification effect. The amplification/deamplification of signal field power P_s is related with pump field power B and OPO threshold power B_{th} as

$$\frac{P_s}{P_s|_{g=0}} = \frac{(1+\frac{B}{|B_{th}|})^2}{(1-\frac{|B|^2}{|B_{th}|^2})^2} \tag{4.43}$$

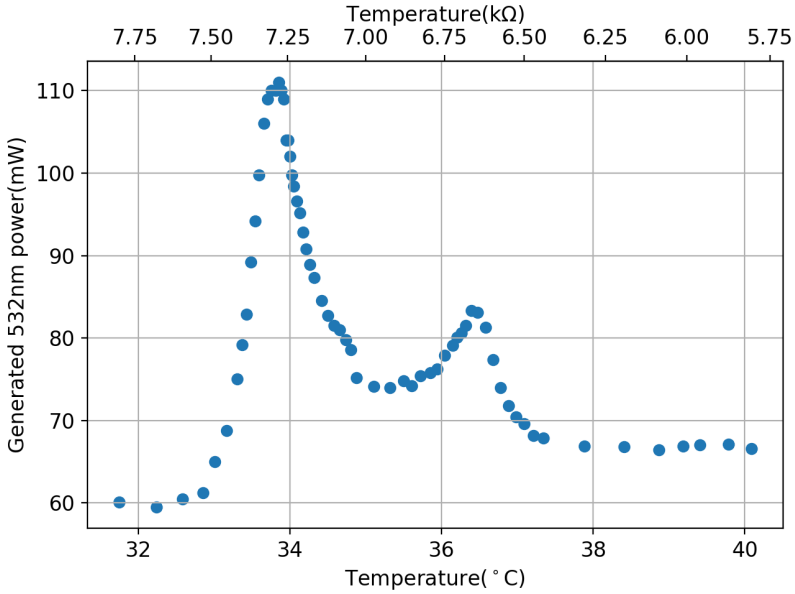

Figure 4.26: By changing OPO temperature, we characterize the phase matching condition of OPO. The operation temperature is also decided to be where the maximum green power is achieved. As we can see, there is also the effect of pump field double pass[119]

So in our case, we send BAB to OPO and measure the amplification or deamplification by scanning green pump phase. The measurement result is shown in figure 4.27.

With the information of OPO threshold, the squeezing level without considering any degradation for different pump power can be predicted by the formula [132]

$$V_{\mp} = 1 \mp \frac{4\sqrt{P_{pump}/P_{threshold}}}{(1 \pm \sqrt{P_{pump}/P_{threshold}})^2} \tag{4.44}$$

where P_{pump} is the pump power, $P_{threshold}$ is the OPO threshold power derived from the parametric gain measurement. For the case of the OPO used in this experiment, the predicted squeezing level for different pump power is shown in figure 4.28.

4.1.6 Balanced homodyne detector

The balanced homodyne detector (BHD) used in our experiment was developed in collaboration with the Albert Einstein Institute (Hannover - DE) and it provides a DC output and an on-board demodulation of RF signal. The on-board demodulation then provides error signal for controlling the homodyne angle using the coherent control. The principle of homodyne detection is introduced in the last chapter. In

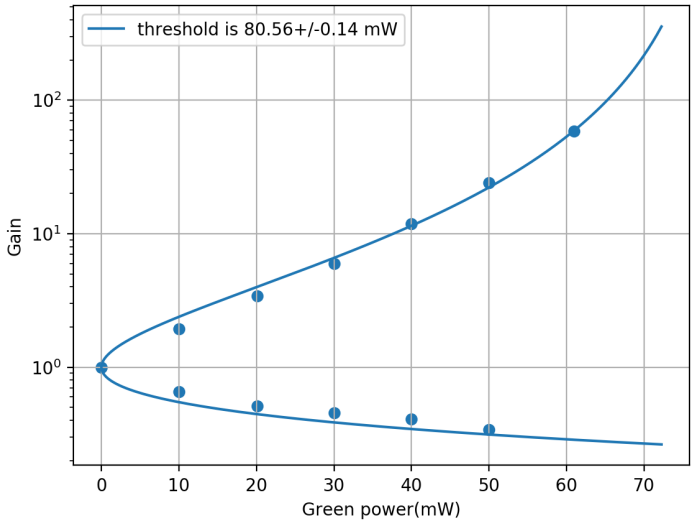

Figure 4.27: The measurement of parametric gain for OPO. The points are measurement result. The plot line is the fit result. The threshold shown in the legend is around 80mW, the error comes from fitting by using python package [131]

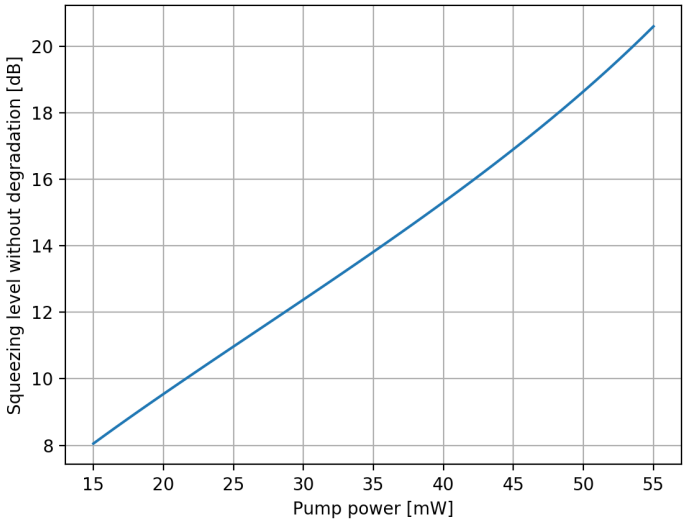

Figure 4.28: The squeezing level as function of pump power inside the OPO or without considering any degradation.

practice, the operation of BHD needs careful balancing. In this section, the optical balancing method and its characterization is reported.

Homodyne optical balancing

According to our BHD design, we are using a current subtracting method, therefore the balancing must be done optically. This is crucial for the performance of BHD. Before doing the optical balancing, the response of separate photodiode was characterized to be almost the same. In this experiment, the balance was only done by adjusting the angle of beamsplitter. The procedure of this adjustment is as following:

1. Choose a stable beam splitter: we procured beam splitter from several different companies and characterized the angle dependence of the power splitting. Due to the space limitation, an even splitting with angle close to 45 degrees is preferred. But a more important requirement is the stability against angle change. An unstable BS usually requires lots of efforts to realign.

2. Balance of local oscillator (LO): balance by adjusting horizontal angle of BS while looking at the transmitted beams power ratio. This is just a rough balance, which is done to mainly find a good position to put BS.

3. Align LO into alignment mode cleaner (AMC). AMC is located in the upper right corner in figure 4.1. This step needs to be done before the final balancing because this alignment will influence the balancing of BS. As shown in the figure 4.1, this step is done by adjusting two steering mirrors between IRMC and BS of BHD.

4. Fine alignment of LO into BHD. The criteria for this alignment will be introduced later.

5. Align BAB into AMC. Now it is clear why we call the triangular cavity as AMC, since it is used for the alignment of BHD. When both LO and BAB are aligned into AMC as well as possible, the detection of squeezing can be done. The influence of this alignment for squeezing will be introduced in section 4.2.1.

The criteria to evaluate balancing is called common mode rejection ratio(CMRR). By either modulating main laser amplitude or IRMC PZT, a peak can be produced

in the spectrum of BHD. The CMRR is the peak height ratio when one of the photo detectors is blocked and open. To maximize CMRR, the angle of honodyne's BS needs to be adjusted. In the end, the CMRR was measured to be around 60dB for LO while around 30dB for signal. A high CMRR for LO is important because LO power is much higher. Since the coherent control field has power of only around 11.5 μW, its CMRR is less important.

A high level of CMRR ensures the measurement of shot noise, which otherwise is covered by common mode noises. To measure shot noise, the signal port needs to be blocked with beam dump properly. Any shiny surface may cause the measurement to be contaminated by back scattering noise. The LO is a coherent state and it has equal fluctuation in two quadrature. So according to equation 3.32, no matter what the LO's phase is, the homodyne output is a constant value. The measurement of this shot noise is shown in figure 4.29.

After a good balancing, BHD is ready for the measurement of squeezing.

4.1.7 Digital synthesis of radio frequencies

All the RF signals are generated from a Direct Digital Synthesizer (DDS) system with the use of AD9959 chip from Analog Devices. These signals are summarized in appendix A. A DDS synthesis RF signal based on the down sampling of a very high frequency clock. The frequency of this reference clock in our system is $500MHz$. So the generated signal always has a frequency lower than the frequency of clock. The frequency of generated signal can be expressed as

$$\nu_{out} = \frac{N}{D}\nu_{ref} \tag{4.45}$$

where N is the frequency tuning word, which tells how many samples the system takes for one period of a reference clock, $D = 2^p$ is the resolution of the sampling while p is the number of bits for the system. So it's easy to get the frequency resolution of our system is $500MHz/2^{32} = 0.116Hz$. This process is similar to an aliasing effect.

The detailed working principle is well explained in the thesis of Marco Vardaro [127], all the discussion in this part is based on his work. Here we mention an important phenomenon of spurs. It can be caused by quantization or truncation. The quantization will give a flat noise floor from 0 to half the clock frequency. The

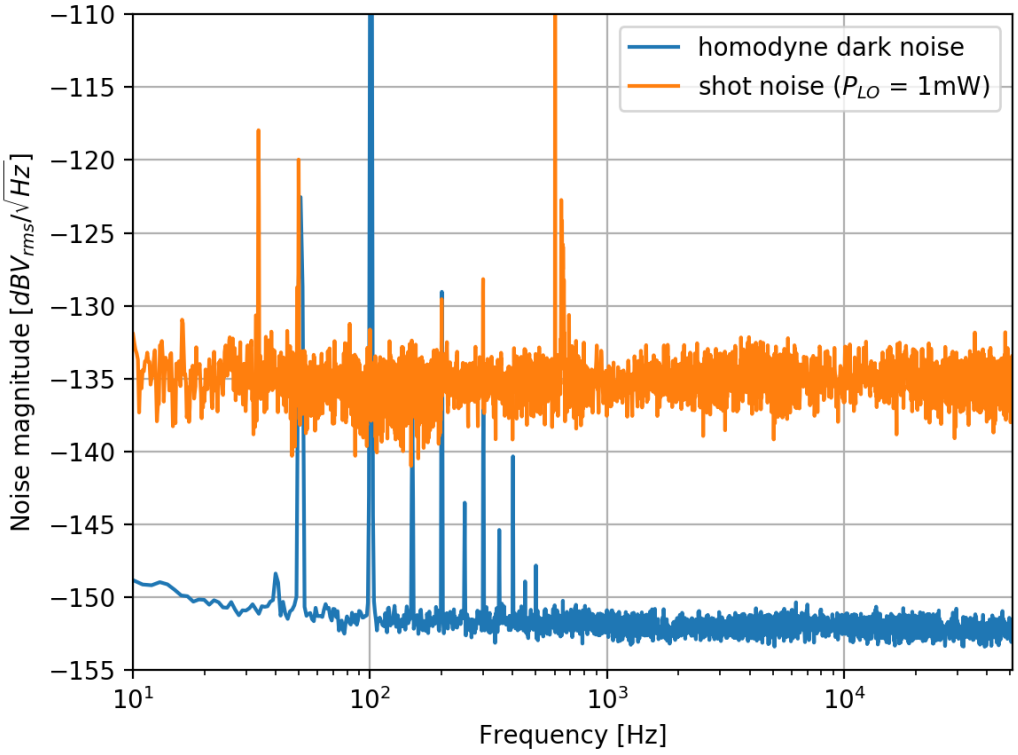

Figure 4.29: Characterization of BHD shot noise after optical balancing. The measurement of shot noise is flat down to 10Hz. The clearance between shot noise and dark noise is more than 15dB. Some of the features initially present in the homodyne dark noise are no longer present in the shot noise spectrum. This was due to a improvement campaign done to remove power source related peaks. In particular the 100Hz peak, which is the largest one present in the dark noise, was removed by switching off the ambient illumination.

noise level N_{DAC} is

$$N_{DAC} = \frac{4}{3}\frac{1}{2^{2q}\nu_{ref}} \tag{4.46}$$

In the case of our $500MHz$ clock, the noise level is $-170dBc/Hz$. This noise causes the generation of high frequency spur components in the output spectrum.

Truncation happens because the numbers of bits for sampling and DAC are different. So some less significant bits is removed. Then spurs appear in the output spectrum.

The output power of the DDS is 10dBm and the phase of each channel can be changed with a precision of 0.005°. The output can be changed from full power to 1/2, 1/4 or 1/8 digitally. Usually this feature is not used in daily lab since it induce an increase of the noise in the output. In place of this digital control, analog attenuators are used.

4.1.8 Customized automatic analogue servo

In order to lock all the cavities and the MZ described before, a multi-purpose analog servo was developed in collaboration with the laboratory of Astroparticles and Cosmology (APC) in France. A general description of our customized analogue servos will be given in this section.

Some advantages of the developed servo are listed in the following.

1. Robustness. Once the circuit is made, the loop configuration is fixed. No limitation from computer related issues. This is both an advantage as well as a disadvantage since the fixed configuration limits the flexibility of the servo. However, thanks to a clever design, we can digitally control several switches on the board to remotely change the servo transfer function.

2. Good frequency spectrum performance. There is no ADC or DAC process, so the problem of digitalization can be well avoided. Moreover, large bandwidth can be achieved since no delay due to digitalization processes is introduced.

Filters design

The principle for designing the servo filters are: providing a phase margin of 30 degrees and gain margin of 10dB in an open-loop transfer function.

For each servo, we can have two low pass filters, an inverter, a differentiator, an integrator (can be switched between 1/f and $1/f^3$) and a gain (can be changed

by a potentiometer). Individual filter configuration is different and decided by each loop's opto-mechanical transfer function. An example of this filter design is given in appendix A.

Servo introduction

Our locking servo has two servo control modes:

1. **Auto mode**. In auto mode, the lock state of the loop will be decided by a logic circuit. As we know, the transmission or reflection of a cavity will go across a peak/dip when the PZT scan through the resonance. The logic circuit compares this signal to a threshold, which can be set by a potentiometer, and simultaneously check the sign of the error signal. If both conditions (presence of pick/dip and good error signal sign) are satisfied, the circuit automatically lock the device.

2. **Manual mode**. In manual mode, lock state of the loop is decided by the operator.

3. **Scan mode**. In scan mode, the output of servo will send out a ramp signal (the ramp signal amplitude and period can be changed by two potentiometers) and the loop is open.

A hierarchy locking scheme enables locking in sequence and makes the whole system work within one minute. A remote control is also available. Many channels are available for many other functions, including the measurement of many transfer functions, the trigger for oscilloscope and servo test.

4.2 Degradation of squeezing

The measurement of squeezing needs special attention since there are many factors which can cause the degradation of the squeezing level. They can either degrade the total squeezing level or introduce some unwanted frequency components in squeezing spectrum. The degradation factors are introduced following the formalism used in the following works [98, 127, 133, 91]. This part is dedicated to analyze the individual degradation factors in this experiment.

4.2.1 Optical losses

Optical losses can be explained using a beam splitter model. The input of this beamsplitter are vacuum fluctuation V_{vac} and squeezed vacuum fluctuation V_{-}. They are mixed at beamsplitter with the ratio of power reflectivity R and losses L (which includes transmission and scattering). This relationship can be expressed as

$$\begin{pmatrix} V'_{vac} \\ V'_{-} \end{pmatrix} = \begin{pmatrix} R & -L \\ L & R \end{pmatrix} \begin{pmatrix} V_{vac} \\ V_{-} \end{pmatrix} \tag{4.47}$$

Since $R + L = 1$, R will be replaced by $1 - L$. Then the original squeezing V_{-} will be affected by optical losses as

$$V'_{-} = L \cdot V_{vac} + (1 - L) \cdot V_{-} \tag{4.48}$$

This model shows how the output squeezing is a mixture between the input one and the vacuum state. The effect of optical losses on squeezed state can be seen in figure 4.30. In the following, several individual losses processes will be introduced.

Escape efficiency of OPO

The escape efficiency of OPO is expressed as

$$\eta_{esc} = \frac{T}{T + L} \tag{4.49}$$

Here T is the transmissivity of in-coupling mirror, L is the round trip power losses coming from crystal HR surface transmissivity, crystal AR surface reflectivity and crystal absorption.

In this experiment, the transmissivity of in-coupling mirror is 8%. L are the intra-OPO round trip losses, which can be estimated as $2 * 0.3\% + 0.005\%$. Here, 0.3% comes from the reflectivity of PPKTP crystal AR coating and 0.005% is the transmissivity of PPKTP crystal HR coating. PPKTP AR coating parameter represents the higher limit of coating reflectivity provided by the manufacturer. Even if should be better, the measured finesse of 70 for OPO, confirms the reflectivity to be close to 0.3%. This gives OPO escape efficiency of 93% therefore a 7% of overall optical losses.

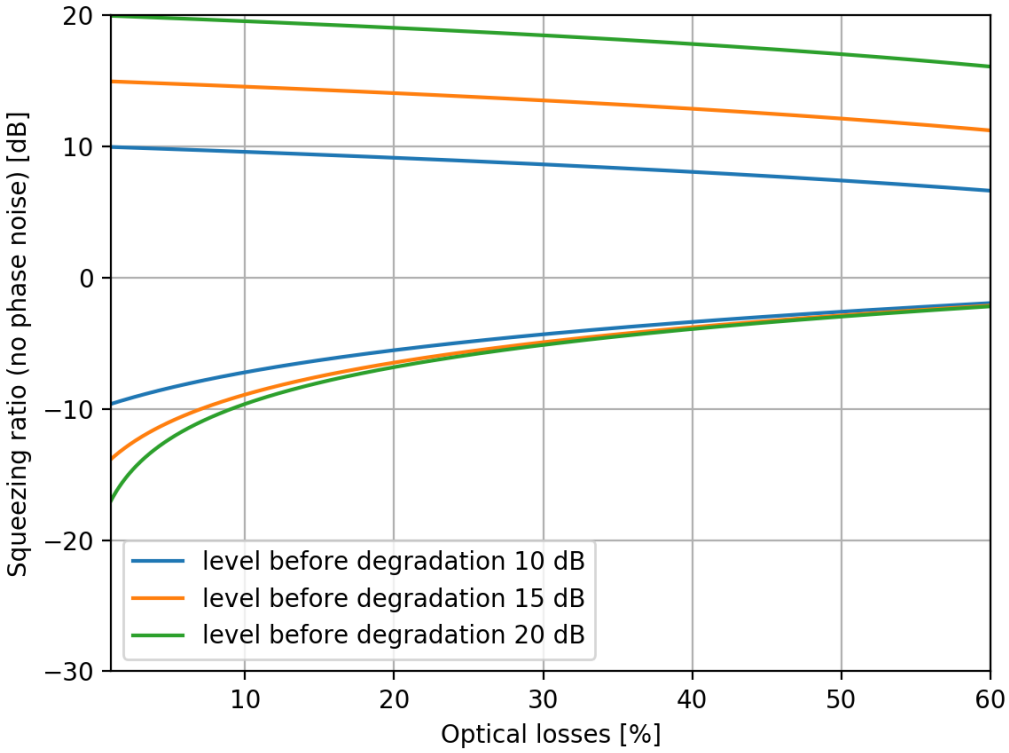

Figure 4.30: Effect of optical losses on squeezed state with different initial squeezing level. It is very clear that the optical losses affect mostly the squeezing while the anti-squeezing is less affected by the optical losses.

Propagation losses

Propagation losses refer to losses caused by the non-perfect reflectivity of HR mirrors, the AR coating reflectivity of lenses, the power losses from Faraday isolator and so on. By doing power measurement, this is measured to be around 5%.

Balanced homodyne detector's detection efficiency

The BHD works with the principle of interference between local oscillator and squeezing. So if there is any mode mismatch between the local oscillator and the squeezing, it can be considered as a source of losses. To achieve the alignment of BHD and measurement of visibility, bright alignment beam needs to be used.

To align homodyne and match LO and BAB, we used a triangular cavity as a reference. As shown in figure 4.1, there is a flipping mirror on the homodyne optical path. When this mirror is in place, the homodyne can be used to do measurement. But if it is taken away, the light beam will go to a triangular cavity. If both BAB and LO match to this triangular cavity, the overlap between BAB and LO at the level of the homodyne is automatically ensured. Since this additional triangular cavity is used for the alignment of BHD, it is usually called alignment mode cleaner (AMC) in our experiment.

The BAB and LO have different power levels. For an interferometric interference between two beams with different power, a perfect interference V can be expressed as

$$V = \frac{2\sqrt{P_1 P_2}}{P_1 + P_2} \tag{4.50}$$

Here P_1 and P_2 are the power of BAB and LO. In the real case, the visibility will be always smaller than this value or at most equal. The measurement of visibility V_{mea} relies on the interference fringe and it can be written as

$$V_{mea} = \frac{V_{max} - V_{min}}{V_{max} + V_{min}} \tag{4.51}$$

The ratio between V_{mea} and V is the visibility VIS of BHD. The detection efficiency is defined as

$$\eta_{BHD} = VIS^2 \tag{4.52}$$

In this experiment, BHD detection efficiency is measured to be 98%.

Quantum efficiency of photo diode

The quantum efficiency of photo diode represents the detection efficiency of photons by a photo diode. Nowadays, quantum efficiency can reach levels as high as 99.5% [83]. The quantum efficiency is usually specified by the manufacture and it can be also calculated from the photo diode responsivity as [93]

$$\eta_{pd} = \frac{\hbar\omega}{e} \times \frac{i}{P} \tag{4.53}$$

where i is photo current and P is incident light power. Usually this ratio is called responsivity and provided by manufacture. In this experiment, the photo diode quantum efficiency is larger than 99%.

4.2.2 Classical noise

As pointed out by Appel [134], dark noise is equivalent to optical losses in the measurement of squeezing. Schreiber [98] further pointed out that the classical noise can be considered as a frequency independent noise and increase shot noise and squeezing spectrum with the same level. Then the observed squeezing level R_-^{obs} will be

$$R_-^{obs} = \left(1 - \frac{V_{class}}{V_{vac}^{obs}}\right) R_- + \frac{V_{class}}{V_{vac}^{obs}} \tag{4.54}$$

By comparing this equation with equation 4.48, we see that the ratio between classical noise level and observed vacuum level $\frac{V_{class}}{V_{vac}^{obs}}^2$ is equivalent to term L.

As we see from figure 4.29, dark noise is $15dB$ lower than shot noise level, so $L = (10^(- 15/10))^2 = 0.09\%$.

Another classical noise may come from the coherent control field because it is a bright field. As mentioned, coherent control field has power of $11.5\mu W$. This will bring a shot noise contribution approximately $20dB$ lower than the one from the local oscillator. The equivalent optical losses will be $L = (10^(- 20/10))^2 = 0.01\%$. This is very small and it seems we can further increase coherent control field. However, as we mentioned in the section of BHD, the CMRR for the LO and for the signal is different. Since we can only make sure to have a large CMRR for LO, a smaller CMRR for coherent control field may cause low frequency classical noise to couple in the measurement. Therefore the coherent control field needs to be kept small to compensate the drawback of smaller CMRR for the signal side.

4.2.3 Phase noise

Phase noise comes from both pump phase fluctuation and local oscillator/squeezing phase fluctuation. These fluctuations cause the mixing of the two quadrature [135, 136]. In this experiment, these two sources of phase noise are controlled by two coherent control loops. Even under control, phase noise still exists. These phase fluctuations influence squeezing measurement in two different ways according to the frequency of the fluctuations [137]. When phase fluctuations occur faster than the measurement time, the measured squeezing level decreases. But when they are slower than the measurement time, the measurement long term stability will not be ensured.

Due to the presence of the coherent controls, phase fluctuations can be considered as a normal distribution with average value to be zero. If the root-mean-square (RMS) deviation is small (i.e. $< 100mrad$), the induced squeezing level change can be approximated as [138]

$$V_{\pm} \simeq V_{\pm} \cos^2\theta_{RMS} + V_{\mp} \sin^2\theta_{RMS} \tag{4.55}$$

The sources of phase noise can be originated from two kinds: laser phase locking electronics and unsuppressed noise at frequencies above unity gain of the electronic control loops [84]. They include OPO length noise, coherent control sensor noise, OPO/SHG length control sidebands, crystal temperature fluctuations, local oscillator sidebands.

By using equation 4.55, the degradation caused only by phase noise for different squeezing level can be plotted. As shown in figure 4.31, phase noise degrade squeezing much more than anti-squeezing. Anti-squeezing is basically not changed by phase noise while squeezing can even become anti-squeezing if the phase noise is large enough. In future GW detectors, higher levels of detected squeezing will be required. This will lead to very stringent requirements on phase noise. Such requirements can be achieved in a table top experiment [84]. However, the phase noise in a real interferometer is much larger [86, 87] and was estimated to be at least $15mrad$.

4.2.4 Back scattered noise

Back scattered noise dominates low frequency noise spectrum for balanced homodyne detection. The light coming from local oscillator which is scattered can propagates

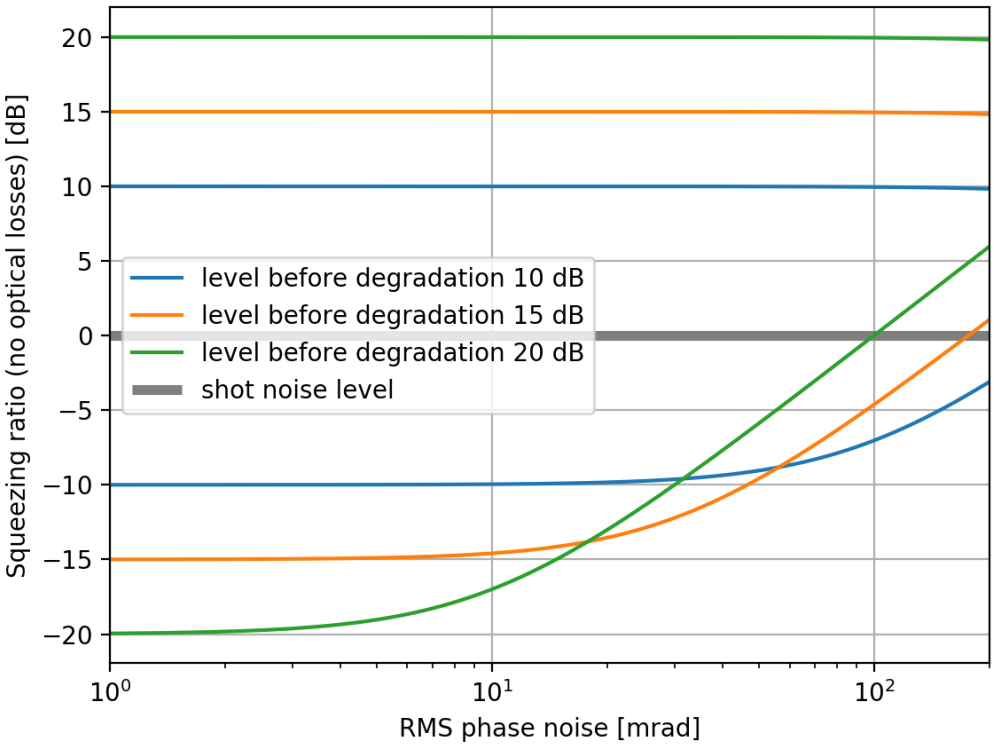

Figure 4.31: Squeezing degradation caused by phase noise for different initial squeezing level. For small value of phase noise, the anti-squeezing is unchanged, while the squeezing is heavily affected, at the level that, for high phase noise, the squeezing becomes anti-squeezing. It is interesting to notice that the larger the initial squeezing level, the larger the impact of the phase noise.

along the inverse direction of the squeezing. As already pointed out [139], the light scattered by a moving surface will interfere with local oscillator and cause back scattered noise.

4.3 Measurement of frequency independent squeezing and its characterization

Once all the previous devices are operated properly, squeezing can be measured. In this section, several squeezing measurement are presented and as well as the characterization of the produced squeezed state in term of losses and phase noise.

4.3.1 Zero span measurement

Even if the phase of the squeezing and BHD angle are not fixed, squeezing can be also characterized. This was the first step of squeezing measurement we performed. The first measurement of frequency independent squeezing was obtained with a zero span measurement at 200kHz. Zero span means the spectrum analyzer only checks around one frequency component of the signal and focus on its time series. The bandwidth of this check is called resolution bandwidth (RBW). RBW was set to be $1kHz$ for that measurement. The video bandwidth (VBW) was set to be $30Hz$. The local oscillator was scanned with a ramp signal of 2Hz. The peak to peak value applied to PZT was 900mV. And the pump power was 30mW. As shown in figure 4.32, around 5dB anti-squeezing and 3dB squeezing was observed.

This first measurement shows the importance of phase noise stabilization since several fluctuation are visible in figure 4.32 which are caused by uncontrolled phase noise.

4.3.2 Measurement of squeezing spectrum

Compared to the zero span measurement, spectrum measurement requires the phase to be stabilized. Before the final measurement of frequency independent squeezing, several upgrade steps were performed:

1. Mode matching improvement for BHD. Between the first measurement of squeezing and recent ones, the mode matching between OPO transmission and IRMC transmission was improved from 95% to 99.5%. Since the detection

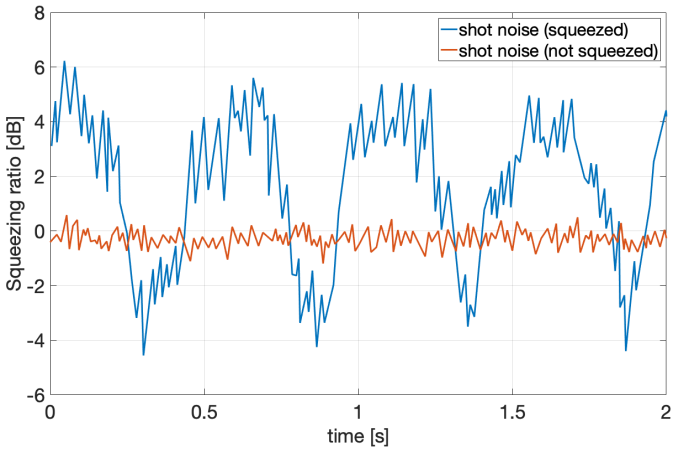

Figure 4.32: Zero span squeezing measurement at 200kHz (RBW = 1kHz, VBW = 30Hz) while homodyne angle is scanned. A flat line is shown in the figure to indicate shot noise level, which represents the vacuum fluctuation entered from singal port of homodyne. After injecting squeezed vacuum into signal port of homodyne, while homodyne is scanned, the squeezed vacuum fluctuation is measured in quadrature plane and shown as an oscillating line. The highest point of this oscillating line indicates anti-squeezing level (5dB) while the lowest point of this line indicates squeezing level (3dB).

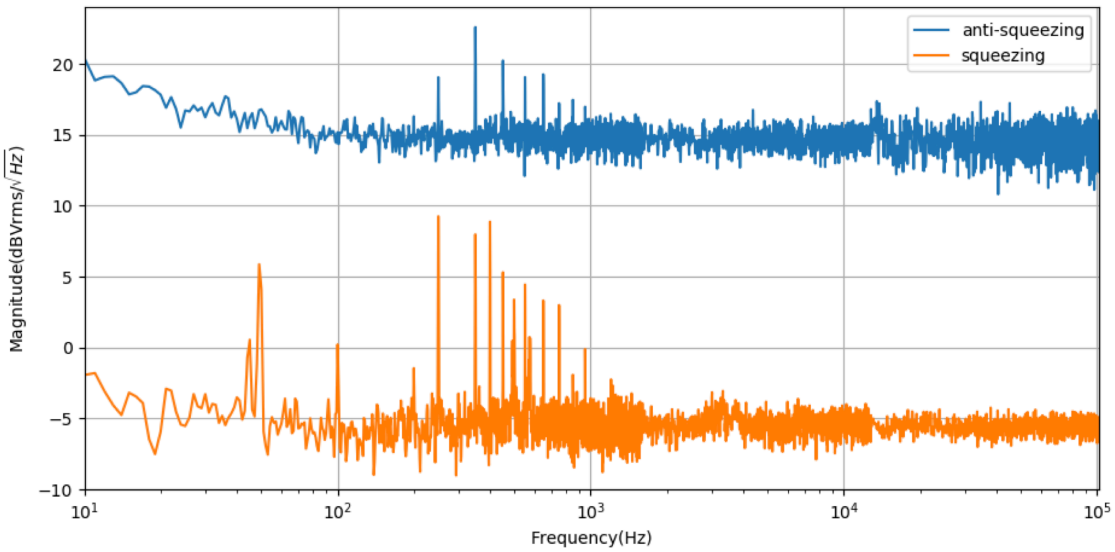

Figure 4.33: Measurement of 6dB squeezing level and 14dB anti-squeezing with a flat spectrum starting from 10Hz. The pump power is 30mW.

efficiency is the square of visibility, this means an improvement of detection efficiency from 90% to 99%.

2. Optical balancing improvement for BHD. During the first measurement, the common mode rejecting ratio was not good. Aligning BHD beam splitter was not easy at the beginning. Although the beam splitter can be easily tuned to make BHD balance, the balance cannot be kept for a long time. Later, we figure out this may relate with the angle dependence of BS. We procured a new BSs and characterized their reflectivity's angle dependence. The result shows the old BS was much more sensitive to angle change with respect to the new ones.

3. Noise eater for coherent control laser. As we discussed in section 4.1.6, the optical balancing requirement sets a limitation for coherent control field power. Therefore we reduced the CC laser power as much as possible. However, we found a very large peak around $300kHz$ in the squeezing spectrum measurement. By investigating the laser source manual, we found this peak may come from laser source amplitude noise. After increasing the CC laser current above 1.2A, this peak disappeared due to the engagement of the laser noise eater.

4. Phase shifter mechanical design improvement. A better mechanical design of the phase shifters allowed for a higher unity gain frequency of the coherent control loops, which was increased from below hundred Hertz to above one kilo Hertz.

5. Installation of additional Faraday isolator. To isolate the OPO from back scattered light, an additional Faraday isolator was installed.

6. Replacement of lenses with super-polished lenses. To reduce optical losses and back scattered light sources.

After all those improvements, the achieved squeezing measurement is shown in figure 4.33. A level of 6dB of squeezing and 14dB of anti-squeezing are measured. The pump power was 30mW, the measured anti-squeezing level is consistent with figure 4.28. Due to the reliability of our system and the mentioned upgrades, the presented result shows a squeezing spectrum that we can easily obtain everyday in the laboratory. This is a remarkable result.

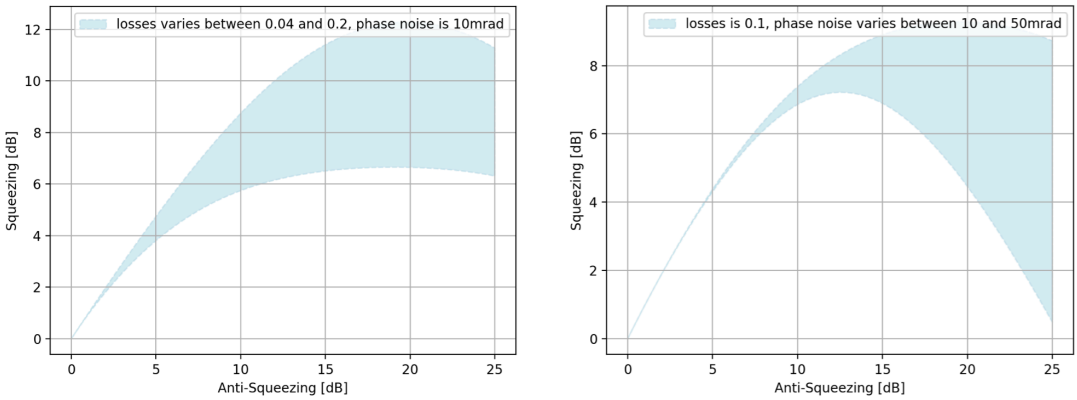

Figure 4.34: Upper: Squeezing and anti-squeezing level for different optical losses. Lower: Squeezing and anti-squeezing level for different phase noise

4.3.3 Squeezing degradation characterization

To understand the whole system and further improve squeezing performance, the estimation of each degradation factor is necessary. The total optical losses and phase noise can be estimated by measuring squeezing and anti-squeezing level for different pump power.

Totally nine measurement of squeezing for different pump power are shown in figure 4.35. The squeezing and anti-squeezing levels shown in the legend of each plot are calculated by comparing level at frequency region higher than 60kHz. As we can see, with the increasing of pump power, more and more structure appear for the squeezing spectrum at low frequency region. This is supposed to be from phase noise and back scattering noise. The maximum squeezing level is achieved with $40mW$ pump power.

By combining equation 4.48 and 4.55, the squeezing degradation formula can be expressed as

$$R_{\pm}^{l,\theta} = (1-l)(R_{\pm}\cos^2\theta + R_{\mp}\sin^2\theta) + l \tag{4.56}$$

where l are the total optical losses, θ is total RMS phase noise. Here we need to note that the sequence of applying optical losses and phase noise is not important. Mathematically, firstly applying phase noise or optical losses are the same. Equation 4.56 for different values of optical losses and phase noise is shown in figure 4.34.

According to the nine measurement shown in figure 4.35, we can obtain the information of squeezing and anti-squeezing levels. Equation 4.56 can be expressed

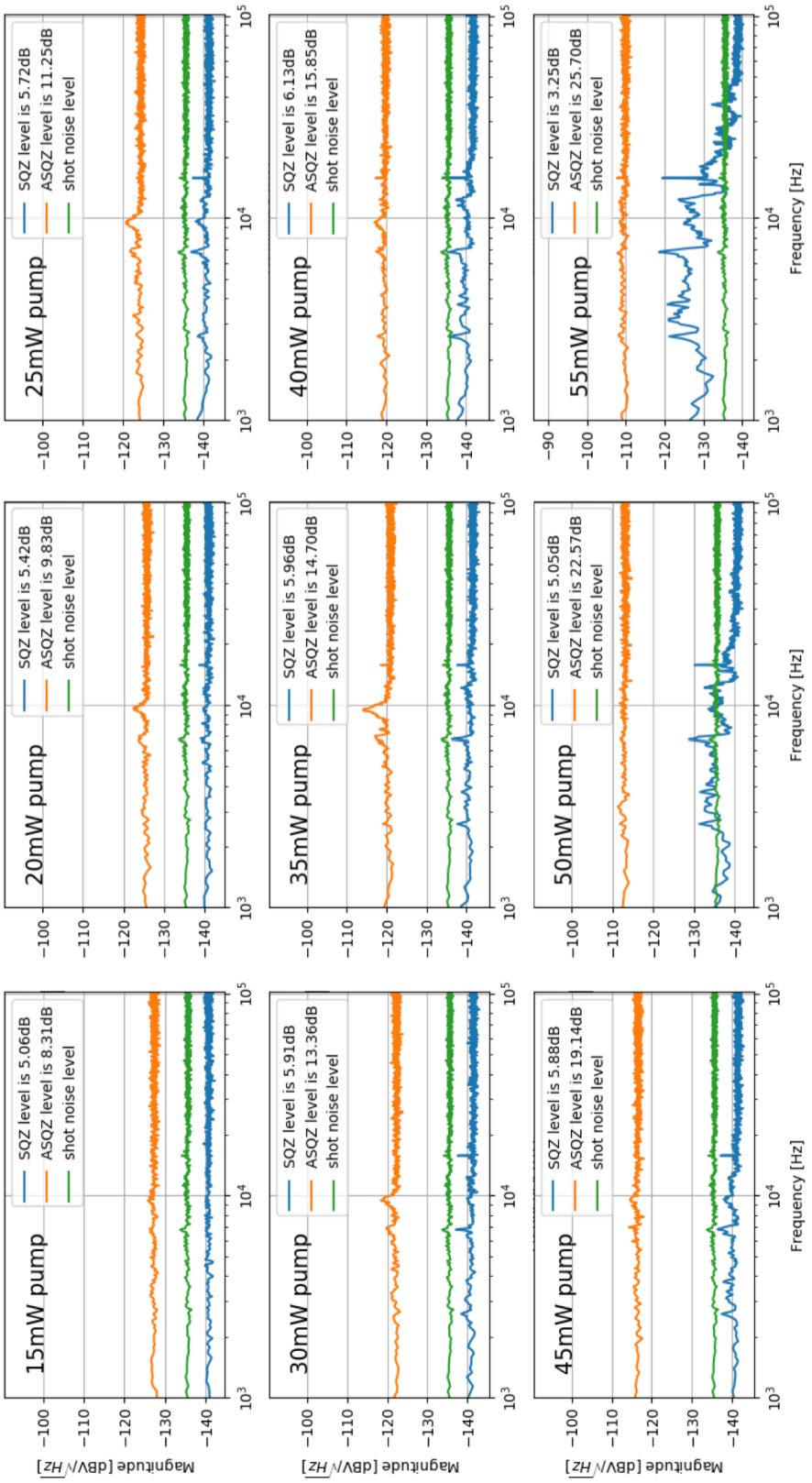

Figure 4.35: Measurement of squeezing and anti-squeezing for different pump power.

as

$$R = \frac{\frac{R_+ - l}{1-l} + \sqrt{(\frac{R_+ - l}{1-l})^2 - 4\cos^2\theta(1-\cos^2\theta)}}{2\cos^2\theta} \tag{4.57}$$

where R is the squeezing ratio without any degradation, R_+ is the measured anti-squeezing level, l are the optical losses and θ is the RMS phase noise. Then the squeezing level can be expressed as

$$R_- = (1-l)\left(\frac{1}{R}\cos^2\theta + R\sin^2\theta\right) + l \tag{4.58}$$

Through the above two equations, we can extract the optical losses and phase noise estimation from the nine measurement of figure 4.35. The result is shown in figure 4.36. From the fit shown in this figure we obtain a total optical losses level of $26\pm3\%$ and a phase noise of $22 \pm 7mrad$.

Comparing the measured optical losses of $26 \pm 3\%$ to the one obtained from separate measurement showing total losses of around 15% (7% from OPO escape efficiency, 5% from optical propagation losses, 2% from BHD detection loss, 1% from PD detection loss), there is discrepancy of about 10%. This discrepancy is considered to come from OPO escape efficiency. Therefore, the OPO escape efficiency should be only around 83%. This is motivated by the measurement of the OPO transmission which is also not compliant with the expectation but can be explained by an excess of losses inside the cavity.

4.3.4 Target reduction of optical losses and phase noise

Our goal is to measure a frequency independent squeezing with level of $9dB$. As shown in figure 4.37, to achieve the goal of 9dB of squeezing, we need to have phase noise of less than $30mrad$ and about 9% of optical losses. Considering the current phase noise of around $20mrad$, the reduction of phase noise is not necessary at the moment. However, the optical losses level must be reduced.

We suspect that additional losses may come from the OPO cavity, therefore a new design will be implemented in the future to tackle this problem and reduce the optical losses.

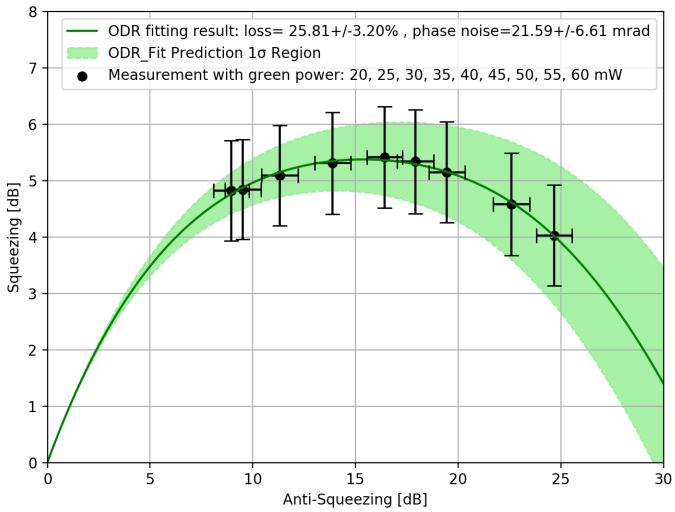

Figure 4.36: Estimation of optical losses and phase noise from squeezing and anti-squeezing measurements. The total optical losses are $26 \pm 3\%$ and the phase noise is $22 \pm 7 mrad$.

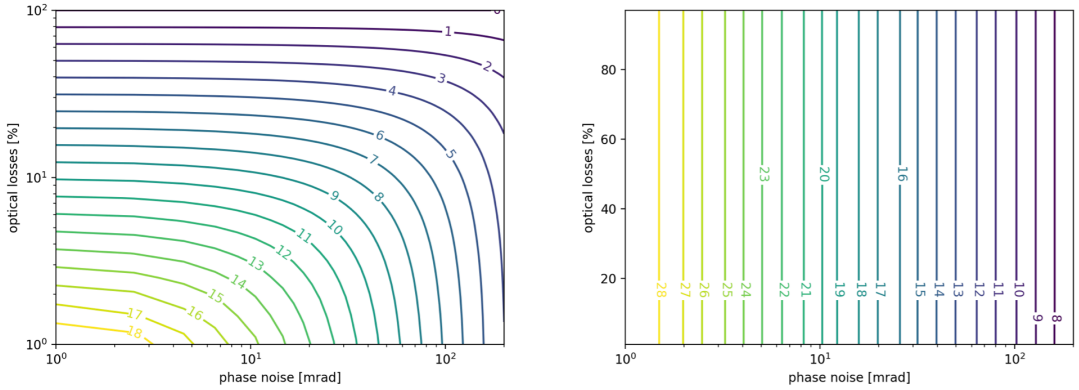

Figure 4.37: Left: The optimal measured squeezing level for different optical losses and phase noise values. Right: The optimal generated squeezing level (before any degradation) for different optical losses and phase noise. This plot shows the optimal generated squeezing level is decided only by phase noise.

4.4 Application of frequency independent squeezing to laser interferometry

Since the first demonstration of squeezing generation, lots of experiments have demonstrated its ability to reduce shot noise. In this section, the steps taken to transit from its first demonstration to the application to GW detectors are reviewed.

4.4.1 Application in small scale experiment

The application of squeezing to a real gravitational wave detector was done step by step. The first application was done in 1987 on Mach-Zehnder [82] and polarization [81] interferometers. After that in 2002, a squeezing enhanced power recycling Michelson interferometer [140] was demonstrated. In 2005, a squeezing enhanced dual-recycling Michelson interferometer [141] was realized. After those demonstration, the squeezing technology was applied to GW interferometer prototypes [142]. In 2010, a squeezing enhanced Sagnac interferometer was realized [143]. Frequency independent squeezing has already been continuously used in GEO600 [85] for around ten years so far. All these efforts made the application of squeezing in gravitational wave detectors successful. Figure 4.38 shows some examples of the squeezing application we mentioned: in the left panel, we can see how signals covered by quantum noise are revealed by the application of squeezing, while on the right side, we can see how squeezing improves the SNR of signals.

4.4.2 Application to the third observation run of LIGO/Virgo

Since last year, frequency independent squeezing was used during the third observation runs of advanced LIGO [86] and advanced Virgo [87]. According to the losses and phase noise information from LIGO/Virgo squeezing paper, the squeezing and anti-squeezing level relation can be derived. All these information and operating points are summarized in figure 4.39.

It's important to notice that especially LIGO could have a significantly higher squeezing level by increasing the parametric gain. However, with the increase of parametric gain, radiation pressure noise will be increased. As reported in [86], unsqueezed radiation pressure noise is not a dominant noise, but in the presence of injected squeezing, it becomes relevant and degrades detector's detection range. As a result, a parametric gain of 2.9 is used in the case of LIGO.

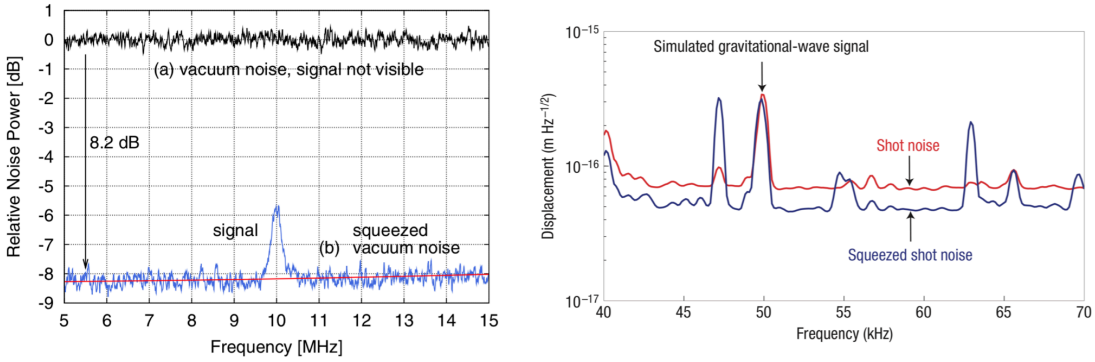

Figure 4.38: Left: Squeezing helps to reveal signals buried in the quantum noise (image from [143]). Right: Squeezing improves the SNR of signals (image from [142]).

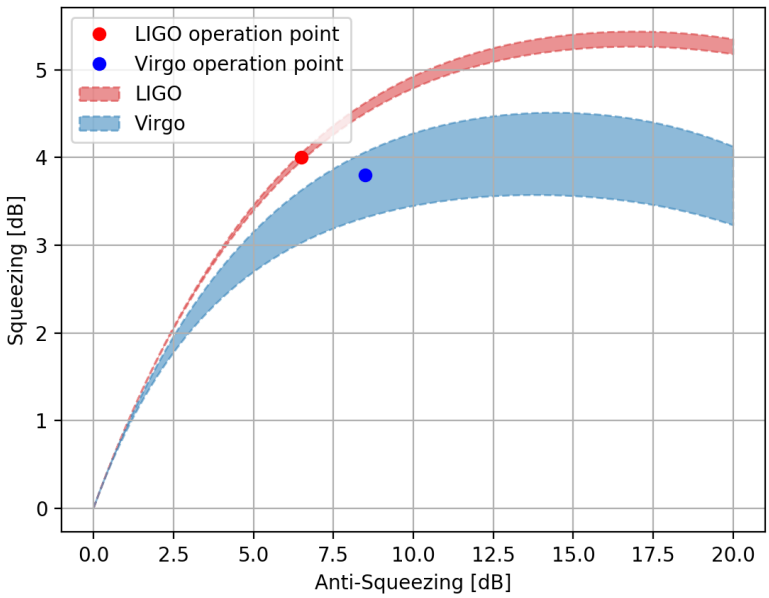

Figure 4.39: Predicted squeezing and anti-squeezing level with the information of LIGO/Virgo optical losses and phase noise. The points are the squeezing/anti-squeezing level reported in the paper during their third observation (O3) run.

A further increase of parametric gain will make radiation pressure noise even more relevant. This made the observation of radiation pressure noise in a large scale experiment possible. The radiation pressure noise was observed [144] by using a parametric gain of 4.4. This indicates that in order to use higher level of squeezing, a mitigation of the radiation pressure noise is mandatory. Fortunately, frequency dependent squeezing can solve this problem and it has been recently demonstrated [2] by our group. This is the main topic of the next chapter.

4.5 Summary of the frequency independent squeezed vacuum source

In this chapter, I introduced the set-up of frequency independent squeezed vacuum source realized in the facility of TAMA300. The achieved measurement of squeezing level is 6dB and it suits well for the detection band of KAGRA. Around the world, there are few labs can realize this type of squeezer.

However, there is still 3dB improvement needs to be done to achieve the goal of 9dB squeezing. To achieve that, I found that the main limitation is the optical losses of this system. Besides, the longest time with stable operation of this squeezer last for around ten hours.

This squeezer is the first realized squeezer suitable for the stable implementation of squeezing technique for KAGRA inside KAGRA collaboration. Therefore, it can be a candidate for improving the sensitivity of KAGRA in the future. Besides, this squeezer is also a crucial component for the final measurement of frequency dependent squeezing, which will be introduced in the next chapter.

Chapter 5

Realization of squeezing rotation around 90Hz by using 300m filter cavity

Frequency dependent squeezing (FDS) with rotation below hundred Hertz are proposed to reduce the quantum noise of gravitational wave detectors broadband. Previously frequency dependent rotation was realized at MHz[101] and kHz[145] region by using a detuned Fabry-Perot cavity (usually called filter cavity).

The generation of FDS below hundred Hertz is more challenging and require the use of a long filter cavity to reduce the effects of squeezing degradation due to cavity losses and thus preserve the squeezing below the rotation frequency. In this experiment, a 300m filter cavity was used to rotate the squeezed vacuum state around 90Hz. Its measurement was also realized and shows to be the best record around the world up to now.

A general introduction of the experimental setup is given in the first section. In the second section, several degradation mechanisms affecting FDS measurement are introduced. After that, a detailed analysis and characterization of each degradation source is given. The requirement on each degradation source is listed in figure 5.8. Finally, the measurement method and results are presented. Besides, there is also discussion about this result and a summary of measured degradation sources which is listed in table 5.3.

5.1 Experimental setup

The whole experimental scheme is shown in figure 5.1. The experiment is composed by an in-air and in-vacuum part. The in-air part provides a 532 nm (green) control beam and 1064 nm (IR) squeezed vacuum beam, which was introduced in the chapter 4. The in-vacuum part is composed by a filter cavity and a telescope to match the in-air beam into it. Four mirrors are suspended in vacuum, corresponding to the four big mirrors in the figure. Their motion is sensed by optical levers, composed by a set of laser diode and position-sensitive detectors (PSD), and controlled by a set of coils and magnet glued on the mirrors. The filter cavity is controlled by locking the main laser frequency on its length. The PDH error signal is taken from the reflected auxiliary green beam extracted using a Faraday isolator. The squeezing is overlapped with the green control beam through a dichroic mirror. The detuning (frequency difference from resonance) of squeezing is set by shifting the laser frequency with an Acousto-optic modulator in the green beam path. The squeezed beam reflected by the filter cavity is extracted through an in-vacuum Faraday isolator. After that, squeezing is sent to a balanced homodyne detector, where frequency dependent squeezing is measured.

5.1.1 Necessity to use a long filter cavity

The use of 100-m scale filter cavities is planned for advanced gravitational wave detectors and even longer (km scale) filter cavities were proposed for next generation gravitational wave detectors [146]. This is due to following reasons:

1. Since the linewidth of the filter cavity is fixed by the detector design, a longer filter cavity requires a lower finesse. This will relax the requirements on the mirror quality, which are usually very strict.

2. A lower finesse will ease the control of the cavity.

3. The effect of detuning fluctuation inducing frequency dependent phase noise is reduced in longer cavities.

4. Long filter cavity can be used as a frequency reference in the future[147].

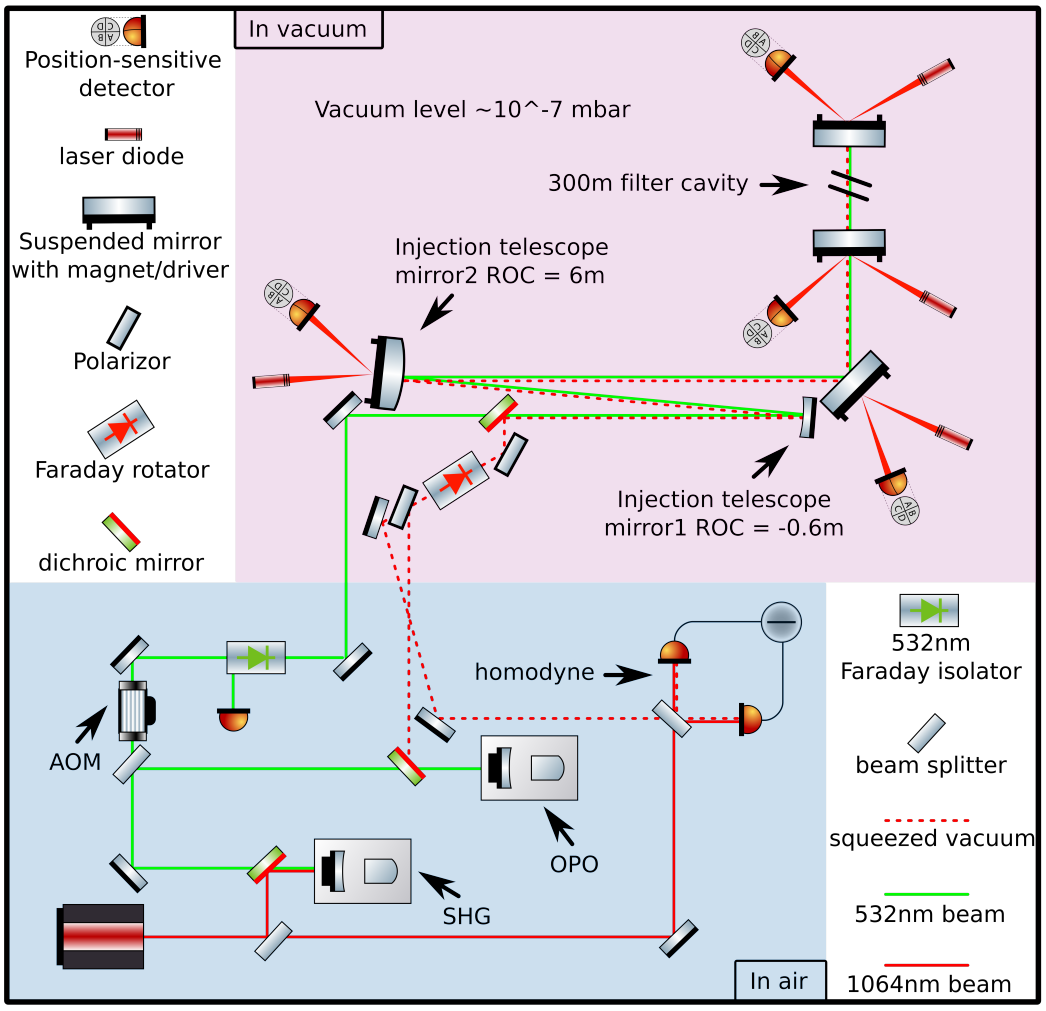

Figure 5.1: The optical scheme for the generation of frequency dependent squeezing. A 532nm/green beam and 1064nm/infrared squeezing is sent from in-air bench to filter cavity. The green beam is used as a control beam for the control of the filter cavity. The reflected squeezing has frequency dependent rotation and is characterized with a balanced homodyne detector.

5.1.2 Optical properties of filter cavity

Two different wavelength beams are sent to filter cavity. The 532nm/green beam is used to control the length of filter cavity/the frequency of main laser. Besides, it will also be used for filter cavity auto-alignment in the future. For 1064nm/infrared squeezing, filter cavity is used to induce a frequency dependent rotation. The two mirrors composing the filter cavity have dichroic coating with different reflectivity for the green and infrared beam.

For the infrared squeezing beam, the main requirement is that the linewidth needs to be below 100 Hertz and the round trip losses have to be small. The linewidth requirement, introduced in chapter 3, decides the frequency at which the rotation takes place. On the other hand, the optical losses limit the achievable squeezing ratio in the low frequency region. On top of that, frequency dependent squeezing is taken from the reflection of filter cavity and its phase needs to be modified. Therefore, an over-coupled configuration is compulsory.

For the green control beam, a larger linewidth is preferred since it will make lock acquisition easier.

Some parameter for the filter cavity are reported below:

1. **Cavity length:** 300m

2. **Input mirror:** Roc is 436.7m, transmissivity (1064nm) is 0.136%, transmissivity (532nm) is 0.7%, optical losses is 40ppm

3. **End mirror:** Roc is 445.1m, transmissivity (1064nm) is 3.9ppm, transmissivity (532nm) is 2.9%, optical losses is 40ppm

According to these information, there are properties of filter cavity calculated from the formula introduced in section 2.3.2. They are listed in table 5.1.

Infrared 1064nm		Green 532nm	
FWHM	116Hz	FWHM	2908Hz
finesse	4313	finesse	172
storage time	2.7ms	storage time	0.1ms
beam waist	16.82mm	beam waist	11.89mm
beam size (input)	20.92mm	beam size (input)	14.79mm
beam size (end)	20.50mm	beam size (end)	14.50mm
FSR		500kHz	
intra-cavity round trip losses		$\sim$ 80ppm	

Table 5.1: Cavity parameters (the parameters related with beam size is diameter)

According to the basic parameters of filter cavity (length and mirror reflectivities) , the cavity power reflectivity/transmissivity/gain can be calculated according to the formulas introduced in section 2.3.1. These are shown in figure 5.2.

To match the squezzed beam into the filter cavity, a mirror based telescope was designed. As shown in figure 5.1, this telescope is composed by two mirrors with radius of curvature of -0.6m and 6m respectively.

5.1.3 Operation of filter cavity

As already said, there are four suspended mirrors in this experiment. According to the hitting sequence of the injection beam, they are named as PR, BS input mirror and end mirror. The name PR and BS has no connection with their function, but they are named like this because they are hosted in the vacuum chamber which were used for former power recycling (PR) and beamsplitter (BS) in TAMA300.

To make filter cavity work for the generation of frequency dependent squeezing, several different systems need to be operated. These systems are introduced in foloowing. In addition, the case of suspended cavity alignment in this experiment is introduced.

Vacuum system

Suspended mirrors need to be operated in vacuum system, otherwise the acoustic noise and air current will bring noise.

Vacuum chambers and vacuum system originally belonging to TAMA300 were used in this experiment. The vacuum level is kept around 10^{-7} mbar during the operation.

Mirror suspension system

The filter cavity suspension system is the same with KAGRA type C suspension system. It is a double pendulum placed on a vibration-isolation 3-stage stacks [148]. A detail introduction of the suspension system can be found in the thesis of E.Capocasa [44].

As introduced in chapter 2, mirror suspension system helps to filter the mirror motion above the resonant frequency of suspension system. This mirror motion can be detected by an optical lever system. As shown in figure 5.1, each suspended mirror in this experiment is equipped with this optical lever, which is composed by a laser diode and a position-sensitive detector (PSD). Therefore, the mirror motion changes

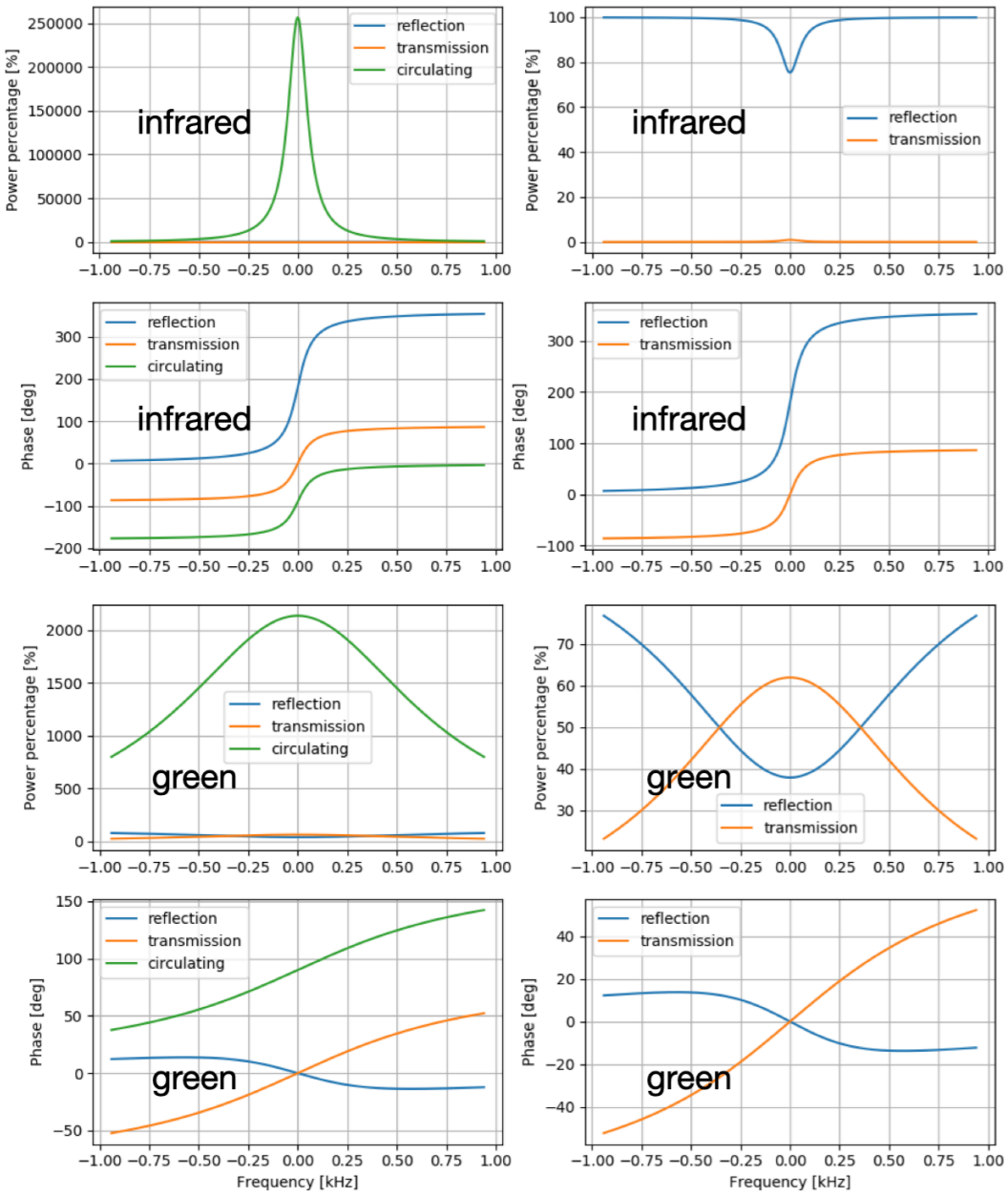

Figure 5.2: **Left:** The comparison of infrared/green cavity power reflectivity/transmissivity/gain when frequency is scanned from -1kHz to 1kHz. **Right:** To see clearly transmission/reflection case, the circulating case is removed and shown on the right side.

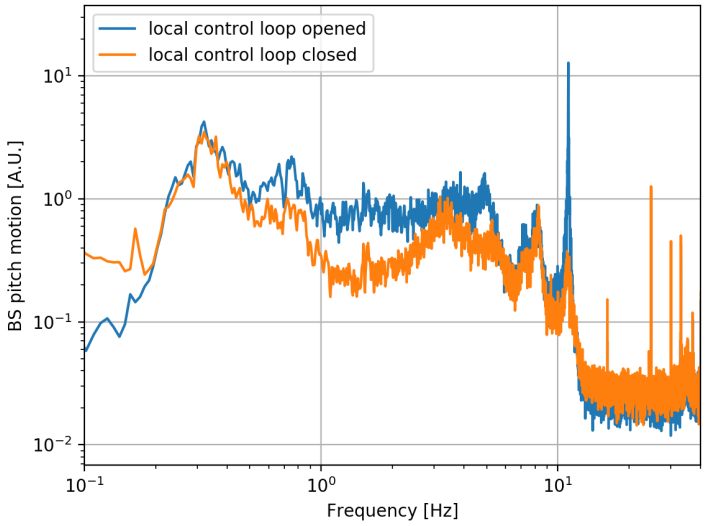

Figure 5.3: BS pitch motion with local control loop open/closed, measured with an optical lever.

the reflected light direction which is detected by the PSD. This signal can be feedback to the coil driver which applies a force on the magnets fixed on mirrors. In this way, the mirror motion caused by suspension system resonance can be counteracted. This control loop is usually called mirror local control. An example of motion reduction obtain with this local control is given in figure 5.3.

In the experiment, a camera is set in the transmission of filter cavity and is used to monitor the cavity transmission light. Without mirror local control loop closed, an obvious beam pointing jitter is usually observed. After the loop is closed, the reduction of beam pointing jitter is observed. This is in agreement with the reduction of mirror motion.

Error signals are acquired and digitally filtered using a digital control system (DGS) of the same kind used in KAGRA.

Filter cavity alignment

In suspension system, the position of suspended mirror changes according to the temperature change, earthquake or tidal effect. These effects can be found in figure 5.4. In this figure, by neglecting the mirror sudden motion, it is quite obvious that BS follows the trend of temperature change. At the same time, input mirror and PR follow the anti-trend of temperature change. Therefore, alignment needs to be done to operate the filter cavity.

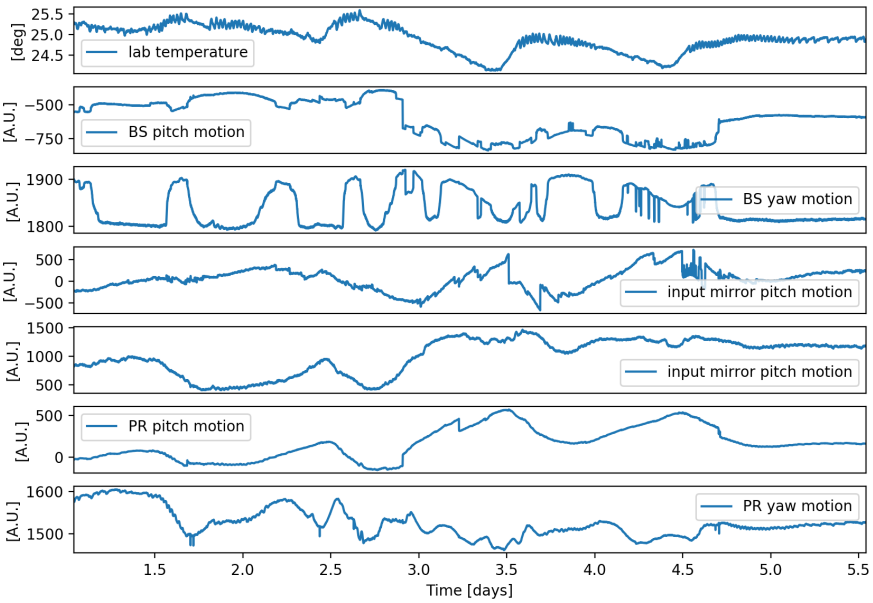

Figure 5.4: A monitor of mirror long time drift together with temperature change. Without considering mirror position sudden change, BS follows the same trend of temperature change and PR/input mirror follow the anti-trend of temperature change.

The quality of cavity alignment can be easily checked after the cavity lock. As introduced in chapter 2, a better alignment makes more power coupled into fundamental mode. Therefore, the best alignment condition corresponds to the highest filter cavity transmission.

Filter cavity and main laser locking system

In order to produce FDS filter cavity need to be stably locked. As introduced in chapter 2, this lock can be obtain either acting on the cavity length or laser frequency. Usually laser frequency is more stable at low frequency and mirror suspension is more stable at high frequency, which was proven to be the same for filter cavity in this experiment[44]. PDH error signal is fedback to the laser frequency which thus follows the cavity length. We also have the possibility to off-load the correction sent to the laser by feeding back the low frequency part of the error signal to the end mirror of the filter cavity . This locking scheme is shown in figure 5.5. The locking servo is similar to the ones designed for on-bench cavities. It has auto-locking functions and can be controlled remotely.

Having five integrators, the gain is quite large at low frequency. As shown in figure, control loop hasa unity gain frequency located at around 14kHz. A higher unity gain frequency compared with on-bench cavities is due to the fact that main resonant peak of laser PZT is higher. As characterized in chapter 4, laser PZT resonance starts to appear around 100kHz.

Filter cavity detuning system

As mentioned in chapter 3, the frequency dependent rotation required filter cavity to be detuned from resonance. Therefore, a detuning set-up system is required.

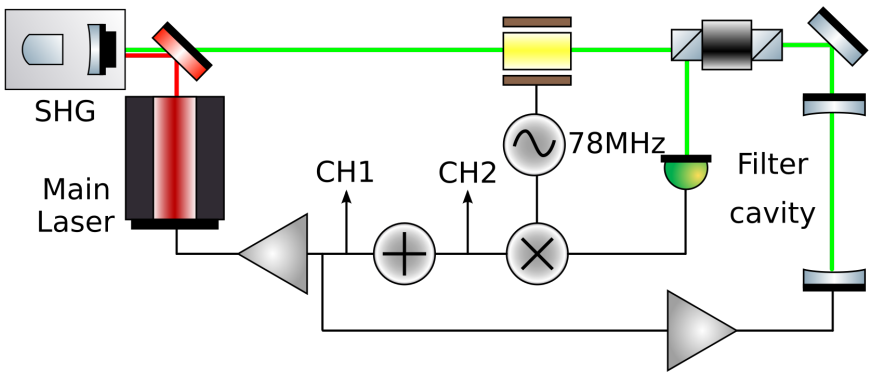

Figure 5.5: Filter cavity frequency lock scheme.

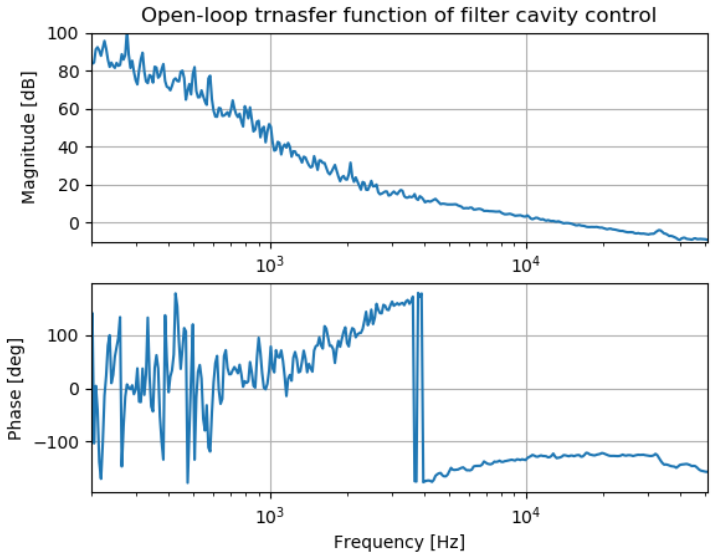

Figure 5.6: Open loop transfer function for filter cavity frequency lock. The unity gain frequency is 14kHz and phase margin is 52°.

As shown in figure 5.1, there is a beam splitter, which splits green beam to OPO and filter cavity. An acousto-optic modulator (AOM) is put after this beam splitter and along the beam path towards filter cavity. It is used to set detuning frequency of squeezing relative to resonance frequency.

RF signal is sent to AOM to drive PZT, so sound wave is generated inside AOM. The sound wave works as an optical grating, therefore the laser goes through it will be diffracted. In this experiment, the first order diffraction used. Therefore, the frequency and amplitude of laser can be changed by changing the applied RF signal to AOM. Since green laser is locked to the filter cavity, the frequency change caused by AOM is compensated by the frequency change of main laser. Therefore, the frequency change also happens in SHG. The frequency changed squeezing is generated accordingly. In this way, the detuning frequency can be set.

5.2 Degradation of frequency dependent squeezing for gravitational wave detector with the use of filter cavity

In chapter 3 we shown how vacuum fluctuation is coupled into the interferometer, generating quantum noise. It was also discussed that frequency dependent squeezing

(FDS) can make broadband reduction for quantum noise. However, this reduction is calculated with an ideal FDS, which is non-degraded and whose rotation angle optimized.

In the real case of FDS realized by filter cavity, there are several degradation sources which can influence the final quantum noise reduction performance. The theoretical description of these degradation sources was done by Kwee et. al. [96]. Based on his work and on the related code written by E. Capocasa [149], the achievable quantum noise reduction in a realistic case is presented. This is done by analyzing the contribution of each degradation source to the final achievable FDS level. The scheme for this theory is shown in figure 5.7.

Note that the quantum noise calculation introduced in this section is normalized to shot noise. Therefore, the result can be directly applied to quantum noise of different detectors.

5.2.1 Interferometer quantum noise calculation with filter cavity and squeezer

In this theory, vacuum is described by an identity matrix v. Each optical element or system is described by a 2×2 transfer matrix T. The output is described by a vector b_ζ, which depends on homodyne angle ζ.

The final quantum noise level is composed by the combination of three vacuum fluctuation fields. As shown in the scheme 5.7, vacuum 1 is the vacuum fluctuation which pass through squeezer and finally arrives at photo detector. During the propagation of vacuum 1, vacuum 2 and vacuum 3 couples in due to optical losses. Vacuum 2 and vacuum 3 degrade the squeezing level. The goal is to reduce the coupling of them to a low enough value. These vacuum fluctuations have different contribution for the final quantum noise level, and it can be expressed as

$$N(\zeta, \Delta_{\omega_{fc}}) = |b_\zeta \cdot T_1(\Delta_{\omega_{fc}}) \cdot v_1|^2 + |b_\zeta \cdot T_2(\Delta_{\omega_{fc}}) \cdot v_2|^2 + |b_\zeta \cdot T_3 \cdot v_3|^2 \tag{5.1}$$

In addition to vacuum 2 and 3, the phase noise follows Gaussian-distribution with average to be zero, which will further degrade squeezing level and make quantum noise to be

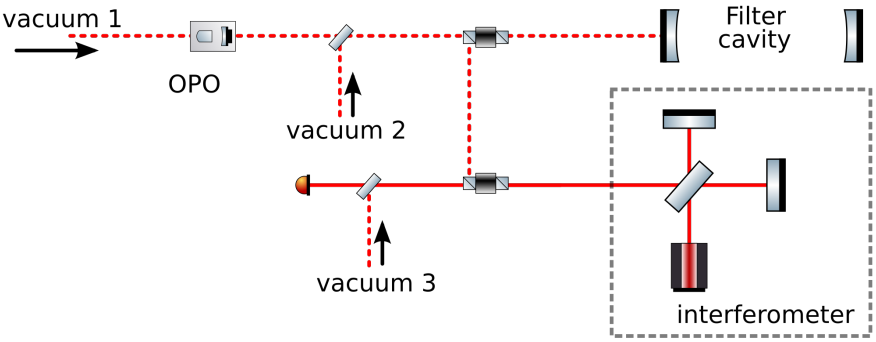

Figure 5.7: A simplified scheme for frequency dependent squeezing enhanced gravitational wave detector. Vacuum 1 is squeezed, rotated by filter cavity, entering GWs detector and in the end detected by photo detector. However, with the propagation of Vacuum 1, there are some degradation. They are represented by the coupling of vacuum 2 and 3. The coupling is shown in a beam splitter model, but they are more complicated. The details are introduced in this section.

$$N_{tot} \simeq \frac{N(\zeta_{RMS},0)+N(-\zeta_{RMS},0)}{2}+\frac{N(0,\Delta_{\omega_{fc}RMS})+N(0,-\Delta_{\omega_{fc}RMS})}{2}-N(0,0) \tag{5.2}$$

Here, vector b_ζ (homodyne angle) takes form

$$b_\zeta = \begin{pmatrix}\cos\zeta\\ \sin\zeta\end{pmatrix} \tag{5.3}$$

and vacuum v takes form

$$v = \begin{pmatrix}1 & 0\\ 0 & 1\end{pmatrix} \tag{5.4}$$

There are three transfer matrix T in equation 5.1, they are defined as

$$T_1(\Delta_{\omega_{fc}}) = \tau_{ro}T_{ifo}(t_{00}T_{fc}(\Delta_{\omega_{fc}})+T_{mm})T_{inj} \tag{5.5}$$

$$T_2(\Delta_{\omega_{fc}}) = \tau_{ro}T_{ifo}\sqrt{1-\frac{(|\tau_2(+\Omega)|^2+|\tau_2(-\Omega)|^2)}{2}} \tag{5.6}$$

$$T_3 = \sqrt{1-\tau_{ro}^2} \tag{5.7}$$

They represent the modification of each vacuum field until the photodetector.

Details are introduced in the next section. Here τ_2 is defined as

$$\tau_2(\Omega) = (t_{00} r_{fc}(\Omega(\Delta_{\omega_{fc}})) + t_{mm})\tau_{inj} \tag{5.8}$$

5.2.2 Transformation matrix for different optical component

T_1 contains all the optical transformation that vacuum 1 experienced. It includes transformation of squeezer (OPO), injection optical losses, filter cavity, interferometer, readout losses and mode matching. The transformation due to squeezer and injection optical losses is described by T_{inj} as

$$T_{inj} = \tau_{inj} S(\sigma_{sqz}, \phi_{sqz}) \tag{5.9}$$

the definition of τ_{inj} is $\tau_{inj} = \sqrt{1 - L_{inj}}$. Here, L_{inj} is injection optical losses. $S(\sigma_{sqz}, \phi_{sqz})$ is squeezer operator defined in equation 3.17, remind that $e^{\sigma_{sqz}}$ is the squeezing ratio and ϕ is the squeezing angle. The squeezing ratio is usually expressed in dB, with $R_{dB} = \sigma \times 20 \log_{10} e$. Note that T_{inj} doesn't have any frequency dependence.

After the transformation of T_{inj}, vacuum 1 arrives at filter cavity. If there is a mismatching, the part matched to filter cavity t_{00} will experience frequency dependent rotation T_{fc}, the mode-mismatched part experiences transformation T_{mm}. The mode matching parameters are expressed as

$$t_{00} = a_0 b_0^* \tag{5.10}$$

$$t_{mm} = c_0 - t_{00} \tag{5.11}$$

$$T_{mm} = |t_{mm}| \mathbf{R}(\arg(t_{mm})) \tag{5.12}$$

Here a_0 is mode-matching between squeezing and filter cavity, b_0 is mode-matching between local oscillator and filter cavity, c_0 is mode-matching between squeezing and local oscillator. $\mathbf{R}$ is rotation matrix which is part of squeeze operator, and defined as

$$\mathbf{R} = \begin{pmatrix} \cos\phi & -\sin\phi \\ \sin\phi & \cos\phi \end{pmatrix} \tag{5.13}$$

The frequency dependent rotation matrix T_{fc} is defined as

$$T_{fc} = e^{i\alpha_m} \mathbf{R}_{\alpha_p} (\rho_p I - i\rho_m \mathbf{R}_{\pi/2}) \tag{5.14}$$

the definition of α_m, α_p, ρ_m and ρ_p are

$$\alpha_m = \frac{\alpha_{fc}(\Omega) - \alpha_{fc}(-\Omega)}{2} \tag{5.15}$$

$$\alpha_p = \frac{\alpha_{fc}(\Omega) + \alpha_{fc}(-\Omega)}{2} \tag{5.16}$$

$$\rho_m = \frac{\rho_{fc}(\Omega) - \rho_{fc}(-\Omega)}{2} \tag{5.17}$$

$$\rho_p = \frac{\rho_{fc}(\Omega) + \rho_{fc}(-\Omega)}{2} \tag{5.18}$$

Here, the ρ_{fc} is the modulus of filter cavity reflectivity, so $\rho_{fc} = |r_{fc}(\Omega)|$. α_{fc} is the phase of filter cavity reflectivity, so $\alpha_{fc} = \arg(r_f c(\Omega))$. The reflectivity of filter cavity is defined as equation 2.12, but the phase term of this equation needs to be replaced as

$$\Phi(\Omega) = (\Omega - \Delta\omega_{fc})\frac{2L_{fc}}{c} \tag{5.19}$$

Here Ω is the sideband frequency, $\Delta\omega_{fc}$ is the detuning of filter cavity, L_{fc} is the length of filter cavity.

Then the squeezed vacuum 1 gets frequency dependent rotation and is sent to interferometer. The interferometer transfer matrix T_{ifo} is introduced in chapter 3 and can be expressed as

$$T_{ifo} = \begin{pmatrix} 1 & 0 \\ -K & 1 \end{pmatrix} \tag{5.20}$$

Here K indicates how the amplitude quadrature vacuum fluctuation is converted by interferometer to the phase quadrature vacuum fluctuation. And it is defined as

$$K = (\frac{\Omega_{SQL}}{\Omega})^2 \frac{\gamma_{ifo}^2}{\Omega^2 + \gamma_{ifo}^2} \tag{5.21}$$

Here γ_{ifo} is the interferometer signal linewidth, Ω_{SQL} is the frequency where shot noise equals to radiation pressure noise. For a broadband signal extraction configuration DRFPMI, they can be expressed as

$$\gamma_{ifo} \simeq \frac{T_{arm}c}{4L_{arm}} \times \frac{1 + r_{sr}}{1 - r_{sr}} \tag{5.22}$$

$$\Omega_{SQL} \simeq \frac{8}{c}\sqrt{\frac{P_{arm}\omega_0}{mT_{arm}}} \times \frac{t_{sr}}{1 + r_{sr}} \tag{5.23}$$

Here T_{arm} is the arm cavity transmissivity, L_{arm} is arm cavity length, P_{arm} is the arm cavity circulating power, ω_0 is the optical carrier frequency, m is the mass of

test mass, r_{sr} is the amplitude reflectivity of signal extraction mirror and t_{sr} is the amplitude transmissivity of signal extraction mirror.

Finally, vacuum 1 experiences readout losses. The definition of readout transformation is τ_{ro} is $\tau_{ro} = \sqrt{1 - L_{ro}}$. Here L_{ro} is the readout optical losses.

For vacuum 2 and vacuum 3, they experience different transformation processes, describes by combination of transfer matrices introduced above.

According to the model introduced in this section, an estimation for the expected frequency dependent squeezing realized by a 300m filter cavity was done by E.Capocasa [149]. The filter cavity losses estimation depends on the quality of the mirrors (which is the same of the initial Virgo test masses). The result is shown in figure 5.8.

5.3 Frequency dependent squeezing degradation sources characterization

As described in the previous section, the main squeezing degradation sources affecting our system are: **mode mismatch, non-optimal locking accuracy, optical propagation losses, phase noise, filter cavity round trip losses.** Besides, there are other technical issues as the instability of the **detuning** and the **backscattering**, which are also discussed in this section.

5.3.1 Mode mismatch

In order to characterize the mode mismatch, a bright alignment beam (BAB) was sent from squeezer to filter cavity. Then two matching were characterized as following:

1. **Mode-mismatch between squeezer and filter cavity:** By changing the detuning frequency, higher order modes can be resonant. By taking the ratio of higher order modes and fundamental mode, the mode mismatch was evaluated.

2. **Mode-mismatch between filter cavity and Homodyne local oscillator (LO):** The BAB reflected from filter cavity and sent to alignment mode cleaner (AMC) was used for this characterization. As introduced in chapter 4, an AMC was used to characterize the overlap between LO and squeezing. Since LO is matched very well into AMC, the mismatched power between BAB to AMC

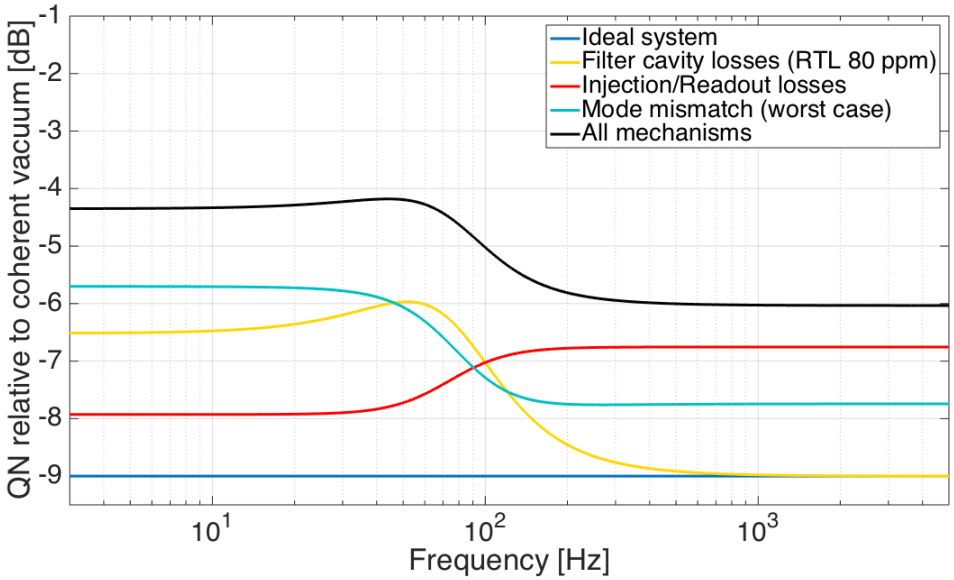

Figure 5.8: Expected frequency dependent squeezing level and degradation from our project. The degradation sources requirement is listed as following: filter cavity round trip losses are 80ppm, propagation losses are 0.1, mode mismatch between squeezer and filter cavity is 0.02, mode mismatch between squeezer and local oscillator is 0.05, filter cavity locking accuracy is 0.3pm. The degradation comes from individual degradation source is presented as color lines. The total degradation from 9dB squeezing to the final measured frequency dependent squeezing is shown as the dark line. According to these degradation sources, 4dB squeezing is expected below and around the rotation frequency while 6dB squeezing is expected above rotation frequency. [149]

will be the total mode mismatch. This mode mismatch was evaluated to be around 2 percent.

The mode mismatch between squeezer and filter cavity is more complicated to characterize in practice and a detailed explanation is given as following.

As already explained we can use AOM to change the auxiliary beam frequency and scan the cavity, which will also induce a change in the main laser frequency when the cavity is locked. Note that since AOM is set along green laser the frequency change is actually two times the frequency change of main laser. For example if we want to scan a whole FSR (which is 500 kHz) with the IR beam we need to change the AOM driving frequency of 1 MHz.

For an effective search of higher order modes it is convenient to know before what is their expected resonance frequency.

According to the equation 2.46 introduced in chapter 2, the mode spacing for fundamental and higher order modes can be written as

$$P(L) = \Sigma_i \frac{p_i}{1 + (2\mathcal{F}/\pi)^2 \sin^2(-2\pi L/\lambda + i\phi_G)} \tag{5.24}$$

power percentage P change with cavity length L, i is the order of modes and starts from zero, p_i is the power percentage for order-i mode which depends on the cavity misalignment/mismatching, $\mathcal{F}$ is cavity finesse, λ is laser wavelength, ϕ_G is Gouy phase defined in equation 2.46. According to this equation we see that consecutive modes have a frequency separation of about 200kHz. This has been experimentally confirmed.

In our the experiment, only first and second higher order modes can be observed. By taking the ratio of higher order modes and total power, we estimate about 6% of mismatch

Mode mismatch includes beam/cavity axes mismatch (also called misalignment) and beam/cavity waist mismatch.

In our case the misalignment is due to the residual fluctuation of mirror position. The power transferred on HOM, L_{mm}, can be related to the RMS of the beam axis shift and tilt as follows:

$$L_{mm} = (\frac{\theta_{RMS}}{\theta_0})^2 + (\frac{x_{RMS}}{\omega_0})^2 \tag{5.25}$$

Here θ_{RMS} and x_{RMS} is the RMS value of cavity axis angular and displacement fluctuation. θ_0 is the divergence of gaussian beam, which is defined as $\theta_0 = \frac{\lambda}{\pi\omega_0}$. ω_0

is the beam waist.

The value of θ_{RMS} and x_{RMS} can be derived from cavity mirrors angular fluctuation and cavity geometry. The angular fluctuation of cavity axis can be written as [41]

$$\theta_{RMS} = \frac{(1-g_2)\theta_1 - (1-g_1)\theta_2}{1-g_1 g_2} \tag{5.26}$$

where g_1 and g_2 are defined in 2.46. The fluctuation of cavity axis displacement can be written as $-z\theta_{RMS}$, here z is the distance between cavity mirror and cavity waist (which is different for each mirror if the waist is not in the center of the cavity) [98]. The mode mismatch caused by mirror angular fluctuation is simulated with FINESSE [150]. The power coupled to higher order modes caused by mirror angular fluctuation is shown in figure 5.9. The finesse code for this simulation can be found in appendix C.

As introduced in the last section, the angular motion of suspended mirrors is reduced with local controls, but even in this case, the angular motion can reach about $6\mu rad$. This angular fluctuation origins a misalignment which is around 6%.

5.3.2 Locking accuracy measurement

As already mentioned, the cavity lock is done by using the green auxiliary beam. The infrared beam is overlapped on the green one and the lock condition is decided with the AOM. Due to the dichroic coating of the mirrors, the beam experiences different cavity poles and in general, their lock accuracy will be different.

As shown in figure 5.10, the high frequency locking performance is quite similar for green and infrared beam while at low frequency they are different. This is also due to the fact that the measurement of the green lock accuracy is an in-loop measurement, while the IR one is an out-of-loop measurement.

Locking accuracy is measured taking the calibrated PDH error signal used for the lock. IR lock accuracy is measured by injecting a Bright alignment beam, which is a pick off of the main laser and is modulated at 15.2MHz. The PDH signal used to estimate the lock accuracy is obtained by demodulating the reflected IR beam.

5.3.3 Stability of the detuning

Detuning determines the frequency at which the rotation takes place. The stability of the detuning is crucial to obtain an optimal quantum noise reduction when the squeezing is injected into the interferometer.

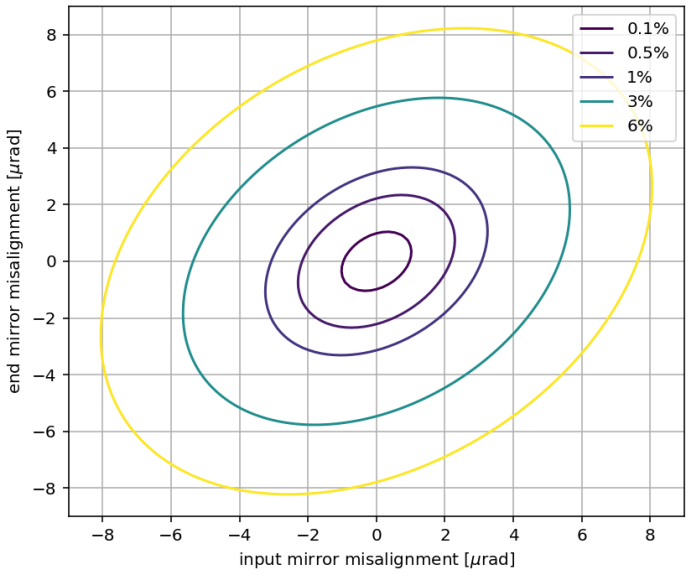

Figure 5.9: Power coupled to higher order modes due to mirror angular fluctuation

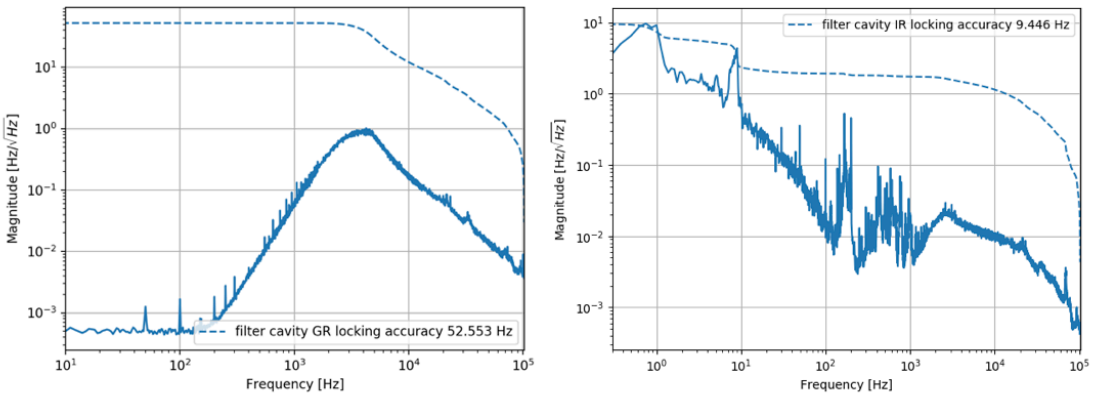

Figure 5.10: **Left:** locking accuracy measurement for green laser. **Right:** locking accuracy measurement for green beam

As introduced, this detuning is set by an AOM. The non-optimal overlap between green control beam and infrared squeezing beam can induce a drift in the detuning.

In order to asses the stability of the detuning we monitored the PDH signal from the BAB as shown in figure 5.11.

From figure 5.11, we can see that alignment condition influences the detuning. Even when filter cavity is kept locked, the detuning has a drifts. This is possibly due to the fact that auto-alignment is done using the green beam. This is a very important issue, which needs to be further investigated.

5.3.4 Filter cavity round trip losses

As we can see from the estimation of expected frequency dependent squeezing in figure 5.8, filter cavity round trip losses is one of the main limitation for the expected squeezing level. Therefore, its characterization is important for evaluate its contribution to the squeezing degradation.

The estimation in work [149] is based on the derivation of round trip losses from mirror map. Therefore, a measurement after the implementation of these mirrors is necessary to confirm these losses.

Cavity round trip losses can be derived from the measurement of cavity reflectivity. This work has been published in [1] and is summarised in this section. We remark that losses can be also extracted from the finesse and the decay time of he cavity but the precision of these measurements is limited by the uncertainty on the input mirror transmissivity while the technique used here has a weak dependence on this quantity.

The reflectivity from a cavity is the square of equation 2.12. When the cavity is on resonance, it can be expressed as

$$R = (\frac{r_1 - r_2}{1 - r_1 r_2})^2 \tag{5.27}$$

here r_1 and r_2 are mirror amplitude reflective coefficient for input and end mirror. Remind the definition of optical losses in equation 2.28, r_2 can be expressed as $\sqrt{1 - T_2 - L_2}$. Here L_2, T_2 is end mirror optical losses and transmissivity.

Optical losses can be considered numerically equivalent to an increase in the end mirror transmissivity (which in this case is below 5 ppm). Therefore, the cavity round trip losses can be expressed as

$$L_{cav} = 1 - R_2 \tag{5.28}$$

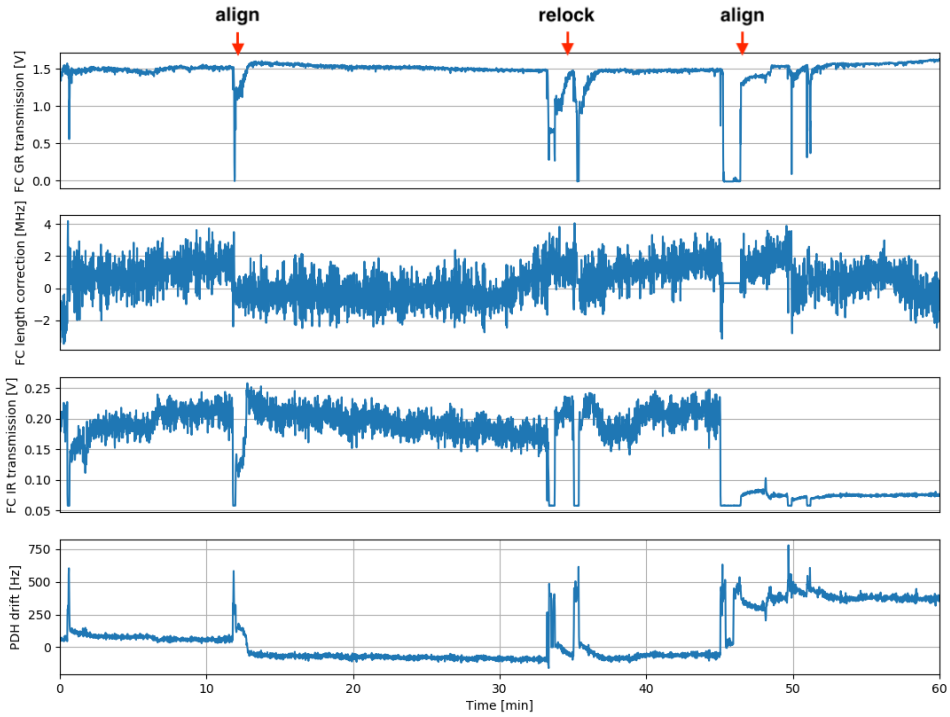

Figure 5.11: The first figure shows filter cavity green transmission, which is basically stable. The second figure shows filter cavity correction signal, which is also stable during each locked period. The third is filter cavity infrared transmission, which is barely stable. The forth figure is filter cavity infrared detuning.

here R_2 is the end mirror reflectivity. By taking equation 5.28 into equation 5.27, cavity reflectivity can be expressed as

$$R = \left(\frac{r_1 - \sqrt{1-L}}{1 - r_1\sqrt{1-L}} \right)^2 \tag{5.29}$$

by solving this equation, optical losses can be expressed as

$$L = 1 - \left(\frac{\sqrt{R} + r_1}{\sqrt{R} r_1 + 1} \right)^2 \tag{5.30}$$

or it can be approximated as

$$L \simeq \frac{T_1}{2} \frac{1-R}{1+R} \tag{5.31}$$

In either equation 5.30 or 5.31, to know optical losses, the information of input mirror reflectivity/transmissivity and cavity reflectivity are required.

The cavity reflectivity can be measured when filter cavity is set on/off resonance. As shown in figure 5.12, the ratio of upper (around 0.3) and lower (around 0.25) level is cavity reflectivity.

The input mirror reflectivity/transmissivity is provided by the manufacturer within an error of one percent. As we see from equation 5.31, optical losses is linearly proportional to input mirror transmissivity T_1. So the optical losses measurement error induced by input mirror transmissivity is within one percent as well, which is small enough.

Besides, non-perfect mode matching and sidebands influence cavity reflectivity, which was considered in the calculation and extensively discussed in [1].

The measurement of the cavity reflectivity was performed many times with different alignment condition. The optical losses is calculated for each measurement and shown in figure 5.13.

As discussed in the paper [1] the difference for each measurement result is considered to be due to slightly different surface quality seen by the beam when hitting the mirror in different points due to different alignment conditions

New measurement of cavity reflectivity

The filter cavity round trip losses reported in the last section was characterized at the beginning of 2018. There were some new measurement done at the beginning of 2020. The measurement result is shown in table 5.2. These measurements give an estimation of filter cavity round trip losses as $123(\pm 20)ppm$. Compared with

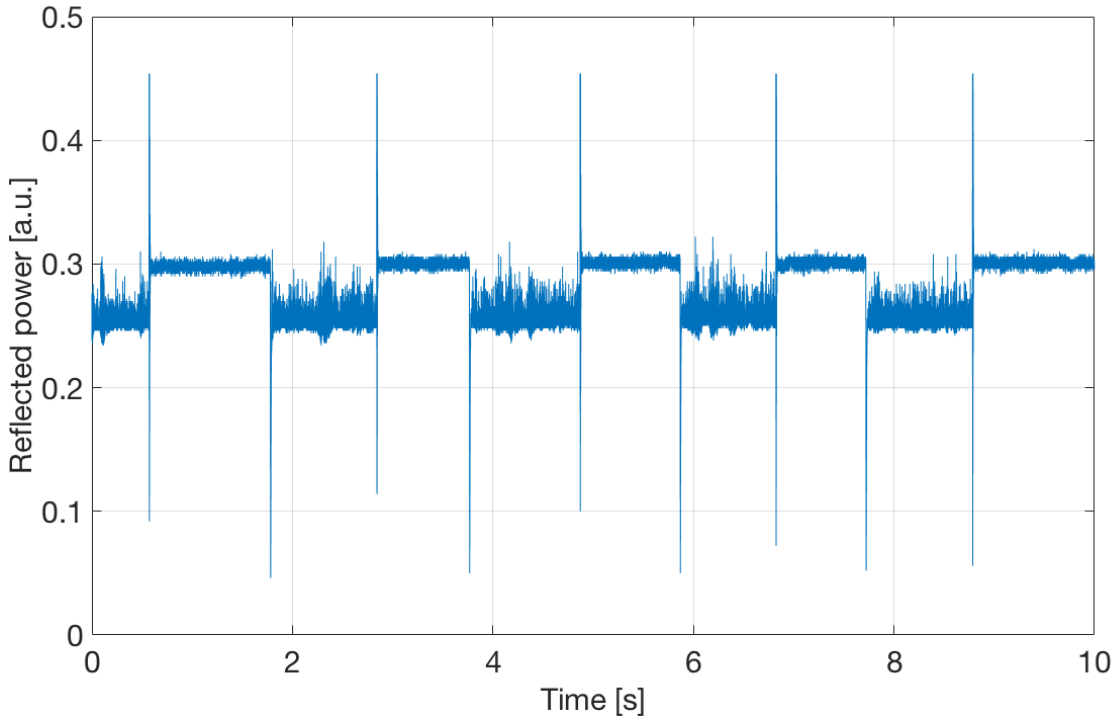

Figure 5.12: Filter cavity reflected power measurement when filter cavity is repeatedly set on/off resonance

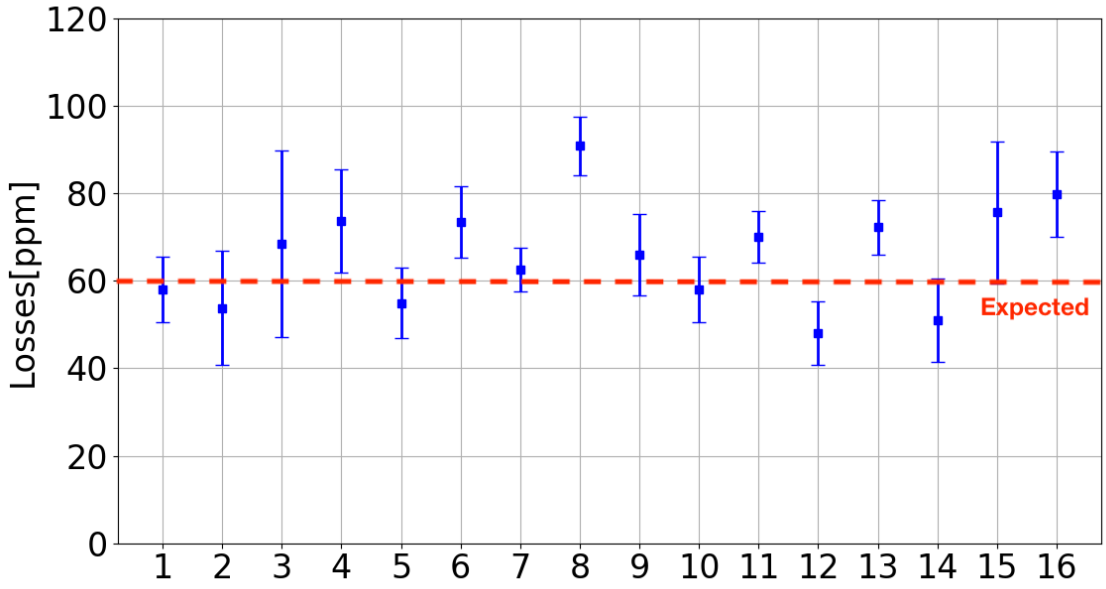

Figure 5.13: Optical losses measured for different alignment condition, the error bar comes from the power RMS deviation

figure 5.13, all the measured values are larger than two years ago. During these two years, the vacuum chambers were opened several times and contamination could have happened. Anyway this larger level of losses was not the liming factor in the achievable frequency dependent squeezing.

measurement day	round trip losses
2019.10.24	100ppm
2020.01.23	148ppm
2020.02.07	122ppm

Table 5.2: Measurement of filter cavity round trip losses on different days

5.3.5 Propagation losses and phase noise

The propagation losses and phase noise was characterized by measuring squeezing and anti-squeezing level at high frequency(10kHz to 100kHz) for different green pump power. The principle of this measurement was introduced in section 4.3.3. The experimental set-up of this measurement is the same with the measurement of FDS (measurement procedure is introduced in appendix D). Therefore, this measurement can tell the information of propagation losses and phase noise for FDS measurement.

The measurement results are plotted in figure 5.14 together with a fit. Comparing with the similar measurement done for frequency independent squeezing measurement, the beam passes through many more optics and some of them are suspended. Therefore propagation losses and phase noise are increased, as expected.

The measured propagation losses is about 40%, which includes about 4% of losses coming from the mode mismatch between squeezing field and local oscillator. Therefore, total propagation losses used for squeezing degradation estimation will be 36% including 1% of error.

The phase noise is taken directly from the fit result, which is 30mrad, with error of 5mrad.

5.3.6 Back scattering noise measurement

As mentioned in chapter 4, back scattering noise can contaminate low frequency measurement. It was also pointed out that the back scattering noise comes from vibrating mirror surface.

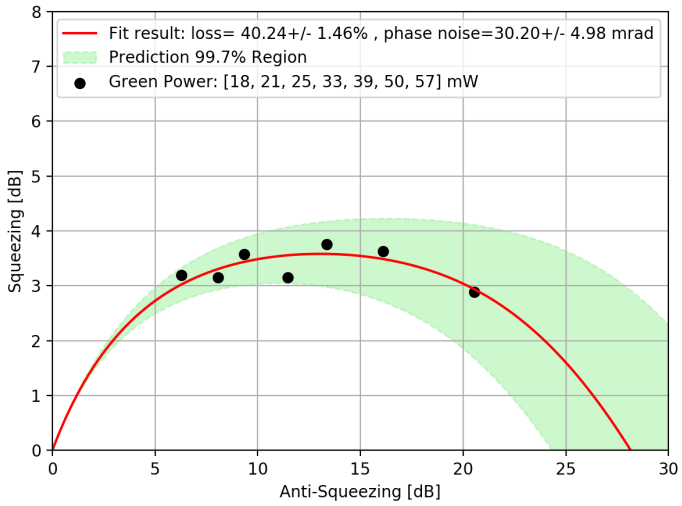

Figure 5.14: Optical losses and phase noise characterization for frequency dependent squeezing measurement.

We observed that back scattering noise varies depending on alignment and amplitude of the mirror motion. A statistic, as shown in figure 5.15, shows back scattering noise varies up to 10dB. The shaded region is the sum of shot noise and a $1/f^2$ noise. In the best condition, we could measure frequency dependent squeezing above 50Hz without contamination of back scattering.

5.4 Measurement of frequency dependent squeezing

As already discussed frequency dependent squeezing is created by reflecting a frequency independent squeezing off a filter cavity and it is then characterized by a balanced homodyne detector. The procedure of this measurement is described in appendix D. Other details of this measurement and results are given in this section.

5.4.1 Frequency dependent squeezing characterization with balanced homodyne detector

Balanced homodyne detector can measure different angle of a squeezed state by setting different local oscillator phase. However, during the measurement, local oscillator needs to be fixed. Therefore, several different measurements are necessary to characterize a frequency dependent squeezed vacuum. Different fixed local oscillator

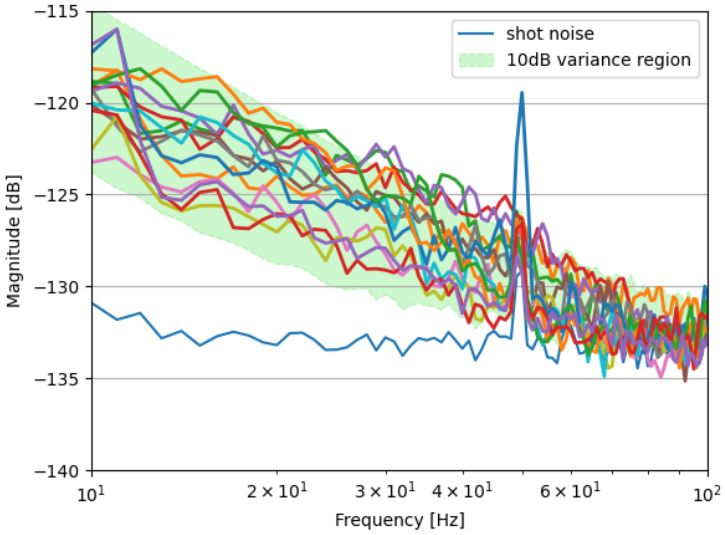

Figure 5.15: Statistic of back scattering noise for frequency dependent squeezing measurement.

phase corresponds to different homodyne angle.

As introduced in chapter 3, frequency dependent squeezing has different squeezing ellipses orientation for different frequencies. This means that when homodyne angle is fixed, it measures the ellipse length (the quatum noise) along this direction at all the frequency. The measurement result will not be flat and the lowest point indicates the highest squeezing level for this homodyne angle.

By using the theoretical model introduced in section 5.2, measurement result can be predicted. In this case, the calculation can be done by using the same equations and setting the transfer matrix of interferometer to be 1. Based also on the characterization done in the last section, the level of squeezing can be also predicted.

An illustration scheme is shown in figure 5.16. A prediction of measurement result is shown in this figure. The lower boundary indicates how much quantum noise can be reduced when this squeezed vacuum source is used in the GW detector.

5.4.2 Frequency dependent squeezing measurement with large detuning

At the beginning, the FDS measurement was done with a large detuning. In fact,the low frequency spectrum is easily covered by classical noise. To confirm the phase changing effect of the filter cavity, a measurement at high frequency is easier. Since

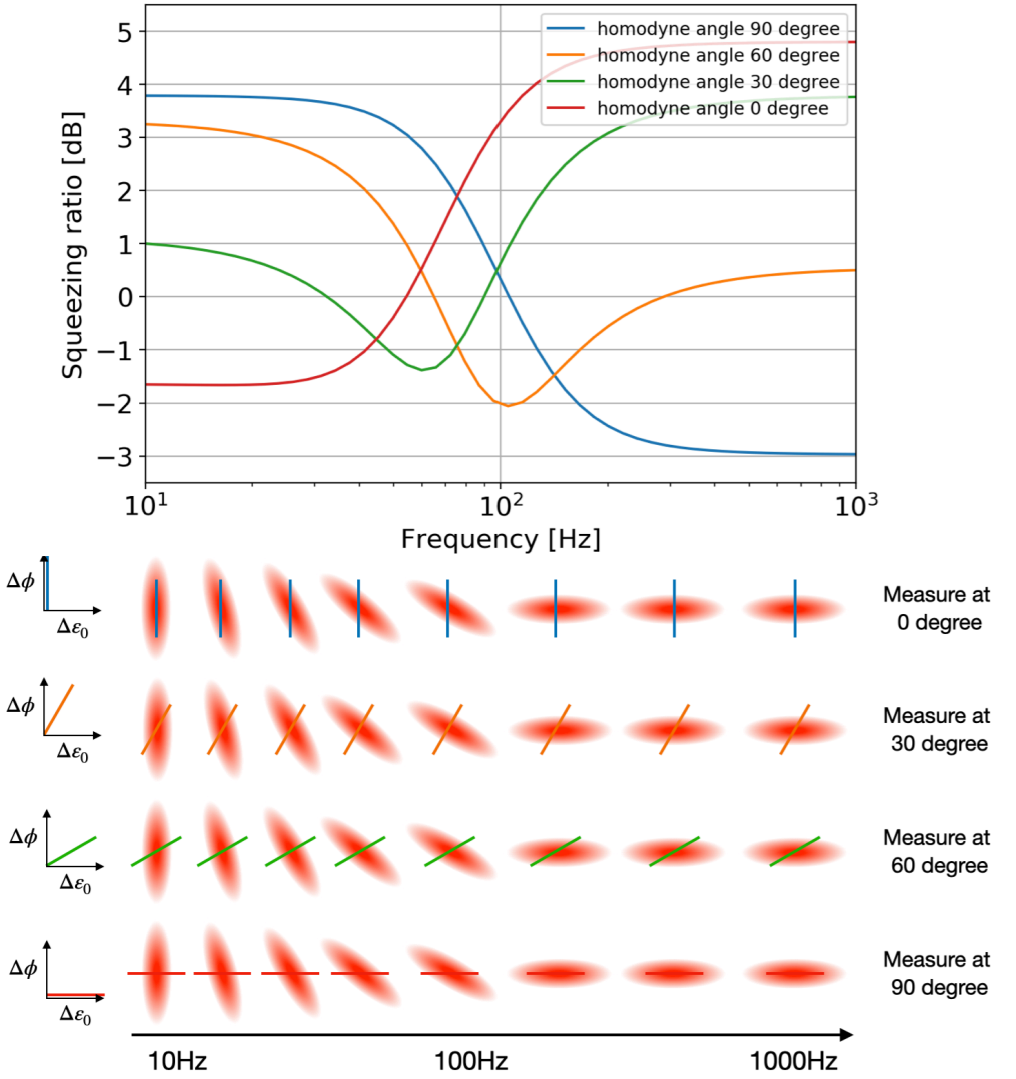

Figure 5.16: **Upper:** Prediction of frequency dependent squeezing measurement in current system with squeezing injection of 8.3dB. Detuning is assumed to be fixed at 90Hz and back scattering noise is not considered. **Lower:** Scheme of the homodyne projection measurement of the squeezing ellipse. Here $\Delta\phi$ is phase fluctuation direction, $\Delta\varepsilon_0$ is amplitude fluctuation direction. The colored line on squeezing ellipses represent the direction along with the squeezing is measured.

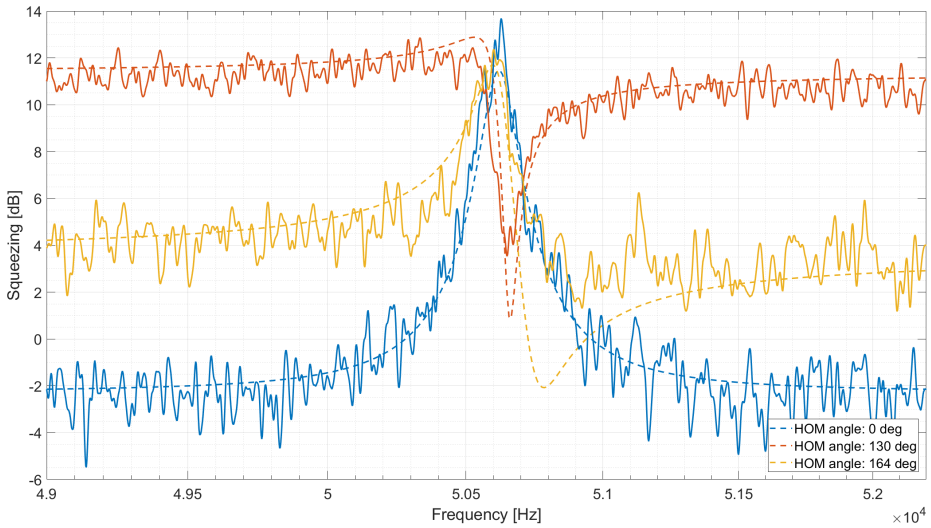

Figure 5.17: The first measurement of frequency dependent squeezing with detuning frequency around 50kHz.

we are sure that high frequency region is quantum noise limited, the fit of measurement result in figure 5.17 will tell us precise information on our system performances.

5.4.3 Frequency dependent squeezing measurement with detuning around 90Hz

After the optimization of the system, we were able to perform the measurement at lower detuning frequency obtaining a rotation frequency at about 90 Hz, as shown in 5.18. A squeezing level of 3.4 ± 0.4 dB above the rotation frequency was measured, along with a squeezing level of at least 1 dB at the rotation frequency and below.

Discussion about detuning and homodyne angle

The values of detuning and homodyne angle shown in figure 5.18 are the result of the fit for each curve. One issue is that detuning of squeezing field is different between each measurement. As already introduced in section 5.3.3, detuning changes when alignment condition is changed and it has a slow drift. These can be explained by the not perfect overlap of green control beam and infrared squeezing field.

In fact a relative misalignment of the squeezed beam with respect to the green beam will not be corrected, as the cavity is locked and kept aligned with respect to the green auxiliary beam. The mechanisms which couple a variation of the alignment with a detuning change are still under investigation. In order to solve these problems,

our team is studying an alternative strategy which uses the already present coherent control field for both length and angular control. [151]. A similar strategy has also been tested in[102].

Discussion about degradation sources

The independent characterization of degradation sources was used to compute the expected measurements plotted as dashed lines in the figure 5.18. The predicted measurement and the real measurement are in very good agreement, which validates the measurement of FDS and the degradation sources characterization.

A summary of degradation sources is shown in table 5.3. For the current system, contribution from different degradation sources can be evaluated from model introduced in section 5.2. The result is shown in figure 5.19. This plot tell us that squeezing level is mainly limited by optical losses at high frequency and mode mismatch at low frequency.

Squeezing degradation parameter	Value
Filter cavity round trip losses	120 ± 30ppm
Propagation losses	36% ± 1%
Mode-mismatch squeezer-filter cavity	6% ± 1%
Mode-mismatch squeezer-local oscillator	2% ± 1%
Filter cavity locking accuracy (rms)	6 ± 1pm
Phase noise	30 ± 5mrad
Produced squeezing	8.3 ± 0.1 dB

Table 5.3: Degradation sources characterization for FDS measurement

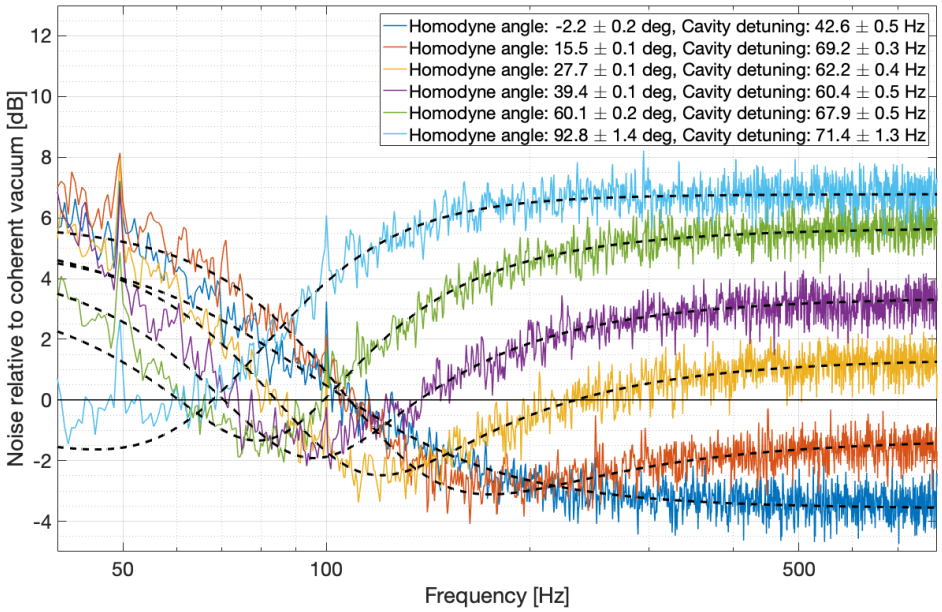

Figure 5.18: Measurement of frequency dependent with different homodyne angle. The dashed line is predicted frequency dependent squeezing level with separately measured system parameters.

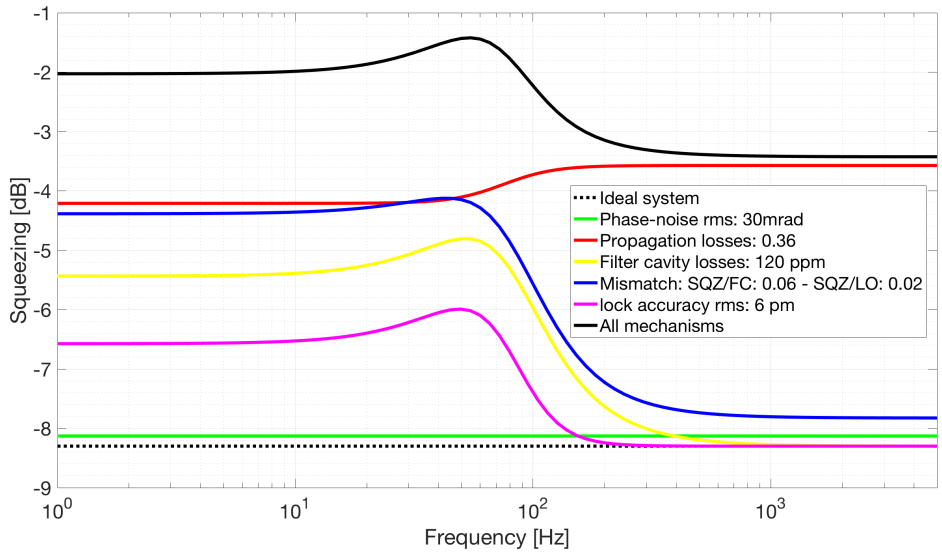

Figure 5.19: Plot of current FDS measurement and contribution of different degradation sources. The top black line indicates the lower bound of FDS measurement at different homodyne angles.

Chapter 6

Frequency dependent squeezing source improvement and its application to gravitational wave detectors

In this chapter, the future improvements of the current frequency dependent squeezed vacuum source will be discussed. In the second part of the chapter, the benefits of the use of this technology in KAGRA will be highlighted.

6.1 On-going improvement for current frequency dependent squeezed vacuum source

A measurement of FDS, which is able to reduce broadband quantum noise in advanced GW detectors was done with the current set-up in TAMA. However, several improvement are planned in order to increase the squeezing level and the stability of the system making it mature for the actual integration in the KAGRA. A summary of the planned improvements is reported below.

6.1.1 Auto-alignment system

Auto alignment system is a widely used technique to maintain the alignment for suspended cavities. It is especially present in advanced gravitational wave detectors where the alignment degree of freedom of several suspended cavities must be

controlled simultaneously. With this system, the injected beam axis and suspended cavity axis will be kept aligned. Currently, a dithering auto-alignment was used in our experiment. This type of control has very low control bandwidth, and therefore is used to compensate mainly long term drifts.

As mentioned in chapter 5, the detuning of the filter cavity depends on its alignment condition. To have stable detuning, an auto-alignment system is necessary. Using wave front sensors (such as position sensitive detector or quadrant photodiodes) to get the alignment error signal will allow for larger control bandwidth compared to the current dithering system and it is expected to solve the problem of power stability and detuning drift of our filter cavity.

6.1.2 Reduction of optical losses

The escape efficiency of OPO is estimated to be around 83% in section 4.3.3. The additional losses compared to the design value are likely due to a non-perfect polishing and coating of the PPKTP crystal. Currently, spare crystals are sent to be polished and coated again. In the future, an improvement of about 15% is expected.

In addition, the in-vacuum Faraday isolator was measured to have about 10% round trip optical losses. The best reported Faraday isolator can have optical losses as low as 1.5% [152]. The realization of a custom Faraday isolator is planned, and a reduction of about 7% of the optical losses is expected.

6.1.3 Filter cavity new locking scheme

A new filter cavity locking scheme for this experiment was proposed by our team [151]. This control use as error signal the CC sidebands also used for the control of the squeezing phase.

According to chapter 4, upper and lower coherent control sidebands (CCSBs) have fixed phase relation due to coherent control loop 1. They propagate together with squeezing beam and arrive at filter cavity. The frequency difference of two CCSBs can be precisely tuned to be double the desirable detuning. In this case, the filter cavity length error signal can be obtained as the beat between the two CCSBs and can be used to lock the filter cavity with the desired detuning.

This locking scheme is expected to be more reliable compared the current locking scheme since CCSBs propagate together with squeezing, therefore it doesn't rely on the overlap between green and infrared beams.

6.1.4 Expected improvement for frequency dependent squeezing

The expected FDS measurement, considering the improvements just discussed, is shown in figure 6.1. Up to 3dB of squeezing at low frequency and 6dB at high frequency are expected. Moreover, a more stable detuning is also expected.

6.2 Potential sensitivity improvement for KAGRA

According to the expected squeezing performances of the filter cavity [149], the improvement in KAGRA sensitivity has been computed, along with the binary neutron star range (using python package inspiral range master [38, 153]). The result is shown in figure 6.2. With the use of FDS, KAGRA can have an improvement of its detection rate for binary neutron stars up to 70%. This correspond to a 5 times improvement of the detection rate (which scales as the detection volume which is the cube of the detection range). In this calculation, only the effect of quantum noise reduction has been considered, while other noises are those expected to achieve the target sensitivity.

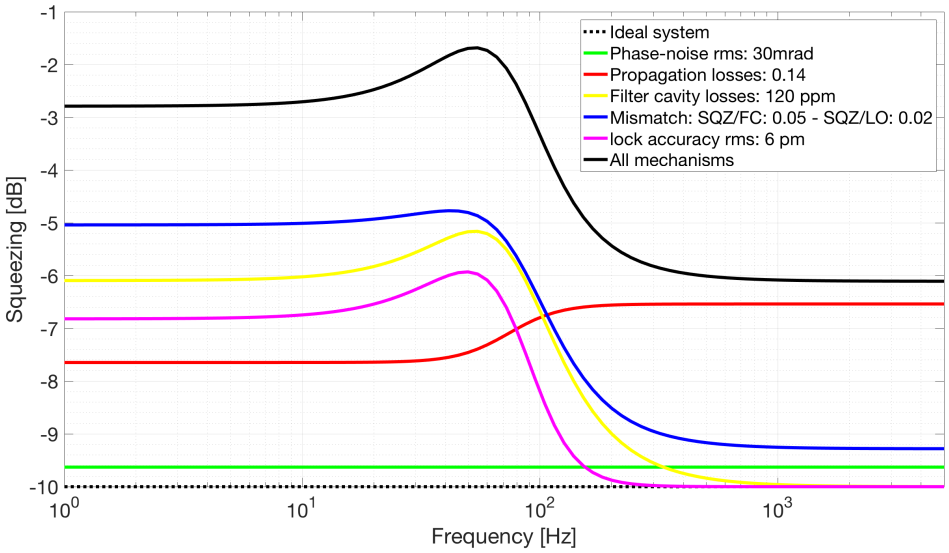

Figure 6.1: Expected degradation budget for future FDS measurement. The black line shows expected FDS measurement. At low frequency 3dB of squeezing and at high frequency 6dB of squeezing are expected.

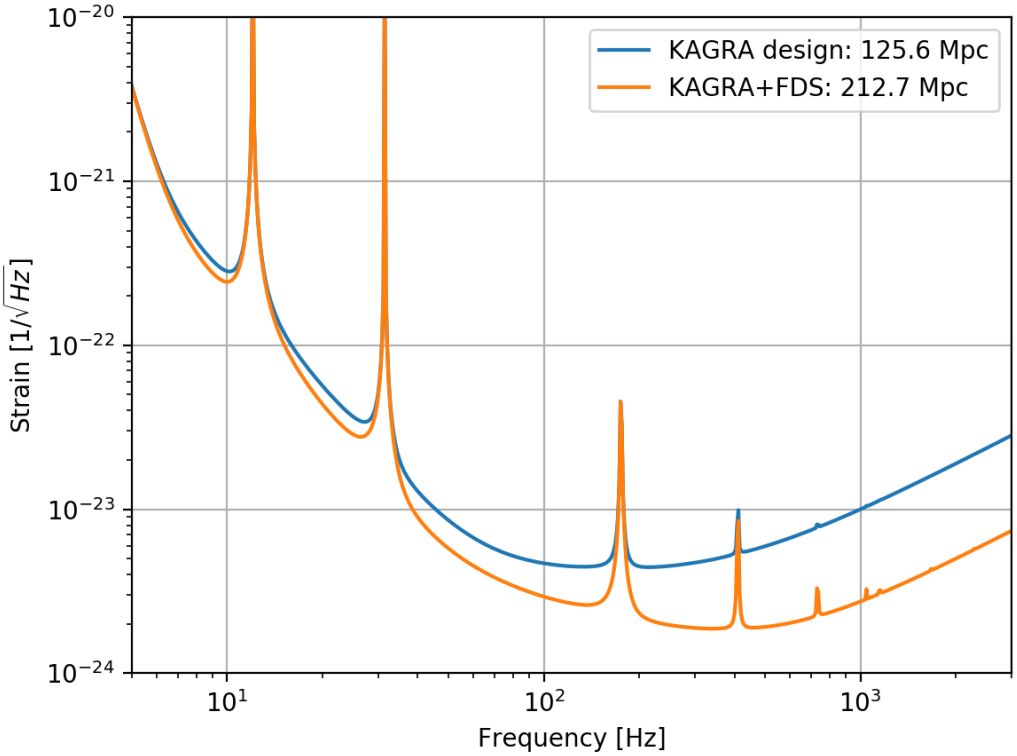

Figure 6.2: Potential sensitivity improvement for KAGRA by using frequency dependent squeezing, the BRSE configuration is assumed. The binary neutron star range of 125.6Mpc is expected to be increased thanks to the use of frequency dependent squeezing up to 212.7Mpc. This is an improvement of 70%. All the noise sources, with the exception of the quantum noise, are kept the same for the two plot.

Conclusion

The era of quantum noise-limited gravitational wave detectors has arrived. To beat this limitation, a frequency dependent squeezed vacuum source using 300m filter cavity was realized and presented in this thesis. My work included the characterization of the filter cavity, the realization of the frequency independent squeezed vacuum source, the injection of the squeezed vacuum into the filter cavity and the consequent measurement of frequency dependent squeezing. A squeezing level of more than 3 dB above the rotation frequency was measured, along with a squeezing level of at least 1dB at the rotation frequency and below. This frequency dependent squeezed vacuum source is best record around the world up to now.

Degradation sources are well understood and the path to increase the squeezing level and its stability is clear. In the near future, FDS will be implemented in advanced gravitational wave detectors, including advanced LIGO, advanced Virgo and KAGRA. In the case of KAGRA, this upgrade is expected to improve the BNS range by 70%.

Even for the next generation GW detectors, frequency dependent squeezing realized with a filter cavity is still the best candidate to reduce quantum noise in the entire detection bandwidth. A requirement of broadband 10dB squeezing is envisaged, which will require an intensive work to reduce squeezing degradation sources and improve the stability of the system.

Appendix A

In this appendix, I give an example about the filter design and characterization.

A general procedure is to first measure opto-mechanical transfer function, then design filters. By modifying corner frequencies of different filters, the requirement of phase margin and gain margin can be fulfilled.

Filters designed for each control servo include several different components. They are

1. **Integrator:** transfer function is $H_{int} = 1 + (1/j)(f_1/f)$ with f_1 as the frequency of zero.

2. **Double integrator:** transfer function is $H_{int2} = 1+(1/j)(f_2/f)+[(1/j)(f_2/f)]^2$ with f_2 as the frequency of zero.

3. **Low pass filter:** transfer function is $H_{lp} = 1/(1 + j * f/f_3)$ with f_3 as the frequency of pole.

4. **Notch filter:** transfer function is is $H_{notch} = [1+(j*f/f_4)^2]/[1+j/Q*f/f_4+(j*f/f_4)^2]$ with f_4 as the frequency of poles and zeros.

A matlab code called virgo2zpk was used in the design of filters. In the code, all filters are described together with their frequency of zero (z), pole (p), gain(k) and quality factor. The plot of opto-mechanical transfer function and the filters overall design is shown in figure 6.3.

After implementing the designed filters in circuit, the open loop transfer function was measured as figure 6.4. This measurement agrees with the simulation done with designed filters.

In the actual implementation, the loop gain can vary a bit around the optimal point. This variation can be due to a power change, for example GRMC is locked to different power according to different application requirement. The gain margin is designed to be 10dB. Therefore, the variation of loop gain should be smaller than

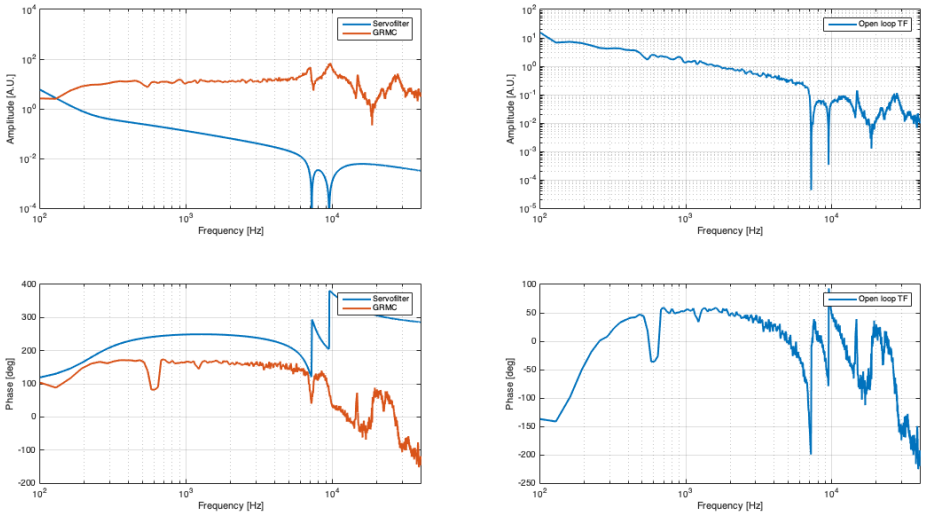

Figure 6.3: Left: measured opto-mechanical transfer function and designed filter for green mode cleaner. Right: the multiplication of left two curves to simulate open loop transfer function.

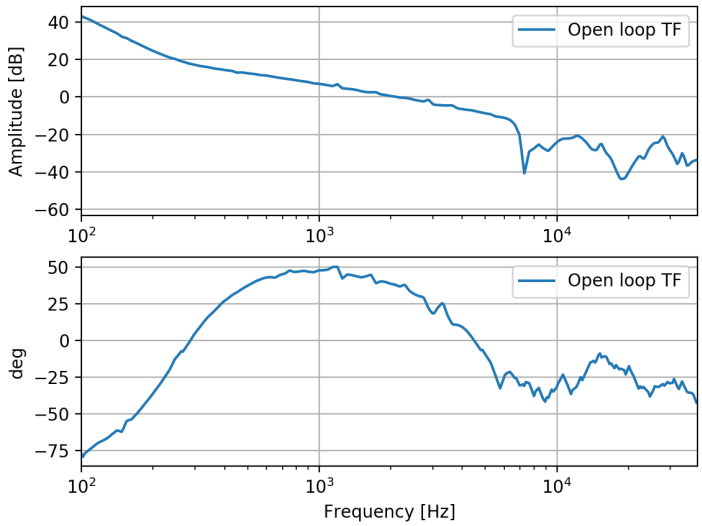

Figure 6.4: Measured open loop transfer function of green mode cleaner

this value. Otherwise, the loop gain needs to be adjusted to maintain the system to be in a stable region.

Appendix B

All RF signals used in the experiment is summarized as following:

- **Two 15.2MHz channels:** One channel is used to drive EOM SHG/IRMC in figure 4.1, which is located just after main laser. The modulated sidebands is used to get the phase information of laser frequency relative to SHG/IRMC cavity length. Beside, it is also used for characterizing filter cavity locking accuracy. The other channel is used as LO for phase detector, which is for the demodulation of RF signals. Although we have at least two channels need to be demodulated, a RF singal power splitter is used to have enough channels.
- **Two 87.6MHz channels:** One channel is used to drive EOM OPO in figure 4.1, which is located after p-pol laser. The modulated sidebands is used to get the phase information of light frequency relative to OPO length. The other channel is used for the demodulation of this signal.
- **Four 78MHz channels:** One channel is used to drive EOM FC/GRMC in figure 4.1, which is located after SHG. The modulated sidebands is used to get the phase information of light frequency relative to filter cavity length and GRMC length. Another two channels are used to do demodulation. Especially, since filter cavity control servo doesn't have phase shifter, the inherent function of phase shifter is used to adjust demodulation phase and have optimal PDH for filter cavity lock. The last channel will be used for wave front sensing technique to achieve filter cavity auto-alignment.
- **Two 7MHz channels:** One channel is used as a local oscillator for CC optical PLL(actually 21MHz). The other is used to do demodulate the beat RF signal between CCSB and homodyne's LO.
- **One 14MHz channel:** It is used to demodulate the beat RF signal between two CCSBs. Since this channel is used for demodulating the second harmonic of 7MHz, it needs to be in the same board with 7MHz channel.

- **One variable channel (change from 32MHz to 56MHz):** This channel is used as a local oscillator for p-pol optical PLL.

Appendix C

The FINESSE code used for simulating power loss due to cavity mirror angular fluctuation is as following:

```
    #laser injection
l laser 0.024 0 n1
s s1 .5 n1 n1a
mod eom1 88M 0.15 2 pm n1a n1b #modulation depth is 0.15
s s2 .5 n1b nbsin
bs BS 0.5 0.5 0 45 nbsin dump nfc nbsout
s s3 1 nfc n2

    #TAMAFC
m ITM 0.993 0.007 0 n2 n3 #input mirror optical property
s sfc 300 n3 n4
m ETM 0.971 0.029 0 n4 n5 #end mirror optical property
attr ITM Rc -436.7 #input mirror geometry
attr ETM Rc 445.1 #end mirror geometry
cav cavfc ITM n3 ETM n4 #define cavity

    #PDr
s sr .5 nbsout npdr
pd ref npdr
pd1 ref1 88M 43.2 npdr

    #PDt
s st .5 n5 npdt
pd tra npdt

    #lock filter cavity
```

```
set err ref1 re
lock z $err 3 10n
put ETM phi $z

    #change cavity mirrors angle
xaxis ITM xbeta lin -8u 8u 100
x2axis ETM xbeta lin -8u 8u 100

    #set maximum mode order to be 3
maxtem 3
```

Appendix D

Detailed procedure to perform frequency dependent squeezing measurement.

1. Lock SHG and confirm that green power sent to filter cavity is the usual value (about 12mW).
2. Engage filter cavity suspension local control. Align filter cavity, lock it and finally engage dithering auto-alignment system.
3. Make sure p-pol beam is sent to OPO and lock OPO.
4. Choose p-pol PLL locking frequency according to the temperature of OPO crystal. Lock p-pol PLL.
5. Make sure BAB is sent to OPO and check BAB power sent to filter cavity is around $400\mu W$. Tune AOM frequency to make BAB on resonance. Check BAB transmission level, which should be around 440 counts. If not, align BAB to reach this level.
6. Check LO alignment into the alignment mode cleaner (AMC).
7. Make sure the signal port is blocked by a beam dump. Lock IRMC and check the shot noise level is the one expected and flat down to 10Hz. If not, align BS of homodyne.
8. Detune BAB by the required detuning frequency (note that frequency change for AOM is the twice of change for detuning. Check BAB alignment relative to AMC and maximize it.
9. Replace BAB with CC and lock CC PLL.
10. Lock Mach-Zehnder and GRMC. After this, green beam is sent to OPO. Usually this alignment is stable since related cavities are fixed on bench. If misaligned, follow the procedure introduced in chapter 4 and realign green pump into OPO.

11. Change p-pol PLL locking frequency by maximizing CC1 error signal. This step can be also used to check if previous steps are done well. The usual CC1 error signal level means squeezing level should be also the same.

12. After locking CC1 and CC2 loop, the frequency dependent squeezing can be measured.

Appendix E

In this appendix, the alignment procedure for OPO and fiber PLL is presented.

Procedure to assembly of the whole OPO cavity:

1. Prepare a beam with a correct beam waist. Make sure the beam is flat both horizontally and vertically. Set a camera to monitor this beam and make a circle on the screen as a reference.

2. Take the crystal part and make light go through this crystal. The crystal part needs to be put on a tilt aligner (Newport 9071). By adjusting the whole crystal part, we need to make sure two things: beam hit the same position on the screen and the injection to crystal HR side needs to overlap with reflection.

3. Put the in-coupling mirror in position and set a photo detector to monitor transmission. While scanning the PZT, adjust the position of the in-coupling mirror. When it is in a good position, the transmission shows a good spectrum. After fixing in-coupling mirror in this good position, the assembly of OPO is finished.

The fiber BS used for mixing main laser and auxiliary laser fields were chosen due to space limitation. The method to couple one laser light into an optical fiber is summarized as follows:

- The incident beam needs to be in a good size, usually the size is provided by manufacture, but needs to be checked by measuring the beam size exciting from fiber collimator.

- The alignment of fiber starts with a large load impedance for fiber photo detector.

- Use multi-mode fiber to align laser into collimator and fiber. Reduce load impedance when there is saturation from PD and then continue to align and maximize transmission.

- After maximizing transmission for multi-mode fiber, replace multi-mode fiber with single-mode fiber.
- While aligning beam into single-mode fiber, there will be several local maximum. Needs to try to find most of local maximum to make sure the real maximum is reached. Usually, the next local maximum of the real maximum is much smaller.
- A half wave plate should be placed in front of the collimator. Rotate half-wave plate to maximize transmission. In the end, the power coupling efficiency reached around 40%.
- After combining beam from main laser and auxiliary laser into fiber BS, there will be beat signal. The optical layout is shown in figure4.15. Fiber BS has two output. One output is used for PLL loop and another is used to monitor beat note on a spectrum analyzer.

Acknowledgement

Looking back these three years in Japan, there are too many people I need to thank for. Without the support of them, the research will be harder to go on.

Firstly, I would like to thank my supervisor Matteo Leonardi for his instruction both on research and life. His tremendous experience on optical experiment and intuitive explanation of physical phenomenon helped me a lot on research. I would like also to thank Eleonora Capocasa, who I always work together with and learn from. She can always find supplement ideas for the experiment and she is rigorous and very kind in every work we did together.

Then I would like to thank my supervisor Raffaele. Without him, I would not have chance to come to Japan and join the experiment of my thesis. I would like also to thank my supervisor Takahashi-san, who takes a lot care of the vacuum system and others about the experiments. My supervisor Aso-san also helped a lot for this experiment, from whom I learn a lot about the situation of KAGRA every week.

During most of the time, I worked together with Aritomi-san, who is a very hard-working student. I learned a lot from him. At the beginning of my PhD, I worked with Tomura-san. His experience and knowledge on optics helped me a lot. During my PhD, Yuefan came to visit many times and we worked and discussed a lot. The life experience of Japan shared from her also helped my a lot. From Marc, I also learned lots of optical skills and the design work of filter cavity. I also worked with younger people during my PhD, for example Eleonora Polini and Pengbo. The questions from them helped me understand experiment even deeper.

We have lots of visitors for this experiment. I learned a lot from Chien-ming and Yao-chin about quantum photonics. Thanks to the invitation of Lee, I visited their lab in NTHU and expended my view. I also had chance to visit INFN LNL and work with Giacomo and Marco Bazzan. This experience helped me explore more about experiment on gravitational wave detection. During the time in INFN, I worked or spent time with Livia, Luca, Jean Pierre, Andrea, Jacopo and Alvise. Thanks for their help and discussion. Pierre designed all circuits for this experiment.

I learnt loop control and circuits from him. Thanks to Matteo Barsuglia and Emil Schreiber helped my experiment at the beginning. Marco Vardaro built PLL for this experiment and taught me a lot about this system. Thanks for Shoda-san for the help in filter cavity suspension system. Thanks for Haoyu for the help on finesse simulation. Thanks for Federico, Irene and Camilla for the environmental characterization done for this experiment. Thanks for Tomaru-san, Akutsu-san and Matsuo-san for the useful comments to improve my thesis.

Although I didn't work a lot with Manuel, we always spend time together in the campus and even during weekends. I learned not only optics knowledge from him, but also lots of Italian. Thanks for Ishizaki-san for taking care of the safty issue of TAMA. And thanks also the help from Hirata-san, Mark, Simon, Okutomi-san, Fujii-san, Tanioka-san and Kuroki-san. Thanks Hayashi-san, Komiyama-san for organizing the observation experiment in Subaru telescope. Thanks Yongming, Yuzhu, Sahoo and Jungha for the discussion on observations.

About the life in Japan, I really would like to thank Shirato-san and Yamanaka-san. They helped a lot on issues such as renting house, register in/out city and others. Thanks also secretaries Inoue-san, Omura-san, Fujimori-san, Yoshizumi-san, Ohyama-san, Harada-san and Ueda-san for the help in lots of paperwork. So that I can focus more on research.

Finally, thanks for my relatives and especially my parents for the always supports.

Bibliography

[1] Eleonora Capocasa, Yuefan Guo, Marc Eisenmann, Yuhang Zhao, Akihiro Tomura, Koji Arai, Yoichi Aso, Manuel Marchiò, Laurent Pinard, Pierre Prat, Kentaro Somiya, Roman Schnabel, Matteo Tacca, Ryutaro Takahashi, Daisuke Tatsumi, Matteo Leonardi, Matteo Barsuglia, and Flaminio Raffaele. Measurement of optical losses in a high-finesse 300 m filter cavity for broadband quantum noise reduction in gravitational-wave detectors. *Physical Review D*, 98(2):022010, 2018.

[2] Yuhang Zhao, Naoki Aritomi, Eleonora Capocasa, Matteo Leonardi, Marc Eisenmann, Yuefan Guo, Eleonora Polini, Akihiro Tomura, Koji Arai, Yoichi Aso, Yao-Chin Huang, Ray-Kuang Lee, Harald L'uck, Osamu Miyakawa, Pierre Prat, Ayaka Shoda, Matteo Tacca, Ryutaro Takahashi, Henning Vahlbruch, Marco Vardaro, Chien-Ming Wu, Matteo Barsuglia, and Raffaele Flaminio. Frequency-dependent squeezed vacuum source for broadband quantum noise reduction in advanced gravitational-wave detectors. *Physical Review Letters*, 124(17):171101, 2020.

[3] Jolien DE Creighton and Warren G Anderson. *Gravitational-wave physics and astronomy: An introduction to theory, experiment and data analysis*. John Wiley & Sons, 2012.

[4] A Einstein. Näherungsweise integration der feldgleichungen der gravitation. sitzungsberichte der königlich preußischen akademie der wissenschaften (berlin). *Translated as "Approximative Integration of the Field Equations of Gravitation," in Alfred Engel (translator) and Engelbert Schucking (consultant), The Collected Papers of Albert Einstein*, 6:1914–1917, 1916.

[5] Gravitation und Elektrizität. Sitzungsberichte der königlich preußischen akademie der wissenschaften zu berlin (1918). *GA II*, pages 29–42.

[6] Benjamin P Abbott, Richard Abbott, TD Abbott, MR Abernathy, Fausto Acernese, Kendall Ackley, Carl Adams, Thomas Adams, Paolo Addesso, RX Adhikari, et al. Observation of gravitational waves from a binary black hole merger. *Physical review letters*, 116(6):061102, 2016.

[7] BP Abbott, R Abbott, TD Abbott, S Abraham, F Acernese, K Ackley, C Adams, RX Adhikari, VB Adya, C Affeldt, et al. Gwtc-1: A gravitational-wave transient catalog of compact binary mergers observed by ligo and virgo during the first and second observing runs. *Physical Review X*, 9(3):031040, 2019.

[8] Sean M Carroll. *Spacetime and geometry*. Cambridge University Press, 2019.

[9] Steven Weinberg. *Cosmology*. Oxford university press, 2008.

[10] Julian Schwinger. *Classical electrodynamics*. CRC Press, 2019.

[11] LIGO Scientific, VIRGO collaborations, BP Abbott, R Abbott, TD Abbott, MR Abernathy, F Acernese, K Ackley, C Adams, T Adams, P Addesso, et al. The basic physics of the binary black hole merger gw150914. *Annalen der Physik*, 529(1-2):1600209, 2017.

[12] Curt Cutler and Kip S Thorne. An overview of gravitational-wave sources. In *General Relativity and Gravitation*, pages 72–111. World Scientific, 2002.

[13] Nelson Christensen. Stochastic gravitational wave backgrounds. *Reports on Progress in Physics*, 82(1):016903, 2018.

[14] Albert A Michelson and Edward W Morley. On the relative motion of the earth and of the luminiferous ether. *Sidereal Messenger, vol. 6, pp. 306-310*, 6:306–310, 1887.

[15] Masaki Ando and Matteo Barsuglia. Fabry–perot cavities and gaussian beams. *Advanced Interferometric Gravitational-Wave Detectors. Volume I: Essentials of Gravitational-Wave Detectors. Edited by Reitze D et al. Published by World Scientific Publishing Co. Pte. Ltd., 2019. ISBN# 9789813146082, pp. 227-255*, pages 227–255, 2019.

[16] Junaid Aasi, BP Abbott, Richard Abbott, Thomas Abbott, MR Abernathy, Kendall Ackley, Carl Adams, Thomas Adams, Paolo Addesso, RX Adhikari, et al. Advanced ligo. *Classical and quantum gravity*, 32(7):074001, 2015.

[17] F Acernese, M Agathos, K Agatsuma, D Aisa, N Allemandou, A Allocca, J Amarni, P Astone, G Balestri, G Ballardin, et al. Advanced virgo: a second-generation interferometric gravitational wave detector. *Classical and Quantum Gravity*, 32(2):024001, 2014.

[18] Masaki Ando, Koji Ishidoshiro, Kazuhiro Yamamoto, Kent Yagi, Wataru Kokuyama, Kimio Tsubono, and Akiteru Takamori. Torsion-bar antenna for low-frequency gravitational-wave observations. *Physical review letters*, 105(16):161101, 2010.

[19] Savas Dimopoulos, Peter W Graham, Jason M Hogan, Mark A Kasevich, and Surjeet Rajendran. Atomic gravitational wave interferometric sensor. *Physical Review D*, 78(12):122002, 2008.

[20] Seiji Kawamura, Takashi Nakamura, Masaki Ando, Naoki Seto, Kimio Tsubono, Kenji Numata, Ryuichi Takahashi, Shigeo Nagano, Takehiko Ishikawa, Mitsuru Musha, et al. The japanese space gravitational wave antenna—decigo. *Classical and Quantum Gravity*, 23(8):S125, 2006.

[21] ES Phinney, Peter Bender, Saps Buchman, Robert Byer, Neil Cornish, Peter Fritschel, William Folkner, Stephen Merkowitz, Karsten Danzmann, Luciano DiFiore, et al. The big bang observer. *NASA Mission Concept Study*, 2003.

[22] Pau Amaro-Seoane, Heather Audley, Stanislav Babak, John Baker, Enrico Barausse, Peter Bender, Emanuele Berti, Pierre Binetruy, Michael Born, Daniele Bortoluzzi, et al. Laser interferometer space antenna. *arXiv preprint arXiv:1702.00786*, 2017.

[23] George Hobbs, A Archibald, Zaven Arzoumanian, D Backer, M Bailes, NDR Bhat, M Burgay, Sarah Burke-Spolaor, D Champion, I Cognard, et al. The international pulsar timing array project: using pulsars as a gravitational wave detector. *Classical and Quantum Gravity*, 27(8):084013, 2010.

[24] PAR Ade, Z Ahmed, RW Aikin, KD Alexander, D Barkats, SJ Benton, CA Bischoff, JJ Bock, R Bowens-Rubin, JA Brevik, et al. Constraints on primordial gravitational waves using p l a n c k, wmap, and new bicep2/k e c k observations through the 2015 season. *Physical review letters*, 121(22):221301, 2018.

[25] Andrea N Lommen. Pulsar timing for gravitational wave detection. *NatAs*, 1:809–811, 2017.

[26] Benjamin P Abbott, Richard Abbott, TD Abbott, MR Abernathy, F Acernese, K Ackley, C Adams, T Adams, P Addesso, RX Adhikari, et al. Astrophysical implications of the binary black hole merger gw150914. *The Astrophysical Journal Letters*, 818(2):L22, 2016.

[27] LIGO Scientific, Virgo Collaborations, BP Abbott, R Abbott, TD Abbott, MR Abernathy, F Acernese, K Ackley, C Adams, T Adams, et al. Tests of general relativity with gw150914. *Physical review letters*, 116(22):221101, 2016.

[28] BP Abbott, R Abbott, TD Abbott, F Acernese, K Ackley, C Adams, T Adams, P Addesso, RX Adhikari, VB Adya, et al. Gw170817: Measurements of neutron star radii and equation of state. *Physical review letters*, 121(16):161101, 2018.

[29] Benjamin P Abbott, R Abbott, TD Abbott, F Acernese, K Ackley, C Adams, T Adams, P Addesso, RX Adhikari, VB Adya, et al. Gravitational waves and gamma-rays from a binary neutron star merger: Gw170817 and grb 170817a. *The Astrophysical Journal Letters*, 848(2):L13, 2017.

[30] LIGO Scientific Collaboration, Virgo Collaboration, 1M2H Collaboration, Dark Energy Camera GW-EM Collaboration, DES Collaboration, DLT40 Collaboration, Las Cumbres Observatory Collaboration, VINROUGE Collaboration, MASTER Collaboration, et al. A gravitational-wave standard siren measurement of the hubble constant. *Nature*, 551(7678):85–88, 2017.

[31] Benjamin P Abbott, R Abbott, TD Abbott, MR Abernathy, K Ackley, C Adams, P Addesso, RX Adhikari, VB Adya, C Affeldt, et al. Exploring the sensitivity of next generation gravitational wave detectors. *Classical and Quantum Gravity*, 34(4):044001, 2017.

[32] Michele Maggiore, Chris Van Den Broeck, Nicola Bartolo, Enis Belgacem, Daniele Bertacca, Marie Anne Bizouard, Marica Branchesi, Sebastien Clesse, Stefano Foffa, Juan García-Bellido, et al. Science case for the einstein telescope. *Journal of Cosmology and Astroparticle Physics*, 2020(03):050, 2020.

[33] Brian J Meers. Recycling in laser-interferometric gravitational-wave detectors. *Physical Review D*, 38(8):2317, 1988.

[34] T Akutsu, M Ando, A Araya, N Aritomi, H Asada, Y Aso, S Atsuta, K Awai, MA Barton, K Cannon, et al. The status of kagra underground cryogenic gravitational wave telescope. In *Journal of Physics: Conference Series*, volume 1342, page 012014. IOP Publishing, 2020.

[35] Masaki Ando, Koji Arai, Ryutaro Takahashi, Gerhard Heinzel, Seiji Kawamura, Daisuke Tatsumi, Nobuyuki Kanda, Hideyuki Tagoshi, Akito Araya, Hideki Asada, et al. Stable operation of a 300-m laser interferometer with sufficient sensitivity to detect gravitational-wave events within our galaxy. *Physical Review Letters*, 86(18):3950, 2001.

[36] Kunihiko Hasegawa, Tomotada Akutsu, Nobuhiro Kimura, Yoshio Saito, Toshikazu Suzuki, Takayuki Tomaru, Ayako Ueda, and Shinji Miyoki. Molecular adsorbed layer formation on cooled mirrors and its impacts on cryogenic gravitational wave telescopes. *Physical Review D*, 99(2):022003, 2019.

[37] Yuta Michimura Kentaro Somiya Kazuhiro Yamamoto Takahiro Yamamoto Yutaro Enomoto, Kentaro Komori. Target sensitivity of bKAGRA. https://gwdoc.icrr.u-tokyo.ac.jp/cgi-bin/private/DocDB/ShowDocument?docid=7038, 2017. [Online; accessed 31-May-2020].

[38] Jolien Creighton Jameson Rollins. GW detector inspiral range calculation tools. https://git.ligo.org/gwinc/inspiral-range/tree/master, 2018. [Online; accessed 31-May-2020].

[39] T Akutsu, M Ando, K Arai, Y Arai, S Araki, A Araya, N Aritomi, Y Aso, S Bae, Y Bae, et al. An arm length stabilization system for kagra and future gravitational-wave detectors. *Classical and Quantum Gravity*, 37(3):035004, 2020.

[40] Herwig Kogelnik and Tingye Li. Laser beams and resonators. *Applied optics*, 5(10):1550–1567, 1966.

[41] Anthony E Siegman. Lasers, chapt. 17, 1986.

[42] Charles Fabry. Theorie et applications d'une nouvelle methods de spectroscopie intereferentielle. *Ann. Chim. Ser. 7*, 16:115–144, 1899.

[43] Patrick Kwee, C Bogan, K Danzmann, M Frede, H Kim, P King, J Pöld, O Puncken, Rick L Savage, F Seifert, et al. Stabilized high-power laser system for the gravitational wave detector advanced ligo. *Optics express*, 20(10):10617–10634, 2012.

[44] Eleonora Capocasa. *Optical and noise studies for Advanced Virgo and filter cavities for quantum noise reduction in gravitational-wave interferometric detectors*. PhD thesis, PhD thesis, Université Paris Diderot, 2017.

[45] Keiko Kokeyama. Status of the input and output optics in kagra phase-2. *JGW-G1808402-v6*, 2018.

[46] ILAN HABER. A Shortcut for Calculating Laser Power Density. https://www.ophiropt.com/blog/laser-measurement/a-shortcut-for-calculating-power-density-of-a-laser-beam/, 2012. [Online; accessed 20-April-2020].

[47] Nur Ismail, Cristine Calil Kores, Dimitri Geskus, and Markus Pollnau. Fabry-pérot resonator: spectral line shapes, generic and related airy distributions, linewidths, finesses, and performance at low or frequency-dependent reflectivity. *Optics express*, 24(15):16366–16389, 2016.

[48] Haixing Miao, Nicolas D Smith, and Matthew Evans. Quantum limit for laser interferometric gravitational-wave detectors from optical dissipation. *Physical Review X*, 9(1):011053, 2019.

[49] Andre Thüring and Nico Lastzka. Jammt-just another mode matching tool." .

[50] JA Arnaud, WM Hubbard, GD Mandeville, B De la Claviere, EA Franke, and JM Franke. Technique for fast measurement of gaussian laser beam parameters. *Applied optics*, 10(12):2775–2776, 1971.

[51] Slawomir Sujecki. *Photonics modelling and design*. CRC press, 2014.

[52] Dana Z Anderson. Alignment of resonant optical cavities. *Applied Optics*, 23(17):2944–2949, 1984.

[53] Julia Casanueva Diaz. *Control of the gravitational wave interferometric detector Advanced Virgo*. Springer, 2018.

[54] Euan Morrison, Brian J Meers, David I Robertson, and Henry Ward. Automatic alignment of optical interferometers. *Applied Optics*, 33(22):5041–5049, 1994.

[55] Euan Morrison, Brian J Meers, David I Robertson, and Henry Ward. Experimental demonstration of an automatic alignment system for optical interferometers. *Applied optics*, 33(22):5037–5040, 1994.

[56] Ilaria Nardecchia. Control of optical aberrations in advanced interferometric gravitational wave detectors. 2017.

[57] Nicolo Pisani. Sviluppo di una lente elettro-ottica per misure di accoppiamento laser-cavita‘ a radiofrequenza. 2017.

[58] E Black. Notes on the pound-drever-hall technique. internal note, ligo, 1998. Technical report, LIGO-T980045-00-D.

[59] Gabriela I González and Peter R Saulson. Brownian motion of a mass suspended by an anelastic wire. *The Journal of the Acoustical Society of America*, 96(1):207–212, 1994.

[60] Gregory M Harry, Andri M Gretarsson, Peter R Saulson, Scott E Kittelberger, Steven D Penn, William J Startin, Sheila Rowan, Martin M Fejer, DRM Crooks, Gianpietro Cagnoli, et al. Thermal noise in interferometric gravitational wave detectors due to dielectric optical coatings. *Classical and Quantum Gravity*, 19(5):897, 2002.

[61] M Evans, Stefan Ballmer, M Fejer, P Fritschel, G Harry, and G Ogin. Thermooptic noise in coated mirrors for high-precision optical measurements. *Physical Review D*, 78(10):102003, 2008.

[62] S Rowan, J Hough, and DRM Crooks. Thermal noise and material issues for gravitational wave detectors. *Physics Letters A*, 347(1-3):25–32, 2005.

[63] Yuta Michimura, Tomofumi Shimoda, Takahiro Miyamoto, Ayaka Shoda, Koki Okutomi, Yoshinori Fujii, Hiroki Tanaka, Mark A Barton, Ryutaro Takahashi, Yoichi Aso, et al. Mirror actuation design for the interferometer control of the kagra gravitational wave telescope. *Classical and Quantum Gravity*, 34(22):225001, 2017.

[64] F Badaracco and J Harms. Optimization of seismometer arrays for the cancellation of newtonian noise from seismic body waves. *Classical and Quantum Gravity*, 36(14):145006, 2019.

[65] Jennifer C Driggers, Jan Harms, and Rana X Adhikari. Subtraction of newtonian noise using optimized sensor arrays. *Physical Review D*, 86(10):102001, 2012.

[66] Donatella Fiorucci, Jan Harms, Matteo Barsuglia, Irene Fiori, and Federico Paoletti. Impact of infrasound atmospheric noise on gravity detectors used for astrophysical and geophysical applications. *Physical Review D*, 97(6):062003, 2018.

[67] Jan Harms. Terrestrial gravity fluctuations. *Living Reviews in Relativity*, 22(1):6, 2019.

[68] Stéphane Brûlé, EH Javelaud, Stefan Enoch, and Sébastien Guenneau. Experiments on seismic metamaterials: molding surface waves. *Physical review letters*, 112(13):133901, 2014.

[69] Herbert B Callen and Theodore A Welton. Irreversibility and generalized noise. *Physical Review*, 83(1):34, 1951.

[70] Yu Levin. Internal thermal noise in the ligo test masses: A direct approach. *Physical Review D*, 57(2):659, 1998.

[71] Yuk Tung Liu and Kip S Thorne. Thermoelastic noise and homogeneous thermal noise in finite sized gravitational-wave test masses. *Physical Review D*, 62(12):122002, 2000.

[72] Yuri Levin. Fluctuation–dissipation theorem for thermo-refractive noise. *Physics Letters A*, 372(12):1941–1944, 2008.

[73] Rana X Adhikari. Gravitational radiation detection with laser interferometry. *Reviews of Modern Physics*, 86(1):121, 2014.

[74] Charlotte Bond, Daniel Brown, Andreas Freise, and Kenneth A Strain. Interferometer techniques for gravitational-wave detection. *Living reviews in relativity*, 19(1):3, 2016.

[75] Walter Schottky. Über spontane stromschwankungen in verschiedenen elektrizitätsleitern. *Annalen der physik*, 362(23):541–567, 1918.

[76] Pierre Meystre, Ewan M Wright, JD McCullen, and E Vignes. Theory of radiation-pressure-driven interferometers. *JOSA B*, 2(11):1830–1840, 1985.

[77] Carlton M Caves. Quantum-mechanical radiation-pressure fluctuations in an interferometer. *Physical Review Letters*, 45(2):75, 1980.

[78] Carlton M Caves. Quantum-mechanical noise in an interferometer. *Physical Review D*, 23(8):1693, 1981.

[79] R_E Slusher, LW Hollberg, Bernard Yurke, JC Mertz, and JF Valley. Observation of squeezed states generated by four-wave mixing in an optical cavity. *Physical Review Letters*, 55(22):2409, 1985.

[80] Ling-An Wu, HJ Kimble, JL Hall, and Huifa Wu. Generation of squeezed states by parametric down conversion. *Physical review letters*, 57(20):2520, 1986.

[81] Philippe Grangier, RE Slusher, B Yurke, and A LaPorta. Squeezed-light–enhanced polarization interferometer. *Physical review letters*, 59(19):2153, 1987.

[82] Min Xiao, Ling-An Wu, and H Jeffrey Kimble. Precision measurement beyond the shot-noise limit. *Physical review letters*, 59(3):278, 1987.

[83] Henning Vahlbruch, Moritz Mehmet, Karsten Danzmann, and Roman Schnabel. Detection of 15 db squeezed states of light and their application for the absolute calibration of photoelectric quantum efficiency. *Physical review letters*, 117(11):110801, 2016.

[84] M Mehmet and H Vahlbruch. High-efficiency squeezed light generation for gravitational wave detectors. *Classical and Quantum Gravity*, 36(1):015014, 2018.

[85] J Abadie, Benjamin P Abbott, R Abbott, Thomas D Abbott, M Abernathy, Carl Adams, R Adhikari, Christoph Affeldt, B Allen, GS Allen, et al. A gravitational wave observatory operating beyond the quantum shot-noise limit. *Nature Physics*, 7(12):962, 2011.

[86] M Tse, Haocun Yu, N Kijbunchoo, A Fernandez-Galiana, P Dupej, L Barsotti, CD Blair, DD Brown, SE Dwyer, A Effler, et al. Quantum-enhanced advanced

ligo detectors in the era of gravitational-wave astronomy. *Physical Review Letters*, 123(23):231107, 2019.

[87] F Acernese, M Agathos, L Aiello, A Allocca, A Amato, S Ansoldi, S Antier, M Arène, N Arnaud, S Ascenzi, et al. Increasing the astrophysical reach of the advanced virgo detector via the application of squeezed vacuum states of light. *Physical Review Letters*, 123(23):231108, 2019.

[88] H Jeff Kimble, Yuri Levin, Andrey B Matsko, Kip S Thorne, and Sergey P Vyatchanin. Conversion of conventional gravitational-wave interferometers into quantum nondemolition interferometers by modifying their input and/or output optics. *Physical Review D*, 65(2):022002, 2001.

[89] Alessandra Buonanno and Yanbei Chen. Quantum noise in second generation, signal-recycled laser interferometric gravitational-wave detectors. *Physical Review D*, 64(4):042006, 2001.

[90] Sheila Dwyer. Limits of high power. *LIGO-DDC-G1700843*, 2017.

[91] Henning Vahlbruch. *Squeezed light for gravitational wave astronomy*. PhD thesis, Gottfried Wilhelm Leibniz Universität Hannover Hannover, Germany, 2008.

[92] Carlton M Caves and Bonny L Schumaker. New formalism for two-photon quantum optics. i. quadrature phases and squeezed states. *Physical Review A*, 31(5):3068, 1985.

[93] Mark Fox. *Quantum optics: an introduction*, volume 15. OUP Oxford, 2006.

[94] Eric Glenn Oelker. *Squeezed states for advanced gravitational wave detectors*. PhD thesis, Massachusetts Institute of Technology, 2016.

[95] Daniel F Walls and Gerard J Milburn. *Quantum optics*. Springer Science & Business Media, 2007.

[96] Patrick Kwee, John Miller, Tomoki Isogai, Lorenzo Barsotti, and Matthew Evans. Decoherence and degradation of squeezed states in quantum filter cavities. *Physical Review D*, 90(6):062006, 2014.

[97] J Robert Johansson, PD Nation, and Franco Nori. Qutip: An open-source python framework for the dynamics of open quantum systems. *Computer Physics Communications*, 183(8):1760–1772, 2012.

[98] Emil Schreiber. *Gravitational-wave detection beyond the quantum shot-noise limit: the integration of squeezed light in GEO 600*. PhD thesis, Laser Interferometry & Gravitational Wave Astronomy, AEI-Hannover, MPI for ⋯, 2018.

[99] Hermann A Haus. *Electromagnetic noise and quantum optical measurements*. Springer Science & Business Media, 2012.

[100] MS Stefszky, CM Mow-Lowry, SSY Chua, DA Shaddock, BC Buchler, H Vahlbruch, A Khalaidovski, R Schnabel, Pa K Lam, and DE McClelland. Balanced homodyne detection of optical quantum states at audio-band frequencies and below. *Classical and Quantum Gravity*, 29(14):145015, 2012.

[101] Simon Chelkowski, Henning Vahlbruch, Boris Hage, Alexander Franzen, Nico Lastzka, Karsten Danzmann, and Roman Schnabel. Experimental characterization of frequency-dependent squeezed light. *Physical Review A*, 71(1):013806, 2005.

[102] L McCuller, C Whittle, D Ganapathy, K Komori, M Tse, A Fernandez-Galiana, L Barsotti, P Fritschel, M MacInnis, F Matichard, et al. Frequency-dependent squeezing for advanced ligo. *Physical Review Letters*, 124(17):171102, 2020.

[103] Travis Horrom, Gleb Romanov, Irina Novikova, and Eugeniy E Mikhailov. All-atomic generation and noise-quadrature filtering of squeezed vacuum in hot rb vapor. *Journal of Modern Optics*, 60(1):43–49, 2013.

[104] Neil V Corzo, Quentin Glorieux, Alberto M Marino, Jeremy B Clark, Ryan T Glasser, and Paul D Lett. Rotation of the noise ellipse for squeezed vacuum light generated via four-wave mixing. *Physical Review A*, 88(4):043836, 2013.

[105] Jiayi Qin, Chunnong Zhao, Yiqiu Ma, Xu Chen, Li Ju, and David G Blair. Classical demonstration of frequency-dependent noise ellipse rotation using optomechanically induced transparency. *Physical Review A*, 89(4):041802, 2014.

[106] Min Jet Yap, Paul Altin, Terry G McRae, Bram JJ Slagmolen, Robert L Ward, and David E McClelland. Generation and control of frequency-dependent squeezing via einstein–podolsky–rosen entanglement. *Nature Photonics*, 14(4):223–226, 2020.

[107] Horace P Yuen. Two-photon coherent states of the radiation field. *Physical Review A*, 13(6):2226, 1976.

[108] Michael A Taylor, Jiri Janousek, Vincent Daria, Joachim Knittel, Boris Hage, Hans-A Bachor, and Warwick P Bowen. Subdiffraction-limited quantum imaging within a living cell. *Physical Review X*, 4(1):011017, 2014.

[109] Kasper Jensen, Wojciech Wasilewski, Hanna Krauter, Thomas Fernholz, Bo Melholt Nielsen, M Owari, Martin B Plenio, A Serafini, MM Wolf, and ES Polzik. Quantum memory for entangled continuous-variable states. *Nature Physics*, 7(1):13–16, 2011.

[110] Mile Gu, Christian Weedbrook, Nicolas C Menicucci, Timothy C Ralph, and Peter van Loock. Quantum computing with continuous-variable clusters. *Physical Review A*, 79(6):062318, 2009.

[111] Tobias Gehring, Vitus Händchen, Jörg Duhme, Fabian Furrer, Torsten Franz, Christoph Pacher, Reinhard F Werner, and Roman Schnabel. Implementation of continuous-variable quantum key distribution with composable and one-sided-device-independent security against coherent attacks. *Nature communications*, 6(1):1–7, 2015.

[112] Warwick P Bowen, Nicolas Treps, Ben C Buchler, Roman Schnabel, Timothy C Ralph, Hans-A Bachor, Thomas Symul, and Ping Koy Lam. Experimental investigation of continuous-variable quantum teleportation. *Physical Review A*, 67(3):032302, 2003.

[113] Henning Vahlbruch, Simon Chelkowski, Boris Hage, Alexander Franzen, Karsten Danzmann, and Roman Schnabel. Coherent control of vacuum squeezing in the gravitational-wave detection band. *Physical review letters*, 97(1):011101, 2006.

[114] Henning Vahlbruch, Moritz Mehmet, Simon Chelkowski, Boris Hage, Alexander Franzen, Nico Lastzka, Stefan Gossler, Karsten Danzmann, and Roman Schnabel. Observation of squeezed light with 10-db quantum-noise reduction. *Physical review letters*, 100(3):033602, 2008.

[115] EG Sauter. *Nonlinear optics*, volume 44. John Wiley & Sons, 1996.

[116] Bahaa EA Saleh and Malvin Carl Teich. *Fundamentals of photonics*. john Wiley & sons, 2019.

[117] Ichiro Shoji, Takashi Kondo, Ayako Kitamoto, Masayuki Shirane, and Ryoichi Ito. Absolute scale of second-order nonlinear-optical coefficients. *JOSA B*, 14(9):2268–2294, 1997.

[118] VA Akulov, SA Babin, SI Kablukov, and KS Raspopin. Intracavity frequency doubling of yb-doped fiber laser with 540–550 nm tuning. *Laser Physics*, 21(5):935–939, 2011.

[119] Matteo Leonardi. *Development of a squeezed light source prototype for Advanced Virgo*. PhD thesis, University of Trento, 2016.

[120] O Gayer, Z Sacks, E Galun, and A Arie. Temperature and wavelength dependent refractive index equations for mgo-doped congruent and stoichiometric linbo 3. *Applied Physics B*, 91(2):343–348, 2008.

[121] Advanced Virgo Squeezing Working Group et al. Advanced virgo squeezer technical design report. *Virgo internal note*, 2015.

[122] Yuefan Guo. *An experiment to test the production of the frequency dependent squeezed vacuum states for the KAGRA gravitational wave detector*. PhD thesis, PhD thesis, Beijing Normal University, 2017.

[123] FJ Raab and SE Whitcomb. Estimation of special optical properties of a triangular ring cavity. *LIGO-T920004*, 1992.

[124] GA Massey and AE Siegman. Reflection and refraction of gaussian light beams at tilted ellipsoidal surfaces. *Applied optics*, 8(5):975–978, 1969.

[125] Henning Vahlbruch, Simon Chelkowski, Karsten Danzmann, and Roman Schnabel. Quantum engineering of squeezed states for quantum communication and metrology. *New Journal of Physics*, 9(10):371, 2007.

[126] Keisuke Goda, Eugeniy E Mikhailov, Osamu Miyakawa, Shailendhar Saraf, Stephen Vass, Alan Weinstein, and Nergis Mavalvala. Generation of a stable low-frequency squeezed vacuum field with periodically poled ktiopo 4 at 1064 nm. *Optics letters*, 33(2):92–94, 2008.

[127] Marco Vardaro. Toward a fully automated and digitally controlled squeezed vacuum source. 2018.

[128] Giacomo Ciani. Coherent Control phase scans. https://logbook.virgo-gw.eu/virgo/?r=44285, 2019. [Online; accessed 21-June-2020].

[129] Crispin W Gardiner and MJ Collett. Input and output in damped quantum systems: Quantum stochastic differential equations and the master equation. *Physical Review A*, 31(6):3761, 1985.

[130] Jöran Bauchrowitz, Tobias Westphal, and Roman Schnabel. A graphical description of optical parametric generation of squeezed states of light. *American Journal of Physics*, 81(10):767–771, 2013.

[131] Eric O. LEBIGOT. Uncertainties: a Python package for calculations with uncertainties. https://pythonhosted.org/uncertainties/, 2016. [Online; accessed 28-April-2020].

[132] ES Polzik, J Carri, and HJ Kimble. Atomic spectroscopy with squeezed light for sensitivity beyond the vacuum-state limit. *Applied Physics B*, 55(3):279–290, 1992.

[133] Tomoki Isogai. *Applications of long storage time optical cavities*. PhD thesis, Massachusetts Institute of Technology, 2016.

[134] Jürgen Appel, Dallas Hoffman, Eden Figueroa, and AI Lvovsky. Electronic noise in optical homodyne tomography. *Physical Review A*, 75(3):035802, 2007.

[135] K Wodkiewicz and M Suhail Zubairy. Effect of laser fluctuations on squeezed states in a degenerate parametric amplifier. *Physical Review A*, 27(4):2003, 1983.

[136] David D Crouch and Samuel L Braunstein. Limitations to squeezing in a parametric amplifier due to pump quantum fluctuations. *Physical Review A*, 38(9):4696, 1988.

[137] S Dwyer, L Barsotti, SSY Chua, M Evans, M Factourovich, D Gustafson, T Isogai, K Kawabe, A Khalaidovski, PK Lam, et al. Squeezed quadrature fluctuations in a gravitational wave detector using squeezed light. *Optics express*, 21(16):19047–19060, 2013.

[138] Takao Aoki, Go Takahashi, and Akira Furusawa. Squeezing at 946nm with periodically poled ktiopo 4. *Optics express*, 14(15):6930–6935, 2006.

[139] SSY Chua, Sheila Dwyer, L Barsotti, D Sigg, RMS Schofield, VV Frolov, Keita Kawabe, M Evans, GD Meadors, M Factourovich, et al. Impact of

backscattered light in a squeezing-enhanced interferometric gravitational-wave detector. *Classical and Quantum Gravity*, 31(3):035017, 2014.

[140] Kirk McKenzie, Daniel A Shaddock, David E McClelland, Ben C Buchler, and Ping Koy Lam. Experimental demonstration of a squeezing-enhanced power-recycled michelson interferometer for gravitational wave detection. *Physical review letters*, 88(23):231102, 2002.

[141] Henning Vahlbruch, Simon Chelkowski, Boris Hage, Alexander Franzen, Karsten Danzmann, and Roman Schnabel. Demonstration of a squeezed-light-enhanced power-and signal-recycled michelson interferometer. *Physical review letters*, 95(21):211102, 2005.

[142] Keisuke Goda, Osamu Miyakawa, Eugeniy E Mikhailov, Shailendhar Saraf, Rana Adhikari, Kirk McKenzie, Robert Ward, Steve Vass, Alan J Weinstein, and Nergis Mavalvala. A quantum-enhanced prototype gravitational-wave detector. *Nature Physics*, 4(6):472–476, 2008.

[143] Tobias Eberle, Sebastian Steinlechner, Jöran Bauchrowitz, Vitus Händchen, Henning Vahlbruch, Moritz Mehmet, Helge Müller-Ebhardt, and Roman Schnabel. Quantum enhancement of the zero-area sagnac interferometer topology for gravitational wave detection. *Physical review letters*, 104(25):251102, 2010.

[144] Haocun Yu, L McCuller, M Tse, L Barsotti, N Mavalvala, J Betzwieser, CD Blair, SE Dwyer, A Effler, M Evans, et al. Quantum correlations between the light and kilogram-mass mirrors of ligo. *arXiv preprint arXiv:2002.01519*, 2020.

[145] Eric Oelker, Tomoki Isogai, John Miller, Maggie Tse, Lisa Barsotti, Nergis Mavalvala, and Matthew Evans. Audio-band frequency-dependent squeezing for gravitational-wave detectors. *Physical review letters*, 116(4):041102, 2016.

[146] Matt Abernathy, F Acernese, P Ajith, B Allen, P Amaro Seoane, N Andersson, S Aoudia, P Astone, B Krishnan, L Barack, et al. Einstein gravitational wave telescope conceptual design study. 2011.

[147] D Sigg et. al. N Kijbunchoo, T McRae. Low phase noise squeezed vacuum for future generation gravitational wave detectors. *LIGO-P2000064*, 2020.

[148] R Takahashi, F Kuwahara, E Majorana, Mark A Barton, T Uchiyama, K Kuroda, A Araya, K Arai, A Takamori, M Ando, et al. Vacuum-compatible vibration isolation stack for an interferometric gravitational wave detector tama300. *Review of scientific instruments*, 73(6):2428–2433, 2002.

[149] Eleonora Capocasa, Matteo Barsuglia, Jérôme Degallaix, Laurent Pinard, Nicolas Straniero, Roman Schnabel, Kentaro Somiya, Yoichi Aso, Daisuke Tatsumi, and Raffaele Flaminio. Estimation of losses in a 300 m filter cavity and quantum noise reduction in the kagra gravitational-wave detector. *Physical Review D*, 93(8):082004, 2016.

[150] Daniel David Brown and Andreas Freise. Pykat, July 2017. http://www.gwoptics.org/pykat.

[151] Naoki Aritomi, Matteo Leonardi, Eleonora Capocasa, Yuhang Zhao, and Raffaele Flaminio. Control of a filter cavity with coherent control sidebands. *Phys. Rev. D*, 102:042003, Aug 2020.

[152] Eric Genin, Maddalena Mantovani, Gabriel Pillant, Camilla De Rossi, Laurent Pinard, Christophe Michel, Matthieu Gosselin, and Julia Casanueva. Vacuum-compatible low-loss faraday isolator for efficient squeezed-light injection in laser-interferometer-based gravitational-wave detectors. *Applied optics*, 57(32):9705–9713, 2018.

[153] Hsin-Yu Chen, Daniel E Holz, John Miller, Matthew Evans, Salvatore Vitale, and Jolien Creighton. Distance measures in gravitational-wave astrophysics and cosmology. *arXiv preprint arXiv:1709.08079*, 2017.